

Femtochemistry of Pericyclic Reactions and Advances towards Chiral Control

Dissertation zur Erlangung des naturwissenschaftlichen Doktorgrades
der
Julius-Maximilians-Universität Würzburg

vorgelegt von
Johannes Buback

aus Göttingen

Würzburg 2011

Eingereicht bei der Fakultät für Chemie und Pharmazie am

Gutachter der schriftlichen Arbeit

1. Gutachter: Prof. Dr. T. Brixner

2. Gutachter: _____

Prüfer des öffentlichen Promotionskolloquiums

1. Prüfer: Prof. Dr. T. Brixner

2. Prüfer: _____

3. Prüfer: _____

Datum des Promotionskolloquiums

Doktorurkunde ausgehändigt am

List of Publications

The material of Chapter 4 and Chapter 5 has been published in the following references:

Chapter 4:

M. Kullmann, S. Ruetzel, J. Buback, P. Nuernberger, and T. Brixner
Reaction Dynamics of a Molecular Switch Unveiled by Coherent Two-Dimensional Electronic Spectroscopy,
J. Am. Chem. Soc. **133**, 13074 (2011).

J. Buback, P. Nuernberger, M. Kullmann, R. Schmidt, F. Würthner, and T. Brixner
Ring-Closure and Isomerization Capabilities of Spiropyran-Derived Merocyanine Isomers,
J. Phys. Chem. A **115**, 3924 (2011).

J. Buback, M. Kullmann, P. Nuernberger, R. Schmidt, F. Würthner, and T. Brixner
Ultrafast bidirectional photoswitching of a spiropyran,
J. Am. Chem. Soc. **46**, 16510 (2010).

Chapter 5:

P. Rudolf, J. Buback, P. Nuernberger, and T. Brixner,
Ultrafast Multisequential Photochemistry of 5-Diazo Meldrums Acid,
J. Am. Chem. Soc. **43**, 15213 (2010).

The material of Chapter 6, Chapter 7 and Appendix B is currently being prepared for publication.

Contents

List of Publications	iii
1 Introduction	1
2 Theory	5
2.1 Ultrashort laser pulses	5
2.1.1 Time dependence	6
2.1.2 Spatial dependence	10
2.2 Polarization in the Jones formalism	11
2.2.1 Polarization	12
2.2.2 Jones formalism	15
2.2.3 Circular-dichroitic media in the Jones formalism	18
2.2.4 Jones calculation in three dimensions	19
2.3 Optical effects of chirality	22
2.3.1 Circular dichroism	22
2.3.2 Optical rotatory dispersion	24
2.3.3 Enantiomeric purity	25
2.4 State and state-change of molecules	25
2.4.1 Born–Oppenheimer approximation	26
2.4.2 Molecular orbitals	27
2.4.3 Vibrational coupling	31
2.4.4 Radiative transitions	33
2.4.5 Potential surface crossing	34
2.5 Pericyclic reactions	35
2.5.1 Frontier molecular orbitals	36
2.5.2 Pericyclic reactions in the FMO picture	38
2.5.3 Conservation of orbital symmetry	40
2.5.4 Electrocyclic reactions	44
2.5.5 Sigmatropic rearrangements	45
3 Techniques	47
3.1 Transient absorption	47
3.1.1 Pump–probe spectroscopy	47
3.1.2 Observable signals	48
3.1.3 Time evolution of the signals	50
3.1.4 Anisotropy with linearly polarized pulses	53
3.1.5 Experimental realization	55

3.2	Generation of ultrashort laser pulses	57
3.2.1	Laser system	57
3.2.2	Nonlinear polarization	58
3.2.3	Frequency conversion	58
3.3	Accumulative spectroscopy	60
3.3.1	Accumulation principle	60
3.3.2	Pros and cons	61
3.3.3	Experimental setup	62
3.3.4	Calibration	63
4	An electrocyclic reaction: The spiropyran–merocyanine system	67
4.1	Introduction	67
4.2	Steady state	69
4.3	Ring open: merocyanine	69
4.3.1	Experimental methods	70
4.3.2	Experimental data	71
4.3.3	Data modeling	77
4.3.4	Modeling results	82
4.3.5	Temporal model 1: No isomerization	83
4.3.6	Temporal model 2: Isomerization through conical intersection	86
4.3.7	Temporal model 3: Isomerization in the excited state	89
4.3.8	Validation of the modeling	91
4.3.9	Discussion: Isomerization	92
4.3.10	Summary: Ring-open form	93
4.4	Ring closed: spiropyran	93
4.4.1	Experimental methods	94
4.4.2	Experimental data	94
4.4.3	Quantum efficiency	94
4.5	Bidirectional switching	96
4.5.1	Experimental methods	96
4.5.2	Experimental data	98
4.5.3	Spectral shape	100
4.5.4	Speed	101
4.5.5	Discussion: Ring closure	102
4.5.6	Discussion: Ring opening	103
4.6	Photochemistry of 6,8-dinitro BIPS	105
4.6.1	Insights into the electrocyclic reaction	105
4.6.2	Insights into the cis/trans isomerization	107
5	A sigmatropic rearrangement: The Wolff rearrangement of DMA	109
5.1	Introduction	109
5.2	Experimental and theoretical methods	110
5.3	Reaction channels identification by steady-state absorption	111
5.4	DFT results for the permanent products	112
5.5	Transient absorption in the mid-infrared	114
5.5.1	Experimental data	115

5.5.2	DMA bleaching	117
5.5.3	Intermediate ketene	118
5.5.4	Enol	118
5.5.5	Ester	120
5.5.6	Diazirine	121
5.5.7	Unidentified species	123
5.5.8	Vibrational cooling	125
5.6	Photochemistry scheme	125
5.7	Insights into the sigmatropic rearrangement	127
6	Enantiodifferentiating photodissociation of methyl p-tolyl sulfoxide	129
6.1	Introduction	129
6.2	Experimental setup	130
6.3	Data acquisition	132
6.4	Relation of the phase to the optical rotation angle	133
6.4.1	Angle amplification	135
6.5	Polarimeter response function	136
6.5.1	Instrument response	136
6.5.2	Total response	138
6.6	Steady-state properties and photoinduced reaction	138
6.7	Exemplary data and their interpretation	138
6.8	Influence of experimental parameters	141
6.8.1	Enantiomer	141
6.8.2	Concentration	141
6.8.3	Pulse energy	141
6.8.4	Solvent	141
6.9	Optical rotation angle and time resolution	142
6.10	Summary	144
7	Polarization-shaped pump–probe experiments for chiral control	145
7.1	Introduction	145
7.2	Setup for polarization mirroring	148
7.2.1	Mirror image of a polarization state	148
7.2.2	Principle idea	149
7.2.3	Collinear recombination	149
7.2.4	Polarization independence	151
7.2.5	Setup	152
7.3	Anisotropy dependent on polarization	153
7.3.1	Pumped distribution	154
7.3.2	Probing probability	156
7.3.3	Anisotropy-free conditions	157
7.3.4	Anisotropy-free conditions combined with pulse shaping and polarization mirroring	159
7.3.5	Suggestion for experimental realization	162
7.4	Ground-state circular-dichroism experiment	164
7.4.1	Simulation description	164

7.4.2	Alignment errors	168
7.4.3	Multiphoton processes	174
7.5	Transient enantiosensitive signals	176
7.5.1	Transient circular dichroism	177
7.5.2	Transient optical rotatory dispersion	178
7.6	Field of application of the accumulative and the pump–probe scheme . .	180
8	Summary and Outlook	181
9	Zusammenfassung und Ausblick	185
A	Relation of extinction coefficient and maximum pump–probe signal	189
B	Anisotropy in pump–probe experiments	193
B.1	Derivation of anisotropy formula for 1-photon processes	193
B.2	Rotation of molecules	200
B.2.1	Rotational diffusion	200
B.2.2	Alignment and orientation of molecules	201
B.3	Multi-photon processes	204
B.4	Magic-angle conditions	205
B.4.1	Linearly polarized pump pulses	205
B.4.2	Circularly polarized pump pulses	206
B.4.3	Arbitrarily polarized pump pulses	206
B.5	Anisotropy of degenerate transition dipole moments	207
B.5.1	Degenerate pump transition dipole moments	207
B.5.2	Degenerate probe transition dipole moments	209
B.6	Anisotropy in pump–repump–probe experiments	211
B.7	Experimental realization	214
C	Jones matrix of symmetric beamsplitters	217
	Bibliography	223
	Acknowledgements	241
	Lebenslauf	243

1 Introduction

Chemistry is the transformation of matter. Modern chemical methods allow for the synthesis of almost any desired molecule. Chemists have gained this control of matter through the determination of the underlying transformation mechanisms via the deduction of rules from the results of chemical reactions and spectroscopy. These reactions were hitherto almost always limited to the pathways accessible from the electronic ground state of a molecule, similar to nature, where the electronic ground state is the starting point for almost all reactions, too. Exceptions to this rule are small in number but the key step to life, e.g. in photosynthesis. Until the invention of ultrafast light sources spectroscopy was restricted to information about the products of chemical reactions, because intermediates with lifetimes shorter than the temporal resolution of the experiments were invisible to the chemist.

Nowadays “femtochemistry”, the combination of femtosecond laser pulses with chemistry, opens on the one hand the time window of the very earliest steps of chemical reactions [1, 2]. Ahmed Zewail was awarded the Nobel Prize for the development of femtosecond spectroscopy in 1999 [3] underlining its revolutionary new possibilities to help to understand chemical reactions.

On the other hand the understanding of the mechanisms has led in the last years to a growing desire to control them [4]. With advancing technology to generate shorter femtosecond laser pulses in almost any spectral regime [5–7] with arbitrary time profiles [8, 9] it has been shown in recent years that a control of chemical reactions on the femtosecond time scale is indeed possible [10]. Various control schemes have been proposed and realized experimentally [11, 12]. In contrast to conventional chemistry, the reactions starting from excited states play a crucial role in these schemes, opening up new pathways to chemical reactions that are often opposite to those starting from the electronic ground state.

Hence, the high intensities and the coherence of femtosecond laser pulses lift on the one hand the limitation to ground-state chemistry, exceeding in its possible reaction pathways the ones available to nature and allow on the other hand the spectroscopy of short-lived intermediates. However, the number of successful control experiments in solution is still very small [4] and mostly restricted to the quantum efficiency of the main photochemical pathway versus the main photophysical pathway. A successful control in solution in which the population of one photochemical pathway is optimized over another would be especially interesting, however, model systems for such an experiment are rare.

Pericyclic reactions possess changed reactivities in the excited state compared to the ground state which complement each other, as can be shown by simple frontier molecular orbital analysis [13]. Hence, most molecules that undergo pericyclic reactions feature two different photochemical pathways. In this thesis an investigation of the first nanoseconds after excitation of Diazo Meldrum’s acid (DMA) is presented in Chapter 5. The

time-resolved absorption change in the mid-infrared spectral region revealed indeed two reaction pathways after excitation of DMA with at least one of them being a pericyclic reaction (a sigmatropic rearrangement). These two pathways most probably start from different electronic states and make the spectroscopy of DMA especially interesting for subsequent control experiments in which the population of one pathway may be optimized over the other. As mentioned above, femtochemistry also allows the spectroscopy of very short-lived intermediates, which will be discussed in context of the sequential mechanism of the Wolff rearrangement of DMA.

An interesting application of pericyclic reactions are molecular photoswitches, i.e. molecules that can be switched by light between two stable states [14]. The necessity to trigger the switching with light also exemplifies that the pathways depend on the electronic state. Chapter 4 presents a photoswitch on the basis of a $6\text{-}\pi$ -electrocyclic reaction, whose reaction dynamics after excitation are unravelled with transient-absorption spectroscopy for both switching directions. Numerous molecular photoswitches are known today. For optical detection, switches undergoing a $6\text{-}\pi$ -electrocyclic reaction are especially attractive, because of the huge electronic changes and subsequent absorption changes upon switching between the ring-open and ring-closed form. Fulgides, diarylethenes, maleimides as well as spiroopyrans belong to this class of switches. Despite the popularity of spiroopyrans, which are for example used amongst other as probes or markers for chemical analysis, nonlinear optics, or sunglasses [15], the femtochemistry of the ring-open form (called in this case “merocyanine”) is still unknown to a great extent. For example a direct proof of an ultrafast ring closure as well as an ultrafast bidirectional switching between the open and closed form were still missing before the work of this thesis (the missing proof for ultrafast bidirectional switching is also true for fulgides, diarylethenes, and maleimides). In this thesis special experiments on this system, e.g. transient-absorption experiments, combined with special modeling algorithms allowed to determine the quantum efficiencies of all reaction pathways of the system, including the ring-closure pathway. With the knowledge of the reaction dynamics, a multipulse control experiment showed that bidirectional full-cycle switching between the two stable states on an ultrafast time scale is possible. Such a controlled ultrafast switching is a process which is inaccessible with conventional light sources and may allow faster switching electronics in the future.

Theoretical calculations even suggest an enantioselective photochemistry, i.e. to influence the chirality of the emerging molecule with the chirality of the light, a field called “chiral control” [12]. The challenges that need to be overcome to prove a successful chiral control are extremely hard, since enantiosensitive signals, such as circular dichroism, are inherently very small. Hence, chiral control calls for a very sensitive detection as well as an experiment that cancels all effects that may influence the enantiosensitive signal.

The first challenge, the sensitive detection, is treated in Chapter 6, in which a polarimeter is presented. It is optimized to be combined with femtosecond spectroscopy. Its specifications, which exceed the ones of commercial polarimeters, are proven by the photodissociation reaction of chiral methyl *p*-tolyl sulfoxide. This polarimeter will be an attractive tool for future chiral-control experiments due to its extreme sensitivity.

The second challenge, the design of an artefact-free experiment, gives rise to a variety of new questions. The polarization state of the light is the decisive property in such

an experiment, because on the one hand the polarization carries the chiral information of the excitation and on the other hand the change of the polarization or the intensity change dependent on the polarization is used as the enantiosensitive probing signal. Thus, a thorough introduction to the Jones formalism [16] to describe the polarization of electromagnetic waves is given in Chapter 2 as well as a short introduction to why polarization plays such an important role for chirality.

A polarization-mirroring setup is proposed in Chapter 7, which will pave the way to polarization-shaped pump-probe experiments as well as transient circular dichroism and transient optical rotatory dispersion experiments, because in contrast to known experimental setups to detect transient circular dichroism, the proposed setup allows simultaneous detection at multiple wavelengths, hence strongly decreasing data acquisition time. A simulation of such an experiment also requires the calculation of the anisotropy on the basis of the Jones vectors of the light, a relation hitherto unknown. The solution to this problem is shown in detail in the Appendix. This new approach demonstrates that in a certain experimental arrangement, polarization-shaped pump-probe experiments are possible without any contributions to the probe signal due to anisotropy. The simulation of such a polarization shaped pump-probe experiment in Chapter 7 allows for an estimation of the necessary precision of the mirror alignments.

Finally Chapter 8 summarizes the thesis and the Appendix contains further calculations showing, amongst other, the derivation as well as the power of the new approach to calculate the anisotropy in pump-probe experiments with polarization-shaped femtosecond pump pulses.

2 Theory

The fundamental processes of chemical reactions occur on the time scale of femtoseconds ($1 \text{ fs} = 1 \times 10^{-15} \text{ s}$) [17]. Advances in pulsed-laser technologies provide pulse lengths down to only few femtoseconds, called ultrashort pulses [18], allowing direct observation of these fundamental processes. In the following section a basic mathematical description of ultrashort laser pulses is given to introduce the quantities used throughout this thesis [19]. The second section introduces the polarization of an electromagnetic wave and with the Jones formalism [16] an intuitive way to describe and calculate polarization change. Subsequently, a short introduction to chirality in chemistry and its effect on electromagnetic waves is given in the third section. In the section thereafter the description of a molecular configuration and its change is explained. The last section aims to explain pericyclic reactions as they are known to chemists to set a common basis for the reader of this thesis. The ultrafast reactions investigated in this thesis with femtosecond spectroscopy belong to this class of reactions.

2.1 Ultrashort laser pulses

All laser pulse phenomena in this thesis obey the inhomogeneous wave equation [19, 20], linking the electric field $\vec{E}(t, \vec{r})$ with the polarization $\vec{P}(t, \vec{r})$ in spatially uniform and nonmagnetic media:

$$-\nabla \times (\nabla \times \vec{E}(t, \vec{r})) - \frac{1}{c^2} \frac{\partial^2}{\partial t^2} \vec{E}(t, \vec{r}) = \mu_0 \frac{\partial^2}{\partial t^2} \vec{P}(t, \vec{r}), \quad (2.1)$$

with the speed of light $c = \frac{1}{\sqrt{\epsilon_0 \mu_0}}$, μ_0 being the magnetic permeability and ϵ_0 being the permittivity of vacuum. This equation includes the possibility that the induced polarization acts back on the electric field. For phenomena discussed here, it is sufficient to assume that the electric field can be separated into a space- and a time-dependent function:

$$\vec{E}(t, \vec{r}) \propto u^+(\vec{r}) \vec{E}^+(t, z) + c.c., \quad (2.2)$$

with *c.c.* being the complex conjugate of the preceding term. For the time-dependent function $\vec{E}^+(t, z)$ the paraxial approximation is assumed so that the electric wave propagates only in z direction. In a simpler picture the time-dependent function (next Section) describes the energy distribution of the laser pulse in propagation direction, $E(t, z)$, and the spatial dependence (Section 2.1.2) describes the energy distribution perpendicular to the propagation direction, $u(\vec{r})$.

2.1.1 Time dependence

The scalar real-valued electric field $E(t)$ of one monochromatic wave serves as starting point,

$$E(t) = A \cos(\phi_0 + \omega_0 t), \quad (2.3)$$

with A being the amplitude, ϕ_0 being the phase offset, ω_0 being the angular frequency, which is related to the frequency ν via $2\pi\nu = \omega$, and t being the time. In Eq. 2.3 the electric field at one point in the propagation direction is of interest and therefore the z -dependence from Eq. 2.2 can be dropped. Furthermore the vectorial property of the electric field \vec{E} is neglected, meaning that the description focusses on linear polarization. The vectorial properties of \vec{E} are covered in Section 2.2.1.

If the electric field were only oscillating with the frequency ν_0 it would need to extend infinitely in time and light pulses would be impossible. Superposition of electric fields with different frequency ν allow for light pulses due to interference. When two waves (propagating collinearly, here in z direction) with frequency ν_1 and ν_2 and amplitude A interfere, the electric field $E(t)$ can be written as

$$E(t) = A \cos(2\pi\nu_1 t + \phi_1) + A \cos(2\pi\nu_2 t + \phi_2), \quad (2.4)$$

or as

$$E(t) = 2A \cos(2\pi\bar{\nu}t + \bar{\phi}) \cos(2\pi\Delta\nu t + \Delta\phi), \quad (2.5)$$

with

$$\bar{\nu} = \frac{\nu_1 + \nu_2}{2} \quad (2.6)$$

$$\Delta\nu = \frac{\nu_1 - \nu_2}{2} \quad (2.7)$$

$$\bar{\phi} = \frac{\phi_1 + \phi_2}{2} \quad (2.8)$$

$$\Delta\phi = \frac{\phi_1 - \phi_2}{2}. \quad (2.9)$$

$$(2.10)$$

The first term in Eq. 2.5 oscillates fast with time (t) with the mean of the contributing frequencies $\bar{\nu}$, whereas the second term modulates the amplitude of this oscillation on a slower time scale with the difference frequency $\Delta\nu$ of the two electric fields. The second term describes the occurrence of constructive and destructive interference, leading to a beating and extinction of the electric field.

An increase of the number of interfering electric fields leads to a beating of the electric field approaching a δ -function behavior in time as shown exemplary in Figure 2.1 for a field of a superposition of $N + 1 = 10000$ modes from $\lambda_f = 775$ to $\lambda_i = 825$ nm ($\nu_i = 3.636 \text{ fs}^{-1}$ to $\nu_f = 3.870 \text{ fs}^{-1}$) with equal amplitude (a square function) and equal energetic distance ($\delta\nu = 2.34 \text{ ns}^{-1}$) to the adjacent mode,

$$E(t) = \sum_{j=0}^N \cos[2\pi(\nu_i + j\delta\nu)t + \phi_j], \quad (2.11)$$

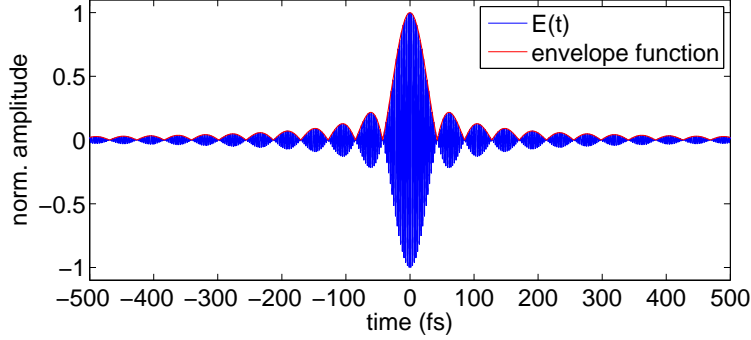


Figure 2.1: Electric field $E(t)$ of a superposition of 9999 modes with the same amplitude, phase offset and frequency ranging equidistantly ($\delta\nu = 2.34 \text{ ns}^{-1}$) from $\nu_i = 3.636 \text{ fs}^{-1}$ to $\nu_f = 3.870 \text{ fs}^{-1}$ (corresponding to light from 775 to 825 nm). The interference of modes with fix phase relation leads to light pulses. The overshoots are due to the unrealistic assumption that the amplitude of the modes is the same for all modes.

with ϕ_j being the phase of the mode with frequency $\nu_i + j\delta\nu$, which is assumed to be $\phi_j = 0$ [21]. This is an example of a fixed phase relation of the modes, which is called “mode-locking” and is essential when generating femtosecond laser pulses. Eq. 2.11 can be simplified to

$$E(t) = A \cos\left[2\pi \left(\nu_i + \frac{N-1}{2}\delta\nu\right)t\right] \frac{\sin(N\pi\delta\nu t)}{\sin(\pi\delta\nu t)}. \quad (2.12)$$

Similar to Eq. 2.5 the first term in Eq. 2.12 oscillates fast with time with the frequency $\nu_i + \frac{N-1}{2}\delta\nu$. This oscillation is modulated by the second term $\frac{\sin(N\pi\delta\nu t)}{\sin(\pi\delta\nu t)}$ which is called the envelope function (red in Figure 2.5). This behavior is not surprising as the Fourier transformation of a square function (equal amplitude for all modes in Eq. 2.11) is a sinc function (as the red envelope function in Figure 2.5). Note that $E(t)$ is sampled every 10 as, and that the fast oscillatory term still leads to so many oscillations in time that single oscillations of the intensity can hardly be identified because the mean frequency corresponds to $\approx 800 \text{ nm}$ light (2.67 fs oscillation period). From the distance of the frequency of the modes, $\delta\nu = 2.34 \text{ ns}^{-1}$, the time distance between the maxima of the adjacent pulses can be calculated to $\Delta T = \frac{1}{\delta\nu}$, giving a pulse-to-pulse time distance of $\Delta T = 426 \text{ ps}$ in the example shown in Figure 2.1 [21].

When assuming that the amplitude of the modes follow a Gaussian distribution centered around 800 nm, the adjacent overshoots disappear as shown in Figure 2.2,

$$E(t) = \sum_{j=0}^N A[2\pi(\nu_i + j\delta\nu)] \cos[2\pi(\nu_i + j\delta\nu)t + \phi_j], \quad (2.13)$$

with $A(\omega)$ being the angular frequency-dependent amplitude that describes the Gaussian distribution (black in Figure 2.2).

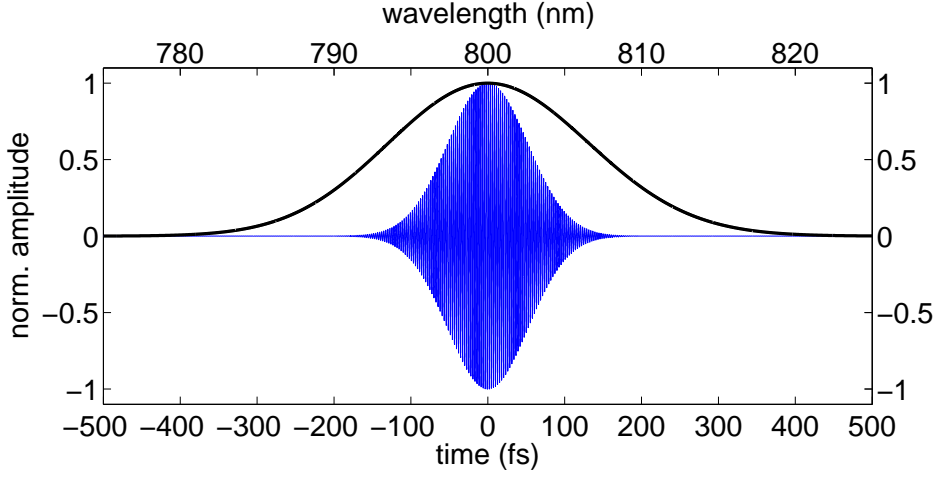


Figure 2.2: Electric field (blue, bottom x axis) from Figure 2.1 with the amplitude of the modes following a Gaussian distribution (black, top x axis). The overshoots visible in Figure 2.1 disappear in case of a Gaussian distribution, leading to one isolated pulse.

The smaller the difference frequency $\delta\nu$ the further apart are the pulses. Developing Eq. 2.11 into a continuum of modes, i.e. $\lim \delta\nu \rightarrow 0$ (corresponding to one isolated pulse and not to a pulse train), one can write the electric field as an integral over all modes with their respective angular frequency ω ,

$$E(t) = \int_{-\infty}^{\infty} A(2\pi\nu) \cos(2\pi\nu t + \phi(2\pi\nu)) d\nu = \frac{1}{2\pi} \int_{-\infty}^{\infty} A(\omega) \cos(\omega t + \phi(\omega)) d\omega, \quad (2.14)$$

with $\phi(\omega)$ being the phase of the mode with angular frequency ω . The expression for the integration is analogous to the Fourier decomposition of $E(t)$ into monochromatic waves [21]

$$E(t) = \frac{1}{2\pi} \int_{-\infty}^{\infty} \tilde{E}(\omega) e^{i\omega t} d\omega, \quad (2.15)$$

with $\tilde{E}(\omega)$ being the complex-valued amplitude distribution of the modes, i.e. the spectrum into which the phase $\phi(\omega)$ is absorbed, obtainable via the inverse Fourier transformation

$$\tilde{E}(\omega) = \int_{-\infty}^{\infty} E(t) e^{-i\omega t} dt. \quad (2.16)$$

Separation of the complex-valued spectrum into an amplitude and a phase gives the intensity $I(\omega)$ and a spectral phase term $\phi(\omega)$,

$$\tilde{E}(\omega) = 2\sqrt{\frac{\pi}{\epsilon_0 c n} I(\omega)} e^{-i\phi(\omega)}. \quad (2.17)$$

It is sufficient further on to calculate the complex valued electric field $E^+(t)$ only from the Fourier transformation of the spectrum of the positive frequencies $\tilde{E}^+(\omega)$,

$$E^+(t) = \frac{1}{2\pi} \int_0^{\infty} \tilde{E}(\omega) e^{i\omega t} d\omega, \quad (2.18)$$

however, the real part of this electric field in the time domain is then only half of the amplitude of the original real-valued electric field $E(t)$,

$$E(t) = 2\Re[E^+(t)]. \quad (2.19)$$

The complex electric field $E^+(t)$ can also be written as an amplitude with a phase,

$$E^+(t) = |E^+(t)| e^{i\Phi(t)}. \quad (2.20)$$

The temporal phase $\Phi(t)$ can be interpreted as the momentary light frequency $\omega(t)$ that depends on the time t ,

$$\omega(t) = \frac{d\Phi(t)}{dt}. \quad (2.21)$$

Usually this temporal phase is developed in a Taylor series. Here it is sufficient to state that the zeroth term of the series is called the absolute phase Φ_0 and the argument of the first term is called the carrier frequency ω_0 ,

$$\Phi(t) = \Phi_0 + \omega_0 t + \Phi_a(t), \quad (2.22)$$

with all higher-order terms being absorbed into $\Phi_a(t)$.

Since the information on the rapidly oscillating term $\omega_0 t$ and the constant phase Φ_0 impede the analysis of the temporal shape of the pulse (see the oscillations in Figure 2.2) it is useful to define a complex envelope function $E_c(t)$ that contains only the amplitude information and the phase term $\Phi_a(t)$,

$$E_c(t) = |E^+(t)| e^{i\Phi_a(t)}. \quad (2.23)$$

This separation is valid if the envelope function varies on a much longer time scale than the oscillations of the electric field (“slowly-varying envelope approximation”). The amplitude of $E_c(t)$ is the amplitude $A(t)$ of the envelope function of the electric field, as shown in red in Figure 2.2.

With modern pulse shaping techniques the spectral phase $\phi(\omega)$ can be altered [9, 22], leading to an altered temporal phase $\Phi(t)$ since $E^+(t)$ and $\tilde{E}^+(\omega)$ are Fourier pairs and hence this technique allows shaping of the electric field on the femtosecond time scale. It is sufficient for this thesis to state that with this approach complex temporal pulse shapes can be constructed, but for the experiments in this thesis pulse shaping was employed only to temporally compress the pulses, so that $\phi_a(\omega) = \text{const}$, called a “flat phase”. This leads in the time domain to the shortest pulse possible [21] (called “transform-limited”) and hence to the best temporal resolution of an experiment in which this pulse enters.

In this thesis, pulses that can be approximated by a Gaussian distribution in the time domain as well as in the frequency domain were used. For these pulses the pulse length Δt is defined via the full-width-half-maximum (FWHM) of the temporal intensity $I(t) = \frac{1}{2}\epsilon_0 cn A(t)^2$. Due to the Fourier transformation that connects the frequency and time domain for a Gaussian pulse the shortest pulse length is given by

$$\Delta t \Delta \omega = 4 \ln 2, \quad (2.24)$$

hence the broader the spectrum ($\Delta \omega$ is the FWHM of the Gaussian distributed intensity $I(\omega)$) the shorter the transform-limited pulse.

2.1.2 Spatial dependence

The previous section described an electromagnetic wave propagating in the z direction. If this wave would extend infinitely into the perpendicular x and y directions the wave would carry infinite energy. In practice the intensity of an electromagnetic wave drops with the distance from the central point [19, 23]. The amplitude is therefore a function of spatial coordinates (x, y, z) . This function depends on the nature of the beam shape. In this thesis only Gaussian-shaped laser pulses are used whose spatial dependence is given by the amplitude $u(x, y, z)$ to

$$u(x, y, z) = \frac{u_0}{\sqrt{1 + \frac{z^2}{z_0^2}}} e^{-i\Theta(z)} e^{\frac{-ik_L(x^2+y^2)}{2R(z)}} e^{\frac{-(x^2+y^2)}{w^2(z)}}, \quad (2.25)$$

with

$$R(z) = z + \frac{\rho^2}{z} \quad (2.26)$$

$$w(z) = w_0 \sqrt{1 + \frac{z^2}{\rho_0^2}} \quad (2.27)$$

$$\Theta(z) = \arctan \frac{z}{\rho_0} \quad (2.28)$$

$$z_0 = \frac{\pi n w_0^2}{\lambda}. \quad (2.29)$$

The meaning of the parameters is shown in Figure 2.3. The drop in amplitude is assumed to be radially symmetric so that $r = \sqrt{x^2 + y^2}$ is used in Figure 2.3. The central point of the beam is at $r = 0$. The beam waist $w(z)$ is taken perpendicular to the propagation direction and describes the distance from $r = 0$ to $r = w(z)$ in which the amplitude has decreased by a factor of $\frac{1}{e}$, e.g. for x direction $u(w(z), 0, z) = \frac{1}{e}u(0, 0, z)$. At $z = 0$ the beam waist runs through a minimum (w_0), this position is called the focus of a beam. The amplitude of the electromagnetic wave at $z = 0$ and $r = 0$ is then u_0 . The wavelength of the light is λ .

The ‘‘Rayleigh range’’ z_0 describes the distance from $z = 0$ in z direction in which the beam waist has increased to $\sqrt{2}w_0$. Only in this range the beam is called ‘‘collimated’’. The radius of curvature of surfaces of constant phase, $R(z)$, is indicated by the dotted

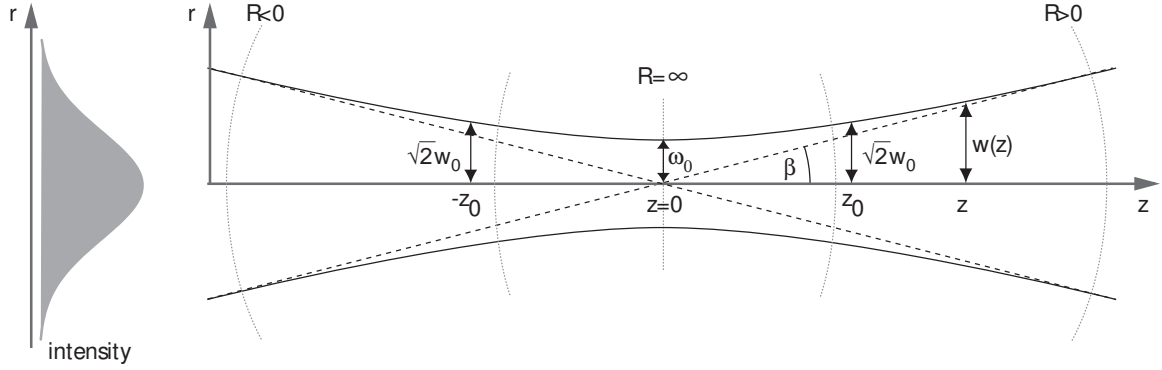


Figure 2.3: Gaussian beam propagation parameters: At any point z the projection of the amplitude on any direction orthogonal to z results in Gaussian distribution, hence the beam is called a Gaussian beam, as shown on the left. The electromagnetic wave propagates in z direction and is focussed at $z = 0$ as shown on the right. The central point of the beam is at $r = 0$. The beam is focussed at $z = 0$, where the beam waist has the value w_0 . The beam waist $w(z)$ increases with the distance from this focus. The range of z in which the beam waist is smaller than $\sqrt{2}w_0$ is the Rayleigh range z_0 . In this range the beam is called collimated. The radius of curvature of surfaces with wave fronts of constant phase is given by R and is negative for the beam before the focus, infinite at the focus, and positive for the beam after the focus.

lines. Its value is infinite at the focus. Outside of the Rayleigh range $R(z)$ can be approximated to $R(z) \approx z$, called the far-field limit. The divergence angle β in this approximation is

$$\beta \approx \frac{w(z)}{z}. \quad (2.30)$$

A rough estimate allows to predict the beam waist in the focus of a lens with focal length f :

$$w_0 \approx \frac{f\lambda}{\pi w(f)}, \quad (2.31)$$

with $w(f)$ being the beam waist at the lens.

2.2 Polarization in the Jones formalism

In Section 2.1 the vectorial properties of the electric field \vec{E} were neglected for simplicity reasons. In the next subsection the phenomena that can be observed when two electric fields with vectorial properties interfere with each other will be illustrated. Afterwards the Jones formalism is introduced that simplifies calculation of the polarization after interacting with polarization changing optical elements. The subsection thereafter exceeds the usual coverage of the Jones formalism by giving the necessary Jones matrices to handle circular-dichroitic media. The last subsection describes how to perform polarization calculations under arbitrary angles between the optical elements and the light propagation vector.

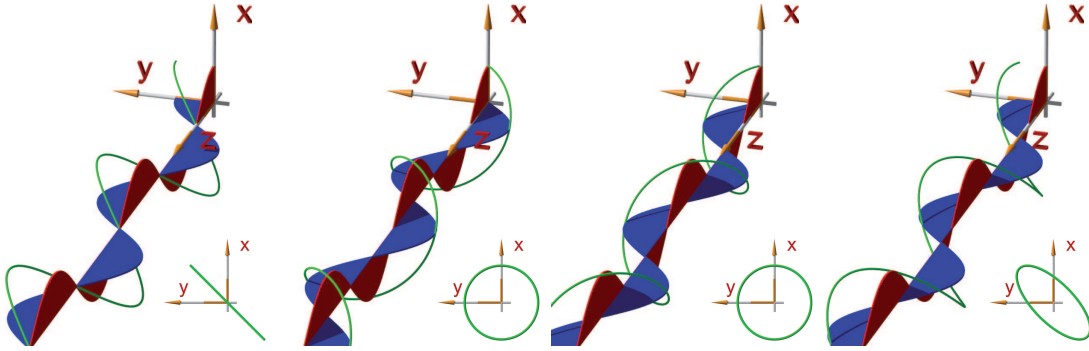


Figure 2.4: Superposition of two orthogonally linearly polarized electromagnetic waves (blue: polarized in y direction, red: polarized in x direction) with the same amplitude. The details show the course of the electric field in z direction, similar to a projection on the x - y plane. Left: With $\delta = 0^\circ$ linear polarization in $+45^\circ$ direction is obtained. Middle left: $\delta = -\frac{\pi}{2}$ results in right-circularly polarized light (*rcpl*). Middle right: $\delta = \frac{\pi}{2}$ results in left-circularly polarized light (*lcpl*). Right: All other δ values result in elliptically polarized light with the major axis in $\pm 45^\circ$ direction.

2.2.1 Polarization

The vectorial property of the electric field is called polarization [24]. Visualization of the polarization is mostly done by projecting the electric field onto the x - y plane (with z being the propagation direction of the electromagnetic wave). For simplicity reasons it is assumed in the following that two fields interfere that are monochromatic and oscillate with the same frequency ω . Superposition of these two electric fields with amplitudes A_1 in x direction (field 1) and amplitude A_2 (field 2) in y direction, i.e. with perpendicular orientation yields

$$\vec{E}(t) = \vec{e}_x A_1 e^{i\omega t} + \vec{e}_y A_2 e^{i\omega(t+t_1)}, \quad (2.32)$$

with the field 2 being delayed by t_1 relative to field 1. The time delay t_1 can also be written in terms of an additional phase δ for the field 2. The phase δ is called “relative phase”,

$$e^{i\omega(t+t_1)} = e^{i\omega t} e^{i\omega t_1} = e^{i\omega t} e^{i\delta}. \quad (2.33)$$

The effect of the relative phase is periodic with 2π for monochromatic waves, hence the effect of the relative field on the polarization is restricted in the following to values of δ from $-\pi$ to π .

When $A_1 = A_2$ the polarization is either linear for $\delta = 0$ with orientation in $+45^\circ$ direction (Figure 2.4, left) with 0° direction corresponding to x direction. In the case of $\delta = \pm\pi$ the orientation is at -45° direction (not shown in Figure 2.4). Right-circular polarization is obtained for $\delta = -\frac{\pi}{2}$ (middle left, “*rcpl*”), left-circular polarization for $\delta = \frac{\pi}{2}$ (middle right, “*lcpl*”) or elliptical polarization in $\pm 45^\circ$ direction for all other δ values (right, with the handedness being right for $-\pi < \delta < 0$ and left for $0 < \delta < \pi$). If the amplitudes of the two interfering fields are unequal, $A_1 \neq A_2$, the orientation of the resulting polarization is not anymore at $\theta = \pm 45^\circ$ but tends towards the orientation of the component with the higher amplitude.

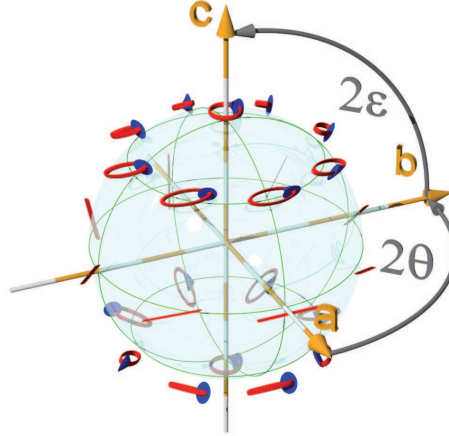


Figure 2.5: Any polarization of an electromagnetic wave can be visualized as a point on the Poincaré sphere. The polarization can either be classified with the real-valued amplitudes A_1 and A_2 of both components and a relative phase δ or via the ellipticity ϵ and the orientation θ in a reference frame, see text for the conversion between these two representations. Note, that the labeling θ is misleading, since in the Poincaré sphere 2θ corresponds to the azimuth angle whereas in polar coordinates θ usually denotes the polar angle. Note also, that the ellipticity ϵ corresponds not directly to twice the polar angle, because the poles are at $\epsilon = \frac{\pi}{4}$ and $\epsilon = -\frac{\pi}{4}$ instead to 0 and π as in conventional polar coordinates. At the poles circular polarization is found that is invariant to rotation around the angle θ and has an ellipticity of $\pm\frac{\pi}{4}$. Linearly polarized light corresponds to an ellipticity of $\epsilon = 0$. Any polarizations in between are elliptical polarizations. The handedness of the polarization is given by the sign of ϵ , with $\epsilon > 0$ being of right handedness and $\epsilon < 0$ being of left handedness. Note also that the light propagates from the center of the sphere to the point on the sphere and that one has to look in propagation direction in order to unambiguously identify the polarization state.

Any polarization state can be interpreted as a point on the Poincaré sphere shown in Figure 2.5 [25, 26]. On this sphere a polarization state can be intuitively classified by its ellipticity ϵ and its orientation θ in the a - b plane, as shown in Figure 2.5. These parameters can be calculated from the amplitudes $|A_1|$ and $|A_2|$ and the relative phase δ [25]:

$$\epsilon = \frac{1}{2} \arcsin(\sin(2\chi) \sin \delta) \quad (2.34)$$

with

$$\chi = \arctan \frac{A_2}{A_1}. \quad (2.35)$$

The orientation θ is given by

$$\tilde{\theta} = \frac{1}{2} \arctan(\tan(2\chi) \cos \delta), \quad (2.36)$$

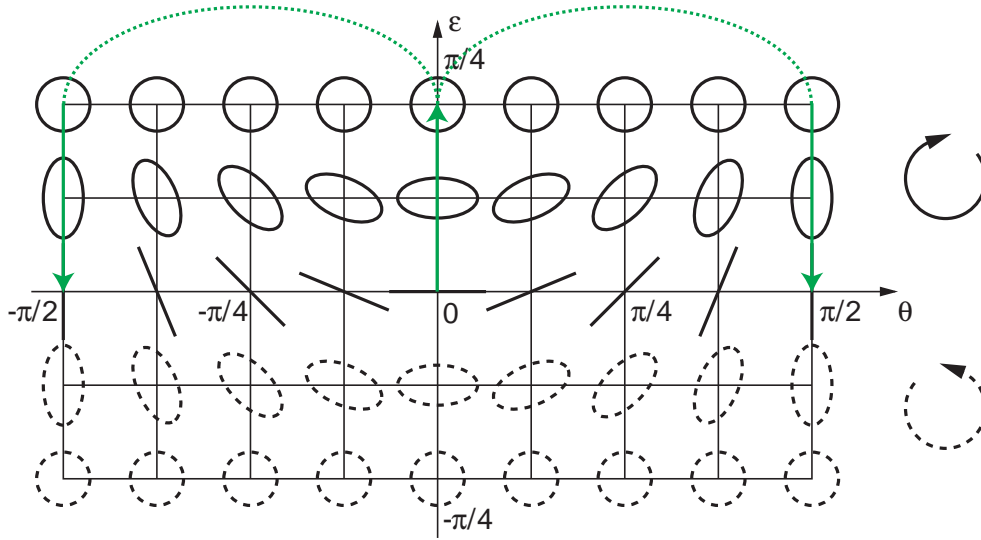


Figure 2.6: Two-dimensional representation of the Poincaré sphere in Figure 2.5. All elements of the top line are *rcpl*, whereas all elements of the bottom line are *lcpl* following [27, 28]. In order to translate between the representation of Figure 2.5 and this two-dimensional representation one has to look from the center of the sphere to the outside of the sphere, i.e. in propagation direction. When going from linearly polarized light in horizontal direction ($\theta = 0$) to linearly polarized light in vertical direction ($\theta = \pm\frac{\pi}{2}$) via the pole *rcpl*, solid green arrows, one has to “jump” in this representation as indicated by the green dashed line when reaching the pole.

with

$$\theta = \begin{cases} \tilde{\theta} & \in [-\pi/4, \pi/4] & \text{if } \chi \leq \pi/4, \\ \tilde{\theta} + \pi/2 & \in [\pi/4, \pi/2] & \text{if } \chi > \pi/4 \wedge \tilde{\theta} < 0, \\ \tilde{\theta} - \pi/2 & \in [-\pi/2, -\pi/4] & \text{if } \chi > \pi/4 \wedge \tilde{\theta} \geq 0. \end{cases} \quad (2.37)$$

An equivalent representation of the Poincaré sphere is the two-dimensional plane in Figure 2.6 [25]. Whereas it is easier to identify the individual polarization states in this representation than in the three-dimensional representation of Figure 2.5, the sets of polarization states treated in Chapter 7 are simpler to illustrate on the three-dimensional sphere, see for example Figure 7.11 on page 161. Note, that all elements of the top and bottom line in Figure 2.6 are the same, *rcpl* in the top and *lcpl* in the bottom. Therefore when going from horizontal polarization ($\theta = 0$) to vertical polarization ($\theta = \pm\frac{\pi}{2}$) one has to “jump” when reaching the top, as indicated by the green dashed line.

Furthermore any polarization state can be divided into a linear and a circular part [29]. With the point on the Poincaré sphere (Figure 2.5) known, the projection onto the *a-b* plane (the equatorial plane) results in the linear part, with the amplitude $A_{linear} = \sqrt{a^2 + b^2}$. Linear polarization ($\delta = 0^\circ$) in the direction $\theta = 0$ always corresponds to polarization in direction of the field with amplitude A_1 , this direction being here the *x* direction. Increase of θ corresponds to a counter-clockwise rotation of the orientation. However, the axes of the Poincaré sphere *a* and *b* do not correspond to the laboratory axes. A linear polarization state in $\theta = 0^\circ$, *a* direction in Figure 2.5, is defined with

Eq. 2.37 as x direction in the laboratory frame. Note that following this definition $\theta = 90^\circ$, y direction in the laboratory frame, does not correspond to b direction in Figure 2.5 but instead to $-a$ direction.

The circular part of the polarization $\vec{E}_{circular}$ is given by the projection onto the c axis. Its sign determines the handedness of the circular polarization (positive $\rightarrow rcpl$ [27, 28]) and the absolute value determines the amplitude. The need for two components (a and b) to describe the linear part versus only one component to describe the circular part (c) is due to the additional freedom of the orientation of the linear polarization (θ , see Figure 2.5).

2.2.2 Jones formalism

Jones vector

The interference of the two fields from the previous section,

$$\vec{E}(t) = \vec{e}_x A_1 e^{i\omega t} + \vec{e}_y A_2 e^{i\omega(t) + i\delta}, \quad (2.38)$$

can be rewritten as a two-dimensional vector

$$\vec{E} = \begin{pmatrix} A_1 \\ A_2 e^{i\delta} \end{pmatrix} e^{i\omega t}. \quad (2.39)$$

The time-dependent phase term $e^{i\omega t}$ can be dropped, because it is the same for both components of the vector, yielding the two-dimensional complex ‘‘Jones vector’’ \vec{E} [16, 30–35], that depends on the amplitudes of the two components, A_1 and A_2 , and their relative phase δ ,

$$\vec{E} = \begin{pmatrix} E_1 \\ E_2 \end{pmatrix} = \begin{pmatrix} A_1 \\ A_2 e^{i\delta} \end{pmatrix}. \quad (2.40)$$

The intensity $I = I_x + I_y$ of the electromagnetic wave can be obtained from

$$\begin{pmatrix} I_x \\ I_y \end{pmatrix} = \begin{pmatrix} |E_1|^2 \\ |E_2|^2 \end{pmatrix}. \quad (2.41)$$

Since the Jones vector is two-dimensional we can apply the two-dimensional active rotation matrix $Rot(\alpha)$,

$$Rot(\alpha) = \begin{pmatrix} \cos \alpha & -\sin \alpha \\ \sin \alpha & \cos \alpha \end{pmatrix}, \quad (2.42)$$

to turn the orientation θ of the polarization by α . Note that a rotation of the coordinate system is achieved by the two-dimensional passive rotation matrix $Rot_p(\alpha)$,

$$Rot_p(\alpha) = Rot^{-1}(\alpha) = \begin{pmatrix} \cos \alpha & \sin \alpha \\ -\sin \alpha & \cos \alpha \end{pmatrix}. \quad (2.43)$$

This is for example necessary for the Fresnel coefficients, which state that the effect of boundary surfaces differs for the component in the plane of incidence from the effect for the component perpendicular to the plane of incidence [24]. The plane of incidence is

thereby the plane containing the wave vector of the incoming as well as the wave vector of the reflected beam. Therefore the Jones vector is usually defined such that the first component describes the component perpendicular to the plane of incidence (s) and the second component describes the component parallel to the plane of incidence (p). Here this is simply done by the transformation $x \rightarrow s$ and $y \rightarrow p$, hence

$$\vec{E} = \begin{pmatrix} E_s \\ E_p \end{pmatrix}. \quad (2.44)$$

Substituting additionally to rotation in Eq. 2.40 the relative phase δ with values for linear, circular and elliptical polarization one can construct any polarization state. The Jones vectors (normalized to $I = 1$) of the most common polarization states are given in Table 2.1.

polarization state	relative phase δ	Jones vector
linear in s direction	undefined	$\begin{pmatrix} 1 \\ 0 \end{pmatrix}$
linear in p direction	undefined	$\begin{pmatrix} 0 \\ 1 \end{pmatrix}$
linear in $+45^\circ$ direction	0	$\frac{1}{\sqrt{2}} \begin{pmatrix} 1 \\ 1 \end{pmatrix}$
right-circular, $rcpl$	$-\frac{\pi}{2}$	$\frac{1}{\sqrt{2}} \begin{pmatrix} 1 \\ -i \end{pmatrix}$
left-circular, $lcpl$	$\frac{\pi}{2}$	$\frac{1}{\sqrt{2}} \begin{pmatrix} 1 \\ i \end{pmatrix}$

Table 2.1: Jones vectors of the most common polarizations normalized to $I = 1$.

Jones matrix

In the Jones formalism the effect of a boundary surface (in the following called also an optical element) is described by a 2×2 matrix, the ‘‘Jones matrix’’ [33, 36, 37]. The Jones vector of the light after the optical element is then obtained by multiplication of the Jones matrix with the Jones vector impinging onto the optical element.

The two diagonal elements of the Jones matrix consist of the additional phase and the amplitude change for the s and p component of the polarization. Hence, a $\frac{\lambda}{2}$ wave plate that adds only a retardation of π between the s and p component while maintaining the amplitudes can be described by

$$M_{\frac{\lambda}{2}} = \begin{pmatrix} e^{i\frac{\pi}{2}} & 0 \\ 0 & e^{-i\frac{\pi}{2}} \end{pmatrix}. \quad (2.45)$$

Multiplication with the Jones vector of linearly polarized light in $+45^\circ$ direction then gives

$$M_{\frac{\lambda}{2}} \cdot \frac{1}{\sqrt{2}} \begin{pmatrix} 1 \\ 1 \end{pmatrix} = \frac{1}{\sqrt{2}} \begin{pmatrix} 1 \\ -1 \end{pmatrix} e^{i\frac{\pi}{2}}, \quad (2.46)$$

i.e. linearly polarized light in -45° direction with an additional phase that can be neglected because it is the same for both components.

A perfect linear polarizer oriented in s direction, i.e. no intensity change for s polarization and no transmittance for p polarization, can then be described by

$$M_{spol} = \begin{pmatrix} 1 & 0 \\ 0 & 0 \end{pmatrix}. \quad (2.47)$$

A simple way to change the orientation angle of an optical element is the rotation of the incoming Jones vector by the active two-dimensional rotation matrix (Eq. 2.42) such that the Jones vector is defined in the reference system given by the optical element. After multiplication of the rotated Jones vector with the Jones matrix the outbound Jones vector can be rotated back to the original reference system of the incoming Jones vector only if the original (previous to rotation) s direction is still orthogonal to the propagation direction after the optical element. If this is the case this procedure is the same as a passive rotation of the Jones matrix itself. A linear polarizer does neither change the wave vector nor change the direction of the s component. A linear polarizer with transmission in θ direction (with $\theta = 0$ corresponding to the s direction, rotation occurs clockwise) can therefore be described by the Jones matrix $M_{pol}(\theta)$ by rotating the Jones matrix of a linear polarizer oriented in 0° direction (M_{spol}) by the angle θ :

$$M_{pol}(\theta) = \begin{pmatrix} \cos \theta & -\sin \theta \\ \sin \theta & \cos \theta \end{pmatrix} \cdot \begin{pmatrix} 1 & 0 \\ 0 & 0 \end{pmatrix} \cdot \begin{pmatrix} \cos \theta & \sin \theta \\ -\sin \theta & \cos \theta \end{pmatrix} = \begin{pmatrix} \cos^2 \theta & \cos \theta \sin \theta \\ \cos \theta \sin \theta & \sin^2 \theta \end{pmatrix}. \quad (2.48)$$

Reflection and transmission

Jones matrices can even be used to describe the reflection or transmission at a boundary surface to another medium (in the following this surface will also be called optical element since it may change the polarization state and the amplitude of an electromagnetic wave). The medium before the surface and the medium after the surface are characterized by their index of refraction n_i and n_t , respectively. In absorbing media, such as metals, the index of refraction is complex [38], whereas nonabsorbing materials, such as dielectric mirrors and glass, generally possess a real-valued index of refraction ≥ 1 . From the index of refraction, the Fresnel coefficients for reflection and transmission can be obtained. The Fresnel coefficients depend not only on the index of refraction but also on the angle of incidence θ_i onto the surface. With Snell's law

$$\cos \theta_t = \sqrt{1 - \left(\frac{n_i}{n_t}\right)^2 \sin^2 \theta_i}, \quad (2.49)$$

the Fresnel coefficients [24, 39] become

$$r_{\perp} = \frac{E_r}{E_0} = -\frac{\sin(\theta_i - \theta_t)}{\sin(\theta_i + \theta_t)} \quad (2.50)$$

$$t_{\perp} = \frac{E_t}{E_0} = \frac{2 \sin \theta_t \cos \theta_i}{\sin(\theta_i + \theta_t)} \quad (2.51)$$

$$r_{\parallel} = \frac{E_r}{E_0} = \frac{\tan(\theta_i - \theta_t)}{\tan(\theta_i + \theta_t)} \quad (2.52)$$

$$t_{\parallel} = \frac{2 \sin \theta_t \cos \theta_i}{\sin(\theta_i + \theta_t) \cos(\theta_i - \theta_t)}, \quad (2.53)$$

with r and t being the reflection (r) and transmission (t) coefficient for p polarized (\parallel) and s polarized (\perp) light, respectively. The angle of incidence with the normal of the boundary surface of the material is θ_i , and the refracted angle in the material is θ_t . In case of complex n_t the term $\cos \theta_t$ may become imaginary when $\sin \theta_i < \frac{n_i}{n_t}$, leading to complex Fresnel coefficients [39] (see also Appendix C).

The Jones matrices to describe reflection (M_r) and transmission (M_t) at a boundary surface can then be constructed to [36]

$$M_r = \begin{pmatrix} r_{\parallel} & 0 \\ 0 & r_{\perp} \end{pmatrix} \quad (2.54)$$

$$M_t = \begin{pmatrix} t_{\parallel} & 0 \\ 0 & t_{\perp} \end{pmatrix}. \quad (2.55)$$

In case of complex coefficients the amplitude of this coefficient corresponds to the intensity change of the component and the phase of this coefficient to an additional phase for the component.

With these tools it is possible to describe the polarization change of polarized light when interacting with linear dichroitic media (i.e. media that act differently on s and p polarized light). However, certain media do not differentiate in their action on the direction of the linear polarization but on the handedness of the circular polarization [40], see ORD and CD effect in Section 2.3. The next subsection shows how those materials can be handled within the Jones formalism.

2.2.3 Circular-dichroitic media in the Jones formalism

Whereas the Jones vector introduced in the previous sections is defined in the basis of s and p direction, an equivalent basis would be right- and left-circularly polarized light, since any polarization can also be expressed as superposition of two circular polarized electromagnetic waves with opposite handedness according to

$$\frac{1}{\sqrt{2}} \begin{pmatrix} 1 \\ i \end{pmatrix} + \frac{1}{\sqrt{2}} \begin{pmatrix} 1 \\ -i \end{pmatrix} e^{i\delta} = Rot \begin{pmatrix} \delta \\ 2 \end{pmatrix} \cdot \begin{pmatrix} 1 \\ 0 \end{pmatrix} e^{i\delta}, \quad (2.56)$$

with δ being the phase between the right- and left-circular polarization [24]. The orientation of the resulting linear polarization is then $\theta = \frac{\delta}{2}$, with 0 corresponding to linearly

polarized light in s direction (see Tab. 2.1). In order to not cause confusion which basis definition is currently used, one can also find Jones matrices in the s and p basis that act only on either circular polarization, as shown below.

A Jones matrix M_{lcpl} that acts only on left-handed circular polarization while leaving the right-handed circular polarization unchanged has to obey

$$\begin{pmatrix} a & b \\ c & d \end{pmatrix} \cdot \begin{pmatrix} 1 \\ i \end{pmatrix} = m \begin{pmatrix} 1 \\ i \end{pmatrix} \quad (2.57)$$

$$\begin{pmatrix} a & b \\ c & d \end{pmatrix} \cdot \begin{pmatrix} 1 \\ -i \end{pmatrix} = \begin{pmatrix} 1 \\ -i \end{pmatrix}, \quad (2.58)$$

with m being the complex coefficient describing the change that the left-circular polarized component experiences (amplitude change and phase shift), similar to the Fresnel reflection and transmission coefficients. The solution to these four coupled equations is

$$M_{lcpl}(m) = \begin{pmatrix} a & b \\ c & d \end{pmatrix} = \begin{pmatrix} \frac{1+m}{2} & -\frac{1}{2}i(-1+m) \\ \frac{1}{2}i(-1+m) & \frac{1+m}{2} \end{pmatrix}. \quad (2.59)$$

Analogously for the right-handed polarization the Jones matrix M_{rcpl} is obtained:

$$M_{rcpl}(m) = \begin{pmatrix} a & b \\ c & d \end{pmatrix} = \begin{pmatrix} \frac{1+m}{2} & \frac{1}{2}i(-1+m) \\ -\frac{1}{2}i(-1+m) & \frac{1+m}{2} \end{pmatrix}. \quad (2.60)$$

These matrices at hand one can construct the Jones matrix of any kind of optical element that is circular dichroitic. A right-circular polarizer corresponds to no transmittance of $lcpl$, hence

$$M_{lcpl}(0) = \begin{pmatrix} \frac{1}{2} & \frac{i}{2} \\ -\frac{i}{2} & \frac{1}{2} \end{pmatrix}, \quad (2.61)$$

whereas a retardation of ϕ for left-circularly polarized light only can be achieved with

$$M_{lcpl}(e^{i\phi}) = \begin{pmatrix} \frac{1}{2}(1+e^{i\phi}) & -\frac{1}{2}i(-1+e^{i\phi}) \\ \frac{1}{2}i(-1+e^{i\phi}) & \frac{1}{2}(1+e^{i\phi}) \end{pmatrix}. \quad (2.62)$$

Finally, a rotation of a circular-dichroitic optical element must not have an effect on its action, hence

$$Rot(\alpha) \cdot M_{rcpl} \cdot Rot(-\alpha) = M_{rcpl}, \quad (2.63)$$

which is fulfilled.

Up to now all optical elements were used in the same reference system, at most a rotation of the optic was performed. In the next subsection an explanation is given how to calculate an arbitrary set of optical elements with arbitrary angles between their surface normals.

2.2.4 Jones calculation in three dimensions

In the previous sections the Jones formalism has been introduced and applied to linear-dichroitic materials as well as circular-dichroitic materials. Whereas the directions of the

s and p component are defined by the plane of incidence at each optical element featuring linear dichroism and not by the polarization state of the light itself, the contrary is true for circular polarization and circular-dichroitic optical elements. Circular polarization is not defined by the plane of incidence at an optical element but only by its handedness, which is directly expressed by Eq. 2.63 in which the action of the circular-dichroitic optical element does not depend on its orientation. However, since almost all optical elements exhibit linear dichroism instead of circular dichroism, the dependence of the polarization on the alignment of the optical element requires a three-dimensional calculation of the effect of an optical element onto the polarization state of the light [36, 37] as shown in this subsection.

Figure 2.7 shows an exemplary setup consisting of two mirrors (that obey the Fresnel coefficients, hence are linear dichroitic) which is used in the following to show how to cope with the linear dichroism of optical elements in the Jones formalism. The electromagnetic wave \vec{E}_0 travels first in z direction,

$$\vec{E}_0 = \vec{J}_0 e^{i(\omega t + \vec{k}_{i1} \cdot \vec{r})}, \quad (2.64)$$

with the wave vector \vec{k}_{i1} being

$$\vec{k}_{i1} = \begin{pmatrix} 0 \\ 0 \\ -1 \end{pmatrix}, \quad (2.65)$$

and the three-dimensional polarization vector \vec{J}_0 with the amplitudes A_1 and A_2 being

$$\vec{J}_0 = \begin{pmatrix} A_1 \\ A_2 \\ 0 \end{pmatrix}. \quad (2.66)$$

In the reference system $x \rightarrow s$ and $y \rightarrow p$, the light possesses the Jones vector \vec{J}_{i1}

$$\vec{J}_{i1} = \begin{pmatrix} A_1 \\ A_2 \end{pmatrix}. \quad (2.67)$$

In Figure 2.7 the beam does not leave the z - y plane after the first mirror. The normal of the plane of incidence \vec{n}_{ik} ($k = 1$ red, $k = 2$ cyan), with k denoting the mirror number, is then defined by the surface normal of the mirror k , \vec{n}_{mk} (green), and either the incoming (\vec{k}_{ik}) or outgoing (\vec{k}_{ok}) wave vector of the beam (blue in Figure 2.7). The choice between incoming or outgoing wave vector changes the sign of the obtained normal. For consistency in the following always \vec{k}_{ik} is used,

$$\vec{n}_{ik} = \vec{k}_{ik} \times \vec{n}_{mk}. \quad (2.68)$$

Mirror 1 defines also the first reference system for the Jones Vector: $y \rightarrow p$ and $x \rightarrow s$. The outgoing wave vector \vec{k}_{ok} can be obtained via vector calculations, either via mirroring \vec{k}_{ik} at the plane that contains \vec{n}_{ik} and \vec{n}_{mk} or by calculating the angle α between \vec{k}_{ik} and \vec{n}_{mk} and rotating \vec{k}_{ik} around $\vec{k}_{ik} \times \vec{n}_{mk}$ by 2α (see three-dimensional rotation matrix in the Appendix Eq. B.5). Either way contains the cross product of two vectors which is

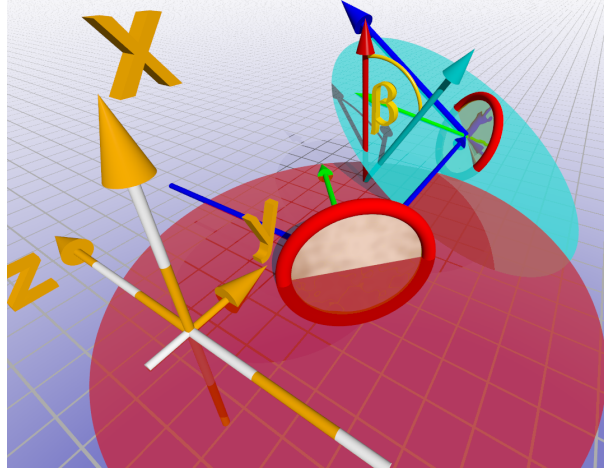


Figure 2.7: Illustration of the angles and vectors used to calculate the polarization of an electromagnetic wave in a three-dimensional beam path. The incoming beam (blue, $-z$ direction) is reflected at the two mirrors (red circles) subsequently. Whereas at the first mirror the beam does not leave the y - z plane, the second mirror reflects the beam partly up. The normals of the optical elements \vec{n}_{mk} (k denoting the mirror number) are given by the green arrows. The plane of incidence of the first mirror is given by the red disk. The normal of this plane \vec{n}_{i1} is parallel to the x axis as indicated by the red arrow. In a right-handed coordinate system the first vector of the cross product to obtain \vec{n}_{i1} is taken here as the incoming beam and the second vector of the cross product is the mirror normal of mirror 1. The plane of incidence of the second mirror is shown as the cyan disk and the normal of that plane as the cyan arrow in \vec{n}_{i2} direction. The angle between \vec{n}_{i1} and \vec{n}_{i2} is β , with the rotation axis being the wave vector of the incoming beam of mirror 2. The Jones vector of the light has to be rotated by this angle in front of the second mirror to include the three-dimensional propagation of the beam into the Jones formalism.

not commutative. Therefore care has to be taken that the sequence is always the same to obtain consistent results. The latter method, via the angle α , is preferred because the Jones matrix of an optical element often depends on the angle of incidence (e.g. Fresnel coefficients) and therefore α always needs to be calculated anyway.

Assuming that the reference system of the incoming beam is the same as the reference system given by the first mirror, the outgoing Jones vector \vec{J}_{o1} is simply obtained by multiplication of the Jones matrix of mirror 1 (J_{m1}) with the incoming Jones vector \vec{J}_{i1} .

This changes at the second mirror. In this case the mirror normal \vec{n}_{m2} has a component in x direction (green arrow in the back of Figure 2.7), leading to a change in the plane of incidence \vec{n}_{i2} (cyan in Figure 2.7). In order to integrate this into the Jones calculation one has to rotate the coordinate system of the Jones vector of the incoming beam of mirror 2 ($\vec{J}_{o1} = \vec{J}_{i2}$) by the angle β (see Figure 2.7) between the normals \vec{n}_{i2} and \vec{n}_{i1} with the passive rotation matrix (Eq. 2.43). To obtain consistent results the rotation axis, which also defines the sign of β (Eq. B.5), is given by the wave vector of the incoming beam of mirror 2. As above the outgoing Jones vector is again obtained by multiplication

with the Jones matrix of mirror 2 (J_{m2}):

$$\vec{J}_{o2} = J_{m2} \cdot Rot_p(\beta) \cdot \vec{J}_{i2}. \quad (2.69)$$

\vec{J}_{o2} cannot be compared directly to the initial Jones vector because it is defined in another reference system. This problem can be solved by artificially reflecting it with a perfect mirror (e.g. $r_{\perp} = 1$ and $r_{\parallel} = 1$) in a direction that its wave vector \vec{k} lies again in the y - z plane, as in the beginning, and subsequent rotation of the Jones vector back into the original reference system.

With this approach the polarization after any combination of optical elements can be calculated (an alternative approach based on the three-dimensional polarization vector can be found in [41]). In the course of this thesis all the calculations of this chapter have been implemented into a LabVIEW program to simulate and visualize experimental setups.

2.3 Optical effects of chirality

If the mirror image of a structure cannot be rotated and/or translated in any way that the original structure is recovered the structure is called chiral [42], i.e. the structure lacks a rotating mirror axis. Chirality is especially important in chemistry, in which a three-dimensional structure is defined by the spatial arrangement of the atoms within a molecule. The original molecule and its mirror image are then enantiomers of each other [43]. The origin of the chirality in molecules can be traced back to stereogenic centers that raise two isoenergetic possibilities for the spatial arrangement of the atoms. This degeneracy of the two arrangements is lifted as soon as more than one stereogenic center is present in a molecule leading to diastereomers [42]. In chemistry the stereogenic centers may for example be an atom with four or more different substituents, an axis, or a helix. When labeling molecules these stereogenic centers are characterized with the corresponding character (often IUPAC nomenclature [42] is used) to describe their configuration.

Although in an achiral environment these enantiomers cannot be distinguished, a chiral environment such as circularly polarized light is often able to differentiate between the two enantiomers. The optical effects observed in this situation are either circular dichroism (CD) or optical rotatory dispersion (ORD). In the following two subsections these two effects will be described.

2.3.1 Circular dichroism

Theoretically the circular-dichroism effect can be derived with the help of quantum mechanical perturbation theory. Within this theory, the system Hamiltonian is divided into two parts as described in more detail in the literature [44, 45]. Following Schellmann [46] it is usually sufficient to neglect the contribution of the magnetic field to the interaction Hamiltonian \hat{V} since its contribution to the potential of the molecule is smaller by a factor of 10^{-4} than the energy due to the interaction of the transition dipole $\vec{\mu}$ with the

corresponding electric field \vec{E} . Hence, the interaction Hamiltonian \hat{V} depends only on the electric field,

$$\hat{V} = -\vec{\mu} \cdot \vec{E}. \quad (2.70)$$

Following this approach all results are not exact, but the error is very small so that the simplification is used almost always. However, due to the missing magnetic interaction of the radiation with the electrons, a description of the circular-dichroism effect is not possible within this simplified model. The inclusion of the magnetic interaction due to the magnetic moment \vec{m} of the molecule and the magnetic field \vec{H} into the interaction Hamiltonian allows for the possibility of a circular dichroism,

$$\hat{V} = -\vec{\mu} \cdot \vec{E} - \vec{m} \cdot \vec{H}. \quad (2.71)$$

The effect of the magnetic interaction on the potential energy \hat{V} is due to the Lorentz force. The Lorentz force, in contrast to the electrostatic force, depends on the direction of the motion of a charged particle relative to the magnetic field,

$$\vec{m} = \frac{e\hbar}{2mc} \sum_i \vec{L}_i, \quad (2.72)$$

with \vec{L}_i being the angular momentum of electron i , e being the elementary charge and m being the mass of an electron. The spin of the electron i is neglected in this case due to its small contribution. This means that the contribution to the perturbation because of the magnetic field changes its sign depending on the direction of motion of the electrons in the magnetic field.

Whereas in achiral molecules, due to the presence of a rotating mirror axis, \vec{m} needs to be the same for image and mirror image, in chiral molecules this operator differs in its sign for the enantiomers. Whereas for the electrostatic term $\vec{\mu} \cdot \vec{E}$ a chirality of the operator and the field is irrelevant, the action on the wavefunction due to the chiral magnetic moment \vec{m} in a chiral magnetic field \vec{H} depends on the chirality of the system. This situation is similar to the occurrence of two stereogenic centers (one corresponding to the magnetic moment operator and one corresponding to the chiral field) that lift the energetic degeneracy of individual stereogenic centers. Hence the perturbation energy depends on the chirality of both components (\vec{H} and \vec{m}).

This effect leads to a small difference between the extinction coefficients for right-circularly polarized light and left-circularly polarized light for one enantiomer and is therefore called ‘‘circular dichroism’’. The effect is illustrated schematically in Figure 2.8, where the extinction coefficients of one enantiomer ϵ_r for *rcpl* (red) is a bit smaller than for *lcpl* (ϵ_l , blue). The difference $\Delta\epsilon = \epsilon_l - \epsilon_r$ is shown in green and is called the circular-dichroism spectrum. The extinction coefficients in achiral light (only fulfilled for unpolarized or linearly polarized light) ϵ_{linear} is given in black and is the mean of ϵ_l and ϵ_r . For electronic absorptions $|\Delta\epsilon|$ is on the order of $\frac{\epsilon_{linear}}{1000}$ for organic molecules [14, 46].

As can be seen from Figure 2.8 the circular dichroism is only observable in the vicinity of an absorption band in contrast to the optical rotatory dispersion described in the next subsection.

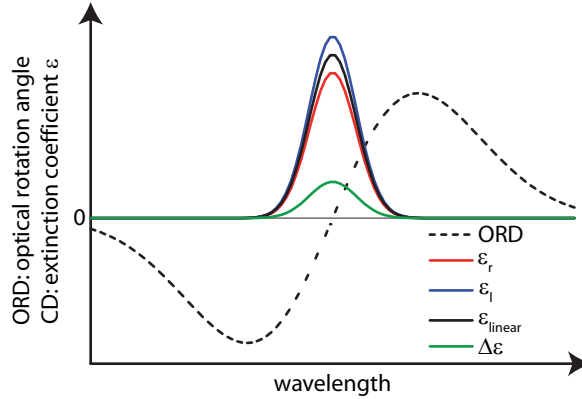


Figure 2.8: The optical effects on light at a resonance of a chiral molecule. The circular dichroism ($\Delta\epsilon$: green) is the difference between the extinction coefficient for *lcpl* (ϵ_l : blue) and *rcpl* (ϵ_r : red) and the extinction coefficient for linear light (ϵ_{linear} : black) is the mean between ϵ_l and ϵ_r . The optical rotatory dispersion (ORD: black dashed) changes its sign at the exact resonance and hence is zero at the exact resonance.

2.3.2 Optical rotatory dispersion

The dispersive and absorptive properties of a material have to obey the Kramers-Kronig relations [24, 46]. Since the absorptive property of chiral media (circular dichroism) depends on the handedness of the circular polarization of the light (as depicted in Figure 2.8), the dispersive property of these media, i.e. the index of refraction, also has to depend on the handedness. Commonly, one is interested in the effect of the media on linear polarization. However, one should keep in mind that the superposition of two circularly polarized electromagnetic waves with the same amplitude but opposite handedness leads to a linear polarization (see Eq. 2.56). The different indices of refraction experienced by the circular polarizations (see Section 2.2.3) change the relative phase between them and therefore the orientation of the resulting linear polarization (see Eq. 2.56). This rotation of the orientation θ of linear polarization by chiral media was first observed in liquids and gases by Jean Baptiste Biot in 1811 and is called optical rotatory dispersion. Similar to the circular dichroism, this effect is very weak and depends on the wavelength. An exemplary and idealized shape of the optical rotatory dispersion is given in Figure 2.8. It is not only present in the proximity of an absorption band but also further away. At the exact position of the transition the optical rotation changes its sign. However, overlapping transition bands entangle the behavior shown in Figure 2.8 to more complex-shaped functions.

The direction of the rotation, corresponding to the sign of the ORD in Figure 2.8, depends on which of the two enantiomers is investigated. The opposite enantiomer has the contrary sign, leading to no optical rotation in racemic mixtures. The name of the enantiomer often begins with the direction of rotation at 589 nm (the Na-D line), e.g. (+)-Glucose indicates that the rotation occurs clockwise [42].

In the literature the specific rotation of an enantiomer $[\alpha]_{\lambda}^T$ is given by the optical rotation of a sample with a path length $l = 1$ dm and a concentration of the enantiomer

of $c = 1$ g/ml. Additionally, the wavelength λ and temperature T of the measurement need to be specified, because the optical rotation depends slightly on these conditions. Usually the specific rotation is measured at $\lambda = 589$ nm, labeled as “D”, and $T = 20$ °C.

The actual rotation angle α at temperature T and wavelength λ can then be calculated from

$$\alpha = [\alpha]_{\lambda}^T cl, \quad (2.73)$$

with c being the concentration in g/ml and l being the path length in dm. The wavelength dependence of the optical rotation $[\alpha]_{\lambda}^T$ can, in a good approximation, be described by the Drude equation [47]

$$[\alpha]_{\lambda}^T = \sum_j \frac{C_j}{\lambda^2 - \lambda_j^2}, \quad (2.74)$$

with every element j of the sum corresponding to a transition at the wavelength λ_j with a contribution C_j . However, this equation is only valid when λ is not close to λ_j . Experimentally, the optical rotation angle is very high when approaching the resonance (up to a few thousands degrees, compared to around 100° for sugars at 589 nm for which $\lambda_j \approx 300$ nm). In Section 6 this increase of the optical rotation with the wavelength is exploited to increase the resolution in a polarimeter.

2.3.3 Enantiomeric purity

The “enantiomeric excess” ee [42] is one expression describing the enantiomeric purity of a sample. It is given by

$$ee = \frac{|c_R - c_S|}{c_R + c_S} 100, \quad (2.75)$$

with c_R and c_S being the concentration of the R- and S-enantiomer, respectively.

Another expression is the “optical purity” op [42] that is determined by the optical rotation angle α_{max} , the optical rotation angle of a solution containing only one enantiomer, and the measured optical rotation angle α_{obs} to

$$op = \frac{\alpha_{obs}}{\alpha_{max}} 100. \quad (2.76)$$

In most cases $op \approx ee$ holds (excluding the case when the wrong enantiomer is measured, which would lead to negative optical purity). Only when a strong nonlinear dependence of the optical rotation on the enantiomer concentration exists or other substances are added to the solution that somehow influence the optical rotation, this approximation is not valid. The optical purity is therefore a good and direct way to determine the enantiomeric excess experimentally.

2.4 State and state-change of molecules

In this thesis, amongst others, the femtosecond time-resolved reaction dynamics of pericyclic reactions is investigated. In order to comprehend the inherent dynamics in molecules one has to find a way to describe the configuration of the molecule as well

as the mechanisms that change this configuration. The basis to describe the possible dynamics is presented in this chapter. It consists of the description of the electronic configuration of a molecule and a selection of pathways that change the configuration of the molecule which are relevant for this thesis. Many approaches have been developed to describe the state and dynamics of a molecule, this chapter introduces one intuitive picture based on molecular orbitals which is widely used by chemists in mechanistic photochemistry [13, 17].

Theoretically, any molecule can be described completely with a wave function Ψ . Following the Born–Oppenheimer approximation (next subsection), this wave function can be separated into an electronic, a nuclear and a spin wavefunction. In the subsequent subsection molecular orbitals are discussed providing a basic understanding for the electronic wavefunctions of a molecule. Finally, the interaction with the nuclear wavefunction, i.e. the vibrational degrees of freedom, to construct potential surfaces is presented, as well as a selection of constitutional and electronic configuration changes that can occur along these degrees of freedom.

2.4.1 Born–Oppenheimer approximation

The Born–Oppenheimer approximation is the most important approximation to simplify the determination of electronic wavefunctions and their energies [48], since it leads to an analytical approach for the calculation. The basic assumption of this approximation is for the movement of the nuclei to be much slower than the motion of the electrons, due to their higher mass ($\times 1000$). The electrons therefore move in a static nuclear framework. Following this approximation the complete wavefunction Ψ of a molecule depends in general on all coordinates of the electrons (\vec{r}) and nuclei (\vec{R}) and obeys the time-independent Schrödinger equation,

$$\hat{H}(\vec{r}, \vec{R})\Psi(\vec{r}, \vec{R}) = E\Psi(\vec{r}, \vec{R}), \quad (2.77)$$

with \hat{H} being the complete Hamiltonian of the molecule and E being the eigenenergy of the wavefunction Ψ . The separation of the nuclei movement from the electron movement is then expressed as a separation of Ψ into an electronic wavefunction $\Psi_0(\vec{r}, \vec{R})$ (the zero expresses the zeroth order of this approximation) in which the nuclear coordinates \vec{R} are parameters, a nuclear wavefunction $X(\vec{R})$ and a spin wavefunction S ,

$$\Psi(\vec{r}, \vec{R}) = \Psi_0(\vec{r}, \vec{R})X(\vec{R})S. \quad (2.78)$$

The spin wavefunction will not be discussed in this thesis, since no spin-dependent phenomena were measured. This equation can in principle be solved for all possible spatial nuclear arrangements to obtain the energy E dependent on the nuclei positions \vec{R} . The arrangement with lowest energy corresponds to the equilibrium configuration of the nuclei. The Born–Oppenheimer approximation gives very good results for stable molecular states, e.g. the ground state of a molecule [17].

However, if one nuclei configuration yields similar energies for two electronic states, this approximation breaks down. These situations are caused by vibronic couplings (or in the case of a strong coupling between Ψ_0 and S , the spin–orbit coupling) and will

be dealt with at the end of this chapter. First a comprehensive approximation to the electronic wavefunction is given in the next subsection by introducing molecular orbitals.

2.4.2 Molecular orbitals

The approximate electronic wavefunction Ψ_0 from Eq. 2.78 can be expanded into a product of one-electron orbitals ϕ_i that are obtained by assuming that the molecule possesses only one electron, hence the approximation neglects the electron–electron repulsion [13, 17],

$$\Psi_0 = \prod_i \phi_i. \quad (2.79)$$

These one-electron orbitals then fulfill the Schrödinger equation (Eq. 2.77) and therefore possess an eigenenergy. In the following a description is given how these one-electron orbitals, called herein molecular orbitals, can be constructed from the atomic orbitals of the participating atoms.

When atoms are in close proximity their atomic orbitals, the eigenfunctions of the atomic Hamilton operator, can be linearly combined to the molecular orbitals [49]. These molecular orbitals may have lower energy than the individual atomic orbitals. This linear combination of the atomic orbitals (LCAO) χ_n results in the molecular orbitals ϕ_i

$$\phi_i = \sum_n c_{n,i} \chi_n, \quad (2.80)$$

with c_n being the coefficient of the atomic orbital χ_n . With the χ_n known, the coefficients can be obtained computationally for example with the Hartree-Fock procedure [50]. From n atomic orbitals n molecular orbitals can be constructed. However, the average energy of the molecular orbitals and the atomic orbitals has to be the same, i.e. $\sum_i (c_{n,i}^2) = 1$ and the molecular orbitals need to be normalized like the atomic orbitals, i.e. $\sum_n (c_{n,i}^2) = 1$ [13].

The construction of the molecular orbitals for the hydrogen molecule is illustrated in Figure 2.9. The two 1s atomic orbitals of the two hydrogen atoms are combined to one molecular orbital with lower energy ($\sigma 1s$) and one molecular orbital with higher energy ($\sigma^* 1s$) [49], such that the average energy does not change (left in Figure 2.9). The probability density of the electrons in this molecular orbital is shown on the right side of Figure 2.9. The combination of the two atomic orbitals with the same sign,

$$\phi_{\sigma 1s} = \frac{1}{\sqrt{2}} \chi_{1s1} + \frac{1}{\sqrt{2}} \chi_{1s2}, \quad (2.81)$$

with χ_{1sx} being the atomic orbital of either atom $x = 1$ or 2 , results in an increased probability to find the electron between the atoms (bottom right in Figure 2.9). Occupation of this orbital with electrons therefore leads to a bond between these atoms and is called a bonding orbital. The combination of the atomic orbitals with different sign,

$$\phi_{\sigma^* 1s} = \frac{1}{\sqrt{2}} \chi_{1s1} - \frac{1}{\sqrt{2}} \chi_{1s2}, \quad (2.82)$$

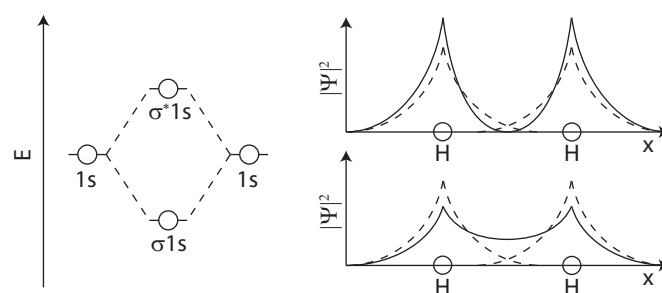


Figure 2.9: Left: Construction of the bonding (σ_{1s}) and antibonding (σ^*_{1s}) molecular orbital out of the two atomic $1s$ orbitals. Whereas the bonding orbital is decreased in energy the antibonding orbital is increased in energy. Right: The density probability $|\Psi|^2$ of the bonding (bottom) and antibonding (top) molecular orbitals (solid lines) as well as the atomic $1s$ orbitals (dashed lines).

	atomic orbitals χ	molecular orbitals ϕ
σ -bonds	 $2s$ $2s$	 σ^*2s $\sigma2s$
	 $2p_x$ $2p_x$	 σ^*2p_x $\sigma2p_x$
π -bonds	 $2p_{yz}$ $2p_{yz}$	 π^*2p_{yz} $\pi2p_{yz}$

Figure 2.10: Construction of σ bonds and π bonds with atomic s and p orbitals. The atomic orbitals that form a bond (left) need to have the same symmetry towards the bond to be generated. The resulting bonding and antibonding molecular orbitals are shown on the right.

leads to decreased probability between the two nuclei, i.e. population of this orbital leads to repulsion (top right in Figure 2.9). This orbital is therefore called antibonding. Since the energy of the bonding orbital is lower than the energy of the antibonding orbital, the bonding orbital is occupied by the two electrons of the hydrogen molecule, whereas the antibonding orbital is left empty.

Besides such σ bonds the π bonds also play a crucial role in organic molecules. Assuming a C_2 molecule, 8 molecular orbitals can be constructed from the 8 atomic orbitals ($2 \times 2s$, $6 \times 2p$) as shown in Figure 2.10. Whereas the $2s$ and $2p_x$ orbitals (the molecular axis is the x axis) result in bonds with similar symmetry to the hydrogen bond (σ : *gerade* for inversion, *gerade* for mirroring at the horizontal mirror plane σ_h that transforms atom 1 into atom 2; σ^* : *ungerade* for inversion, *ungerade* for mirroring), the combination of the $2p_y$ and $2p_z$ orbitals lead to molecular orbitals with different symmetry. The resulting bond is called a π bond. In contrast to σ bonds the binding molecular orbital

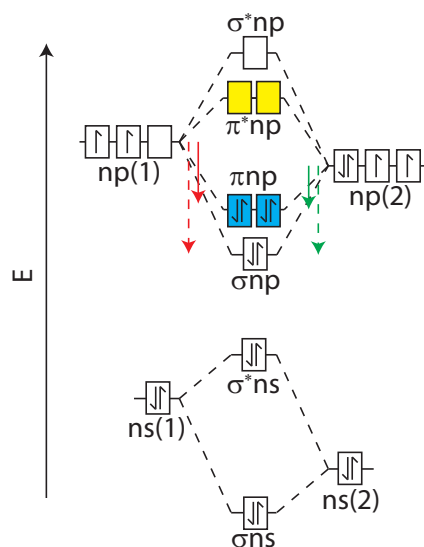


Figure 2.11: Molecular orbital diagram for a heteroatomic molecular orbital (the two atoms have different electronegativity leading to atomic orbitals with different energies). The bonding orbitals in this case have more character of the energetically lower atomic orbital whereas the antibonding orbital has more character of the energetically higher atomic orbital.

is *ungerade* with respect to inversion and *gerade* for mirroring, whereas the antibonding molecular orbital is *gerade* with respect to inversion and *ungerade* for mirroring. Usually the π bonds are weaker than σ bonds due to the smaller spatial overlap of the electronic wavefunctions.

Figure 2.11 shows the molecular orbital diagram for a heteroatomic molecule consisting of two atoms. In this case the orbital energies of atom 2 (right) are lower than those of atom 1 (left). The bonding molecular orbitals (σns , σnp and πnp in Figure 2.11) then tend to the atomic orbital with lower energy. Following Eq. 2.80 the coefficients of atom 2 in the bonding molecular orbitals are greater than those of atom 1. The corresponding antibonding orbitals ($\sigma^* ns$, $\sigma^* np$ and $\pi^* np$) on the other hand are then energetically more similar to the atomic orbital of atom 1. The molecular orbitals are filled with the electrons from the bottom, leading to occupied and unoccupied orbitals. Knowing that the energies of the atomic orbitals correlate with the electronegativity of the atom, ionic bonds can also be understood as the limit of this relation. The anion possesses the atomic orbital with low energy, therefore the molecular orbital is very similar to this atomic orbital, hence the electrons are located mostly at this atom, while the cation remains with a positive charge.

The reduction in energy due to the occupation of the molecular orbitals depends on the energy difference between the atomic orbitals (the greater the difference, the smaller the reduction in energy) and the spatial overlap between the atomic orbitals. The reduction in energy in the case of Figure 2.11 would then be two times each solid arrow plus once each dashed arrow, since all three bonding orbitals are occupied by two electrons, whereas the corresponding antibonding orbitals are unoccupied.

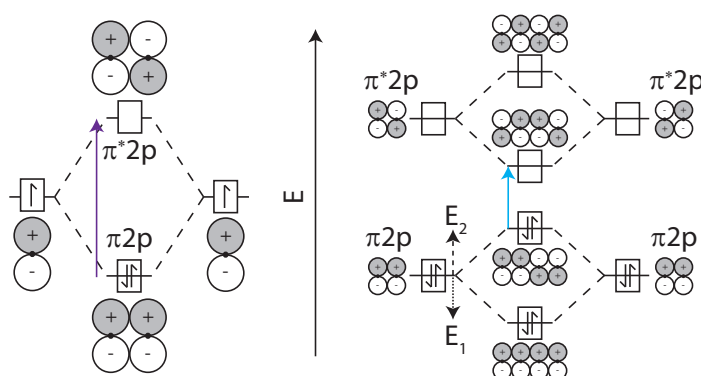


Figure 2.12: Left: Molecular orbital diagram of the ethene π bond. The first transition energy needed to excite one electron from the HOMO to the LUMO is marked by the purple arrow. Right: Molecular orbital diagram of butadiene. It can be constructed by overlapping the bonding orbitals of two ethene molecules to form two new bonding molecular orbitals (lower half on the right) and by overlapping the antibonding orbitals of two ethene molecules to form two new antibonding molecular orbitals (upper half on the right). The HOMO \rightarrow LUMO excitation can be achieved with less energy in this case. The butadiene system is energetically favored over two individual ethene molecules ($|E_1| > |E_2|$) as explained in the text.

The bond order of a chemical bond B is then defined as

$$B = \frac{\text{electrons in bonding orbitals} - \text{electrons in antibonding orbitals}}{2}. \quad (2.83)$$

The highest occupied molecular orbital (HOMO, blue in Figure 2.11) as well as the lowest unoccupied molecular orbital (LUMO, yellow in Figure 2.11) are called frontier molecular orbitals and play a crucial role in mechanistic explanations of chemical reactions, as will be discussed in Section 2.5.

Delocalized systems

In polyatomic molecules most molecular orbitals still consist in a good approximation only of two atomic orbitals. Only delocalized systems, e.g. benzene, possess molecular orbitals to which atomic orbitals from three or more atoms contribute. Figure 2.12 shows the molecular orbital of butadiene. The construction of its molecular orbitals is in the first step straightforward when the molecule is regarded as a “bi-ethene”, i.e. two ethene molecules (molecular-orbital diagram on the left of Figure 2.12) form a bond between them [13]. The bonding and antibonding molecular orbitals of the two ethene molecules can then overlap either constructively or destructively to form new molecular orbitals (right in Figure 2.12). Up to now the total energy reduction of the two individual ethene molecules and the butadiene as shown in Figure 2.12 is zero (the dashed, E_2 , and pointed, E_1 , black arrow are still equally long, $E_1 = -E_2$), therefore there is no reason for the bond to be formed contrary to the experimental observation.

This discrepancy can be explained, when looking at the coefficients $c_{n,i}$ of the partic-

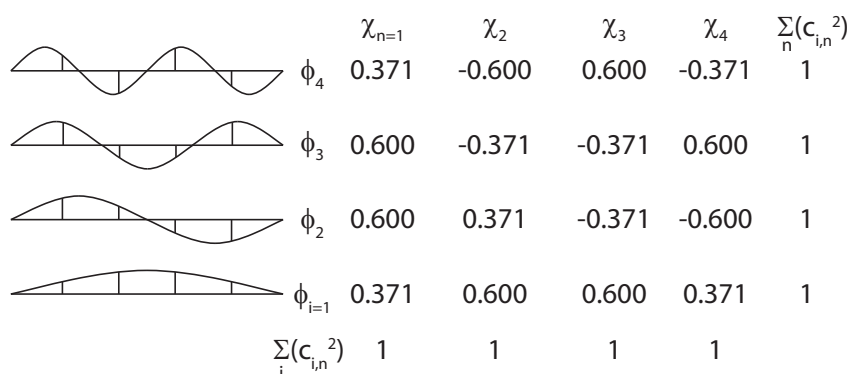


Figure 2.13: The molecular orbitals Ψ_x of butadiene and the coefficients [51] of the participating p orbitals, see Figure 2.12. In Ψ_2 the node is located between two p orbitals with low coefficients, hence the antibonding contribution to this molecular orbital due to the node is lowered. Therefore butadiene is energetically favored over two individual ethene molecules.

ipating atomic orbitals,

$$\phi_i = \sum_{n=1}^4 c_{n,i} \chi_n, \quad (2.84)$$

with ϕ_i denoting the molecular orbital starting with the orbital with lowest energy ($i = 0$) and χ_n denoting the participating p orbital of the n -th atom. Assuming that the four atomic orbitals span a box for the electrons, the orbitals can be described as a series of sines, as depicted in Figure 2.13 on the left. Laying the atomic orbitals with different amplitude underneath these sines, with the size corresponding to the coefficient (illustrated as black vertical lines), results in a qualitative picture of the coefficients of the atomic orbitals in the molecular orbitals and the wavefunction ϕ_i . The exact numerical values of the coefficients $c_{n,i}$ are given on the right side of Figure 2.13 [51].

The bonding contribution in ϕ_1 is stronger than the antibonding contribution in ϕ_2 since the nodal plane in the latter is adjacent to orbitals with small coefficients whereas in the case of ϕ_1 the orbital passes through a maximum at that position. Therefore a bonding contribution remains, i.e. $|E_1| > |E_2|$ in Figure 2.12.

The extension of the ethene π system by 2 atoms, each contributing with their p orbital, yields a smaller energy difference between the HOMO and LUMO (the “band gap”), as indicated by the purple and blue arrow in Figure 2.12. This energy is the smallest energy needed for photochemical excitation of the π system. Further extending the π system results in huge delocalized systems with decreasing band gap. Those systems play an important role in nature for example as sun-light absorbing materials in photosynthesis.

2.4.3 Vibrational coupling

Up to this section the time-independent energies of nonvibrating molecules have been discussed. In this chapter the normal modes of a molecule will be included into the

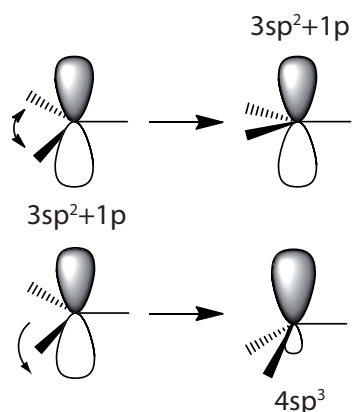


Figure 2.14: The planar methyl cation (left) possesses a mirror plane in which all atoms are contained. An in-plane normal mode (top) obeys this symmetry and leaves the empty orbital unchanged. However, the bending mode (bottom) changes the electronic configuration in such a manner that additional s character is mixed into the empty orbital, leading to a tetrahedral structure and sp^3 hybridization. The two electronic states ($3sp^2+1p$ and $4sp^3$) are therefore coupled by such a bending mode.

picture of the processes in molecules [17, 48]. As long as the molecular configuration corresponds mostly to only one electronic state (the energies of other electronic states at the same configurations are too high) the Born–Oppenheimer approximation (Eq. 2.78) is valid. However, if through the motion of the nuclei an arrangement is reached that can be attributed to different electronic states with small energy difference, the actual electronic state of the molecule becomes a mixture of these states. An example for such a process is shown in Figure 2.14.

The planar methyl cation CH_3^+ possesses an empty p orbital and a mirror plane containing all atoms (top in Figure 2.14). When the hydrogen atoms are substituted with more electronegative atoms like fluorine, the empty orbital becomes a sp^3 orbital and the molecule takes up a tetrahedral structure with the original mirror-plane symmetry being lost (bottom right). The normal modes that couple the $3sp^2+1p$ state with the $4sp^3$ state therefore have to disobey the mirror-plane symmetry. Such a mode is for example the bending mode in which two of the hydrogen atoms move out of the mirror plane (also called umbrella mode, as shown in the bottom of Figure 2.14). Along this normal mode additional s character is mixed into the empty orbital so that rehybridization from p to sp^x takes place. Therefore the electronic wave function is coupled strongly to the nuclear motion through this bending mode. Vice versa the normal modes that obey the mirror-plane symmetry cannot mix s character into the empty p orbital (top). Therefore along those modes weak coupling between the electronic and vibrational motion is observed. Which electronic state the molecule prefers is determined by the energies of the tetrahedral and planar structure and depends on electronic as well as steric effects.

Mathematically this vibrational coupling can be described with quantum mechanical perturbation theory [45]. The perturbation operator describing a vibronic interaction \hat{P}_{vib} “distorts” an electronic wavefunction Ψ_1 . In the case of the bending mode from

the previous example the operator projects $\Psi_1 = 3sp^2 + 1p$ into $\Psi_2 = 4sp^3$, hence the orthogonality of the two eigenfunctions is destroyed: The two electronic eigenfunctions of the molecule ($\Psi_1 = 3sp^2 + 1p$ and $\Psi_2 = 4sp^3$) are coupled by the bending mode. The extent of this coupling is given by

$$\langle \Psi_1 | \hat{P}_{vib,bm} | \Psi_2 \rangle, \quad (2.85)$$

with $\hat{P}_{vib,bm}$ being the operator for the bending mode vibration. However, the states are not only coupled by this vibrational mode but also by any other vibrational mode to a characteristic extent. Weakly coupling modes, like the in-plane vibrational modes in the previous example, would result in a value close to zero for the coupling (Eq. 2.85). Experimentally this relation can be measured by the rate constant k_{obs} describing the transition between two states of the molecule,

$$k_{obs} = k_{max}^0 \left(\frac{\langle \Psi_1 | \hat{P}_{vib} | \Psi_2 \rangle^2}{\Delta E_{12}^2} \right) (\langle X_1 | X_2 \rangle^2), \quad (2.86)$$

with k_{max}^0 being the maximum possible rate constant, $\langle X_1 | X_2 \rangle^2$ being the Franck-Condon factor (Figure 2.15) that is a measure of the similarity of the nuclei arrangements X_1 and X_2 , and ΔE_{12} being the energy difference between the eigenstates Ψ_1 and Ψ_2 .

From this equation it follows that the velocity of a transition is either limited by the process of the perturbation to make Ψ_1 look like Ψ_2 or by the speed of the nuclei to relax back into a state in which the nuclear wavefunction X_1 looks like X_2 . Since the nuclei move much slower than the electrons, in most cases the latter contribution is the rate determining step. Therefore the perturbation first induces a change in the electronic configuration and secondly the excess energy due to the change is channeled into the vibrational modes that make X_1 look like X_2 .

In chemical reactions such a situation can be encountered for example for intramolecular reactions as pericyclic reactions (see Section 2.5) or for intermolecular reactions as bimolecular or higher order reactions. In these cases the reactants have to be distorted towards the product to reach the transition state of the reaction. This approach is the basis for computational methods such as transition state theory to obtain reaction rates numerically [48, 49]. The energy of the system dependent on the nuclear arrangement is called the potential surface. The normal modes serve as the routes in this multi-dimensional potential surface that are available to the system to reach the transition state.

2.4.4 Radiative transitions

In radiative transitions the perturbation operator \hat{P}_{vib} is replaced by the transition dipole moment operator $\hat{\mu}$ (see also Eq. 2.71) describing the interaction of the electric field with the dipole moment of the molecule [48]. The electronic excitation (the vertical arrows in Figure 2.15) takes only 10^{-15} to 10^{-16} s [17]. In this process the molecule jumps from the ground-state potential surface S_0 to the S_1 potential surface (in case of the lowest electronic excitation). After this electronic excitation a large amount of excess energy is available since the excitation most often does not end in the vibrational ground state

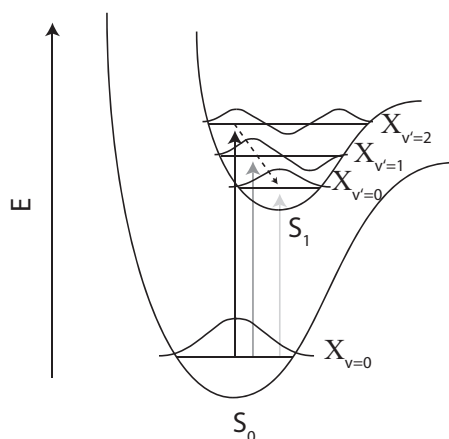


Figure 2.15: The final state of a radiative transition is governed by the Franck–Condon factors that are a measure of the overlap of the nuclear wave functions X_i . The most probable transition in this example is therefore the population of the $X_{v'=2}$ vibrational state (black arrow), whereas the other transitions (grey) are weaker. After excitation the nuclei undergo vibrational relaxation towards the $X_{v'=0}$ state (black dashed arrow).

$v' = 0$ but in a vibrationally excited state (for example $v' = 2$ in Figure 2.15) because of the Franck–Condon factor $\langle X_1 | X_2 \rangle^2$ in Equation 2.86. This vibrational excess energy is dissipated into the environment either via coupling to other vibrational modes (internal vibrational relaxation) or coupling to the solvent to reach $v' = 0$ (dashed black arrow). This process can be observed in transient-absorption experiments (described in Section 3) as “vibrational cooling”.

2.4.5 Potential surface crossing

In the Born–Oppenheimer approximation it is assumed that the electronic wavefunction instantaneously adapts itself to the nuclei arrangement X_i , leading to only one electronic distribution for the ground state at a certain arrangement and different distributions in each excited state. This assumption leads to adiabatic potential surfaces. However, when two electronic states are very close in energy at a certain nuclei configuration the instantaneous adaptation of the electronic wavefunction is not given. In these cases the Born–Oppenheimer approximation breaks down since the coupling matrix element, e.g. Eq. 2.85, between the two electronic eigenstates becomes infinite [17].

Avoided crossings

In such situations the two zeroth-order electronic wavefunctions Ψ_1 and Ψ_2 in Figure 2.16 can mix (left) such that at the point where the two adiabatic surfaces would cross (the critical point, r_c in Figure 2.16) the potential energy surfaces are a linear combination of Ψ_1 and Ψ_2 [17]. This is often called the “noncrossing rule”. The zeroth-order adiabatic potential surfaces Ψ_1 (red) and Ψ_2 (green) are given by the colored lines in Figure 2.16. A molecule with these potential surfaces sees, due to the noncrossing rule, only the

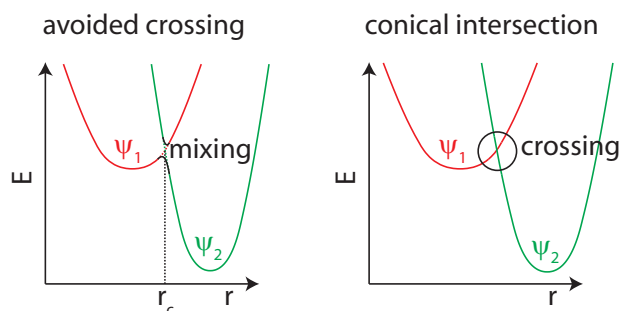


Figure 2.16: Left: The noncrossing rule states that two zeroth-order electronic states (Ψ_1 (red) and Ψ_2 (green)) must not cross. In the vicinity of their crossing at r_c (the colored dashed lines) the two states mix resulting in an avoided crossing as depicted by the solid lines. Right: Molecules with lower symmetry do not obey the noncrossing rule leading to true potential surface crossings called conical intersections. The double-cone shape of a conical intersection can be perceived in the cut marked by the black circle.

electronic states given by the solid lines in which the potentials avoid each other at the critical point. After excitation into the upper excited state (the potential in the middle, consisting partly of Ψ_1 and Ψ_2) the system relaxes into the vibrational ground state (the black part of the upper potential) and “jumps” vertically spontaneously into the electronic ground state [52, 53]. The probability of the jump increases with decreasing energy between the two electronic states. Hence, the stronger the coupling between the electronic states, the further apart are the coupled states and the smaller is the probability of the jump. Whether the molecule proceeds into the ground state of Ψ_1 or Ψ_2 after the jump depends on the exact location and curvatures of the potential surfaces.

Conical intersections

The noncrossing rule is only strictly followed in highly symmetric molecules, especially diatomic molecules that possess axial symmetry [17]. Since organic molecules consist of many atoms that give rise to many normal modes, the symmetry in these molecules is generally low so that potential surfaces can indeed cross. These crossings are called conical intersections (right of Figure 2.16) [54–56] because the potential surface has the shape of a double cone with the vertex being the point of intersection r_c . The black circle in Figure 2.16 on the right marks the double cone shape as a cut. Conical intersections offer a very efficient funnel for an excited molecule to reach the electronic ground state. The time scale of such a transition is on the order of a vibrational period (around 100 fs).

2.5 Pericyclic reactions

In the last section the basis for the description of the state and the dynamics of a molecule has been introduced with the help of molecular orbitals and potential surfaces. Although

mechanistic photochemistry is very complex and most often quantum mechanical calculations are needed to understand the dynamics, the frontier molecular orbital (FMO) theory allows for an intuitive approach to some photochemical reactions. Especially for the understanding of pericyclic reactions the FMO theory is a viable tool. Throughout this section the previously introduced molecular orbitals and conical intersections are used to derive the mechanism and selection rules for pericyclic reactions. The section ends with the application of the derived selection rules applied to two pericyclic reactions, the electrocyclic reaction and the sigmatropic rearrangement. In Chapter 4 and 5 the speed of these two reactions is determined with transient-absorption techniques.

2.5.1 Frontier molecular orbitals

The crucial parameter in the kinetics of chemical reactions is the activation energy ΔE , that is to be overcome for a reaction to occur [13]. Klopman [57] and Salem [58, 59] have derived ΔE for a bimolecular reaction between molecule 1 and molecule 2 starting from quantum mechanical perturbation theory to be

$$\Delta E = - \sum_{ab} (q_a + q_b) \beta_{ab} S_{ab} + \sum_{k < l} \frac{Q_k Q_l}{\epsilon R_{kl}} + \left(\sum_r^{\text{occ.}} \sum_s^{\text{unocc.}} - \sum_s^{\text{occ.}} \sum_r^{\text{unocc.}} \right) \frac{2 (\sum_{ab} c_{ra} c_{sb} \beta_{ab})^2}{E_r - E_s}, \quad (2.87)$$

with

- q_a : electron density of the atomic orbitals a , $q_a \geq 0$
- β_{ab} : resonance integral: interaction energy between the atomic orbitals a and b that are not located at the same atom, $\beta_{ab} \leq 0$,
- S_{ab} : overlap integral: proportional to the energy reduction due to the overlap of the atomic orbitals a and b , $S_{ab} \geq 0$,
- Q_k : charge at atom k ,
- ϵ : local dielectricity constant,
- R_{kl} : distance between atom k and l ,
- $c_{ra} c_{sb}$: coefficient of the atomic orbital a of the molecular orbital r (located at molecule 1) multiplied by the coefficient of the atomic orbital b of the molecular orbital s (located at molecule 2),
- E_r and E_s : energy of molecular orbital r and s , respectively.

Although this equation is very fundamental for almost all chemical reactions, a complete investigation would be beyond the scope of this work. A detailed interpretation of the terms and the influence of the parameters can be found in the literature [13].

When two molecules approach, the electron densities in the orbitals repel each other, which is described by the first term in Eq. 2.87 (including the minus sign). It is always

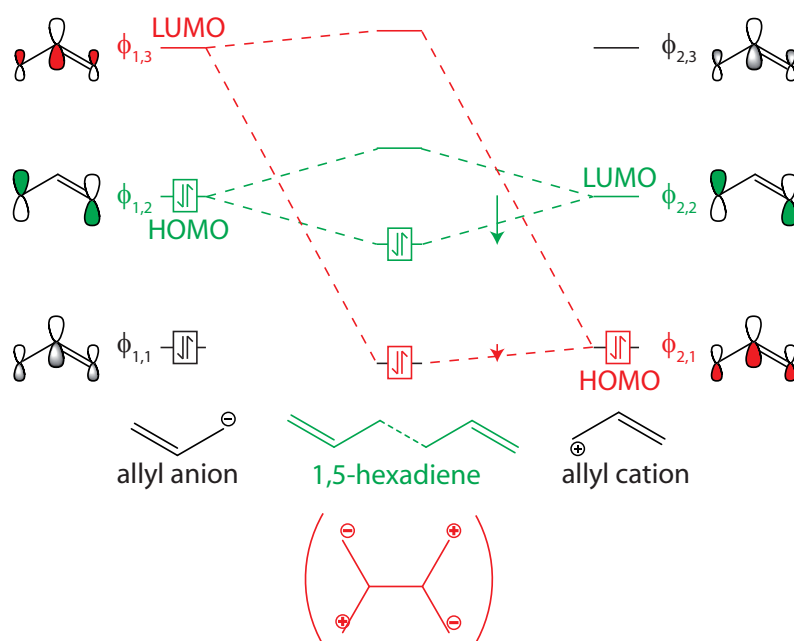


Figure 2.17: Reaction of an allyl anion with an allyl cation. The interaction can either be the red one (HOMO of allyl cation and LUMO of allyl anion) or the green one (HOMO of allyl anion and LUMO of allyl cation). The reduction in energy, as marked by the green and red arrow, due to the interaction is far better for the green pathway than for the red one. The coefficients of the participating molecular orbitals determine the product to be formed (bottom).

positive, i.e. increases the activation energy ΔE . The second term contains the electrostatic interactions of the two reactants, i.e. ΔE increases when molecule 1 and 2 would both be negatively or positively charged, whereas it is reduced when they carry opposite charges.

The third term of Eq. 2.87 contains the stabilization energy due to the overlap of the occupied molecular orbitals of molecule 1 (labeled r) with the unoccupied molecular orbitals of molecule 2 (labeled s) and vice versa. For this contribution mostly only the frontier molecular orbitals, i.e. the HOMO and LUMO are relevant, because their energy difference $E_r - E_s$ is the smallest. (If in the third term $E_r \approx E_s$ the interaction is better described as charge-transfer with the form $\sum_{ab} 2c_{ra}c_{sb}\beta_{ab}$, nevertheless the principle is the same, the more similar the energy, the lower the activation energy ΔE [13]).

The application of this equation to the reaction of the allyl anion and the allyl cation is shown in Figure 2.17. Since the frontier molecular orbitals are the π orbitals, the σ orbitals are omitted in the molecular orbital diagrams for clarity from now on.

The molecular orbitals of both reactants are energetically almost the same. In the anion the two lowest orbitals are occupied whereas in the cation only the lowest orbital is occupied. The relevant interaction between the reactants is between the HOMO of the anion and the LUMO of the cation (green in Figure 2.17),

$$|E_{\phi_{1,2}} - E_{\phi_{2,2}}| < |E_{\phi_{1,3}} - E_{\phi_{2,1}}|. \quad (2.88)$$

This can be experimentally verified when looking at the product of this reaction, 1,5-hexadiene (green, bottom in Figure 2.17). The orbitals $\phi_{1,2}$ and $\phi_{2,2}$ have their largest coefficient located on the outer atoms, whereas at the central atom these orbitals have a nodal plane (the sines from Figure 2.13 can also be applied to the allyl anion and cation). The new bond is created between the reaction centers, which are the atoms with the highest coefficients in this case. Since the reaction occurs between the orbitals $\phi_{1,2}$ and $\phi_{2,2}$ this leads to 1,5 hexadiene. If it were the other way round (red in Figure 2.17) another molecule would be the product, since $\phi_{1,3}$ and $\phi_{2,1}$ both have their largest coefficient at the central atom.

The applicability of this concept to almost any reaction is the reason for its popularity when reaction mechanisms are to be explained. It is even one of the few concepts that gives intuitive explanations for the mechanism of some singlet photochemical reactions, to which the pericyclic photochemical reactions, one topic of this thesis, belong.

2.5.2 Pericyclic reactions in the FMO picture

Forming and breaking up a ring (= cycle) in a molecule is the same reaction, only the direction of the reaction changes. During the breaking of a cycle the reaction center, i.e. in this case one bond, evolves into two reaction centers. Hence in the reverse reaction, the formation of a cycle, the two reaction centers form the new bond synchronously. The application of the frontier molecular orbital theory to these type of reactions, i.e. cyclic systems, results in special selection rules [60] derived in the following.

Thermal reactions

Assuming the thermal reaction of butadiene (1) with ethene (2) to cyclohexadiene (similar to a “ring closure”) as shown on the left in Figure 2.18, the relevant interaction can either be the HOMO of 1 and LUMO of 2 (top) or vice versa (bottom). Note that the ethene molecule approaches the butadiene from the bottom and not from the side, as indicated by the bent curve connecting the corresponding atomic orbitals. (Top and bottom refers to the half space above and below the plane containing the atoms. The p orbitals then extend into both half spaces.) The bond formation occurs simultaneously at the right and left side of the π system. The participating orbitals determine whether the overlap between the two molecular orbitals is constructive, i.e. the atomic orbitals at the two reaction centers have the same sign in the overlap region (green curves in 2.18), or destructive (dashed red curves), i.e. the overlapping atomic orbitals have opposite sign in the overlap region.

In the case of the reaction of butadiene with ethene both possibilities (top and bottom left) are constructive and therefore both possibilities are called “symmetry allowed”. Furthermore the two new σ bonds are formed on the same side of both π systems (in the same half space), classified as “suprafacial”. The complete name of the reaction is then $[4\pi_s + 2\pi_s]$, because in butadiene 4π electrons add to a 2π system, with both reactants reacting suprafacially (s).

In the case of the dimerization of ethene, shown on the right in Figure 2.18 the suprafacial interaction $[2\pi_s + 2\pi_s]$ between the HOMO and LUMO leads to a nonconstructive

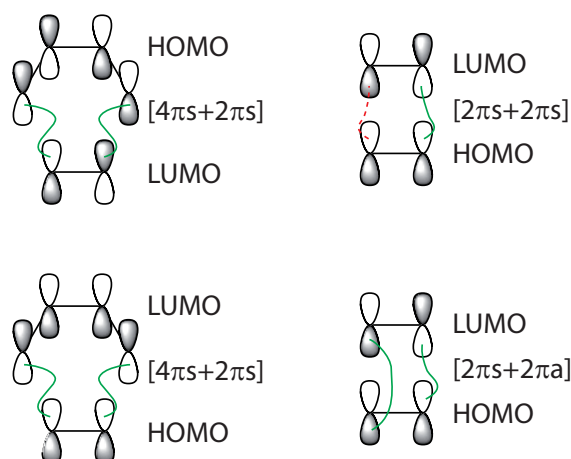


Figure 2.18: Possible pathways in the 4+2 cycloaddition (left) and 2+2 cycloaddition (right). The green lines indicate constructive overlap between the connected halves of the atomic orbitals of the reaction centers that decrease the activation energy. The red dashed line indicates destructive overlap that increases the activation energy for a reaction.

overlap at the left atom (dashed red line), this reaction is therefore “symmetry forbidden”. However, if the atomic orbitals would form the new bonds by reacting from opposing sides of the π system, as depicted in Figure 2.18 (bottom right), the overlap would be constructive and “antarafacial” (a) and hence be called a $[2\pi s + 2\pi a]$ reaction. Despite this pathway, the dimerization reaction does not occur because the geometrical demand for the antarafacial overlap cannot be met. Based on the condition derived above, the Woodward–Hoffman rules for thermal processes summarize which reactions can take place spontaneously and which cannot: “A pericyclic reaction in the electronic ground state is symmetry-allowed if the total number of the $(4q + 2)s$ - and $(4r)a$ components is odd”. Here a component is a reactant. For example in the cycloaddition of butadiene and ethene, both reactants react suprafacial. Butadiene has 4 electrons $(4q)s$ and ethene 2 electrons $(4q + 2)s$ (with $q = 0$). Hence in the reaction participate one $(4q + 2)s$ component and zero $(4r)a$ components, the reaction is therefore symmetry-allowed in the suprafacial pathway.

Photoreaction

In the case of photochemical excitation one electron is excited into an unoccupied orbital. The excitation wavelength determines from which of the occupied orbitals this electron originates and into which unoccupied orbital it is transferred. In the case of the longest-wavelength excitation the transition occurs from the HOMO to the LUMO, as shown on the left side of Figure 2.19 for ethene. In the following the orbitals after excitation are called “HOMO” and “LUMO” to state their meaning before excitation.

Two interactions are now possible, HOMO–“HOMO” (green in Figure 2.19) and LUMO–“LUMO” (red). In both cases the interacting orbitals possess the same energy and the same symmetry leading to a constructive overlap and a very strong re-

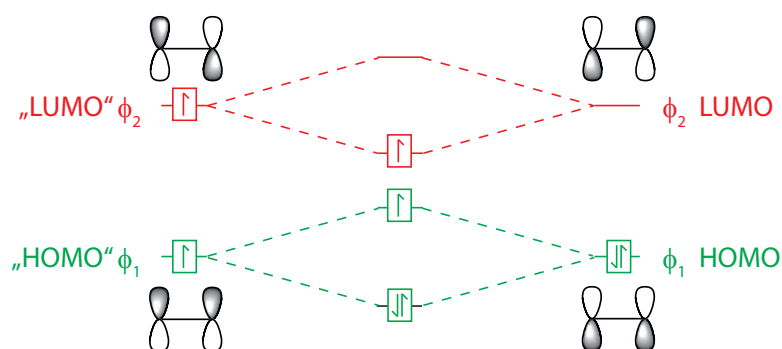


Figure 2.19: The reaction pathways of the photochemical 2+2 cycloaddition. After photoexcitation of the left ethene, both pathways, the red and the green one, lead to a decrease in activation energy. Hence the photochemical dimerization of ethene is allowed whereas the thermal pathway (Figure 2.18, top right) is forbidden.

duction of the activation energy for the reaction. The HOMO–“HOMO” interaction leads to only one electron in the antibonding and two in the bonding orbital. LUMO–“LUMO” leads to only one electron in the bonding orbital. Therefore the photochemical dimerization of ethene is symmetry allowed, whereas the thermal pathway is symmetry forbidden (see Figure 2.18, top right). This inversion of the selection rules is universal for pericyclic reactions, the Woodward–Hoffman rules for photochemical reactions are therefore: “A pericyclic photochemical reaction is symmetry allowed if the total number of the $(4q + 2)s$ - and $(4r)a$ components is even.”

The introduced terms “symmetry allowed” and “symmetry forbidden” are set into the context of Section 2.4.5 in Figure 2.20. In the electronic ground state S_0 the pericyclic reaction can either proceed only along the pathway with the lower activation energy to the product S_{0P} (Eq. 2.87). This pathway is therefore called symmetry allowed (dashed red line) and the pathway with the higher activation energy is therefore called symmetry forbidden (solid red line). From the excited-state potential surface S_1 a conical intersection exists to the product ground state S_{0P} . This conical intersection is only accessible without a barrier by the symmetry-allowed excited-state reaction pathway (solid black line). The symmetry-forbidden excited-state reaction pathway (dashed black line) is separated from the conical intersection by a barrier with the minimum preceding this barrier leading back to the reactant electronic ground state S_0 .

2.5.3 Conservation of orbital symmetry

The conservation of orbital symmetry [61] is an alternative approach to explain the outcome of pericyclic chemical reactions with the transformation that the molecular orbitals experience during the reaction. Considering a concerted reaction in which the binding molecular orbitals of the reactant can be continuously transformed during the reaction into binding molecular orbitals of the product, leads to a low activation energy since no bonding molecular orbital moves up very much in energy. Depending on whether such a pathway exists or not, the reaction is called symmetry allowed or symmetry

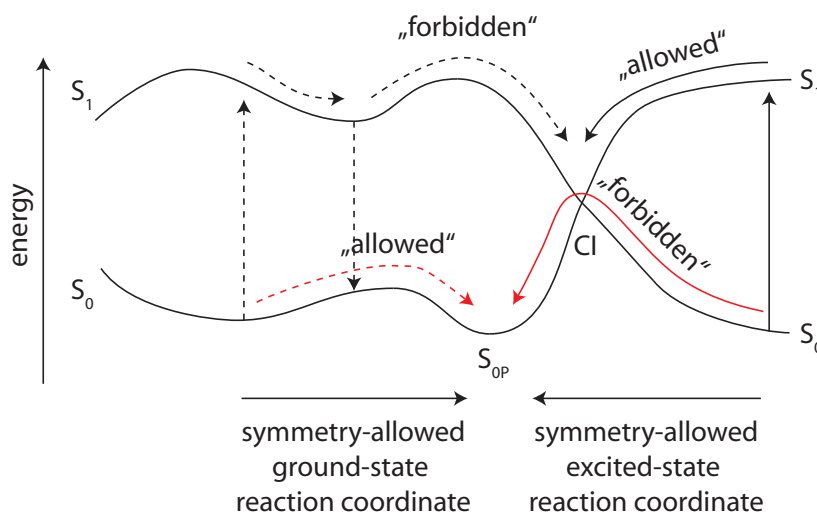


Figure 2.20: A simplified and generalized potential surface scheme of a pericyclic reaction to illustrate the terms “symmetry allowed” and “symmetry forbidden”. The product is the electronic state S_{0P} and the reactants electronic state is S_0 . Whereas for the thermal reaction the symmetry-allowed ground-state reaction pathway proceeds along a pathway with a low activation energy (red dashed line), the thermal symmetry-forbidden pathway (red solid line) proceeds along a pathway with high activation energy (see Eq. 2.87). The photochemical pathway allows access to the conical intersection CI (that could also be an avoided crossing, depending on the system) connecting reactant excited state and product ground state only for the symmetry-allowed excited-state pathway (black solid line). The symmetry-forbidden excited-state pathway (black dashed line) is separated by a barrier from the conical intersection and after photoexcitation the reaction proceeds in that case from the preceding minimum back to the reactant ground state.

forbidden, respectively.

The continuous transformation of the bonding molecular orbitals of the reactant into the bonding molecular orbitals of the product also expresses the connection towards the potential surface crossing in Section 2.4.5. During the reaction course the molecule reaches a geometry in which the electronic wavefunctions of the reactant and the product are isoenergetic [17]. At this point usually a conical intersection or an avoided crossing is located in pericyclic reactions along which the molecule reacts (see Figure 2.20).

The concept is illustrated by the reaction of cyclobutene and butadiene in Figures 2.21 and 2.22. The transformation of the σ orbital of cyclobutene (bottom left in Figure 2.21) can either be “conrotatory”, i.e. the orbitals rotate in the same direction (bottom in Figure 2.22), or “disrotatory”, i.e. the orbitals rotate in opposite direction (top).

In the last step the jump towards an orbital of the product with the same symmetry occurs. This is the same phenomenon as described in Section 2.4.5. The interaction of two electronic states leads to a mixing of the lower orbital into the upper orbital in a bonding (stabilizing) way and to a mixing of the upper orbital into the lower orbital in an antibonding (destabilizing) way (avoided crossing) or to a true crossing (conical intersection).

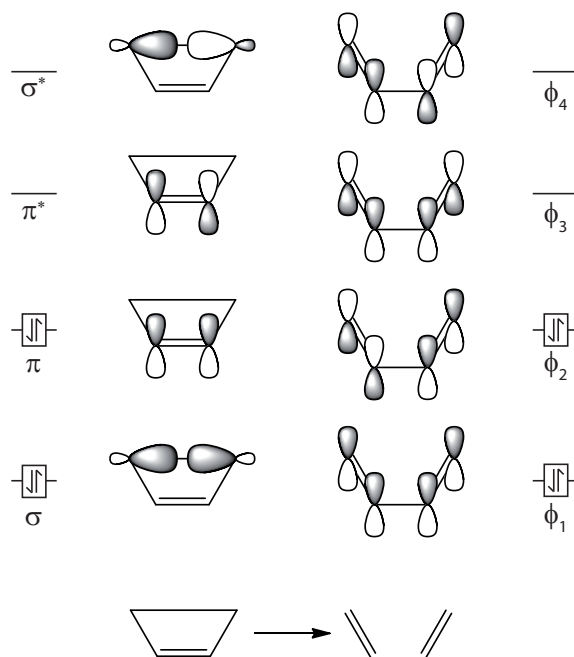


Figure 2.21: The two highest occupied and two lowest unoccupied molecular orbitals of cyclobutene (left) and butadiene (right).

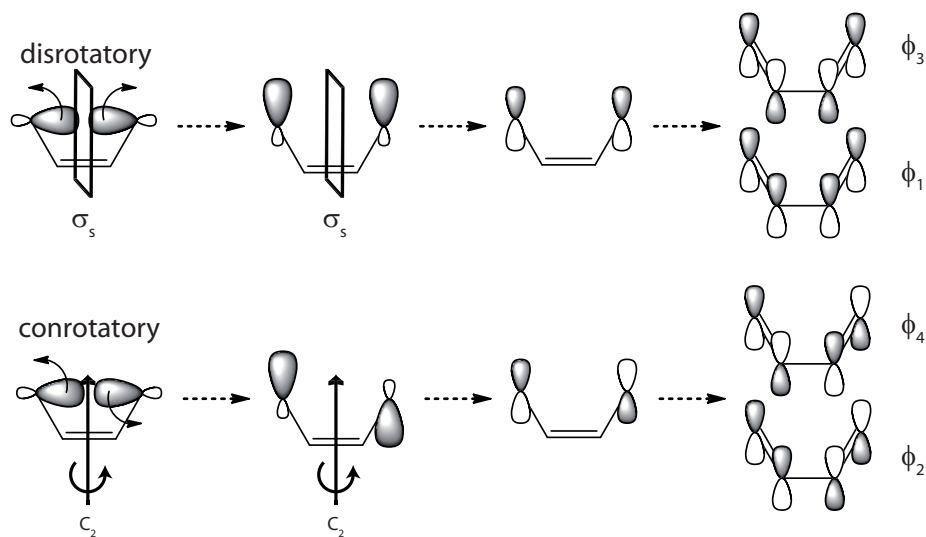


Figure 2.22: The change of symmetry of the reactant σ -molecular orbital (left) during the ring-opening reaction. The generated product molecular orbital in the case of disrotatory (top) opening needs to be symmetric towards the mirror plane, whereas conrotatory (bottom) opening leads to an asymmetric product molecular orbital towards the mirror plane. The possible product orbitals that the reactant molecular orbital can be converted into are shown on the right.

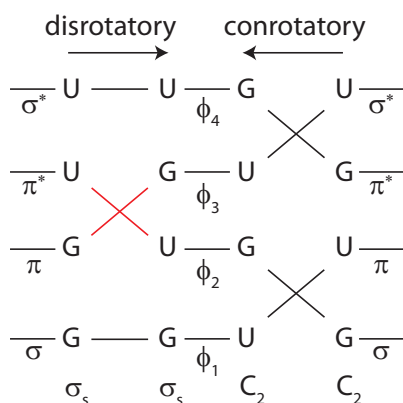


Figure 2.23: The conservation of orbital symmetry (G: *gerade*, U: *ungerade*) with respect to the rotation axis C_2 and the mirror plane σ_s (see Figure 2.22) during the ring-opening reaction. In the disrotatory pathway the HOMO reactant occupied molecular orbital ϕ_2 is converted into the LUMO of the product (π^*) which is higher in energy. Hence the activation energy for this reaction is increased. In the conrotatory pathway both occupied reactant molecular orbitals (ϕ_1 and ϕ_2) are converted into bonding orbitals of the product (σ and π).

σ orbital

In case of the disrotatory reaction (Figure 2.22 top) the reactant orbital σ in Figure 2.21 on the left can interact with the reactant orbital π and from thereon be transformed either into the ϕ_1 or ϕ_3 orbital on the right (see also Figure 2.23). These two product orbitals both do not have a node between the two middle atoms and the coefficients of the outer atoms have the same sign, as required by the disrotatory pathway (see Figure 2.22). In case of conrotatory rotation the σ orbital is either transformed into the ϕ_2 or ϕ_4 orbital (Figure 2.22 bottom).

π orbital

The π orbital of the reactant (Figure 2.21 on the left) does not change during the reaction in contrast to the σ bond. It is contained in its original structure (bonding character between the p orbitals) only in the ϕ_1 or ϕ_3 orbitals (Figure 2.21 on the right). Therefore in both pathways, disrotatory as well as conrotatory, the π orbital of the reactant can be transformed only into ϕ_1 or ϕ_3 in the product (see Figure 2.22).

Disrotatory pathway

In the disrotatory pathway both bonding and occupied reactant orbitals can be transformed into ϕ_1 (bonding) or ϕ_3 (antibonding). However only one orbital, the σ or the π orbital, can be transformed into the bonding orbital ϕ_1 , the other orbital needs to be transformed into ϕ_3 . Hence a bonding orbital is transformed into an antibonding orbital and vice versa ($\pi \rightarrow \phi_3$ and $\pi^* \rightarrow \phi_2$) in the disrotatory pathway, as marked by the red lines in Figure 2.23. The disrotatory pathway is therefore symmetry forbidden.

Conrotatory pathway

In case of the conrotatory pathway the π orbital can also be transformed into ϕ_1 or ϕ_3 . In contrast to the disrotatory pathway the σ orbital can be transformed into the ϕ_2 or ϕ_4 orbital. Hence both bonding and occupied orbitals can be transformed into bonding orbitals of the product ($\sigma \rightarrow \phi_2$, and $\pi \rightarrow \phi_1$), as depicted in Figure 2.23. This pathway is therefore symmetry allowed.

A shortcut to construct orbital correlation diagrams is to classify the molecular orbitals as *ungerade* (“U” in Figure 2.23) or *gerade* (“G”) with respect to a certain symmetry present in reactant and product. In case of butadiene these symmetry elements are the C_2 axis and the σ_s mirror plane. Since in the conrotatory pathway the rotation of the two reaction centers are C_2 to each other (see Figure 2.22), the orbitals that can transform into each other need to have the same character towards this symmetry operation. In the disrotatory pathway the rotation of the orbitals at the reaction centers are mirror images of each other (see Figure 2.22), i.e. the orbitals that are compatible need to possess the same character towards the symmetry operation σ_s .

Similar to the Woodward–Hoffman rules the pathways that are thermally symmetry forbidden are photochemically symmetry allowed. Whereas the orbital correlation stays the same, the occupation of the orbitals with electrons changes. After excitation the “LUMO” is occupied with one electron. Following the orbital correlation diagram in Figure 2.23 the energy of this “LUMO” always increases in case of the conrotatory pathway, hence this pathway is photochemically forbidden. However, in the disrotatory pathway the “LUMO” becomes the “HOMO” and vice versa. Thus no total additional antibonding character is introduced along this pathway and the reaction is symmetry allowed.

2.5.4 Electrocyclic reactions

Electrocyclic reactions are intramolecular cycloaddition reactions (as an example see Figure 2.18). During the course of the reaction a single bond is either formed (ring closure) or broken (ring opening). In that context the reaction of cyclobutene to butadiene from the previous section (Figure 2.21) is a ring opening.

In the context of the Woodward–Hoffman rules (see Section 2.5.2) this ring-opening reaction can be interpreted as a cycloaddition of the σ bond to the π bond. In the conrotatory pathway (right in Figure 2.24) a constructive overlap between the σ orbital (which is not the HOMO in this molecule) and the π^* orbital (the LUMO) is possible. The opposite is true for the disrotatory pathway, as shown on the left in Figure 2.24. With one reaction center being the middle of the σ bond, the “ σ bond” reacts antarafacial, whereas the π orbital reacts suprafacial. Following the terminology given above this is a $[2\pi s+2\pi a]$ reaction, which is symmetry allowed.

The explanation of electrocyclic reactions in the context of the conservation of orbital symmetry has been explained in the previous subsection. It can be applied to larger systems, leading to the rule that all systems containing $(4n+2)\pi$ -electrons should react thermally along the disrotatory pathway and photochemically along the conrotatory pathway. Vice versa for systems containing $(4n)\pi$ -electrons the opposite is true.

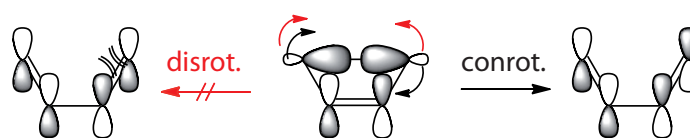


Figure 2.24: Interpretation of the ring opening as a cycloaddition of the σ bond to the π bond allows for the classification with the Woodward–Hoffman rules. In the disrotatory pathway (red arrows) the orbitals do not overlap both constructively (reaction to the left). However, in the conrotatory pathway (black arrows) the reaction is symmetry allowed (reaction to the right).

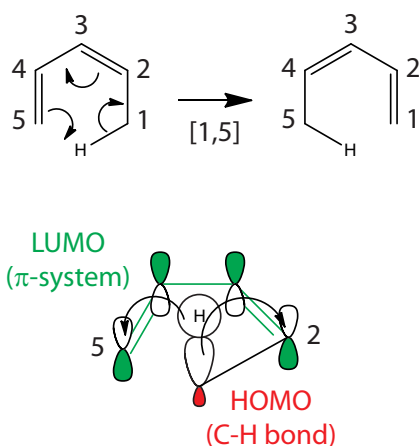


Figure 2.25: The [1,5] sigmatropic rearrangement is suprafacially symmetry-allowed. In the transition state (bottom) the HOMO of the σ bond (red) can overlap constructively with the LUMO at both reaction centers of the π system.

2.5.5 Sigmatropic rearrangements

In a sigmatropic rearrangement a substituent of a conjugated system shifts its position within the conjugated system. In Figure 2.25 the substituent is the H atom, whereas the conjugated system contains in the transition state (not shown) all carbon atoms.

With frontier molecular orbital theory it follows that the overlap between the LUMO of the diene (consisting of the carbon atoms with green orbitals and the green bonds) and the HOMO of the σ -C-H bond (red orbital) needs to be constructive at both reaction centers (black arrows) to be allowed. As shown in Figure 2.25 this is the case if the reaction proceeds suprafacial, i.e. the hydrogen atom does not switch to the other side (side defined by the plane containing all carbon atoms) of the π system.

However, if the hydrogen atom would switch sides during the reaction, i.e. react in an antarafacial way, the overlap at the left reaction center would not be constructive and therefore the antarafacial pathway is symmetry forbidden.

The reaction in Figure 2.25 is called a [1,5]-sigmatropic rearrangement, because the bond is broken at position 1 and formed at position 5 of the π system (Figure 2.25, top).

In case of a [1,3]-sigmatropic rearrangement the LUMO is *gerade* with respect to in-

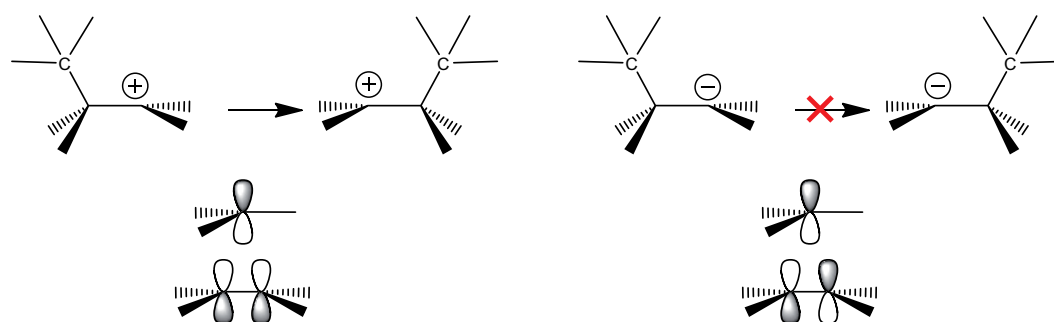


Figure 2.26: In the [1,2] sigmatropic rearrangement it follows from the frontier molecular orbital theory that the rearrangement can only take place in a cationic species (left), because only then the LUMO is *ungerade* towards inversion. In an anionic species (right) the LUMO possesses the wrong symmetry to overlap constructively with the wandering group.

version (π^* orbital in Figure 2.12), whereas *ungerade* symmetry is needed for a suprafacial pathway (carbon atoms 2 and 5 in Figure 2.25, bottom). Hence the suprafacial [1,3]-sigmatropic rearrangement is symmetry forbidden. The antarafacial pathway is symmetry allowed, however, due to steric strain the reaction does not take place. In contrast, the antarafacial [1,7] sigmatropic rearrangement takes place, because due to the greater ring the steric strain is reduced. In the transition state of this reaction the π system looks like a helix, with the hydrogen atom connecting both ends from opposing sides.

A special case is a [1,2]-sigmatropic rearrangement that can be encountered for example in the Wolff rearrangement that will be investigated in Chapter 5. Following the arguments given above, the LUMO of the π system needs to be *ungerade* towards inversion for a suprafacial reaction. In a π system consisting of two atoms as shown in Figure 2.26 this can only be achieved with a π orbital. Hence the reaction is only allowed for the cation (left) and not for the anion (right).

3 Techniques

In the following the experimental techniques employed in this thesis are presented. References for experimental setups that have been used and whose design and construction was not part of this thesis are given in the corresponding sections. In the first section the principle of pump–probe spectroscopy is explained and its experimental realization as transient absorption as used in this thesis is presented. The second section discusses the ultrafast light sources, beginning with the laser system delivering the ultrashort fundamental pulses. The nonlinear processes that convert these ultrashort pulses to the desired frequency are given thereafter. Part of this thesis is the construction of a fast polarimeter for accumulative femtosecond spectroscopy, which will be discussed in the third section of this chapter.

3.1 Transient absorption

Most of the experimental data presented in this thesis are obtained from transient-absorption experiments. Transient absorption has proven to be a powerful method to investigate chemical reaction dynamics [62, 63]. Its main purpose is to trace the transient states that a chemical reaction passes through. The main limit of its applicability is given by the used light source. It is based on the pump–probe principle that is explained in the next subsection. Afterwards a hypothetical transient-absorption experiment with the explanation of the observed signals is given. Due to the femtosecond temporal resolution anisotropy effects induced by the laser pulse might obscure the underlying reaction dynamics. A way to cancel this effect is given in the third subsection. The fourth subsection shows the experimental setup used to perform transient-absorption experiments.

3.1.1 Pump–probe spectroscopy

Most reactions used in chemical synthesis proceed on the electronic ground states of the reactants through thermally reached transition states. The macroscopic speed of a reaction is therefore determined by the probability for a molecule to reach the transition state. Nevertheless each reaction step of a single molecule occurs in most cases on the time scale of molecular vibrations, i.e. < 100 fs [17]. The pump–probe principle on the femtosecond time scale provides access to these dynamics by setting a starting point in time at which suddenly many molecules possess enough energy to react. The molecules in question get the energy from a light pulse (pump pulse, blue beam in Figure 3.1) resulting (in all experiments of this thesis) at first in an electronically excited state. Afterwards the excited population evolves in time [62]. At a certain time after the

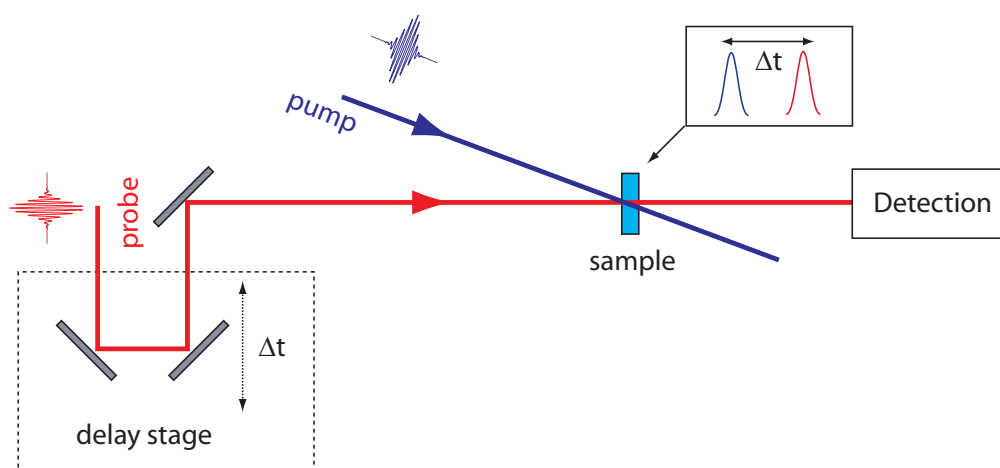


Figure 3.1: In a pump–probe experiment, a pump pulse excites a subensemble of the molecules in the sample. The excited population evolves in time. During this evolution the optic properties of this population changes. This change, most of the times the absorption, is probed by a probe pulse after a tunable time delay Δt . Temporal resolution is determined by the pulse length of the pump and probe pulse.

pump pulse, illustrated as the delay time Δt in Figure 3.1, a second pulse (probe pulse, red beam in Figure 3.1) probes the excited molecules. Scanning of this time delay allows the tracing of the reaction and gives insight into the reaction mechanism. For pump–probe experiments it is necessary that the pump and probe pulses are shorter than the dynamics in question. With conventional techniques pulse lengths down to a few fs [18, 64] are feasible, allowing even tracing of coherent vibrational dynamics [62] or the direct observation of conical intersections [1, 2, 65–67]. Furthermore it is necessary that the induced dynamics lead to changes for the probe pulse interaction that are sufficiently large to be detectable experimentally. For the analysis of the probe pulse interaction with the sample several detection techniques are used. For example in the gas phase pump–probe experiments one can probe the intensity of the transmitted beam [68] or, in case of ionizing probe pulses, the mass spectra [69] or the photo-electron spectra or the laser-induced fluorescence and many more. In this thesis only liquid-phase experiments have been conducted, where detection of the transmitted intensity of the probe is the standard approach to record the transient absorption [63]. An example of such a transient-absorption experiment in the liquid phase including its analysis is given in the next subsection.

3.1.2 Observable signals

In a transient-absorption experiment the decisive property is the intensity change of the probe pulse due to the illumination of the sample with the pump pulse. This is calculated as either the transmittance change $\Delta T(\lambda, \Delta t)$ or the absorption change $\Delta A(\lambda, \Delta t)$ (also

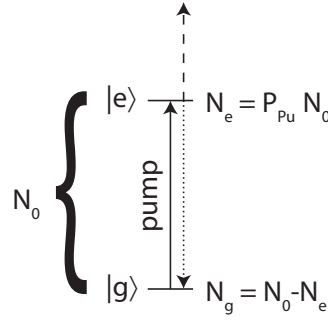


Figure 3.2: Whereas before the pump all molecules (N_0) are in the ground state $|g\rangle$, interaction with the pump pulse excites a subensemble of N_e molecules into the excited state $|e\rangle$. This population of the excited state is in a good approximation linear to the concentration ($N_e = P_{pu}N_0$). The remaining population in the ground state is then given by $N_g = N_0 - N_e$. The excited-state population gives rise to new absorption bands to higher-lying electronic states, as indicated by the dashed line. These transient-absorption bands are labeled excited-state absorption. The excited population can also return to the ground state via stimulated emission (pointed line). This process is stimulated by a photon of the correct wavelength and during this process a second photon coherent to the stimulating photon is emitted.

often labeled as $\Delta\text{Abs}(\lambda, \Delta t)$ or $\Delta\text{OD}(\lambda, \Delta t)$) by the intensity $I_0(\lambda)$ of the probe pulse without pump and the intensity $I(\lambda, \Delta t)$ of the probe pulse with pump via

$$\Delta A(\lambda, \Delta t) = -\log_{10} \frac{I(\lambda, \Delta t)}{I_0(\lambda)} \quad (3.1)$$

$$\Delta T(\lambda, \Delta t) = \frac{I - I_0}{I_0}, \quad (3.2)$$

with $\Delta t = t - t_0$ denoting the time between pump (t_0) and probe pulse (t).

The transmission change and the absorption change lead to the opposite sign, e.g. a positive transmission change corresponds to a negative absorption change. In this thesis only absorption changes ΔA are given.

Assume a sample consisting of N_0 molecules in the electronic ground state “ $|g\rangle$ ” (Figure 3.2), then interaction with the pump pulse leads to $N_e = P_{pu}N_0$ molecules in the excited state “ $|e\rangle$ ”, with P_{pu} being a function of the pump intensity, the beam diameter, the sample thickness (optical path length), the concentration and the extinction coefficient of the molecule at the pump wavelength (see Appendix A). The number of molecules in the ground state is therefore directly after excitation $N_g = N_0 - N_e$. Since the absorption A according to the Beer–Lambert law is proportional to the concentration c ,

$$A = \epsilon l c, \quad (3.3)$$

with ϵ being the extinction coefficient and l being the optical path length, the absorption of the molecules in the ground state after excitation is decreased by a factor of $\frac{N_g}{N_0}$. This negative absorption change is called “ground-state bleach”. Population of the excited state with N_e molecules gives in the most cases rise to new absorption bands to higher-lying excited states, indicated by the dashed arrow starting from $|e\rangle$ in Figure 3.2. The

spectral shape of this excited-state absorption is different from the ground-state absorption and can therefore be observed as additional absorption, i.e. a positive absorption change, in the transient-absorption signal. Note, that the excited state can also be an intermediate product, i.e. a ground state of a transient species. Stimulated emission from the excited state $|e\rangle$ towards a lower electronic state (in most cases the ground state, as indicated by the pointed arrow starting from $|e\rangle$ in Figure 3.2) leads to an increased number of photons and therefore a greater intensity I at the corresponding wavelength. Hence this process appears as a negative absorption change.

3.1.3 Time evolution of the signals

After the initial population of the excited state, the population decays back to the energetic minimum that is accessible after excitation. In most cases this corresponds to a return to the electronic ground state.

Monoexponential decay

No product formation In the simplest case the decay from the excited to the ground state can be described by a monoexponential decay, hence one characteristic time constant τ and one amplitude a with the unit “OD”,

$$\Delta A(\Delta t) = ae^{-\frac{\Delta t}{\tau}}. \quad (3.4)$$

Time-dependent quantum mechanical perturbation theory states that the time constant is related to the energy difference and the transition dipole moment between these two electronic states [17].

After decay of the excited-state population all molecules are again in the ground state (excluding the possibility of other pathways from the excited state, which may be product formation such as a dissociation reaction). A probe pulse interacting at this time with the sample therefore experiences the same absorption as a probe pulse interacting with the sample without the pump pulse, $I_0(\lambda) = I(\lambda, \Delta t \rightarrow \infty)$, hence $\Delta A(\lambda, \infty) = 0$. The time-resolved absorption change $\Delta A(\lambda, \Delta t)$ starts with the absorption after the initial excitation ($\Delta t = 0$) and decays to the original absorption ($\Delta A = 0$) monoexponentially. This applies to all absorption signals starting from the excited and the ground state. In the case of the ground state the decay of the excited state reverts the initial bleach, the process is therefore called “ground-state bleach recovery”.

Product formation If a pathway from the excited state to a product “ $|p\rangle$ ” different from the ground state $|g\rangle$ exists, e.g. isomerization reactions, the ground-state bleach recovery with amplitude a_{gsr} does not reach zero absorption change as shown in Figure 3.3 and Tab. 3.1. Instead the molecules that have formed the product are missing in the ground state after decay of all dynamics, leading to a remaining negative absorption change a_f , since a few molecules have been permanently bleached. The quantum efficiency Φ of the product formation pathway is defined as the percentage of the excited population following that pathway:

$$\Phi = \frac{a_f}{a_f + a_{gsr}}, \quad (3.5)$$

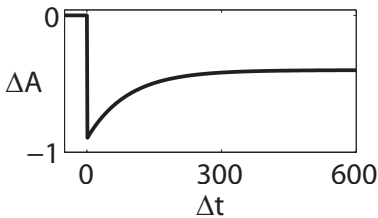
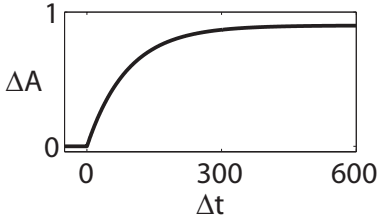
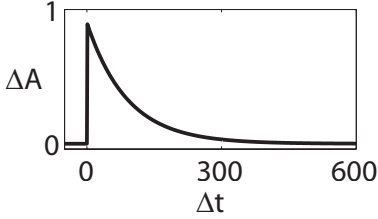
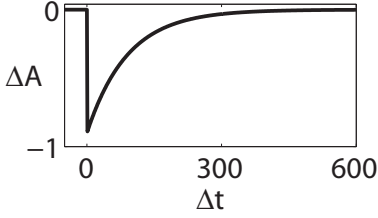
process	typical course	$\Delta A = ae^{-\frac{\Delta t}{\tau}} + a_f$	
		a	a_f
GSR: ground-state bleach with partial recovery		< 0	< 0
product formation		< 0	> 0
ESA: excited-state absorption or intermediate-product absorption		> 0	0
SE: stimulated emission		< 0	0

Table 3.1: In a transient-absorption experiments in which the dynamics follow monoexponential behavior, the most prominent signals are the four signals depicted above. The explanation of the signals is explained in detail in the text. Each process can be described by an amplitude, an offset and a time constant. As can be seen in the two last columns the processes can be identified in the experiment by the amplitude and the remaining offset. The time constant of these processes is the same only when the process starts from the same state, i.e. excited-state absorption and the corresponding stimulated emission have the same time constant.

with $a_f + a_{gsr}$ being the total excited population. Although theoretically easily describable through this equation, the measurement in the experiment is often disturbed by parallel processes, as will be shown in Section 4.3.3.

The product formation can often also be observed directly at an absorption band of the product. In this case the transient absorption starts after excitation at $\Delta A = 0$ and increases monoexponentially with the product formation time. However, it has to be noted, that the product species possesses different extinction coefficients from the reactant. Therefore all amplitudes can be converted into concentrations only with the

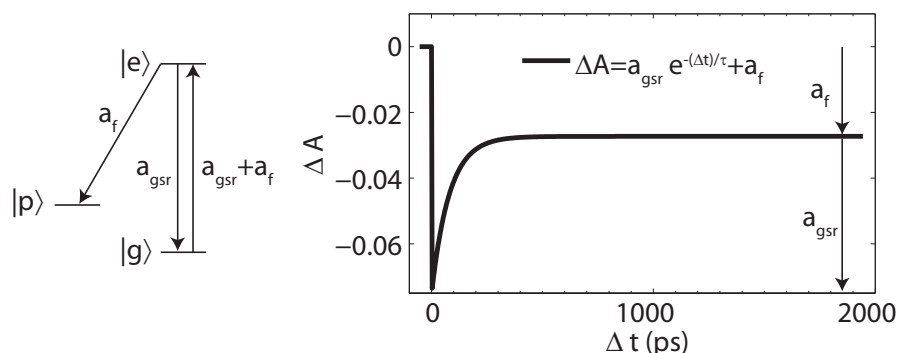


Figure 3.3: A possible fate for a portion of the excited reactant molecules, i.e. starting from $|g\rangle$ and being excited into $|e\rangle$, is product $|p\rangle$ formation. Quantitatively the amplitude of the ground-state bleach recovery is then given by the initial bleach minus the population reacting to the product. In terms of the measured amplitudes of the monoexponential processes of Tab. 3.1 the amplitude of the ground-state bleach recovery is then a_{gsr} , whereas the offset is a_f . The initial bleach is then $a_{gsr} + a_f$. Product formation would then be measured with the amplitude a_f , however, this species has different extinction coefficients, impeding such a direct analysis via the amplitudes.

extinction coefficients of both species known.

Higher order decay

If the decay of the dynamics cannot be described satisfactorily with a monoexponential decay, the decay may be a higher-order exponential decay. This means that multiple pathways with different time constants exist or that two completely independent processes that overlap spectrally are observed. Whereas for the latter case Eq. 3.4 is developed as the sum of i exponential decays,

$$\Delta A = \sum \left(a_i e^{-\frac{\Delta t}{\tau_i}} \right) + a_f, \quad (3.6)$$

in the former case a complex kinetic model has to be developed and its parameters fitted to the experimental data to extract the relevant parameters [70]. The processes observed in this thesis are all assumed to be monoexponential.

Wavelength dependence

Up to now only the time dependence of the transient absorption has been shown in Figure 3.3 and Table 3.1. However, the wavelength dependence is an important feature of the transient absorption, too. In Figure 3.4 an exemplary transient-absorption map is shown. Whereas a vertical cut, $\Delta A(\lambda_c = \text{const.}, \Delta t)$, is a “transient” at probe wavelength λ_c (also shown on the right side of Figure 3.3), a horizontal cut, $\Delta A(\lambda, \Delta t_c = \text{const.})$, is called a difference spectrum at the time Δt_c . Assuming that the dynamics can be described with Eq. 3.6, each decay amplitude a_i as well as the remaining offset a_f has its

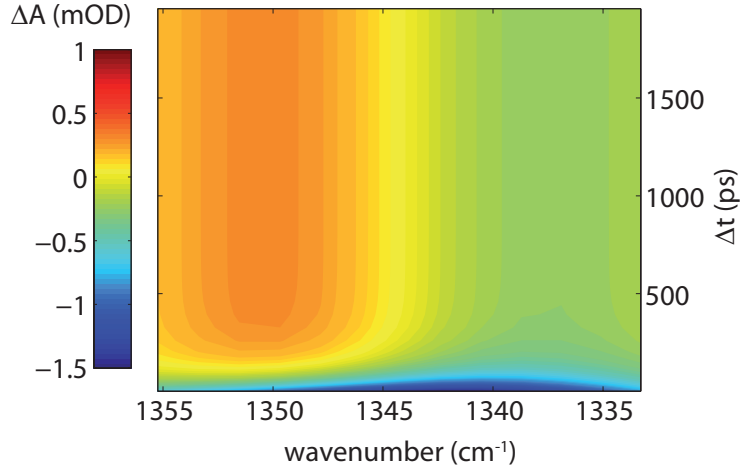


Figure 3.4: Idealized transient-absorption map. The color indicates the absorption change ΔA , with blue corresponding to a negative change and red corresponding to a positive change. Ground-state bleach and its partial recovery is observed around 1340 cm^{-1} , whereas product formation is observed around 1350 cm^{-1} .

own wavelength dependence,

$$\Delta A(\lambda, \Delta t) = \sum_i \left(a_i(\lambda) e^{-\frac{\Delta t}{\tau_i}} \right) + a_f(\lambda). \quad (3.7)$$

This wavelength dependence is called a “decay-associated spectrum”. This decay-associated spectrum allows the intuitive disentanglement of spectrally overlapping processes, if Eq. 3.7 is valid, which is often the case.

3.1.4 Anisotropy with linearly polarized pulses

In a pump–probe transient-absorption experiment two transitions within the molecule take place, the pump process and the probe process. The probe process can be any of the processes shown in Tab. 3.1. In the following this process is assumed to take place from state $|2\rangle$ to $|3\rangle$ ($|1\rangle$ would correspond to the ground state). Pump and probe process are characterized by two independent transition dipole moments, that enclose an angle α , which gives rise to an anisotropic distribution of the excited population. Note that even the use of unpolarized light induces anisotropy in an isotropic sample because it is a transverse wave. The effect of the probe and pump polarization and the angle between the pump and probe transition on the measured signal is derived in detail in the Appendix in Section B.1.

The pump–probe signal ΔA is a product of the maximum pump–probe signal ΔA_{max} derived in Appendix A and the probability P_{Pr} for successful probing. The probability $P_{Pr}(\alpha, \chi_{Pu}, \delta_{Pu}, \chi_{Pr}, \delta_{Pr}, \beta)$ is thereby determined by the Jones vector of pump $\begin{pmatrix} \cos \chi_{Pu} \\ \sin \chi_{Pu} e^{i\delta_{Pu}} \end{pmatrix}$ and probe $\begin{pmatrix} \cos \chi_{Pr} \\ \sin \chi_{Pr} e^{i\delta_{Pr}} \end{pmatrix}$, the angle α between the transition dipole moments of pump and probe transition and the angle β between the wave vectors of

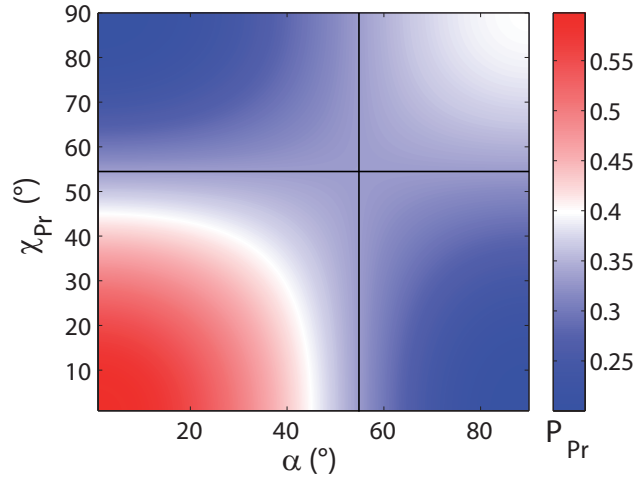


Figure 3.5: Probability $P_{Pr}(\alpha, 0, 0, \chi_{Pr}, 0, 0)$ for successful probing after excitation with s polarized light dependent on the angle α between pump and probe transition dipole moment and dependent on the angle χ_{Pr} between the linear polarizations of the pump and probe pulse. When pump and probe transition dipole are parallel ($\alpha = 0^\circ$), the probability for interaction is maximum ($P_{Pr} = 0.6$) if pump and probe are polarized in the same direction ($\chi_{Pr} = \chi_{Pu} = 0^\circ$). At $\alpha \approx 54.7^\circ$ the pump–probe signal is independent off χ_{Pr} . The opposite case $\chi_{Pr} \approx 54.7^\circ$ is called magic-angle configuration. Under this angle the pump–probe signal is independent of α .

pump and probe (see also Figure 7.8 on page 157). Assuming that the pump and probe pulse propagate collinearly ($\beta = 0$), that the pump is linearly polarized in s direction ($\chi_{Pu} = 0$) and the probe is linearly polarized in direction χ_{Pr} , then $P_{Pr}(\alpha, 0, 0, \chi_{Pr}, 0, 0)$ is given by

$$P_{Pr}(\alpha, 0, 0, \chi_{Pr}, 0, 0) = \frac{1}{20} \left(7 + \cos(2\alpha) + \frac{3}{2} \cos(2(\alpha - \chi_{Pr})) + \cos(2\chi_{Pr}) + \frac{3}{2} \cos(2(\alpha + \chi_{Pr})) \right). \quad (3.8)$$

The resulting P_{Pr} , which is proportional to the measured transient-absorption signal ΔA (Eq. B.24), is shown in Figure 3.5. P_{Pr} changes by a factor of three depending on α and χ_{Pr} . However, at either $\alpha \approx 54.7^\circ$ or $\chi_{Pr} \approx 54.7^\circ$, P_{Pr} is independent of the respective other angle, as indicated by the black lines. This angle is called “magic angle” and its exact value is $\chi_{MA} = \arccos \frac{1}{\sqrt{3}}$. When the linear polarizations of the probe and pump enclose this angle, anisotropy does not contribute to the signal and therefore only population changes are detected. For a more detailed derivation, see the Appendix B.4.1.

The anisotropy r , which can be transferred in its meaning from steady-state fluorescence experiments [71], is defined as

$$r = \frac{I_{\parallel} - I_{\perp}}{I_{\parallel} + 2I_{\perp}}, \quad (3.9)$$

with I_{\perp} and I_{\parallel} being the intensity measured with a perpendicular and parallel analyzer with respect to the polarization of the excitation, respectively. In case of transient-absorption experiments these quantities are replaced by the transient-absorption signals ΔA_{\perp} and ΔA_{\parallel} with orthogonal (\perp) and parallel (\parallel) polarization of pump and probe, i.e. $\chi_{Pr} = 90^{\circ}$ and $\chi_{Pr} = 0^{\circ}$ (if the pump is linearly polarized in $\chi_{Pu} = 0^{\circ}$ direction), respectively. For 1-photon processes the maximum value of the anisotropy is $r = 0.4$ for $\alpha = 0^{\circ}$ and $r = -0.28$ for $\alpha = 90^{\circ}$. The inversion of Eq. 3.9 gives the dependence of the anisotropy on α [71],

$$r(\alpha) = \frac{1}{10}(1 + 3 \cos(2\alpha)) = \frac{2}{5} \frac{3 \cos^2 \alpha - 1}{2}. \quad (3.10)$$

Measuring the transient-absorption signal with parallel polarization and orthogonal polarization of the probe therefore affords the computation of the angle α between the exciting and probing transition dipole moment with

$$\alpha = \arccos \frac{\sqrt{1 + 5r}}{\sqrt{3}}. \quad (3.11)$$

If not stated otherwise the transient-absorption experiments were performed in magic-angle configuration, thus only population changes contribute to the detected signal.

3.1.5 Experimental realization

In the course of this thesis the setup in Figure 3.6 to perform transient-absorption experiments was conceived and realized. It allows on the one hand the simultaneous use of two pump pulses with different color, a requirement for the experiments in Chapter 4, and on the other hand broadband probing as well as single-wavelength probing.

The green path represents femtosecond laser pulses obtained in a non-collinear optical parametric amplification process [72], “VIS light”, see also Section 3.2.3. The violet path, “UV light” may be either femtosecond pulses with the wavelength of the fundamental (800 nm), the second-harmonic of the fundamental (400 nm) or the third-harmonic of the fundamental (266 nm). The white-light (multicolor or black path), used for probing, is generated by focussing a small portion of the fundamental 800 nm femtosecond laser pulses in a linearly moving CaF_2 plate. The time delays Δt_{VIS} and Δt_{UV} between the three pulses are adjusted by two linear stages.

The focussing elements (focal length f) of the individual paths are chosen such that the UV light and the VIS light have almost equal beam sizes ($f = 20$ cm) in the sample (small red box), while the probe light is much smaller in the sample ($f = 12.5$ cm). Achromatic optics are used for the VIS light and the white light, whereas for the UV light BK7 glass lenses are used for focussing and HR266 mirrors to guide the beam. When not using the third-harmonic (266 nm) these mirrors need to be replaced.

Furthermore in the course of this thesis the broadband shot-to-shot probing via the broadband spectrometer (bottom in Figure 3.6) was implemented, meaning that the spectrum of every probe pulse of the 1 kHz pulse train of femtosecond laser pulses is recorded individually. It is very attractive for many different experiments, since on the one hand the spectrograph (Acton SP2500) allows easy adjustment of the central probe

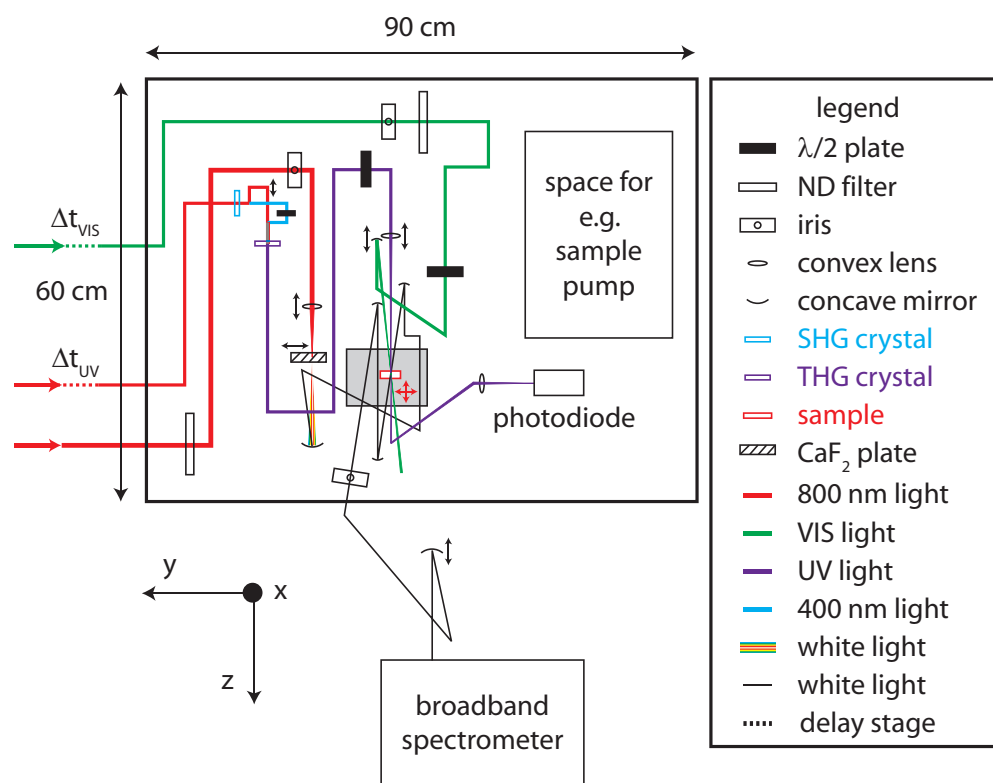


Figure 3.6: Transient-absorption setup allowing for simultaneous use of two pump pulses with different color, broadband probing, and single-wavelength probing. The pump beams (purple line: 266 nm femtosecond laser pulses, “UV light”; green line: femtosecond laser pulses from the visible spectral range, “VIS light”) can be individually delayed by 3.6 ns. Both pump beams are equipped with a $\frac{\lambda}{2}$ plate to rotate the linear polarization, e.g. to achieve magic-angle conditions. The white light (multicolor line and black line) is used for broadband probing. It is generated in a linearly moving (y direction) CaF_2 plate and its polarization is vertical (x direction). Note, that the CaF_2 plate can be rotated around the z axis. The optical elements focussing the pump beams into the sample (red box, also moveable in y and z direction) are placed on a linear stage to achieve optimal spatial overlap with the white-light beam in the sample.

wavelength and on the other hand the resolution can be adjusted to the experimental requirements via three different gratings. Furthermore the large dynamic range of $\approx 65000 : 1$ of the TEC-cooled (-80°C) CCD chip (Princeton Instruments Pixis 2K) allows for very good signal-to-noise ratios. The broadband shot-to-shot probing is therefore used in many projects [73–77] and its detailed working principle has been described elsewhere [73, 74].

The broadband spectrometer has been implemented in such a way that any simultaneous signal may be acquired in a synchronized manner to the broadband probing while not losing the assignment between the individual laser pulse and its corresponding simultaneous signal. This can for example be used to simultaneously use the broadband probing, e.g. in the visible spectral range, and the single-wavelength probing, e.g. in

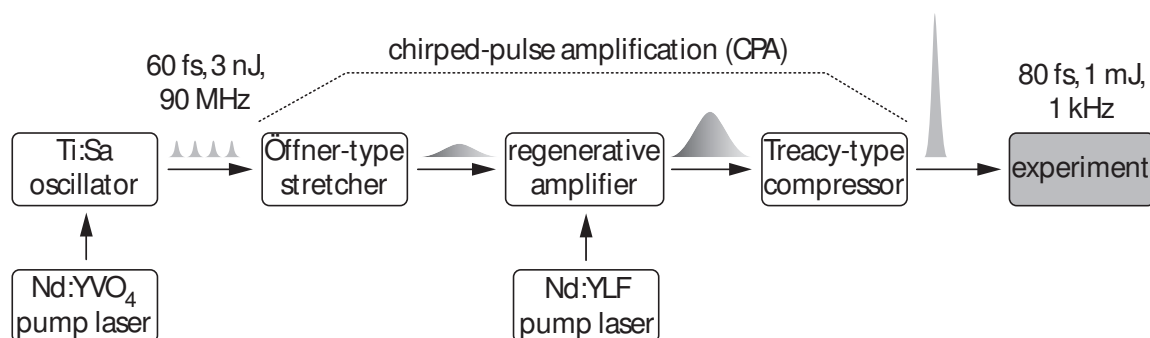


Figure 3.7: Laser system used in this thesis. An oscillator delivers 60 fs pulses with a repetition rate of 90 MHz. Every millisecond one pulse is amplified via chirped-pulse amplification [78]. First the selected pulse is stretched to a pulse length of a few hundred picoseconds. Afterwards this pulse is amplified via stimulated emission in a regenerative amplifier. At last the amplified pulse is compressed back to 80 fs. The obtained pulses have an energy of 1 mJ and a wavelength of 800 nm.

the deep UV, via the photodiode in Figure 3.6.

3.2 Generation of ultrashort laser pulses

Femtosecond laser pulses in the desired wavelength regime are the basis of all the experiments in this thesis. This section describes the experimental setups used to obtain these pulses. The source of the fundamental laser pulses is the laser system, described first. The frequency conversion processes to convert the fundamental pulses into other wavelength regimes that match the experimental requirements are illustrated in the second subsection.

3.2.1 Laser system

The laser system (Figure 3.7) consists of an oscillator, pumped with a continuous-wave Nd:YVO₄ laser (Coherent Verdi V6) operating at 532 nm, delivering 3 nJ pulses centered at 800 nm with a FWHM pulse length of 60 fs. These pulses are amplified via chirped-pulse amplification [20, 78]. The pulses therefore pass a stretcher (“Öffner-type”) in which a large linear chirp is applied with a combination of gratings and concentric mirrors resulting in a pulse length of ≈ 120 ps. These pulses are afterwards used as seed pulses in a regenerative amplifier, that is pumped by a ns-pulsed Nd:YLF laser (Coherent Verdi 15) with a repetition rate of 1 kHz. At last a folded “Treacy-type” compressor removes the linear chirp introduced by the stretcher so that 1 mW pulses at 800 nm with a pulse length of 80 fs at a repetition rate of 1 kHz are obtained. These fundamental pulses are converted afterwards with the experimental methods given in the next subsection to the spectral region required by the experiment.

3.2.2 Nonlinear polarization

The experiments in this thesis necessitate laser pulses in the ultraviolet, visible and mid-infrared spectral range. Conversion of the fundamental laser pulses from 800 nm to these spectral regions is achieved via “nonlinear processes” [19, 79, 80]. Whereas in Eq. 2.1 the response of the medium to the electric field was assumed to be linear, the high intensities of femtosecond laser pulses require the incorporation of nonlinear responses of the polarization to the electric field,

$$\vec{P} = \epsilon_0 \chi \left(\vec{E} \right) = \epsilon_0 \chi^{(1)} \vec{E} + \epsilon_0 \chi^{(2)} \vec{E}^2 + \epsilon_0 \chi^{(3)} \vec{E}^3 + \dots + \epsilon_0 \chi^{(j)} \vec{E}^j \quad (3.12)$$

$$= P^{(1)} + P^{(2)} + P^{(3)} + \dots + P^{(j)}, \quad (3.13)$$

with the electric field \vec{E} and the polarization \vec{P} being vectorial quantities and the response function of the medium $\chi^{(j)}$ being a tensor of rank $j + 1$. This tensor relates a product of j input fields (that may be of different or the same frequency) to a component of the polarization of the order j [19]. The frequency-response function is also known as susceptibility tensor [81].

Nonlinear crystals such as BBO (β -barium borate) are especially useful media in which the optical susceptibility tensor $\chi^{(j)}$ has high values also for even values of j . Furthermore the nonlinearity of those crystals is electronic and nonresonant, hence they do not have a memory effect and their response to the electric field is instantaneous on the time scale of the pulse duration [19]. In the time domain this allows for the direct correlation of the polarization at the time t to the electric field at time t in Eq. 3.13.

The second-order polarization $P^{(2)}$ then has the form of

$$P^{(2)}(t) = \epsilon_0 \chi^{(2)} \frac{1}{4} [\tilde{\epsilon}_1 e^{i(\omega_1 t - k_1 z)} + \tilde{\epsilon}_2 e^{i(\omega_2 t - k_2 z)} + c.c.]^2. \quad (3.14)$$

In this equation a new oscillation at frequency $\omega_1 + \omega_2$ is generated because of

$$e^{i(\omega_1 t - k_1 z)} e^{i(\omega_2 t - k_2 z)} = e^{-i[(k_1 + k_2)z - (\omega_1 + \omega_2)t]}. \quad (3.15)$$

This can be extended to terms of even higher polarization $P^{(j)}$ with $j > 2$ giving rise to many new oscillation frequencies. However the fundamental waves of these new frequencies that are generated at every position in the medium must interfere constructively at all positions so that an electromagnetic wave at that frequency leaves the medium (“phase matching”). This is adjusted by rotating the optical axis of the nonlinear crystal to the input polarization of the fields so that generated field and generating field have the same index of refraction in the medium.

3.2.3 Frequency conversion

The nonlinear polarization therefore allows for frequency conversion processes. The most prominent frequency conversion processes are shown in Figure 3.8.

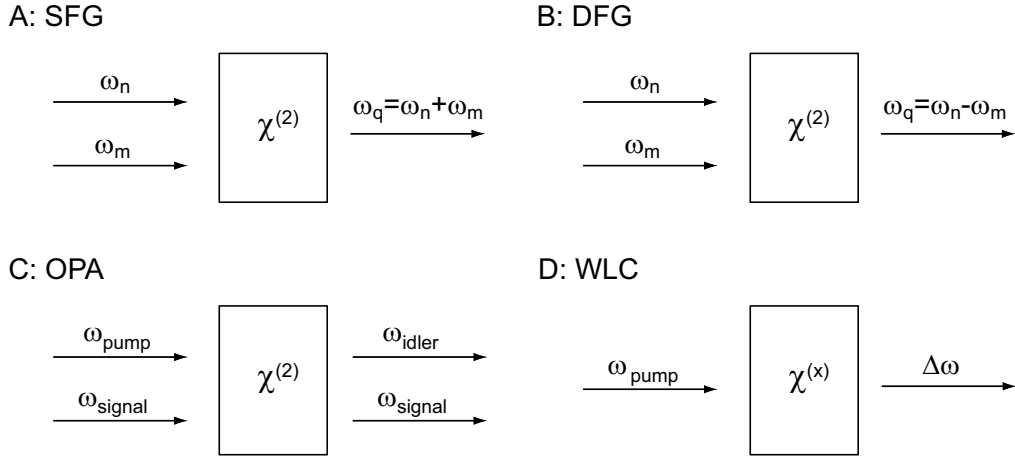


Figure 3.8: Prominent frequency conversion processes based on nonlinear optical processes. A: In sum-frequency generation (SFG) the frequency of the generated electromagnetic wave (ω_q) is the sum of the two incident fields (ω_n and ω_m). B: In difference-frequency generation the SFG process is inverted. The generated wave has the difference frequency of the two incident fields. C: In optical parametric amplification (OPA) a pump photon spontaneously collapses into a signal photon coherent to the incident field with frequency ω_{signal} and an idler photon. The pump photon needs to have a higher frequency than the signal photon. D: focussing a femtosecond laser pulse very hard leads to many nonlinear optical processes. These processes lead to a white-light continuum (WLC) that is spectrally very broad.

Sum-frequency generation

In “sum-frequency generation” (SFG, top left) two input fields with frequency ω_n and ω_m generate a new oscillation at $\omega_q = \omega_n + \omega_m$. However, not only the conservation of energy needs to be obeyed in this process but also the conservation of momentum that dictates the direction in which the generated field ω_q propagates,

$$\vec{k}_q = \vec{k}_n + \vec{k}_m, \quad (3.16)$$

with \vec{k} being the wave vector of the corresponding field.

Difference-frequency generation

The “difference-frequency generation” (DFG, top right) process is the inverse of the sum-frequency generation. Two input fields ω_n and ω_m generate a field ω_q oscillating with the difference frequency $\omega_q = \omega_n - \omega_m$. Similar to the sum-frequency generation the conservation of momentum needs to be obeyed.

Optical parametric amplification

In the optical parametric amplification process one photon of the field with frequency ω_{pump} interacts with one photon of the frequency ω_{signal} in such a manner that the pump

photon is split into a photon with frequency ω_{signal} and a second photon with frequency ω_{idler} ,

$$\omega_{\text{pump}} = \omega_{\text{signal}} + \omega_{\text{idler}}. \quad (3.17)$$

This optical parametric amplification process allows the generation of very short pulses in the visible spectral range [72] and in the mid-infrared spectral range [82].

White-light continuum

Focussing a beam with frequency ω_{pump} to a very small beam waist into a transparent medium (see also Figure 2.3) gives rise to many nonlinear processes. These processes lead to a very broad spectrum $\Delta\omega$ with low intensity. The spectrum is so broad that it appears as white light on a sheet of paper, therefore called white-light continuum. It combines spatial temporal effects and up to now has not been understood completely. Nevertheless, it is a tool for broadband detection in ultrafast spectroscopy [83, 84] and is extensively used in this thesis.

3.3 Accumulative spectroscopy

The purpose of transient absorption is always time-resolved spectroscopy. However, the aim of any photochemistry is to be able to do photochemical reactions to synthesize a product. This discrepancy can be solved by accumulating the photoproducts of the femtosecond laser pulses [72], as will be shown in the next subsection. In special applications this approach even exceeds transient absorption in its spectroscopic possibilities with a greater signal-to-noise ratio and a better detectability of photochemical pathways with very low quantum efficiency [85]. The requirements on the experiment to be attractive for accumulative spectroscopy are given in the second subsection. An experimental realization of an accumulative setup is presented thereafter [86]. To disentangle quantitative results in an accumulative experiment from diffusion effects, calibration procedures need to be performed for an accumulative setup, which will be shown in the last subsection [86].

3.3.1 Accumulation principle

In transient-absorption experiments the sample volume is exchanged between N sequential measurements at the same time delay (each consisting of one interaction with a combination of laser pulses) leading to statistically independent measurements. Acquisition time of an experiment is then given by the repetition rate of the laser, e.g. 1 kHz, and N . All results are averaged (usually N is on the range of hundred to a few thousands) to increase the signal-to-noise ratio. Therefore the standard deviation of the measured absorption change $\sigma_{\Delta A}$ scales with the inverse of the square root of N ,

$$\sigma_{\Delta A} = \frac{\sigma_{\Delta A0}}{\sqrt{N}}, \quad (3.18)$$

with $\sigma_{\Delta A0}$ being the error of a single experiment.

In an accumulative experiment the sample volume is not exchanged [85, 86]. Instead, N copies of a pulse combination interact with the same sample volume and the formed photoproducts are accumulated. Assuming that no saturation effects take place, the absorption change after the accumulation ΔAe scales linearly with the number of laser pulses N interacting with the sample,

$$\Delta Ae = N\Delta A, \quad (3.19)$$

with ΔA being the absorption change after one interaction. The error in the measured absorption change is then given by

$$\sigma_{Ae} = \frac{\sigma_{A0}}{N}, \quad (3.20)$$

i.e. it can be much smaller than in regular transient-absorption experiments, thus facilitating the detection of photochemical channels with low quantum yield.

3.3.2 Pros and cons

Besides the higher signal-to-noise ratio of the accumulative scheme versus the transient-absorption scheme, the concept possesses a few limitations that constrain the applicability of this concept, since a stable photoproduct (lifetime longer than the total acquisition time) has to be generated in the course of the photoreaction. In the optimal case the quantum efficiency of this photoproduct is small, and the main portion of the excited reactants fall back to their electronic ground state, which is fulfilled for multiphoton processes for example. In this case the linear scaling of the absorption change with N is most valid and saturation effects, i.e. the consumption of reactants can be neglected. If combined with a reaction of high quantum efficiency saturation effects might be relevant already after a few pulses. Considering a bleach of the reactant of $\Delta A = -0.01$ OD with an initial absorption of $A = 0.3$ OD already the second pulse achieves only $\Delta A = -0.0096$ OD and decreases even further (monoexponentially) in absolute value. Equation 3.20 therefore can only be applied to the first pulses.

As the relevant quantity in accumulative spectroscopy is the change after N interactions, only the sum of the dynamics during this time is probed. On the one hand this allows the use of continuous-wave (CW) light sources for probing, but on the other hand limits the temporal resolution to effects within the pump pulse shape. With the temporal resolution of the probe being on the order of milliseconds to seconds anisotropy effects due to polarized excitation sources can be neglected, because rotational diffusion takes place on a much shorter time scale. This facilitates analysis of experiments with altering pump polarization.

Whereas rotational diffusion is much faster than the temporal resolution translational diffusion needs to be considered carefully. In femtosecond transient-absorption experiments the sample volume exchange is mostly achieved with some sort of pump combined with a flow cell containing the sample. With the flow rate of the sample through the flow cell one can assume to a very good approximation that during the time span of a few nanoseconds the pumped sample volume does not move. Furthermore, the time scale of

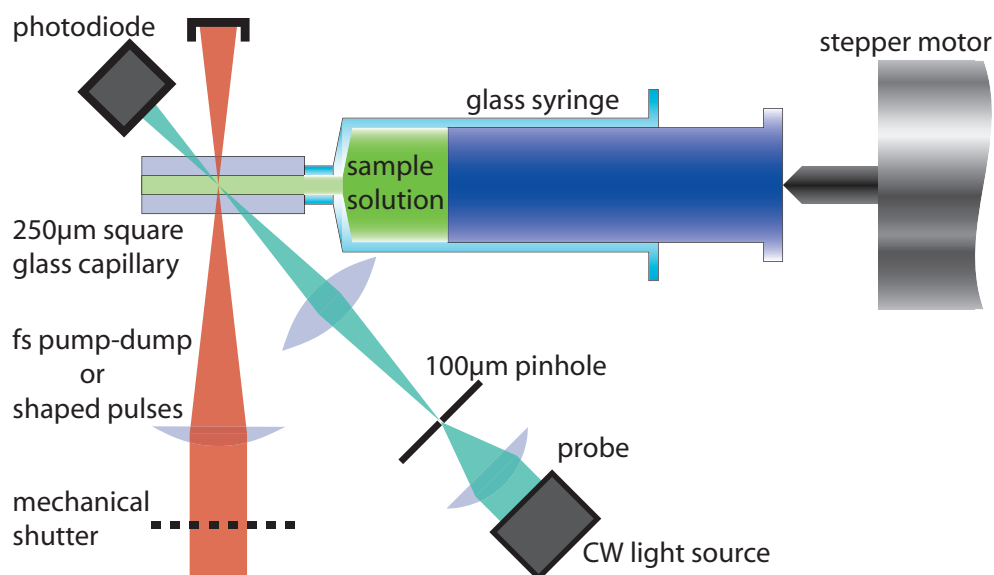


Figure 3.9: Experimental realization of an accumulative setup, taken from [72]. Pump and probe beam are spatially overlapped in the probe volume in the sample, a glass capillary. For every new experiment the previous probe volume is exchanged by a new volume from the glass syringe sample solution by using the stepper motor to press on the flask.

translational diffusion processes of at least milliseconds is much longer than the maximum time delay of the probe. However, in case of accumulative spectroscopy diffusion into unilluminated sample takes place on the probing time scale, leading to a complex decrease of the pump-induced signal with time. This translational diffusion has to be taken into account and each time an accumulative setup has to be calibrated before its use to extract quantitative information about the reactants. A simple way of doing this is given in Section 3.3.4.

Whereas the slow temporal resolution gives rise to diffusion processes it has also the advantage that one can use continuous-wave light sources, since the system is probed on a time scale of several milliseconds to seconds. Hence, one does not need to use pulsed probe light sources that carry pulse-to-pulse intensity fluctuations. Instead continuous-wave light sources can be used which have a very low intensity noise and can furthermore be averaged for long times to achieve a lower standard deviation of the experiment.

Concluding, the accumulative principle has some drawbacks over conventional pump-probe spectroscopy, but all these drawbacks can be turned into an advantage when applied to special situations.

3.3.3 Experimental setup

An experimental setup that was used for accumulative spectroscopy [85] is shown in Figure 3.9.

It consists of the central glass capillary, whose canal is 25 mm long and has side-walls at mutual distances of 250 μm, equipped with a stepper motor, a glass syringe

and a pump (red) and probe beam (green). An experiment begins with the stepper motor movement to exchange the old sample volume from the capillary with a fresh one (the mechanical shutter is closed throughout this step). Afterwards the new volume is illuminated for a period of time (the mechanical shutter is opened) with the pump beam. Any femtosecond temporal resolution achievable by the setup has to be contained in the temporal shape of the electromagnetic wave, e.g. a temporal double pulse. After the illumination (the mechanical shutter is closed again) the sample volume is probed by the continuous-wave light source and the absorption change is detected by the photodiode. During this time diffusion into and out of the sample volume takes place, which is treated quantitatively in the next section.

3.3.4 Calibration

In the calibration procedure the pump-induced signals including the diffusion effects are recorded in a time-dependent manner [86]. Subsequently, the parameters of a simple diffusion model are fitted to the experimental data. Since an analysis by applying the full diffusion equation [87] would be complex, a simplified model based on rate equations is used. For the diffusion model three volumes are defined as shown in the top of Figure 3.10. In each volume the relevant quantity for the experiment is the concentration of the reactant:

- Pump volume: The sample volume that is irradiated by the pump beam, i.e. the femtosecond laser pulses. The concentration of the reactant in this volume is $c_{pu}(t)$.
- Probe volume: The sample volume that is probed with the probe beam. The concentration of the reactant in this volume is $c_{pr}(t)$. The probe volume is contained within the pump volume.
- Outer volume: The sample volume that is not irradiated with either the probe or pump beam. The concentration of the reactant in this volume is c_0 . This volume is assumed to be infinitely large so that the concentration of this volume does not change with the illumination of the pump volume.

Before illumination

Before the sample is illuminated the pump and probe volumes have been exchanged with a new sample, therefore the concentrations follow

$$c_{pu}(0) = c_{pr}(0) = c_0. \quad (3.21)$$

During illumination

The exposure of the pump volume to the femtosecond laser starts at $t = 0$ and lasts for an exposure time τ . During this time the concentrations in the pump and probe volume are the same, hence

$$c_{pr}(0 < t \leq \tau) = c_{pu}(0 < t \leq \tau). \quad (3.22)$$

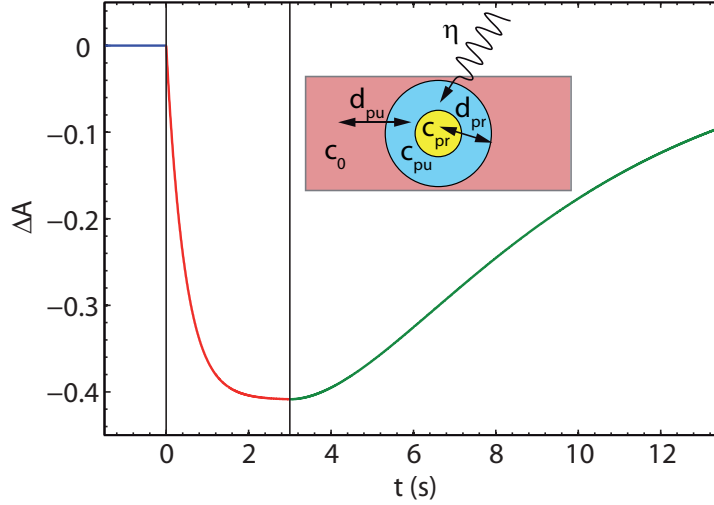


Figure 3.10: Exemplary course of the experimental data to illustrate the assumed model for the calibration procedure. The inset shows the definitions of the pump and probe volume used in the model. The probe volume is irradiated by the probe light, whereas the pump volume is irradiated with the pump light. The surrounding is assumed to be infinitely large. During irradiation a reactant concentration gradient is created, which leads to diffusion processes. These processes are quantitatively described by rate equations, leading to the fit model in Eq. 3.26. In the experimental data three steps occur. First (blue) before irradiation the reactant concentration does not change, hence $\Delta A = 0$. During irradiation (red) the reactant is bleached leading to a negative absorption change. After irradiation (green) the diffusion leads to a partial recovery of the bleach.

Due to the exposure with femtosecond laser pulses the concentration of the reactant decreases in the pump and probe volume. The extent of this decrease is dependent on the concentration of the reactant itself, $-\eta c_{pu}(t)$, with η being the converted reactant molecules per unit time. Assuming simple exchange rates along the concentration gradient between the outer volume and the pump volume, the concentration of reactant inside the pump volume increases linearly with $d_{pu}(c_0 - c_{pu}(t))$ yielding a total differential equation

$$\frac{dc_{pu}}{dt} = d_{pu}(c_0 - c_{pu}(t)) - \eta c_{pu}(t). \quad (3.23)$$

After illumination

After illumination only diffusion of the outer volume into the pump volume,

$$\frac{dc_{pu}}{dt} = d_{pu}(c_0 - c_{pu}(t)), \quad (3.24)$$

and diffusion of the pump volume into the probe volume,

$$\frac{dc_{pr}}{dt} = d_{pu}(c_{pu}(t) - c_{pr}(t)), \quad (3.25)$$

persists.

The solution of these coupled differential equations is [86, 88]

$$c_{\text{pr}}(t, \tau) = c_0 \times \begin{cases} 1 & t < 0 \\ \frac{d_{\text{pu}} + \eta \exp[-(d_{\text{pu}} + \eta)t]}{d_{\text{pu}} \exp[d_{\text{pr}}(\tau - t) - (d_{\text{pu}} + \eta)\tau] \{-1 + \exp[(d_{\text{pu}} + \eta)\tau]\} \eta - d_{\text{pu}}(d_{\text{pu}} + \eta)} & 0 \leq t \leq \tau \\ + \frac{d_{\text{pr}}(d_{\text{pu}} + \{1 - \exp[d_{\text{pu}}(\tau - t)] + \exp(-d_{\text{pu}}t - \eta\tau)\} \eta)}{(d_{\text{pr}} - d_{\text{pu}})(d_{\text{pu}} + \eta)} & t > \tau \end{cases} . \quad (3.26)$$

For a set of typical parameters the concentration change (as absorption change) observed during an accumulative experiment is given in Figure 3.10. Before illumination the concentration, i.e. the absorption, does not change. During illumination the reactant concentration decreases until the exchange with the surrounding outer volume compensates the illumination as shown by the saturation level for $t > 2$ s. Illumination stops at $t = 3$ s and the diffusion of reactant from the outer volume through the pump volume into the probe volume leads to an increase of reactant concentration.

This model can be transferred directly to the measurement of optical rotation [88] in Section 6 instead of absorption/concentration measurement, since the optical rotation is also directly proportional to the concentration (see Eq. 2.73).

4 An electrocyclic reaction: The spiropyran–merocyanine system

4.1 Introduction

Photochromic systems are defined by a controllable light-induced change of color. They have a vast variety of applications, from sun glasses to data storage [14, 89, 90]. Among the molecular switches, those with a reversible ring closure have drawn much attention due to well-separated absorption bands of the open and closed form and large configuration changes in the switching process. The electronic changes caused by the switching process make such reactions potential candidates for optical memories [91], whereas the structural changes could be used as a switch of molecular or even biological properties, enhancing or stopping processes [92–94].

Since the usability of photochromic molecular switches depends on the switching time scales and the respective quantum yields for both directions, for an optimization of molecular switches it is essential to understand the participating photoreactions on a molecular level. Therefore ultrafast studies have been performed, e.g. on dithienylethene derivatives [95, 96], fulgides and fulgimides [97, 98], and spiropyrans [99–105]. Tab. 4.1 shows a comparison of the quantum yields for these molecules. The quantum yields of the ring-closure and ring-opening reactions can be chemically tuned. Either ring closure can be achieved with very high quantum yield at the cost of the quantum efficiency of ring opening, or vice versa. Typically though, the achievable molecular quantum yield is higher for ring closure than for ring opening (Tab. 4.1). Also, in some cases the reaction rates are slow due to triplet-state pathways. However, for switching applications good quantum yields and high speed are desired for switching in both directions. For spiropyrans only photochemical ring opening has been directly demonstrated so far [99, 100, 104, 105]. In this chapter, it is shown that a suitable spiropyran–merocyanine system can be switched photochemically in both directions with competitive quantum yields on an ultrafast time scale (Tab. 4.1).

The photochemical and thermal ring opening of several spiropyrans has been investigated on the second to femtosecond time scale. It has been shown that for unsubstituted spiropyran (1',3',3'-trimethylspiro[2H-1-benzopyran-2,2'-indoline] = BIPS) the photoinduced reaction is fast (28 ps) but inefficient [99, 100, 109]. The efficiency is strongly enhanced if a nitro group is substituted in 6 position of the pyran moiety (6-nitro BIPS). However for such a substituted compound the reaction time scale increases to nanoseconds due to a triplet pathway [104, 110–112]. Furthermore, although sketched in most spiropyran reaction schemes in the literature, there is no direct proof that the completely relaxed ring-open form can be switched back photochemically at all [101]. Only for the

Derivative of	ring closure (trans → cis)	ring opening (cis → trans)
Dithienylethene [106] ^a	50%	<2%
Dithienylethene [106] ^b	86%	0.15%
Indolyl-Fulgimide [107] ^c	28%	14%
Furyl-Fulgide [65]	20%	12%
Azobenzene [108]	25%	50%
6,8-dinitro BIPS ^d	40%	9%

Table 4.1: Comparison of quantum efficiencies of exemplary molecular switches based on a 6π -electrocyclic reaction.

^abis(2,4-dimethyl-5-phenylthiophen-3-yl)perfluorocyclopentene substituted with benzonitrile: 50% not capable of ring closure

^bpolymer of bis(2,4-dimethyl-5-phenylthiophen-3-yl)perfluorocyclopentene: isomer not capable of ring closure suppressed in polymer

^cisomer not capable of ring-closure: <3%

^dresult of this thesis

substituted compound with a second nitro group in 8 position (6,8-dinitro BIPS), it has been shown that irradiation with 400 nm light leads to a bleach of the visible absorption band on the ps time scale. This indirectly indicates formation of the ring-closed form [103].

In this chapter the femtochemistry of the closed form as well as the open form of 6,8-dinitro BIPS is investigated. The aim is to identify the pathways, their quantum efficiency and their reaction speed. However, the results of conventional pump–probe transient-absorption spectroscopy are not sufficient to disentangle the photochemical pathways and determine these quantities. Therefore additional experiments are performed in which the excitation wavelength is varied. This allows amongst others the identification of two ring-open isomers and the determination of the interconversion quantum efficiency. The measurement of the reaction speeds for the two directions of the 6π -electrocyclic reaction (ring closure and ring opening) calls for a multipulse control experiment in which a subensemble is selectively steered between the open and closed form in a bidirectional switching manner. Variation of the time delay between the switching actions affords finally the switching times of 6,8-dinitro BIPS.

The chapter is organized in such a way that first the steady-state properties of the molecular switch are presented. Afterwards the open form of the spiropyran–merocyanine system, the merocyanine, is investigated with transient-absorption spectroscopy. Subsequently transient-absorption experiments on the closed form, the spiropyran, are presented. The knowledge of these three sections serves as basis for Section 4.5 in which ultrafast bidirectional switching between the open and closed form is shown. Afterwards the photochemistry of the molecular switch is summarized and in the last section the insight into the pericyclic mechanism of the reaction is presented.

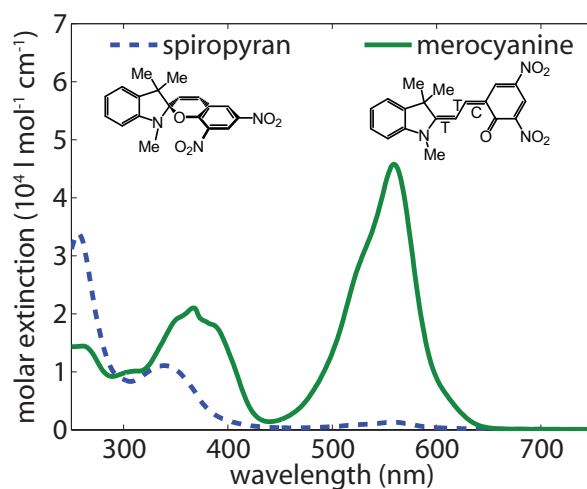


Figure 4.1: Spiropyran and merocyanine main isomers (TTC, describing the configuration around the three central double bonds) of 6,8-dinitro BIPS and their corresponding steady-state absorption spectra in chloroform. The ring-closed spiropyran can be opened with light from the ultraviolet spectral region whereas the merocyanine can be closed with light from either the ultraviolet or the visible spectral region. The spiropyran spectrum was obtained after almost complete merocyanine bleaching (a small portion of the visible absorption band of the merocyanine is still present).

4.2 Steady state

The ring-closed form of the spiropyran form of 6,8-dinitro BIPS (left structure in Figure 4.1) consists of a pyran and an indoline moiety with orthogonal orientation. Thus both moieties are independent [113] and absorb in the ultraviolet only. Ring opening completely changes the molecule's electronic and structural properties. In the ring-open form (merocyanine, right structure in Figure 4.1) the two chromophores are positioned such that one large planar π system emerges (see Figure 2.12), leading to a strong absorption in the visible spectral region [114].

The steady-state fluorescence spectrum (excitation and emission spectrum) is shown in Figure 4.2. One can identify two maxima, one at an excitation wavelength of $\lambda_{Ex,c} = 560$ nm, with maximum emission at $\lambda_{Em,c} = 600$ nm, and one at an excitation wavelength of $\lambda_{Ex,t} = 600$ nm, with maximum emission at $\lambda_{Em,t} = 630$ nm.

4.3 Ring open: merocyanine

In this section the photochemical and photophysical pathways of the open form, the merocyanine (Figure 4.1, top right) will be investigated with femtosecond transient-absorption spectroscopy. First the obtained experimental data will be shown. Afterwards a simple model is presented that describes the femtosecond transient-absorption dynamics. This model gives access to all the relevant photochemical and photophysical parameters.

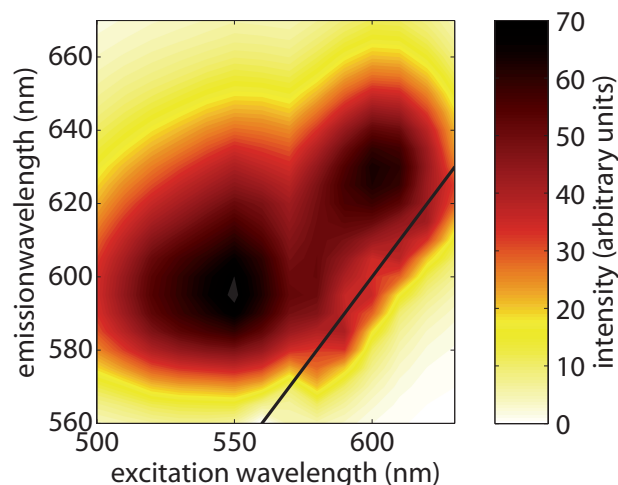


Figure 4.2: Steady-state fluorescence spectra of 6,8-dinitro BIPS in chloroform. Two excitation maxima can be identified, one at $\lambda_{Ex,c} = 560$ nm, with maximum emission at $\lambda_{Em,c} = 600$ nm, and one at an excitation wavelength of $\lambda_{Ex,t} = 600$ nm, with maximum emission at $\lambda_{Em,t} = 630$ nm.

4.3.1 Experimental methods

VIS pump pulses Pump pulses in the visible spectral range were generated in a home-built noncollinear optical parametric amplifier (NOPA), resulting in 2 μ J pulses with about 50 fs FWHM duration tunable across the visible spectral range. The polarization of the pump pulses was rotated to the magic angle by an achromatic wave plate. In the course of the transient-absorption experiments on the merocyanine form the pump pulse wavelength was varied from $\lambda_p = 545$ to 625 nm. The normalized pump spectra (see Figure 4.3) were recorded by an Ocean Optics HR2000+ spectrometer during the experiment.

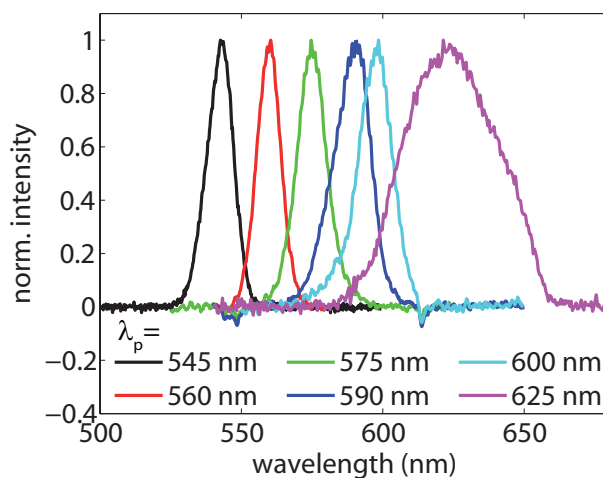


Figure 4.3: Normalized pump spectra used to excite the merocyanine form.

Probe pulses White-light probe pulses ranging from 390 to 720 nm were generated by focussing a small portion of the 800 nm pulses into a linearly moving CaF_2 plate. Mid-infrared probe pulses were obtained as described in Section 5.2.

Sample 6,8-dinitro BIPS was synthesized by our collaborators from the “Institut für Organische Chemie der Universität Würzburg” in the group of Prof. Würthner via the Knoevenagel condensation of commercially available 1,2,3,3-tetramethyl-3H-indolium and 3,5-dinitrosalicylaldehyde resulting in the merocyanine form of 6,8-dinitro BIPS in 79% yield according to the literature [89] and characterized by HPLC, 400 MHz NMR spectroscopy, and high-resolution mass spectrometry. Pump and probe pulses were spatially overlapped in a 200 μm flow cell containing a 0.5 mM solution of 6,8-dinitro BIPS (in the merocyanine form) in chloroform.

Detection The visible probe pulses were coupled into a single-mode fiber, spectrally dispersed in an Acton SP-2500 spectrograph and digitized by a CCD (Princeton Instruments Pixis 2K) with 1 kHz acquisition rate. Every second pump pulse was chopped to reduce noise. Temporal resolution in this setup is better than 50 fs and wavelength resolution is $\Delta\lambda \approx 1.4$ nm.

4.3.2 Experimental data

Transient-absorption data

The transient absorption in the visible spectral range of the merocyanine form of 6,8-dinitro BIPS up to 3.4 ns after interaction with a pump pulse centered at $\lambda_p = 560$ nm (Figure 4.3) is shown in Figure 4.4. Three processes can be identified in roughly three separate spectral regions: excited-state absorption (ESA) for $\lambda < 500$ nm, bleach with partial ground-state recovery (GSR) for $500 \text{ nm} < \lambda < 600$ nm and stimulated emission (SE) for $\lambda > 600$ nm (see Tab. 3.1).

The dynamics during the first 20 ps are disturbed by vibrational cooling effects with a time constant of $\tau_{vc} = 3.6 \pm 0.2$ ps (Figure 4.5). For this process, both vibrational cooling [101, 104] and solvent-molecule interaction due to changed dipole moments [115] in the excited state are suggested in the literature for similar systems [116]. After this contribution has decayed the dynamics in Figure 4.4 can be described by a sum of two exponential decays (Eq. 3.7) with the same fast time constant ($\tau_C = 98 \pm 3$ ps) and slow time constant ($\tau_T = 830 \pm 120$ ps) for all wavelengths. The spectral fitting amplitudes a_{vc} , a_C and a_T are fitted individually for each wavelength resulting in the decay-associated spectra shown in Figure 4.5.

The spectral distribution of the fast component (a_C , blue line) has a local minimum at 560 nm (blue arrow), the maximum of the merocyanine absorption band (Figure 4.1, solid line). The shoulder of the slow component (a_T , red solid line) between 580 and 610 nm (red solid arrow) is in agreement with the very small shoulder of the steady-state spectrum of the merocyanine at 600 nm (Figure 4.1, solid line).

Furthermore, the global minima of the fitting amplitudes a_C (610 nm) and a_T (645 nm) are located very close to the maxima of the steady-state emission spectra (Figure 4.2) at

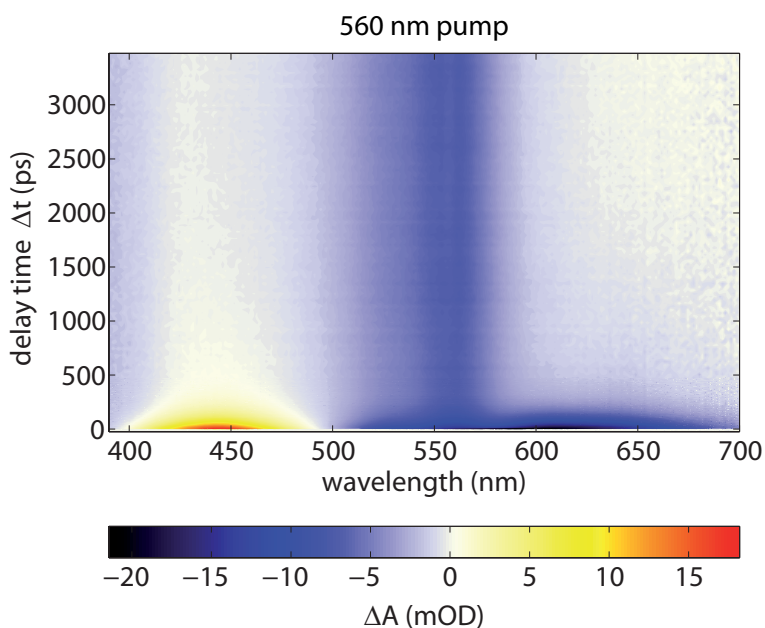


Figure 4.4: Transient absorption in the visible spectral range after exciting 6,8-dinitro BIPS in chloroform with pump pulses centered at 560 nm. In the blue spectral region ESA (around 440 nm) is visible, whereas in the red spectral region SE (around 640 nm) appears. The bleach is centered at 560 nm (see also Figure 4.5).

$\lambda_{Em,c} = 600$ nm for an excitation wavelength $\lambda_{Ex,c} = 560$ nm, and at $\lambda_{Em,t} = 630$ nm for $\lambda_{Ex,t} = 600$ nm, as marked by the dashed vertical arrows to the top in Figure 4.5. Similar to previous findings for spiropyran-derived merocyanines [101] these results indicate that two isomers are present in thermal equilibrium at ambient temperature. This is confirmed by the two ground-state absorptions (560 and 600 nm), the two time constants (98 and 830 ps) and the two emission maxima (600 and 630 nm). Isomer **1** is responsible for the dynamics with 98 ps, has its maximum absorption band at 560 nm and its maximum emission band at 600 nm. Isomer **2** relaxes with 830 ps with a maximum absorption at 600 nm and maximum emission at 630 nm.

According to NMR line shape analysis the main isomer is TTC (isomer **1**, $\lambda_{TTC} = 560$ nm) and the minor isomer is TTT (isomer **2**, $\lambda_{TTT} = 600$ nm) [117]. Since the NMR line shape analysis in Ref. [117] was performed with 6,8-dinitro BIPS in chloroform, the exact same system as investigated here, the assignment of the isomers is unambiguous. However, it is exactly opposite to the assignment of Wohl et al. [101] for the structurally related 6-nitro BIPS, for which also two isomers are present in solution ($\lambda_{TTT-6-nitro} = 568$ nm and $\lambda_{TTC-6-nitro} = 600$ nm). Their assignment was based on the relative energies of the isomers determined by calculations. The difference may arise because in contrast to 6,8-dinitro BIPS, the equilibrium of the isomers for 6-nitro BIPS $\left(\frac{[568\text{nm}]}{[600\text{nm}]} \right)$ lies on the side of the 600 nm centered isomer.

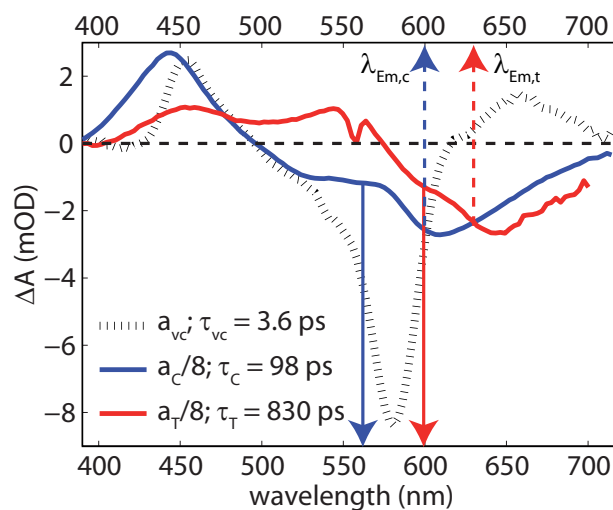


Figure 4.5: Decay-associated spectra a_{vc} (black dotted), a_C (blue solid, divided by 8) and a_T (red solid) obtained after triexponential global fitting of the transient map from Figure 4.4. The steady-state emission maxima ($\lambda_{Em,c} = 600$ and $\lambda_{Em,t} = 630$ nm) are marked by dashed vertical arrows to the top. The steady-state merocyanine absorption maximum (Figure 4.1, solid line) is marked by the blue arrow to the bottom, whereas the shoulder in the merocyanine steady-state absorption (Figure 4.1, solid line) is marked by the red arrow to the bottom. The process with time constant τ_{vc} corresponds to vibrational cooling. The Stokes shift is reflected in the black dotted line by the negative amplitude at 580 nm (a SE contribution decaying with 3.6 ps) and the positive amplitude above 610 nm (an additional 3.6 ps rise of the SE). The same dynamics is also seen in the ESA below 500 nm, where the absorption at 460 nm decreases, whereas at 415 nm a small absorption contribution grows in with τ_{vc} .

Product identification in the MIR

Since the produced spiropyran does not absorb in the visible spectral region (see Figure 4.1) the photobleach from the visible probing experiments for both isomers only indirectly suggest that spiropyran is formed. By contrast, direct evidence for the formation of spiropyran is found by probing the photoreaction in the MIR spectral region. For the structurally related 6-nitro BIPS it is known that ring closure shifts the symmetrical stretching mode of the nitro group to slightly higher frequencies and the absorption band becomes much stronger [118]. The top left panel of Figure 4.6 shows a difference FTIR spectrum after 2 minutes of illumination of the 6,8-dinitro BIPS merocyanine with green continuous-wave (CW) light. The result is a similar shift and intensity change of the absorption as it has been observed in 6-nitro BIPS. Therefore this absorption change and shift is used in the transient absorption of 6,8-dinitro BIPS as direct spectroscopic indication for ring closure.

The transient-absorption map for 6,8-dinitro BIPS shown in the bottom left panel of Figure 4.6 was obtained after pumping with 400 nm light and probing between 1310 and 1360 cm^{-1} . The main features of the map are a merocyanine bleach (from 1327 to 1346 cm^{-1}) and an additional slightly blue-shifted absorption band centered at 1344 cm^{-1} (band from 1336 to 1351 cm^{-1}) that can be attributed to spiropyran formation due to the similarity of the dynamics to the structurally related 6-nitro BIPS and

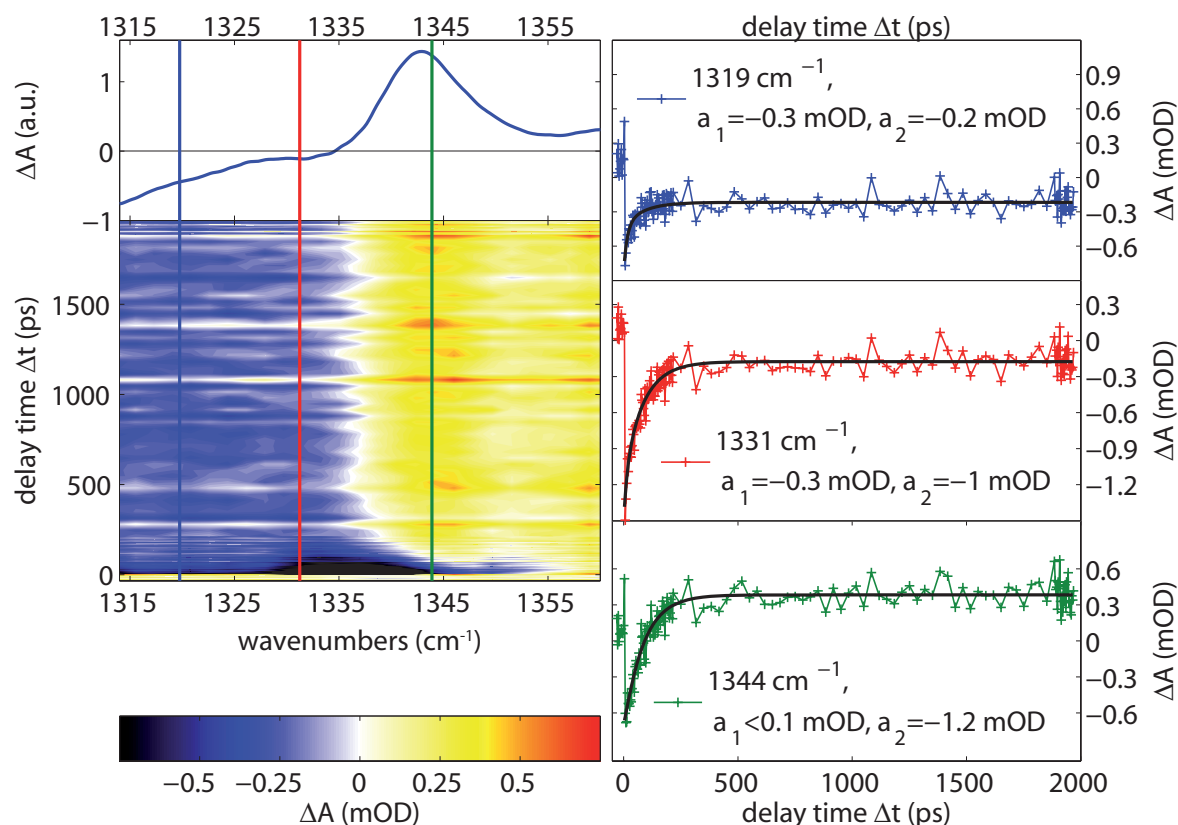


Figure 4.6: Transient-mid-infrared-absorption spectroscopy of 6,8-dinitro BIPS. Top left panel: FTIR difference spectrum after 2 minutes of irradiation of merocyanine with green CW light. Product absorption can be seen above 1335 cm^{-1} whereas reactant bleach can be seen below 1335 cm^{-1} ; bottom left panel: transient-absorption map of the same spectral region ($\Delta\tilde{\nu} = 1.8\text{ cm}^{-1}$) with a pump wavelength of 400 nm showing merocyanine bleach and recovery centered from 1327 to 1346 cm^{-1} and the partially overlapping spiropyran formation at 1344 cm^{-1} (from 1336 to 1351 cm^{-1}); right panel: single transients of the left map (blue, red, green) with the transients obtained via the biexponential global fit routine in black ($\tau_1 = 12 \pm 10\text{ ps}$, $\tau_2 = 86 \pm 5\text{ ps}$). All transients are dominated by the merocyanine ground-state bleach recovery ($\tau = 98\text{ ps}$ in the VIS, see Figure 4.4 and $\tau = 86\text{ ps}$ in the MIR, deviations due to product formation). Spiropyran formation is proven in agreement with the FTIR spectrum by the remaining positive absorption at 1344 cm^{-1} .

in the steady-state difference spectrum. This experiment was also performed with pump pulses centered at 560 nm resulting in the same characteristics.

All dynamics seen in the transient map decay during the first 500 ps. A global fit routine with two exponential decays taking into account only data points for times greater than 2 ps results in time constants of $\tau_1 = 12 \pm 10\text{ ps}$ and $\tau_2 = 86 \pm 5\text{ ps}$. The time constant of 98 ps for the merocyanine ground-state bleach recovery that was measured in the visible spectral range (Figure 4.4) is in close agreement with the time constant of 86 ps obtained from these measurements in the MIR. Therefore the second time constant of 12 ps is attributed to vibrational cooling of either the merocyanine or spiropyran ground state [102].

The spiropyran formation on the other hand can be seen in the individual transients displayed in the 3 panels on the right of Figure 4.6. The obtained global fit transients are shown in black to prove that all transients behave very similar. As mentioned above they all start with a negative absorption change due to missing merocyanine ground-state absorption. The dynamics thereafter are dominated by the corresponding merocyanine ground-state bleach recovery with only small deviations at early times due to vibrational cooling. Nevertheless they differ in the remaining absorption change for delays > 500 ps. The product formation is best seen in this remaining absorption: The absorption change at 1344 cm^{-1} is initially negative owing to the bleach and becomes positive after 100 ps due to the product formation. If there were no absorption of the product at this position, a negative absorption change would remain here too, as seen in the transients at 1319 cm^{-1} and 1331 cm^{-1} . Since absorption due to spiropyran formation is overlaid with the bleach recovery and the characteristic decay changes from 98 ps to 86 ps, this indicates that spiropyran formation is faster than merocyanine ground-state bleach recovery.

Variation of the pump-pulse wavelength

To substantiate the findings that two isomers are present in solution the sample was excited with a stepwise variation of the pump-pulse wavelength between 545 and 625 nm (see Figure 4.3). The transient absorption up to 3.4 ns for 625 nm excitation is shown in Figure 4.7. Again three processes in different spectral regions can be identified, but compared to Figure 4.4 with a red-shift: ESA for $\lambda < 560$ nm, bleach with GSR for $560\text{ nm} < \lambda < 630$ nm and SE for $\lambda > 620$ nm.

A biexponential global fit starting after 20 ps to exclude vibrational cooling results in a spectral distribution very similar to the one shown in Figure 4.5 but with a different relative amplitude of the fast with respect to the slow component.

As is evident from Figures 4.4 and 4.7 the bleach after 3.4 ns depends strongly on the pump wavelength λ_p . The normalized remaining bleach after 3.4 ns at pump wavelengths from 545 to 650 nm is shown in Figure 4.8, illustrating the shift with increasing pump wavelength from mainly exciting isomer **1** (TTC) centered at 560 nm to mainly exciting isomer **2** (TTT) centered at 600 nm. When λ_p is lower than 600 nm the remaining bleach is centered at 560 nm. With $\lambda_p = 575, 590, \text{ or } 600$ nm a shoulder centered at 600 nm appears. The bleach centered at 560 nm disappears at $\lambda_p = 625$ and 650 nm and only the contribution centered around 600 nm remains. The comparison with the steady-state spectrum (also shown in Figure 4.8 as black dashed line, multiplied by -1) reveals that TTC centered at 560 nm is the major isomer in solution, while TTT at 600 nm is the minor isomer.

In the decay-associated spectra of Figure 4.5, only weak minima indicate the GSR (marked by the colored arrows in Figure 4.5) since the SE and the ESA overlap with the GSR. A calculation of the quantum efficiency by simply comparing the remaining bleach (Figure 4.8) with the initial signal after excitation is therefore not possible directly due to these overlapping processes. To extract the quantum efficiency from these experimental data in an alternative approach, the processes observed in Figures 4.4 and 4.7 and in additional spectrotemporal datasets recorded with different pump wavelengths are fully

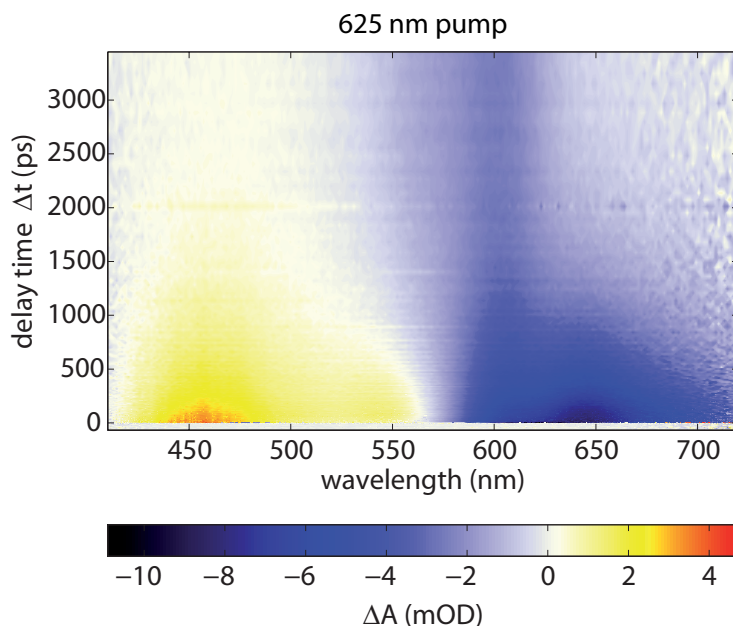


Figure 4.7: Transient absorption in the visible spectral range after exciting 6,8-dinitro BIPS in chloroform with pump pulses centered at 625 nm. Two ESA bands are visible (455 and 540 nm), SE appears at 650 nm and the bleach is centered at 600 nm. Compared to the transients in Figure 4.4, the main transient species have a longer life-time (see also Figure 4.5).

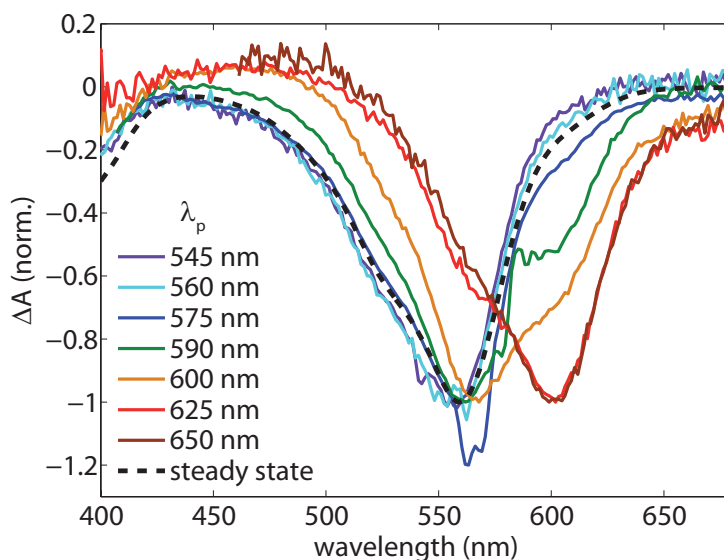


Figure 4.8: Normalized difference spectra (i.e. the remaining bleach signal) after 3.4 ns for different pump wavelengths λ_p . The bleach shifts from 560 to 600 nm with increasing λ_p , confirming the existence of two isomers in solution. The bleach at $\lambda_p = 575$ nm is partly disturbed by stray light.

modeled in the next section. This method will also allow the determination of the quantum efficiency for ring closure and isomerization for both isomers.

4.3.3 Data modeling

The reaction mixture consists of two merocyanine isomers having different spectral signatures in the ground state as well as in the excited state. The signals of all processes contributing to the transient-absorption maps in Figures 4.4 and 4.7 overlap with each other, aggravating a straightforward analysis of the basic properties, e.g. the quantum efficiency of the photoreaction. The quantum efficiency Φ of a reaction is the portion of initially excited molecules that follows the reaction pathway in question, in the simplest case given by the remaining bleach b_f and the initial bleach b_i via:

$$\Phi = \frac{b_f}{b_i}, \quad (4.1)$$

or in the case of single-exponential GSR via Eq. 3.5. In more complex systems, however, many reaction channels starting from the reactant, as well as reaction channels leading to the reactant starting from other present molecules, impede the determination of Φ . In these cases, it is crucial to know the amount of the initially excited molecules, the quantum efficiency for all other pathways and the amount of molecules that are formed starting from another reactant, e.g. through isomerization. Quantum-efficiency measurements based on prolonged irradiation also yield correct results only as long as no reactant formation occurs, thermally or photochemically, from other molecules in solution. The problem is elucidated in Figure 4.9, where the quantum efficiencies of TTC and TTT are on the one hand determined via Eq. 4.1 (solid lines), and on the other hand with Eq. 3.5 (dashed lines) for the remaining bleach b_f and the amplitudes of the GSR of the global fit of Figure 4.5 (i.e. an extrapolation to $t = 0$ to exclude contributions due to fast processes, e.g. vibrational cooling in Figure 4.5).

Note at this point that Figure 4.9 does not show quantum efficiency dependent on pump wavelength but dependent on probe wavelength. The variation of the values in Figure 4.9 with probe wavelength is due to parallel processes disturbing a correct determination of the quantum efficiency.

The quantum efficiency should be independent of the probe wavelength, hence the slope of the quantum efficiency should be zero. This is for example observed for TTC, where a plateau can be detected around its absorption maximum at 560 nm ($\Phi = 40 - 50\%$) in Figure 4.9. The quantum efficiency of TTT on the other hand can less easily be read off, since the slope is never zero around the ground-state absorption (GSA) maximum at 600 nm, but the values vary from 45% for 590 nm to 25% for 620 nm. This behavior is due to the proximity of the excited-state absorption and the stimulated emission with its high oscillator strength (see Figure 4.5). The combination of the two isomers, as is the case in solution, impedes any determination of the quantum efficiencies even further, since the remaining offset in Eqs. 4.1 and 3.5 at a given probe wavelength λ is the result of the photochemistry of both isomers. Therefore, the transient-absorption data $\Delta A(\lambda_p, \lambda, \Delta t)$ obtained for six pump wavelengths λ_p are jointly modeled in the

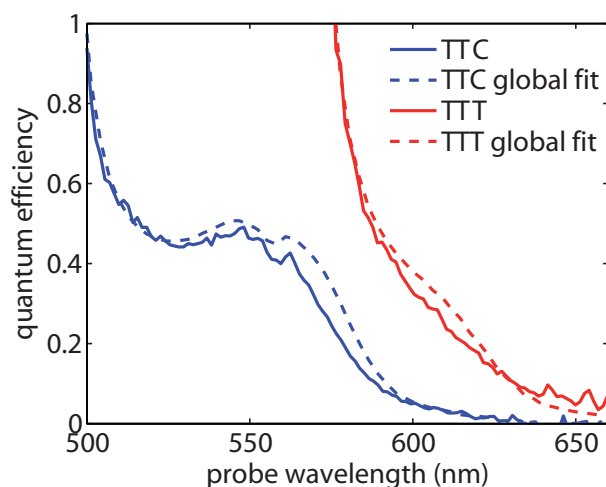


Figure 4.9: Quantum efficiencies obtained assuming Eq. 4.1 or Eq. 3.5 are applicable. Whereas for TTC (blue) a plateau near the GSA at 560 nm can be detected with quantum efficiencies between 40 and 50% (without global fit, using Eq. 4.1, solid line) or 45-50% (with global fit using Eq. 3.5, dashed line), no plateau is observed for TTT (solid red line without global fit, dashed red line with global fit). As can be seen Eq. 4.1 as well as Eq. 3.5 yield defective results, because quantum efficiencies cannot be greater than 1 and they should be independent of the probe wavelength. This discrepancy is one of the reasons to model the data in a special way as shown in this chapter.

following sections. This allows the extraction of the quantum efficiency for ring closure and isomerization for both isomers.

The excitation wavelength clearly has an impact on how many molecules of each isomer are excited. But also characteristics describing the dynamics of each isomer individually might change with λ_p , like the shape and strength of the different spectral signatures (e.g. fluorescence due to different amounts of excess energy introduced into the system), as well as the quantum yield of isomerization and ring closure. In order to take all possible dependencies into account and achieve the most general model, many additional parameters would have to be introduced that might cause rather ambiguous modeling results. A different approach is followed here in which the six $\Delta A(\lambda_p, \lambda, \Delta t)$ sets are modeled with the number of parameters as small as possible by assuming that the quantum efficiencies and the spectral shapes of the contributing processes (SE, ESA, GSR) for both isomers are in first approximation independent of the pump wavelength. The validity of this assumption is checked later on by looking at the deviations of the quantum efficiency found by jointly modeling all six data sets from the quantum efficiency as retrieved for each data set after the modeling. Clear λ_p -dependent trends and strong inconsistencies between modeled and measured data sets would indicate that the assumptions make the model too inaccurate.

Assumed model

The analysis combines the results of six measurements with pump wavelengths $\lambda_p = 545, 560, 575, 590, 600$ and 625 nm (see Figure 4.3). Each dataset is a spectrotemporal map

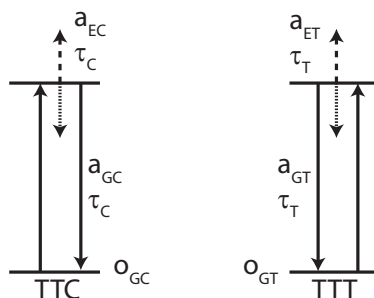


Figure 4.10: Scheme used in the modeling. For each isomer, after vibrational cooling GSR (amplitude a_{GC} for TTC and a_{GT} for TTT), ESA and SE (a_{EC} for TTC and a_{ET} for TTT) occur, while isomerization or ring-closure dynamics cannot be monitored directly. The third determinable amplitude for each isomer is the remaining offset o_{GC} for TTC and o_{GT} for TTT. Note that the wavelength-dependent length of each arrow as it would be depicted in a conventional energy-level diagram is obtained after the spectral fitting procedure from the position of the maxima in Figure 4.13. In reality of course, transitions are possible at all those wavelengths (i.e. different arrow lengths) with nonzero amplitude in Figure 4.13. The transition probability is given as the product of a_X and the respective shape from Figure 4.13. If that product is positive excited-state absorption dominates over stimulated emission (dashed arrow) and vice versa for a negative value (dotted arrow). In case of *GSR* the respective amplitude a_{GX} is always negative (see Tab. 3.1).

$\Delta A(\lambda_p, \lambda, \Delta t)$. Therefore the spectral and the temporal part of all signal contributions have to be modeled.

Spectral model In the spectral model expressions have to be found for the spectral shapes of the GSA (and hence the GSR), the ESA and the SE for both isomers, see involved states in Figure 4.10. In the following, the assignment of these expressions are explained, together with the number of parameters this introduces to the fit model. For the shape of the GSA of TTC (abbreviated *GC* in the following), the steady-state absorption is fitted with two skewed Gaussians for the TTC contribution, plus a red-shifted copy of these two skewed Gaussians to separate the contribution of TTT around 600 nm. In the fit all experimentally known parameters (skew factor > 0 , shift : 38 – 42 nm, see Figure 4.8) are set constrained. The obtained fit is used for *GC*, thereby removing the part of the S_2 absorption below 450 nm (see Figure 4.1) and the contribution of TTT in comparison to the steady-state spectrum. Skewed Gaussians are asymmetric Gaussian functions, compressed towards one direction and stretched towards the other direction to better reflect asymmetrical absorption bands by introducing an additional parameter [119, 120].

Figure 4.11 shows the steady-state spectrum (solid blue), the difference spectrum at 3.4 ns from Figure 4.8 (solid red) and the red-shifted steady-state spectrum (dashed red). In the region where excited-state absorption and stimulated emission do not contribute to the difference spectrum (580-620 nm, see Figure 4.7), the spectral shape of the difference spectrum is very similar to the steady-state spectrum. Due to the strong agreement of the two red curves (the edges are influenced by signals of the SE and ESA, see Figure 4.7)

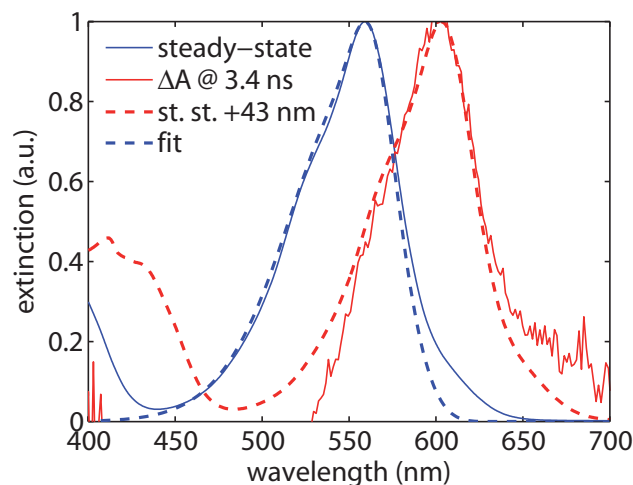


Figure 4.11: Steady-state absorption (blue solid) fitted with two skewed Gaussians plus a red-shifted copy of these two with a relative amplitude. The copy is used to remove the contribution of TTT, the sum of the other two (blue dashed) is taken as the GSA of TTC (*GC*). Contributions of the S_2 absorption below 450 nm are not considered for the modeling. The red-shifted *GC* (red dashed) agrees well with the difference spectrum (red solid) at 3.4 ns for 650 nm excitation (see Figure 4.8). Deviations at the edges arise from small contributions of SE and ESA remaining at 3.4 ns.

it is assumed that the GSA and GSR of TTT (abbreviated *GT*) can be expressed as the red-shifted *GC* (red-shift: 1 parameter). With the fitting method described above the *GC* spectrum (blue dashed) is obtained. Later on the theoretical relative excitations of both isomers at different pump wavelengths will be compared with the measured relative excitation to validate this assumption.

The spectral shapes of the SE of the two isomers (abbreviated *SEC* and *SET*, respectively) are taken as the red-shifted mirror image of the GSA of the respective isomer (red-shift: 1 parameter for each isomer). For the ESA of TTC (abbreviated *ESAC*) one Gaussian [119, 120] is assumed (FWHM: 1 parameter, λ_{max} : 1 parameter), since only one maximum is visible in the decay-associated spectrum in Figure 4.5. The excited-state absorption of TTT (*ESAT*) on the other hand is represented by two Gaussians with the same FWHM (FWHM: 1 parameter, λ_{max} : 2 parameters) and relative amplitude (1 parameter), since two maxima are visible in the decay-associated spectrum in Figure 4.5.

Furthermore it is assumed that SE and ESA of one isomer have a fixed relative amplitude x . The excited-state spectral shape is therefore $EC = SEC + x_C ESAC$ (x_C : 1 parameter) for TTC and $ET = SET + x_T ESAT$ (x_T : 1 parameter) for TTT.

A total amount of 11 parameters is therefore needed to reproduce the spectral shapes involved in the transient-absorption data.

Temporal model The modeling approach is only able to detect the population changes via the spectral shape functions as displayed in Figure 4.10, i.e. GSR and excited-state processes (ESA and SE) of both isomers. Three temporal models will be discussed. In

the simplest model it is assumed that both isomers are completely isolated from each other, meaning no isomerization pathway exists. For this a basic temporal model is assumed, consisting only of single-exponential GSR of both isomers (τ_C and τ_T in Figure 4.10: 2 parameters). The amount of parameters therefore rises to 13. It will be seen below, however that this does not suffice to describe the experimental data accurately and thus, extended models are required taking into account isomerization. Those extended models will use the same amplitudes as the simple model but with additional cross-links connecting the different isomers (see Figure 4.18 and Figure 4.19). Energy transfer pathways between the isomers are neglected due to the small concentration of merocyanine (0.5 mM) used in this study. With the knowledge at hand that 6,8-dinitro-BIPS does not form aggregates [117] the mean distance between two molecules is about 15 nm. Since energy transfer would only be possible from the major isomer **1** to the minor isomer **2** the probability for energy transfer is decreased even further due to the small fraction of molecules present as TTT (see Figure 4.11).

Amplitudes

The transient-absorption maps, e.g. Figures 4.4 and 4.7, are further characterized by the individual contribution of each process. Since the four spectral shapes (*GC*, *GT*, *EC*, *ET*) are each linked to only one time constant so far, each dataset needs four amplitudes (a_{GC} , a_{GT} , a_{EC} , a_{ET}) and two remaining offsets (o_{GC} , o_{GT}), as shown in Figure 4.10. For example, a_{GC} , a_{EC} and o_{GC} , the spectral shapes linked to TTC, are greater in value than a_{GT} , a_{ET} and o_{GT} , the spectral shapes linked to TTT, for pump wavelengths smaller than 575 nm (see Figure 4.8). Every dataset is therefore connected to six amplitude parameters.

The six parameters obtained for every dataset, as will be explained in the next section, will be called *linear* parameters in contrast to the previous 13 parameters needed for the spectral and temporal model that will be called *nonlinear* parameters.

Fitting procedure

The fitting procedure consists of a loop that optimizes the 13 nonlinear parameters with a Levenberg-Marquardt algorithm (see Figure 4.12) in which the linear amplitude parameters are obtained via constrained linear fits (bold boxes). Here the spectral shapes are first used as basis functions to reproduce every difference spectrum of all datasets. In the next step, the obtained amplitudes for every spectral shape are fitted with the respective temporal behavior, i.e. single-exponential decay without remaining offset for excited-state processes (*EC* and *ET*) and single-exponential decay with remaining offset for GSR (*GC* and *GT*). For this step, the basis functions are the decays with the associated time constants τ_C and τ_T (the time constants are optimized in the loop and taken as fixed value in this step) and in the cases with remaining offset a constant value function.

The coefficients obtained in this linear fit correspond to the six linear parameters for each dataset. In the last step the theoretical transient-absorption map is reconstructed from these amplitude parameters, spectral shapes and time constants, and used as feedback for the nonlinear algorithm in the loop. With this procedure only 13 nonlinear pa-

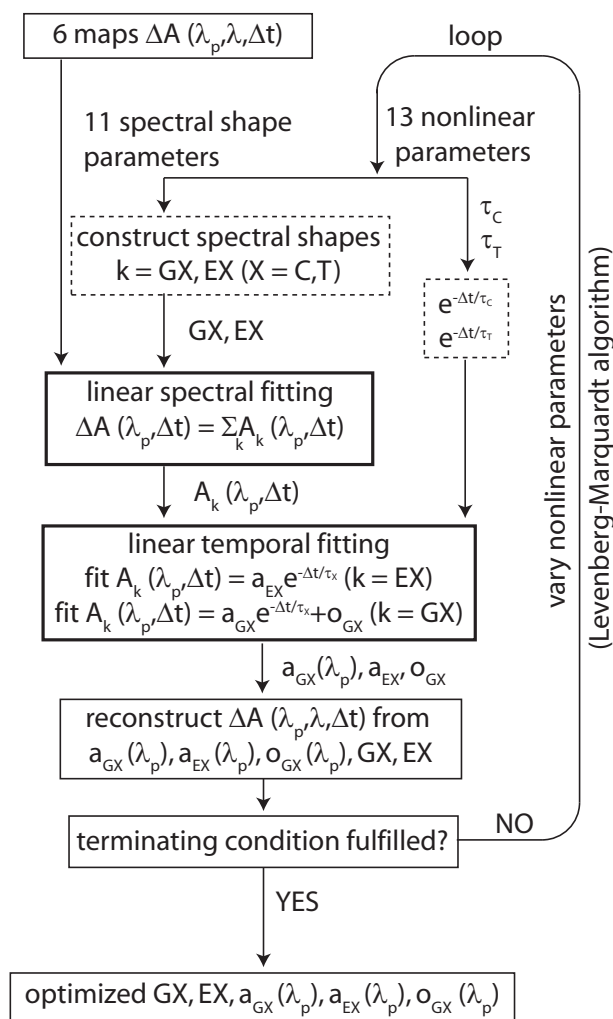


Figure 4.12: Fitting procedure: A loop optimizes the 13 nonlinear parameters to give optimal basis functions for the spectral shapes (used in the linear spectral fitting) and exponential decays (used for the linear temporal fitting).

rameters with starting values are needed to reproduce all 6 transient-absorption maps. For the linear fits no starting value is needed, since the optimal solution in a linear combination of basis functions can always be found [70].

4.3.4 Modeling results

The modeling results in the spectral shapes shown in Figure 4.13. To allow a visual comparison, Figure 4.14 shows the modeled and experimental transient-absorption maps for three representative pump wavelengths out of the complete set, namely for $\lambda_p = 560$ nm (mainly TTC), 600 nm (almost equal contribution of TTC and TTT) and 625 nm (mainly TTT). The most obvious parameters for the estimation of the fit quality are the SE of both isomers, peaking at $\lambda_{SEC} = 615$ nm and $\lambda_{SET} = 648$ nm (see Figure 4.5 for comparison), the position of the GSA of TTT at $\lambda_{GT} = 600$ nm (see Figure 4.8

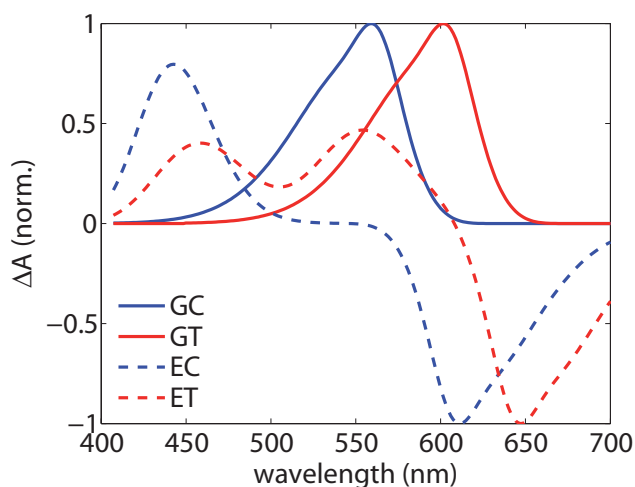


Figure 4.13: Spectral shapes found by the modeling procedure.

for comparison), the position of the ESA at $\lambda_{\text{ESAC}} = 442.5$ nm and $\lambda_{\text{ESAT1}} = 458$ nm (see Figure 4.5 for comparison), and the obtained time constants ($\tau_C = 93.8$ ps and $\tau_T = 902$ ps). All values are in very good agreement with the values from Section 4.3.2. The amplitudes obtained from the modeling are shown in Figure 4.15 and will be discussed in detail in the following.

The modeling allows for the determination of the amplitudes for GSR, ESA and SE with one of the two time constants. Yet, molecules contributing to the dynamics with e.g. τ_C do not necessarily always have to be in the TTC geometry, but they also could either become a different isomer or originate from a different isomer. Hence, the ring-closure and isomerization pathways have to be added to describe the dynamics more accurately.

4.3.5 Temporal model 1: No isomerization

Assuming that no isomerization in either direction occurs, the reaction scheme from Figure 4.10 is extended by the ring-closure pathway to the spiroopyran (SP) in Figure 4.16, which then is responsible for the remaining offsets (σ_{GC} and σ_{GT}). The quantum efficiencies for this ring closure are calculated with Eq. 3.5 with the amplitude of the GSR (+) and the remaining offset (\times) from Figure 4.15, and are displayed in black (\circ) for TTC and TTT in Figure 4.17. In the case where isomer TTC is mainly excited ($\lambda_p = 545, 560, 575$ nm) this approach yields quantum efficiencies for TTC ring closure independent of the pump wavelength (TTC: 40 – 45%, as seen in Figure 4.17 (left, black \circ)). Similarly, when mainly TTT is excited ($\lambda_p = 600, 625$ nm), the quantum efficiency for TTT ring closure (Figure 4.17, right, black \circ) is independent of λ_p for these wavelengths (TTT: 32-38%). This validates the assumption that the quantum efficiencies are in first approximation independent of the pump wavelength. However, there are deviations of the quantum efficiency at pump wavelengths where the isomer in question is not the predominantly excited isomer, e.g. TTC at 600 and 625 nm and TTT at 545 and 560 nm, respectively. These deviations indicate that an isomerization process also occurs, which

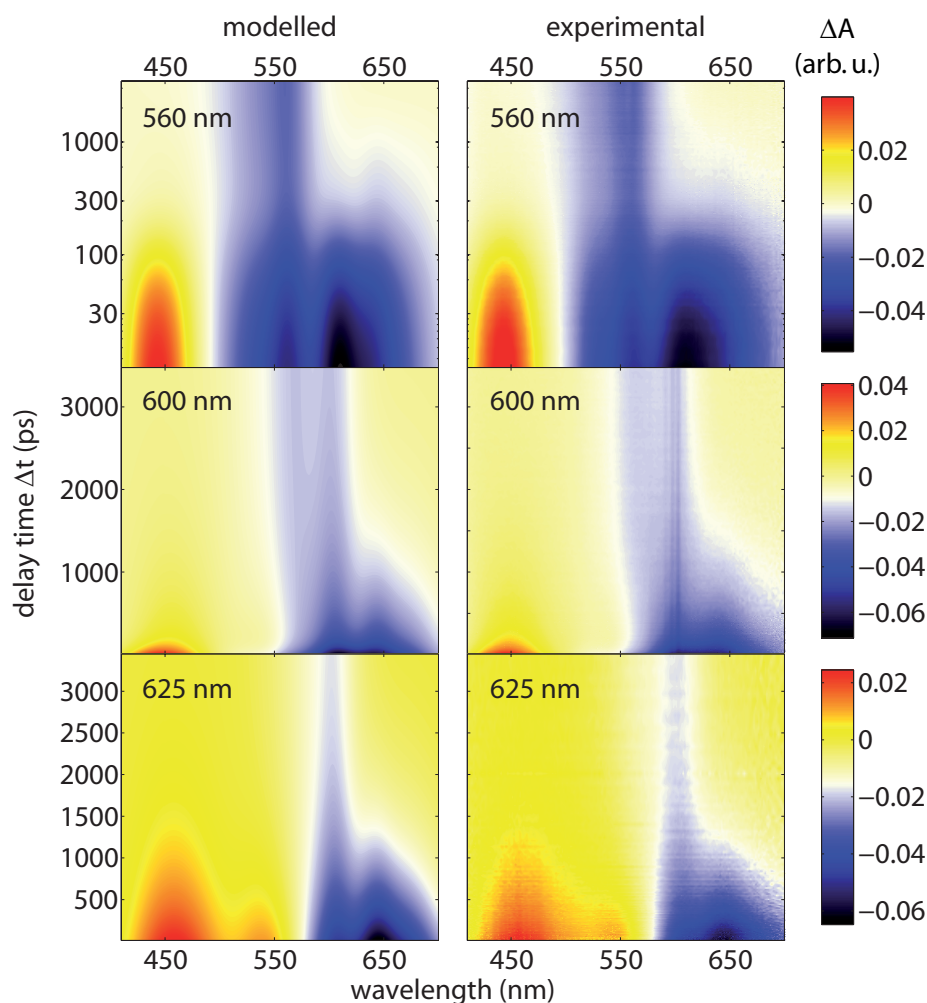


Figure 4.14: Comparison of the modeled (left) and experimental (right) transient-absorption maps $\Delta A(\lambda_p, \lambda, \Delta t)$ with $\lambda_p = 560$ nm (top), 600 nm (middle) and 625 nm (bottom). Note the logarithmic time axis for $\lambda_p = 560$ nm for better visualization of the fast 90 ps dynamics of TTC. The color codes are the same between each pair of experimental and modeled data and optimized for maximum contrast for interpretability (i.e. white does not necessarily represent zero absorption change). The maps are normalized such that the integral of the remaining bleach is the same.

explains the GSR without offset for TTT (at 545 and 560 nm in Figure 4.15) and a small positive offset for TTC (at 625 nm in Figure 4.15). Without an isomerization pathway, a remaining offset of zero would mean the improbable case of no ring closure, while a positive offset cannot be explained at all with temporal model 1.

Hence, an isomerization process occurs and it is necessary to include it in the modeling. For 6,8-dinitro BIPS or similar spiropyran-derived merocyanine systems, isomerizations are proposed in the literature, based on experimental results [101] as well as theoretical results [121, 122]. To include isomerization pathways, barrierless excited-state isomerization will not be considered, which e.g. is applicable for very fast isomerization reactions in monomethine cyanines [67, 123–126], due to the observed decays lasting hundreds

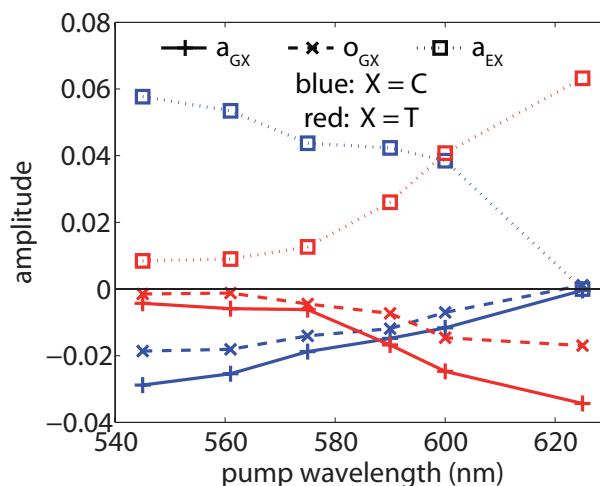


Figure 4.15: Amplitudes of the processes shown in Figure 4.10 obtained from the modeling (TTC: blue, TTT: red). The remaining offsets o_{GC} and o_{GT} are shown as (\times), the amplitudes of GSR a_{GC} and a_{GT} are shown as ($+$) and the amplitudes of excited-state processes (a_{EC} and a_{ET}) are shown as (\square) (see Figure 4.10).

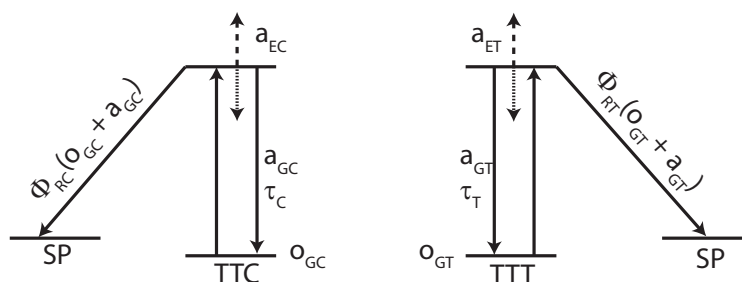


Figure 4.16: Temporal model 1. No isomerization occurs. The remaining offset is only due to ring closure to spiropyran (SP).

of ps. Instead, two models from the literature are chosen which comprise at least one excited-state barrier.

In the cases with mainly excitation of one isomer, the other isomer shows a remaining offset (see Figure 4.15) which does not scale linearly with the respective GSR, indicating isomerization towards this isomer, e.g. isomerization from TTC to TTT is seen at $\lambda_p = 545$ and 560 nm, resulting in GSR but no offset for TTT. The effect is seen better in the quantum efficiencies of TTT in Figure 4.17 resulting from temporal model 1: at 545 and 560 nm the quantum efficiencies (black \circ) are much lower (≤ 0.25) than at the other wavelengths. Isomerization from TTT to TTC is seen at 625 nm, with a small positive offset for TTC and also at 600 nm via a slightly deviating quantum efficiency (38% at 600 nm in contrast to 40%-45% for 545 to 590 nm, see Figure 4.17 on the left) due to isomerization towards TTC (hence, b_f in Eq. 3.5 is too small due to the additionally formed TTC). In the next subsection an attempt to quantify these observations to obtain quantum efficiencies for isomerization, ring closure and GSR is shown.

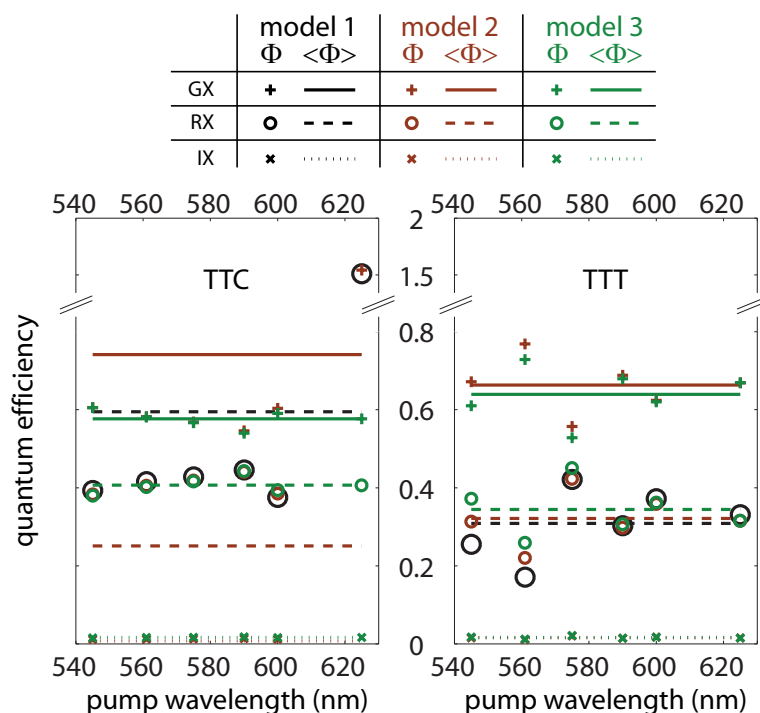


Figure 4.17: Colored lines: Quantum efficiencies obtained with temporal model 1 (black), 2 (brown) and 3 (green) for reaction channels [ground state recovery Φ_{GX} : solid line (single values: +), ring closure Φ_{RX} : dashed line (single values: o) and isomerization Φ_{IX} : dotted line (single values: x)] from both isomers (left: TTC, right: TTT) as shown in Figures 4.16, 4.18 and 4.19. Temporal model 1 assumes no isomerization at all. Temporal model 2 assumes isomerization through a conical intersection, leading to quantum efficiencies for ring-closure, isomerization and GSR that agree much at all pump wavelengths for TTT (especially at 545, 560 and 575 nm). The outlier at 625 nm for TTC cannot be corrected completely. Even better performs temporal model 3, yielding consistent quantum efficiencies of TTC and TTT for all pump wavelengths (including $\lambda_p = 625$ nm). Note that $\Phi_{IX} + \Phi_{RX} + \Phi_{GX} = 1$.

4.3.6 Temporal model 2: Isomerization through conical intersection

For the temporal model 2, a scheme is adopted in which a conical intersection connecting both isomers exists, but a certain amount of excess energy is necessary to reach it, as shown in Figure 4.18 [127, 128]. Thereby it is assumed that after vibrational cooling, it is unlikely that the barriers are crossed. Concerning the assumption that the quantum efficiencies are independent of the pump wavelength, for example an energetically high-lying Franck-Condon region relative to the barrier would result in a very small influence of the excess energy on the photochemistry.

After excitation very fast isomerization through the conical intersection can occur, but because of the barrier a certain amount of population remains in the excited state and is deactivated through slower reaction paths (internal conversion, fluorescence). A situation where the conical intersection is not a minimum of the excited state but rather energetically higher-lying than the minima to which the population can relax [56] might give similar results.

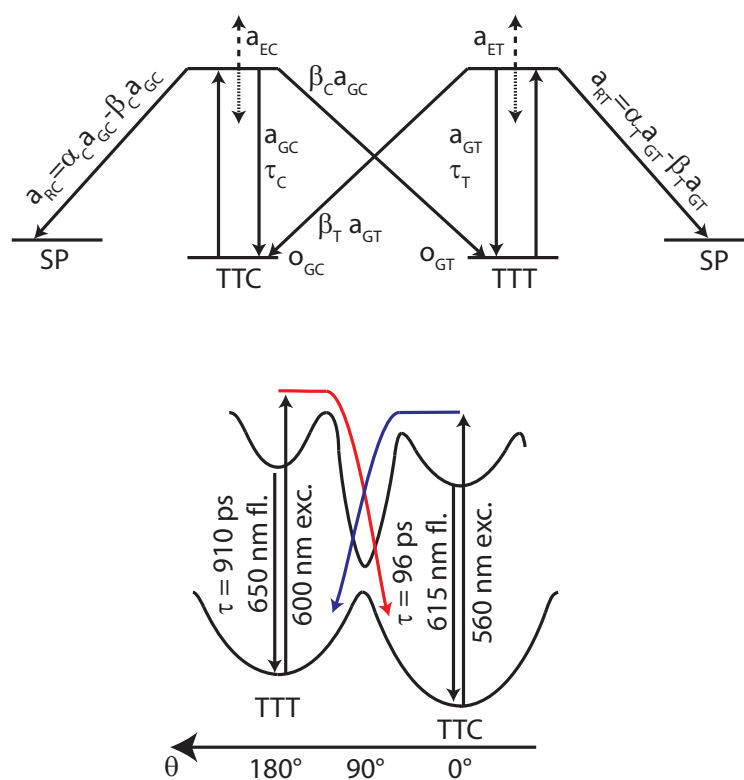


Figure 4.18: Temporal model 2. Top: An illustration of the introduced parameters. The parameter α_X describes the ratio between ring closure plus isomerization to the amplitude of the GSR of isomer X and the parameter β_X describes the ratio of isomerization to GSR of isomer X. Bottom: Potential energy sketch showing that isomerization may occur through a conical intersection initially after excitation, for which a small amount of excess energy is needed. The return to the ground state of the reactant through the conical intersection is neglected in this model.

The reaction path going through the conical intersection should give rise to fast-decaying features during the first few ps. From the experimental data, one can already derive that this reaction pathway does not contribute strongly. Population passing the conical intersection can either go back to their initial or to the other isomer geometry. Because the modeling starts only after 10 ps, the latter case will be observable through the remaining offset, while the former is not covered (the molecules have relaxed back to their initial configuration so fast as if they were not excited at all), so that the determined quantum efficiencies might be underestimated due to this effect.

We add to the reaction scheme from Figure 4.16 the isomerization pathway for both directions in Figure 4.18. After excitation, molecules either undergo ring closure, isomerization, or GSR. Those reacting along the isomerization pathway through the conical intersection can only be detected in the remaining offset $o_{GC}(\lambda_p)$ and $o_{GT}(\lambda_p)$. The amplitudes of GSR $a_{GC}(\lambda_p)$ and $a_{GT}(\lambda_p)$ do not depend on the isomerization quantum efficiency of the other isomer, but the total amount of excited molecules may be different, due to the new pathway, from what was obtained in temporal model 1.

The parameters α_X and β_X ($X=T$ for TTT and $X=C$ for TTC, respectively) are

X	α_X	β_X	Φ_{RX}	Φ_{IX}
C	0.706	-0.022	0.25 (0.40) ^a	0.0075 (0.012)
T	0.522	-0.026	0.32	0.016

Table 4.2: Fit results for temporal model 2.

^aValues in brackets are without the data point at 625 nm.

now introduced to describe the ratios between ring closure, GSR, and isomerization. α_X describes the ratio of the number of excited X molecules not returning to the X ground state to the number of excited X molecules returning to the X ground state. Hence, $\alpha_X a_{GX}(\lambda_p)$ is then the amount of bleached molecules (due to isomerization plus ring closure). With this parameter the percentage of GSR from molecules that did not isomerize can be calculated as:

$$\Phi_{GX} = \frac{1}{\alpha_X + 1} . \quad (4.2)$$

The parameter β_X describes the ratio between GSR and isomerization, i.e. $\beta_X = 1$ would mean that isomerization is as probable as GSR. The amplitude $a_{RX}(\lambda_p)$ for ring closure is then the fraction of molecules not returning to the ground state minus the fraction proceeding along the isomerization pathway:

$$a_{RX} = \alpha_X a_{GX}(\lambda_p) - \beta_X a_{GX}(\lambda_p) . \quad (4.3)$$

The measured offsets are determined by the bleach due to excitation of the isomer in question plus the contribution of isomerization leading towards this isomer. The offsets $o_{GC}(\lambda_p)$ and $o_{GT}(\lambda_p)$ then become:

$$o_{GC}(\lambda_p) = \alpha_C a_{GC}(\lambda_p) + \beta_T a_{GT}(\lambda_p) , \quad (4.4)$$

$$o_{GT}(\lambda_p) = \alpha_T a_{GT}(\lambda_p) + \beta_C a_{GC}(\lambda_p) . \quad (4.5)$$

The definition of α_X and β_X results in a system of linear equations with the measured quantities $o_{GT}(\lambda_p)$, $o_{GC}(\lambda_p)$, $a_{GT}(\lambda_p)$ and $a_{GC}(\lambda_p)$ from Figure 4.15. Since the experimental data consist of six λ_p values, this gives rise to 12 equations to fit the values (α_C , α_T , β_C and β_T).

From the obtained values the average quantum efficiencies of the ring-closure and isomerization pathways can be calculated via

$$\Phi_{RX} = \frac{\alpha_X - \beta_X}{\alpha_X + 1} , \quad (4.6)$$

$$\Phi_{IX} = \frac{\beta_X}{\alpha_X + 1} . \quad (4.7)$$

The results are summarized in Tab. 4.2. Since α_X and β_X are now known, Eqs. 4.4 and 4.7 can be used for each λ_p to eliminate the contribution to the offset originating

from the other isomer. With Eq. 3.5 the corrected quantum efficiencies for ring closure (brown \circ in Figure 4.17), isomerization (brown \times) and the GSR (brown $+$) for both isomers can be calculated.

These quantum efficiencies now lie in a more reasonable range for TTT also for those pump wavelengths where mainly the other isomer is excited, in contrast to the deviations observed with temporal model 1. For TTC, an improvement can be seen at 600 nm but the unrealistic value of 5 for 625 nm (due to almost no excitation of TTC at this wavelength) cannot be corrected completely. The comparison with temporal model 1 [black (\circ) in Figure 4.17] shows that temporal model 2 gives more consistent quantum efficiencies for both isomers and all reaction channels.

4.3.7 Temporal model 3: Isomerization in the excited state

Calculations have shown that a barrier in the excited state may exist between the isomers [121, 122, 129] and no isomerization through a conical intersection to the ground state [130, 131] occurs, as depicted in the potential scheme in Figure 4.19. This model, which has also been employed in the literature to describe isomerization reactions of polymethine dyes [132, 133], is adopted as temporal model 3. The isomerization occurs in the excited state initially after excitation (no conical intersection is considered), but the barrier is too high to be overcome after vibrational cooling. This is confirmed by the experimental data, since a continuous equilibration between excited TTT and TTC is not observed, else one would always observe the same transient-absorption dynamics independent of the relative excitation of the isomers (see Figures 4.4 and 4.7).

The total bleach signal of molecules being excited from the ground state to the excited state is defined as $c_{GC}(\lambda_p)$ and $c_{GT}(\lambda_p)$ (see Figure 4.19) for TTC and TTT, respectively. In this model, Φ_{GX} describes the percentage of excited molecules $c_{GX}(\lambda_p)$ that return to the ground state, whereas Φ_{IX} describes the percentage of all excited molecules $c_{GX}(\lambda_p)$ to proceed along the isomerization pathway. Note that the ring-closure quantum efficiency Φ_{RX} is related to the other efficiencies through $\Phi_{RX} = 1 - \Phi_{GX} - \Phi_{IX}$. While the TTC isomerization contribution $\Phi_{IC} c_{GC}(\lambda_p)$ increases the absolute value of the amplitude $a_{GT}(\lambda_p)$ of the GSR of TTT, and vice versa,

$$a_{GT}(\lambda_p) = \Phi_{GT} c_{GT}(\lambda_p) + \Phi_{IC} c_{GC}(\lambda_p) , \quad (4.8)$$

$$a_{GC}(\lambda_p) = \Phi_{GC} c_{GC}(\lambda_p) + \Phi_{IT} c_{GT}(\lambda_p) , \quad (4.9)$$

the offset is decreased in value by the isomerization contribution, since additional molecules which were not in this configuration initially are formed:

$$o_{GT}(\lambda_p) = (1 - \Phi_{GT}) c_{GT}(\lambda_p) - \Phi_{IC} c_{GC}(\lambda_p) , \quad (4.10)$$

$$o_{GC}(\lambda_p) = (1 - \Phi_{GC}) c_{GC}(\lambda_p) - \Phi_{IT} c_{GT}(\lambda_p) . \quad (4.11)$$

The sum of the GSR amplitude and the offset (two values known from Figure 4.15) yields the value of all excited molecules, $c_{GC}(\lambda_p)$ and $c_{GT}(\lambda_p)$, and is independent of isomerization contributions:

$$a_{GC}(\lambda_p) + o_{GC}(\lambda_p) = c_{GC}(\lambda_p) , \quad (4.12)$$

$$a_{GT}(\lambda_p) + o_{GT}(\lambda_p) = c_{GT}(\lambda_p) . \quad (4.13)$$

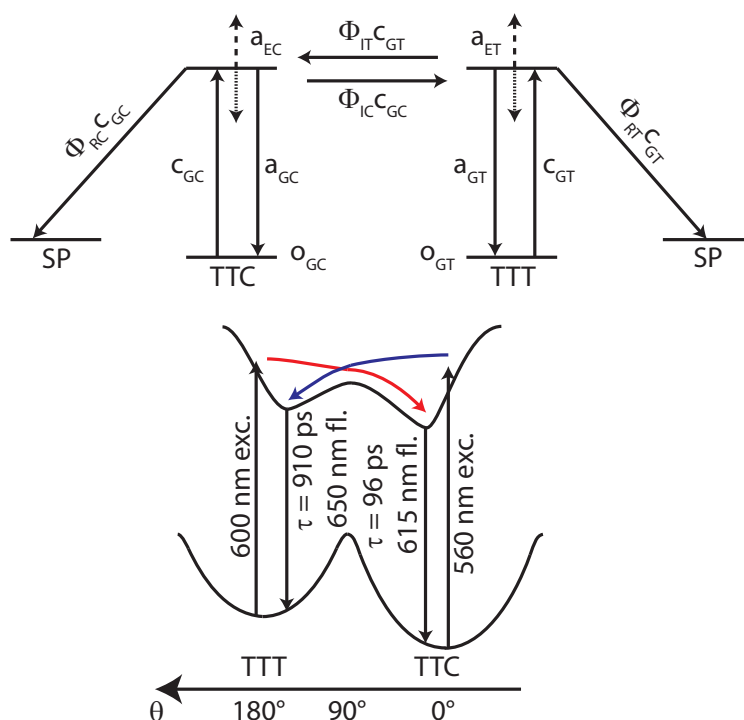


Figure 4.19: Temporal model 3. Top: An illustration of the introduced parameters. c_{GX} is the amplitude of all excited molecules, Φ_{IX} the quantum efficiency for isomerization and Φ_{RX} the quantum efficiency for ring closure. Bottom: Potential energy scheme showing that isomerization occurs in the excited state initially after excitation. Vibrationally cooled excited states can not isomerize because the two excited states are separated by a small barrier. No conical intersection is considered in this model.

With $\gamma(\lambda_p)$ (see solid red line in Figure 4.20) being

$$\gamma(\lambda_p) = \frac{c_{GC}(\lambda_p)}{c_{GT}(\lambda_p)}, \quad (4.14)$$

one can derive

$$\frac{1}{\frac{o_{GC}(\lambda_p)}{a_{GC}(\lambda_p)} + 1} = \Phi_{GC} + \frac{\Phi_{IT}}{\gamma(\lambda_p)}, \quad (4.15)$$

$$\frac{1}{\frac{o_{GT}(\lambda_p)}{a_{GT}(\lambda_p)} + 1} = \Phi_{GT} + \gamma(\lambda_p) \Phi_{IC}. \quad (4.16)$$

Similar to temporal model 2 a system of 12 linear equations is obtained with expressions for the four unknown values of Φ_{GC} , Φ_{GT} , Φ_{IC} and Φ_{IT} with the solution listed in Tab. 4.3. Looking at Figure 4.17, one can see that TTC has a higher quantum efficiency than TTT for ring closure [dashed green line with green (\circ) in Figure 4.17 (left versus right, respectively)]. However, the quantum efficiencies for isomerization (dotted green line and green +, left versus right) are very similar and low for TTC and TTT. Model 3 thus yields an even more consistent result for all pump wavelengths than model 2.

X	δ_X	Φ_{IX}	Φ_{RX}
C	0.576	0.016	0.40
T	0.639	0.016	0.35

Table 4.3: Fit results for temporal model 3.

4.3.8 Validation of the modeling

In the modeling it was assumed that the spectral shape of TTT is the red-shifted shape of TTC. With the optimized spectral shapes (Figure 4.13) and the known pump laser pulse spectra (Figure 4.3) one can calculate the relative excitation $\gamma(\lambda_p)$ at the different pump wavelengths with the relative concentration of the isomers as free parameter. The experimental value is calculated with the modeling results shown in Figure 4.15 for model 2 via (see Figure 4.18):

$$\gamma(\lambda_p) = \frac{(1 + \alpha_C - \beta_C)a_{GC}}{(1 + \alpha_T - \beta_T)a_{GT}} \quad (4.17)$$

and for model 3 via (see Figure 4.19):

$$\gamma(\lambda_p) = \frac{c_{GC}}{c_{GT}}. \quad (4.18)$$

The comparison with the experimental values in Figure 4.20 (experimental: solid lines, fit: dashed lines) shows very good agreement for a concentration ratio $\frac{TTT}{TTC} = 0.30$ for model 3 (green in Figure 4.20) and $\frac{TTT}{TTC} = 0.34$ for model 2 (brown in Figure 4.20). These values do not correspond completely to the relative amplitude obtained in the spectral fit to obtain *GC* (0.15). The values are influenced by the absorption coefficient of TTT that remains unknown, but due to the very similar spectral shape a strong difference in the oscillator strengths of TTT and TTC is not expected. The unknown absorption coefficient of TTT also has an impact on the isomerization quantum efficiencies in both directions (linear for $TTC \rightarrow TTT$, reciprocal for $TTT \rightarrow TTC$), but cannot be considered in the modeling due to missing spectroscopic information.

It was also assumed that the stimulated emission spectra *SE* were similar to the mirror image of the respective *GSA*. To first approximation, errors in the spectral shapes of the stimulated emission and excited-state absorption would not influence the outcome of the temporal models 2 and 3, since the stimulated emission amplitudes are not involved in the determination of the quantum efficiencies. The comparison of the modeled with the experimental datasets (Figure 4.14) shows that the modeled spectral shapes for stimulated emission (Figure 4.13) are a bit too sharp at their maxima, but this error is very small and therefore acceptable.

The last assumption was that the quantum efficiencies are independent of the pump wavelength. This assumption is validated via the results for temporal model 1. In the cases where one isomer is predominantly excited, almost no trend dependent on the excess energy can be observed, e.g. in Figure 4.17 for TTC excitation (left) the variation of the quantum efficiency is less than 5% and for TTT excitation (right) the quantum efficiencies at the corresponding TTT wavelengths are statistically spread around 0.37.

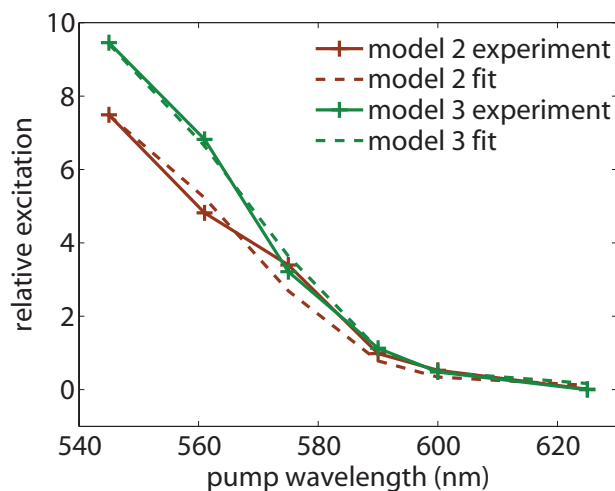


Figure 4.20: Relative excitation, $\gamma(\lambda_p)$, resulting from temporal model 2 (brown) and 3 (green). A relative excitation of 1 corresponds to a pump wavelength that excites both isomers in the same amount with regard to their concentrations in solution. The solid lines are obtained with the modeling results from Figure 4.15 and Eq. 4.17 for model 2 and Eq. 4.18 for model 3. The dashed lines correspond to the relative excitation $\gamma(\lambda_p)$ obtained via the spectral shapes G_X in Figure 4.13 and the pump laser pulse spectra in Figure 4.3, yielding a concentration ratio of $\frac{TTT}{TTC} = 0.34$ (brown, model 2) and 0.30 (green, model 3).

The mentioned assumptions allowed the reconstruction of all six datasets with only 13 nonlinear parameters (≈ 2 for every dataset), yielding very good agreement with the experimental data at all pump wavelengths (Figure 4.14).

4.3.9 Discussion: Isomerization

The results from models 2 (Section 4.3.6) and 3 (Section 4.3.7) show that isomerization can indeed explain the experimental data better than model 1 (Section 4.3.5) which does not include any isomerization pathway. But in both models, the isomerization plays a minor role in the photochemistry of 6,8-dinitro BIPS, with quantum efficiencies that are much smaller than those for ring closure, which clearly is the predominant photochemical pathway not returning to the reactant after excitation. All models yield quantum efficiencies for ring closure higher than 32% for the minor isomer TTT and higher than 35% for the major isomer TTC, respectively. The isomerization quantum efficiency is very small and models 2 and 3 result in very similar quantum efficiencies (1.6% for model 2 and 1.6% for model 3 starting from TTT and 1.2% for model 2 and 1.6% for model 3 starting from TTC, respectively, see Tab. 4.2 and Tab. 4.3).

An actual conclusion which model describes the data in a better way is difficult to draw, since the experimental data can be expressed with both models acceptably and much better than without isomerization pathway. Temporal model 3 surpasses model 2 at correcting the quantum efficiencies. This is best seen at a pump wavelength of 625 nm in Figure 4.17: model 2 results in a much too high GSR efficiency (brown line with brown +) of TTC, whereas model 3 gives 0.57 in agreement with the values at

other pump wavelengths (green line with green +). The analogous behavior can also be observed for TTT at pump wavelengths lower than 590 nm leading to a GSR quantum efficiency which is always a bit higher than with model 3, giving strong arguments towards model 3.

In a further comparison the relative excitations ($\frac{TTT}{TTC}$) in both models (Eq. 4.17 for model 2 and Eq. 4.18 for model 3) can best be described with a $\frac{TTT}{TTC}$ ratio of 0.34 (model 2, brown lines in Figure 4.20) or 0.30 (model 3, green lines in Figure 4.20). Again model 3 with the smaller percentage of TTT seems to be more realistic because NMR investigations have shown that the relative concentration of TTC should be low [117] (although no quantitative percentage is provided in that study).

From a theoretical point merocyanines possess excited-state potentials that are unlike those of stilbene. The odd number of π orbitals leads to a charge transfer rather than biradicaloid structure in the twisted excited state [130]. A conical intersection for the isomerization pathway as depicted in Figures 4.18 or 2.20 can only exist in the biradicaloid structure, giving further strong arguments to prefer model 3 over 2.

4.3.10 Summary: Ring-open form

The presented experiments revealed the presence of two merocyanine isomers in solution. The isomeric separation is directly elucidated by color variations of the visible femtosecond pump pulses that rendered isolated excitation of the red-shifted isomer possible. Whereas excitation pulses centered at 560 nm resulted in a permanent bleach around 560 nm [TTC isomer, $\tau(S_1) = 93.8$ ps], excitation pulses centered at 625 nm were mainly responsible for merocyanine bleaching around 600 nm [TTT isomer, $\tau(S_1) = 902$ ps]. For discussion of the bleach and the ring-closure reaction see Section 4.5.5.

Disentanglement of the involved processes of the open form (cis/trans isomerization as well as bleaching), in order to extract the quantum efficiencies of both isomers for the bleaching and isomerization pathway, was achieved with a global modeling approach. Three models were applied that all allow bleaching. Considering the isomerization pathway the first one did not allow isomerization at all, the second model included isomerization via a conical intersection, and the third model described isomerization completely in the excited state. While the first model proved to be too inaccurate, the latter two models resulted in very similar quantum efficiencies of all involved reaction channels, showing that isomerization plays a role. Furthermore the model without the conical intersection seems to describe the isomerization pathway more correctly than the model involving a conical intersection. Whereas isomerization between TTT and TTC is a minor pathway ($\Phi_{IC} = 1 - 2\%$ starting from TTC and $\Phi_{IT} = 1 - 2\%$ starting from TTT), bleaching (and thus ring closure) occurs with high quantum efficiency for both isomers ($\Phi_{RCC} = 40\%$ for TTC and $\Phi_{RCT} = 35\%$ for TTT).

4.4 Ring closed: spiropyran

After the investigation of the ring-open form, in this section the ring-closed form, the spiropyran, is investigated with transient absorption. The experimental data will be

presented first. However, on the basis of these data an interpretation is not unambiguous. Therefore the interpretation of these data is delayed until Section 4.5.6 where the bidirectional switching experimental data allows for a clearer assignment of the processes involved.

4.4.1 Experimental methods

Additionally to the methods used for the transient-absorption experiments on the ring-open form (Section 4.3.1) the sample reservoir has been illuminated with green LEDs during the experiment to generate the closed form. This results in an almost complete shift of the equilibrium to the ring-closed form. The ring-closed form was excited with 1 μ J 266 nm pulses with a pulse duration of 100 fs and a diameter in the sample of 100 μ m. Temporal resolution of this pump and probe combination is about 125 fs.

4.4.2 Experimental data

Figure 4.21 shows the visible transient absorption after excitation with 267 nm laser pulses. Nonlinear optical processes and two-photon absorption in the solvent strongly contribute to the dynamics during the first picosecond after excitation. This prevents a simple analysis of data from these early times. After the decay of the initial dynamics a broad transient-absorption band covering the whole visible spectral range from 400 to 700 nm ($\lambda_{\text{max}} = 500$ nm) (Figure 4.21) is apparent. The difference spectra at 500 and 2600 ps (see Figure 4.22 a) reveal that the absorption evolves into a spectrum with distinguishable shoulders at 445, 525 and 560 nm (black arrows), and a flat positive offset above 620 nm. While the absorption decreases at 445 nm, it increases at 525 and at 560 nm. An isosbestic point can be found at 485 nm. It should be noted that the shape and wavelength do not match the steady-state merocyanine absorption band in Figure 4.1 completely. For a more quantitative analysis of the dynamics the transient absorptions at different wavelengths are plotted in Figure 4.22 b. The data after 500 ps show increasing absorption at 525 nm (blue dots) and decreasing absorption at 445 nm (red circles). In contrast, the isosbestic point at 485 nm (green crosses) shows no dynamics after an initial fast decay. A fit of a single exponential to the data (black line) yields a time constant of 36 ps for this fast decay. The bidirectional switching results from Section 4.5 will help to interpret the dynamics found in the transient data of Figure 4.22. Hence the interpretation is deferred to the end of the Section 4.5.6. It will be shown that the broad absorption band visible in Figures 4.21 and 4.22 is at least partly due to merocyanine in its electronic ground state.

4.4.3 Quantum efficiency

Although the dynamics observed in Figure 4.21 cannot be interpreted so far, the quantum efficiency for ring-opening can be calculated in a good approximation from the photostationary equilibrium $\frac{[\text{Me}]}{[\text{Sp}]}$ obtained while illuminating with 267 nm light. For this purpose 267 nm fs-laser pulses with a beam diameter of 3 mm were used leading to a decrease in intensity by a factor of 9×10^{-6} compared to the transient-absorption

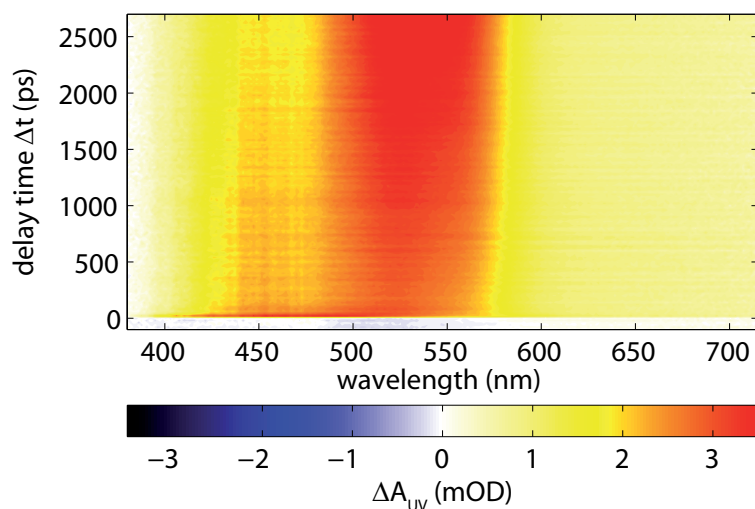


Figure 4.21: Transient-absorption spectrum of the ring opening with 267 nm pump and visible probe. After excitation, a positive absorption band emerges at 450 nm and decays with increasing time. Around 550 nm different absorption bands associated with merocyanine structures increase with time.

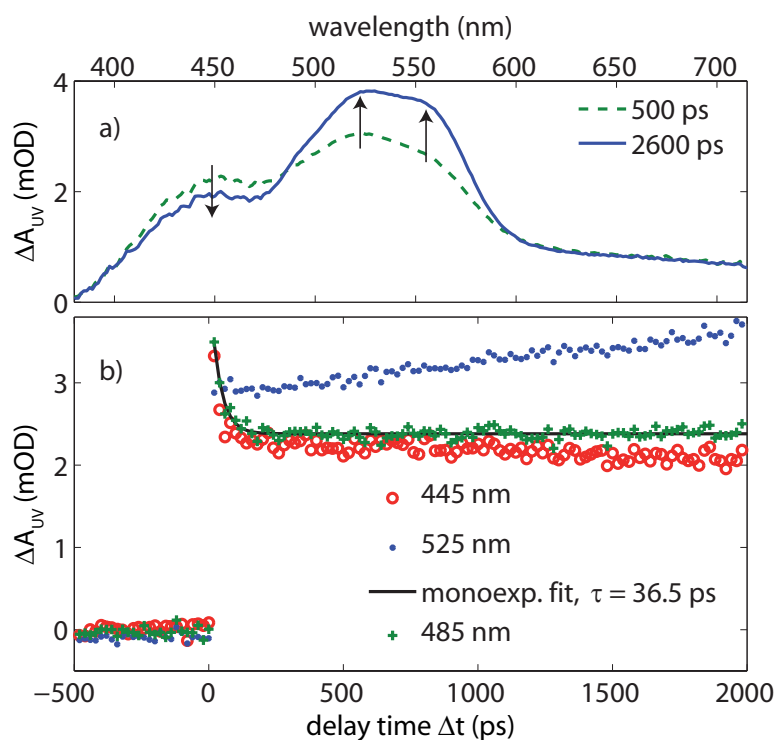


Figure 4.22: a: Difference spectra of the ring opening at 500 and 2600 ps after excitation of the spiropyran form with 267 nm pulses. The development of the shoulders at 445, 525 and 560 nm is indicated by the black arrows. Further an isosbestic point is identified at 485 nm. b: Transients at two (445 nm, red hollow circles and 525 nm, blue dots) of the three shoulders of the absorption band of Figure 4.21 and at the isosbestic point (green crosses) and a monoexponential fit ($\tau = 36$ ps, black) to the transient at the isosbestic point.

experiments thereby excluding contributions of two-photon processes. A contribution of the thermal ring closure and ring opening is neglected in this approximation since those reactions proceed on a time scale of minutes. Therefore the extinction coefficients at 267 nm of both forms and the quantum efficiencies for ring opening and ring closure determine the equilibrium. The quantum efficiencies for ring closure of the merocyanine excited to the S_1 (Φ_{RC560}) and S_2 (Φ_{RC400}) [103] states seem to be very similar (40%), which was also one assumption in the modeling of the transient-absorption data of the open form in Section 4.3.3. Hence a similar quantum efficiency for 267 nm excitation ($\Phi_{RC267} = \Phi_{RC560} = 40\%$) is assumed. In this case one can roughly calculate the quantum efficiency for ring opening after complete relaxation (Φ_{RO267}) with

$$\frac{[\text{Me}]}{[\text{Sp}]} = \frac{\Phi_{RO267} \epsilon_{Sp267}}{\Phi_{RC} \epsilon_{Me267}}, \quad (4.19)$$

where $\frac{[\text{Me}]}{[\text{Sp}]}$ is the ratio of equilibrium concentrations. The extinction coefficients $\epsilon_{Me267} = 14000 \text{ dm}^3\text{mol}^{-1}\text{cm}^{-1}$ and $\epsilon_{Sp267} = 32900 \text{ dm}^3\text{mol}^{-1}\text{cm}^{-1}$ can be determined from Figure 4.1, and the quantum efficiency for ring closure Φ_{RC} is known from the previous section.

The photostationary equilibrium while irradiating with 267 nm fs laser pulses lies at approximately 50% of the initial merocyanine concentration, and therefore the quantum efficiency for ring opening is $\Phi_{RO267} \approx 9\%$.

4.5 Bidirectional switching

In this section not only either ring opening or ring closure is investigated but both reactions are combined into one experiment. The experiment starts at the open or closed state, switches to the respective other state, and directly afterwards (< 100 ps) switches back to the original state. For such an experiment the two pump pulses from Sections 4.3.1 (VIS pump) and 4.4.1 (UV pump) are combined into a pump–repump–probe experiment, with repump denoting the second pump pulse (VIS or UV). A special data acquisition allows the setup to be only sensitive to the molecules interacting with both pump pulses (pump and repump) as will be shown in the next subsection. The experimental results are presented in the subsequent subsection. From the results the quantum efficiencies and reaction times for ring opening and ring closure can be extracted to give the photochemical scheme in the last subsection.

4.5.1 Experimental methods

For the bidirectional switching experiments, the solution was converted to the spiropyran form with green LEDs as in Section 4.4.1. Pump and repump pulses were polarized orthogonal to each other. In order to isolate the dynamics induced by the pump–repump combination from the single-pump dynamics, two optical choppers with 90° phase difference were employed to block two consecutive pulses and let the next two pass. Since this was done for both pump pulses, this procedure gives rise to four pump–pulse combinations and corresponding transmitted probe light intensities:

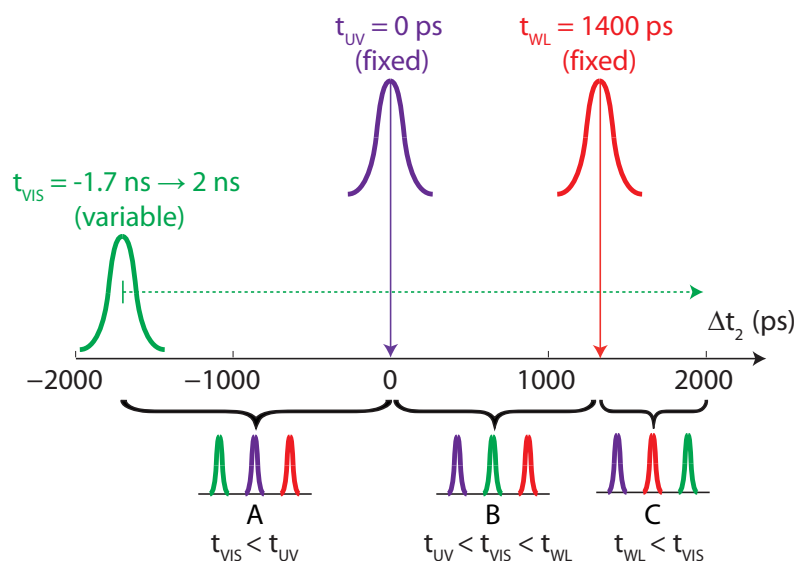


Figure 4.23: Scheme of the pump–repump–probe experiments. Whereas the UV pump (purple) and the visible probe beam (red) remain at fixed positions (t_{UV} and t_{WL} , respectively), the delay of the visible pump (green) (t_{VIS}) is varied as indicated by the dashed green arrow. This results in the three different delay regions with different pulse sequences (A, B, C) shown at the bottom.

1. VIS pump (I_{VIS}),
2. VIS pump and UV pump (I_{UV+VIS}),
3. UV pump (I_{UV}),
4. no pump ($I_{no\ pump}$).

Here the transmitted probe intensities for a certain pump–probe combination is denoted with I and the respective subscript. From this three transient-absorption signals are obtained (absorption changes ΔA):

1. $\Delta A_{VIS} = -\lg \frac{I_{VIS}}{I_{no\ pump}}$,
2. $\Delta A_{UV} = -\lg \frac{I_{UV}}{I_{no\ pump}}$,
3. $\Delta A_{UV+VIS} = -\lg \frac{I_{UV+VIS}}{I_{no\ pump}}$.

Recording all three combinations of transient-absorption signals, the cooperative absorption signal due to interactions with both pump pulses (ΔA_{2p}) is obtained via

$$\Delta A_{2p} = \Delta A_{UV+VIS} - \Delta A_{UV} - \Delta A_{VIS}. \quad (4.20)$$

Figure 4.23 illustrates the scanning scheme used in the pump–repump–probe experiments. The green pulse in this scheme represents the visible pump pulse (VIS) that induces ring closure of present merocyanine. The purple pulse represents the ultraviolet

pump pulse (UV) that mostly induces ring opening of spiropyran since almost no merocyanine is present due to the constant illumination with the LED array. The red pulse represents the white-light probe pulse (WL). UV and WL are both fixed in time and were set to 0 ps and 1400 ps, respectively, on the time delay axis Δt_2 .

For investigating both switching directions the VIS pulse is scanned from before the UV pulse to after the WL pulse ($\Delta t_2 = -1.7 \text{ ns} \rightarrow \Delta t_2 = +2 \text{ ns}$). Thus the VIS pulse coincides with the UV pulse at $\Delta t_2 = 0 \text{ ps}$ and with the white-light pulse at $\Delta t_2 = 1400 \text{ ps}$. This gives rise to three delay regions A, B and C with the different pulse sequences given at the bottom of Figure 4.23.

4.5.2 Experimental data

In Figure 4.24 the transient cooperative absorption signal $\Delta A_{2p}(560 \text{ nm})$ as defined in Eq. 4.20 averaged over the wavelengths from 550 to 570 nm with respect to the delay time axis Δt_2 in Figure 4.23 is shown. The stronger noise compared to the two-pulse experiments from e.g. Figures 4.4, 4.7 or 4.21 is due to the fact that the cooperative three-pulse signal is two orders of magnitude lower ($\approx 0.4 \text{ mOD}$ compared to $\approx 20 \text{ mOD}$). Nevertheless, the measurement technique described in the previous subsection allows recovery of this transient with excellent sensitivity.

Zero signal in Figure 4.24 corresponds to a situation where the combination of both pump pulses yields the same result as the sum of the signals of the two individual pump–probe experiments (see Eq. 4.20). A positive value means that due to the combination of the two pump pulses a higher absorption is present at the time of the WL pulse. In the relaxed system (excluding reaction intermediates and thereby the dynamics seen in the bottom of Figure 4.24) such a positive value can only result from a higher spiropyran concentration at the time of the second pump pulse (which then induces more ring opening than in the individual experiment). Vice versa, a negative value can be explained by a spiropyran concentration decrease, e.g. a merocyanine concentration increase, at the time of the second pump pulse (which then induces more ring closure than in the individual experiment). Therefore for an intuitive interpretation of Figure 4.24 one can say that the transient absorption corresponds to the change of the spiropyran concentration due to the first pulse at the time of the second pulse.

In region A, a small but nevertheless clearly positive absorption is visible, corresponding to a positive spiropyran concentration change. In this region of the time delay, the VIS pulse comes before the UV pulse. Since the used LED array does not completely close all merocyanine, the VIS pulse closes some of the small portion that is still present in the solution and thereby increases the spiropyran concentration by $\approx 1/50$ ($\Delta A_{UV} \approx 5 \text{ mOD}$, $\Delta A_{2p} \approx 0.1 \text{ mOD}$). The dynamics of the absorption change at 560 nm due to this ring closure are the same as those recorded in the two-pulse experiment (ΔA_{VIS} , see Figure 4.4). Therefore these dynamics are cancelled in the cooperative signal ΔA_{2p} . However, the following UV pulse acts on an increased spiropyran concentration ($\approx 1/50$ higher), resulting in a slightly higher merocyanine production than recorded by ΔA_{UV} and a small positive offset remains when probing the effects of both pump and repump pulses.

Changing the pulse sequence to the delay region B (UV pulse before VIS pulse) the

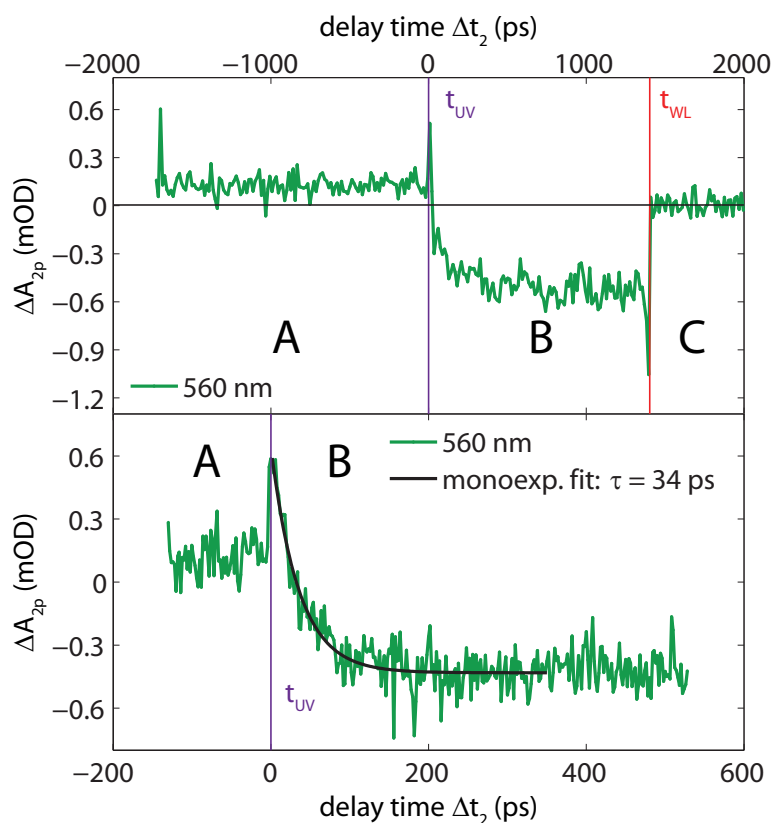


Figure 4.24: Cooperative transient-absorption signal (ΔA_{2p}) at 560 nm (averaged from 550 to 570 nm) due to the combination of the two pump pulses. The transient absorption can be divided into the three regions associated with the different pulse orderings explained in Figure 4.23 (A: closure-reopening, B: opening-reclosure, C: no pump–repump signal). Top: Signal from -1.7 ns to 2 ns. The positions of the UV pulse and the WL probe pulse are indicated by purple and red vertical lines, respectively. Bottom: Measurement with higher temporal resolution for the transition from region A to region B. Here, the signal dynamics at the beginning of region B are emphasized. The black line corresponds to a monoexponential fit that results in a time constant of 34 ps.

UV pulse mostly excites the spiropyran, since on the one hand the equilibrium is almost completely shifted to this form and on the other hand at 267 nm the extinction coefficient of the spiropyran is 2.5 times higher than that of the merocyanine. Again, the absorption change due to this process is not visible in ΔA_{2p} since it is the same as in ΔA_{UV} . However, the following VIS pulse acts on a higher merocyanine concentration and therefore bleaches more of the merocyanine compared to ΔA_{VIS} . This explains the negative absorption change in delay region B of Figure 4.24.

When the VIS pump reaches the sample after the probe pulse (delay region C), the signal ΔA_{2p} is equal to zero and only exhibits some noise, because the absorption change ΔA_{UV+VIS} is the same as ΔA_{UV} , whereas ΔA_{VIS} is zero.

Therefore the signal in Figure 4.24 is due to ultrafast bidirectional switching.

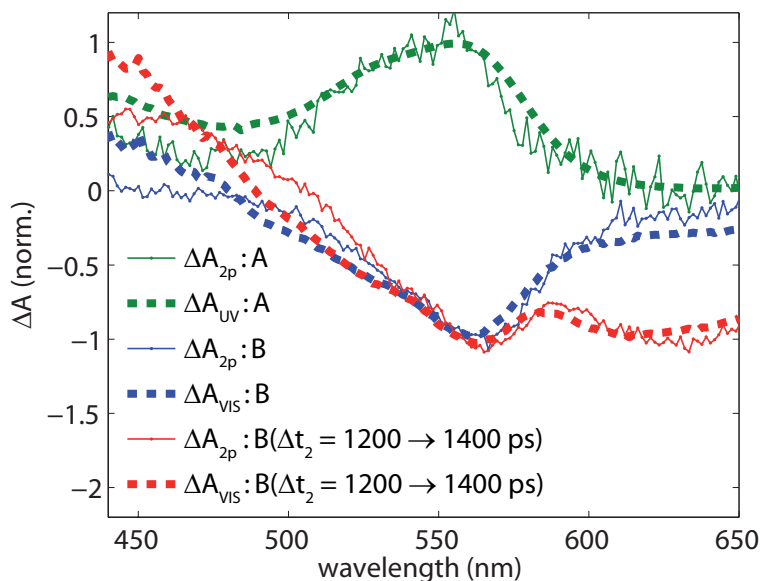


Figure 4.25: Comparison of the absorption change due to the pump–repump combination (ΔA_{2p} , solid lines) to the absorption changes due to the single-pump experiments (ΔA_{UV} and ΔA_{VIS} , dashed lines). The data are scaled for better comparison. To decrease the noise the difference spectra were averaged over 20 delay positions. The signals ΔA_{2p} and ΔA_{UV} , averaged over the first nanosecond of region A, are shown in green. Spectra ΔA_{2p} and ΔA_{VIS} of region B are averaged from 400 ps to 900 ps and shown in blue. The red curves represent the signals ΔA_{2p} and ΔA_{VIS} at later times of region B (delay times from 1200 ps to 1400 ps).

4.5.3 Spectral shape

Additional measurements for the spectral shapes of the absorption changes in the delay regions A and B are shown in Figure 4.25 to provide further proof for bidirectional switching. One has to consider that different isomers/conformers with different spectral shapes account for small deviations in the following comparisons, because the conformeric distribution after excitation is most certainly different from that in thermal equilibrium.

The thin green line represents the difference spectrum ΔA_{2p} of region A (averaged from -1700 to -700 ps). The dashed green line represents the difference spectrum recorded with the UV pump only (ΔA_{UV}). Following the arguments given above, the two transient spectra should be very similar, because the UV pulse acts on a slightly increased concentration of the spiropyran. This is indeed reflected by the comparison of the two green lines in Figure 4.25.

The blue curves in Figure 4.25 are taken from the delay region B (averaged from 400 to 900 ps). In region B the spectral shape of ΔA_{2p} (solid) is similar to the shape of ΔA_{VIS} (dashed). This confirms the previous assignment of the underlying processes.

The red curves were also taken from delay region B, however at greater delay times such that the VIS pump is close in time to the white-light probe (averaged from 1200 to 1400 ps). The general features that can be identified in the cooperative three-pulse signal ΔA_{2p} (red solid line in Figure 4.25) correspond to the dynamics in the transient map

for the two-pulse ring closure of merocyanine (Figure 4.4), and thus also the difference spectrum (red dashed line in Figure 4.25) agrees. These dynamics are excited-state absorption (400 – 500 nm), ground-state bleach (550 – 600 nm) and stimulated emission (600 – 650 nm).

4.5.4 Speed

The experiment with higher temporal resolution of the transition from region A to region B shown in the bottom of Figure 4.24 allows the determination of the speed of merocyanine as well as spiropyran formation.

Ring opening: $A \rightarrow B$.

Beginning with the ring-opening reaction, i.e. merocyanine formation, the dynamics of merocyanine formation can be read off from the transition from region A to region B. Initially (at $\Delta t_2 = 0$ in Figure 4.24), a sharp peak can be detected in the three-pulse transient. Within approximately the first 100 ps after this sharp peak a decrease from positive to negative absorbance is recorded. Whereas in delay region A the first pulse (VIS) decreases merocyanine concentration, in delay region B the first pulse (UV) increases merocyanine concentration. Therefore the negative slope of the absorption change is expected. The decrease towards negative absorption change does not start at $\Delta A_{2p} = 0$ for $\Delta t_2 = 0$ because reaction intermediates or hot spiropyran are formed after excitation of the spiropyran. For comparison see Figure 4.21 during the first 100 ps from 420 nm to 570 nm and Figure 4.22 b. These intermediates absorb the VIS pulse without being able to re-close afterwards. This corresponds to an effective reduction of VIS pump power that only applies to ΔA_{UV+VIS} and not to ΔA_{VIS} . Since ΔA_{VIS} at 560 nm is negative, the subtraction of ΔA_{VIS} from ΔA_{UV+VIS} leads to a positive ΔA_{2p} . The transient signal from Figure 4.24 also cannot be explained by a dominating remaining merocyanine triplet state. Such a merocyanine triplet state would have similar effects to the ones observed for times slightly greater than zero in Figure 4.24. Hence, the signal in delay region B would always be positive.

For the following interpretation it is assumed that the transient-absorption band from 420 nm to 570 nm during the first 100 ps mentioned above in Figure 4.21 is not due to hot spiropyran molecules but reaction intermediates. This assumption is supported by the fact that the absorption band is not continuous from the visible spectral range to the spiropyran absorption in the ultraviolet spectral range but rather subsides at 420 nm. The subsiding of these reaction intermediates and the population increase of the merocyanine ground state have the same time constant. Thus, the dynamics after $\Delta t_2 = 0$ are interpreted as the dynamics of formation of merocyanine in the ground state. A monoexponential fit, shown as black line in the bottom panel of Figure 4.24 starting at the temporal overlap of the two pulses results in a time constant of 34 ps for the merocyanine ground-state formation. These dynamics are in agreement with the time constant of 36 ps at 485 nm that was determined in Figure 4.22. Changing the polarization angle between the two pump pulses from 0° to 90° did not lead to a change in the observed time constant.

Ring closure: $B \rightarrow A$.

An upper boundary for the ring-closure, i.e. spiropyran formation, reaction time can be extracted from the transition from region B to A. In Figure 4.24 the signal is nearly constant (≈ 0.1 mOD) up to $\Delta t_2 = -6$ ps. When the pump pulses cross (crossing at $\Delta t_2 = 0$ from left to right in Figure 4.24), the absorption changes abruptly. Spiropyran formation is therefore very fast considering the large conformational change. This very fast reaction, whose signal is also obscured by vibrational cooling, does not allow an identification of putative intermediate merocyanine conformers. Nevertheless the high speed of the ring closure is in good agreement with the mid-infrared transient-absorption experiments (Figure 4.6) which disclosed that ring closure is faster than the bleach recovery.

4.5.5 Discussion: Ring closure

It is known that the investigated merocyanine does not aggregate except in aliphatic solvents due to the steric bulkiness of the 3,3'-dimethylmethylene unit of the electron-donating indoline heterocycle [117, 134]. Therefore the possibility that dimer aggregates could be responsible for any observed signal is excluded.

Bleach

To prove that indeed photochemical ring closure is responsible for the bleach in Section 4.3 the following discussion focusses on the MIR probe data (Figure 4.6) to support the identification of the product. Experiments on the structurally related, unsubstituted and 6-nitro substituted spiropyran compounds were published by Fidler et al. [99, 102, 104]. By probing the ring-opening reaction with MIR pulses they found that the two spiropyran absorption bands which do not overlap with merocyanine absorption bands are centered at 1340 cm^{-1} and 1610 cm^{-1} . These frequencies are very close to the vibrational modes assigned to the nitro group in 6-position. For the present molecule, 6,8-dinitro BIPS in chloroform, an isolated band at 1610 cm^{-1} is not seen in the ring-closure experiments. Instead a strong ground-state bleach is observed at this spectral position. This is also confirmed by the FTIR data. A spiropyran absorption at 1344 cm^{-1} , on the other hand, is present in 6,8-dinitro BIPS and can be traced back to the same vibrational mode as the absorption at 1340 cm^{-1} in 6-nitro BIPS (see the steady-state experiments and calculations in the literature [118, 135]). Although the absorption change at 1344 cm^{-1} after 2 ns due to the product formation is very small (Figure 4.6, green transient), it is nevertheless clearly positive. The direct conclusion from this positive absorption is that spiropyran is formed on an ultrafast time scale after photoexcitation of the merocyanine form of 6,8-dinitro BIPS.

Speed

Considering the large conformational changes inherent to the ring-closure reaction from the open form (see Figure 4.1) the upper boundary for the speed of 6 ps seems very fast.

However, CASSCF simulations have shown that a pure singlet reaction pathway via two conical intersections exists for the ring closure [121].

In view of this ring-closure mechanism, TTC needs to proceed via one isomerization step to reach the conical intersection leading to the spiropyran on the TCC potential surface [121, 122], whereas TTT needs two isomerization steps to reach TCC (which is in line with the slightly lower ring closure quantum efficiency of TTT compared to TTC found in our studies). If ring closure of TTT would start with isomerization to TTC, one would expect a much higher isomerization quantum efficiency, since $\approx 30\%$ of the excited TTT would have to follow this pathway. Therefore the initial step towards ring closure seems to be isomerization around the middle double bond (TXT), to TCT and TCC. This barrier seems to be lower than the TTC-TTT barrier, because the isomerization quantum efficiency is lower than the ring-closure quantum efficiency. Different energy barriers along torsional coordinates have been shown to exist in cyanines as well as in merocyanines [129]. Whereas the third double bond (TTX) according to theoretical analysis has a lower activation barrier than the second double bond (TXT) in free polymethine chains [129], the influence of the partial locking due to the chromene unit in 6,8-dinitro BIPS might impede torsional motion around the third double bond in the excited state [136].

Since no transient signal that could be attributed to the first isomerization step of TTT to TCT is observed in the transient-absorption experiments, it seems likely that no conical intersection to the TCT ground state exists. This first isomerization step towards TCX therefore might proceed in the excited state without a conical intersection, similar to the cis/trans isomerization from TTT to TTC and vice versa (Section 4.3.9). From the TCC geometry the conical intersection can already be accessible, because the TCC is equally far distanced from the cycle as CCC (although possessing different energy [122]), in both cases an angle of 90° is missing along the torsional degree of freedom of the first double bond. Hence although the conformational change seems to be very large for TTC, on the hyper potential surface only one barrier is located with certainty on the reaction pathway (for TTT two barriers). Having passed this barrier the gradient can always be negative towards the conical intersection leading to such high quantum efficiencies as determined for the TTC and TTT form of $\approx 40\%$.

4.5.6 Discussion: Ring opening

For a better understanding of the dynamics after UV excitation of ring-closed 6,8-dinitro BIPS a brief review of the known processes for the most investigated similar spiropyrans, 6-nitro BIPS and unsubstituted BIPS is given. For 6-nitro BIPS it was found that the triplet reaction plays a crucial role and rivals a possible singlet route [137]. It has been proposed that following S_1 excitation of the closed form a rather complex succession of reaction intermediates takes place on the μs and ms time scale [137]. At 435 nm a slowly subsiding transient absorption has been found and at 580 nm a slowly increasing absorption has been found. These findings have been assigned to the intersystem crossing of the merocyanine triplet state to the merocyanine ground state. It has been found that 500 fs after excitation of the spiropyran in tetrachlorethene the triplet of a vibrationally hot merocyanine isomer is formed [105]. This hot triplet relaxes with a time

constant of 17 ps to the vibrational triplet ground state. The cooling process follows an isomerization to a second isomer in the triplet state. However, electron diffraction investigations [138] of the ring opening of 6-nitro BIPS have found that after UV excitation 30% relax to the S_0 ground state of spiropyran, 39% relax to the triplet ground state of spiropyran and all molecules that undergo ring opening, the remaining 31%, end up in the singlet state of the CTC isomer of merocyanine. In contrast to 6-nitro BIPS no triplet contribution at all was found after photoexcitation of the unsubstituted BIPS. According to transient-mid-infrared-absorption experiments the ring-opening reaction of the unsubstituted BIPS occurs on a time scale of 28 ps [99]. In the gas phase it has been shown that after excitation with 267 nm (in the chromene subunit) a cascade of three reactions for unsubstituted and nitro-substituted BIPS occurs [69]. C-O bond breaking with 40 fs is followed by isomerization to a cis-configured merocyanine around the central methine bond with 250 fs. The last reaction step with a time constant of 12 ps was attributed to the cis-trans isomerization of the central methine bond. The authors did not find any evidence for the two reaction mechanisms (one triplet, one singlet) suggested by TD-DFT calculations [122]. They assumed a singlet process for all molecules based on the observed relaxation times.

These summarized findings from the literature are compared in the following to the findings on 6,8-dinitro BIPS. Analogous to the literature a decreasing absorption at 450 nm is seen and an increasing absorption centered at 550 nm (Figures 4.21 and 4.22). However, during the first nanosecond the band changes much faster than the triplet pathway that was observed in 6-nitro BIPS [112]. The broad, constant background above 600 nm observed in Figure 4.21 might suggest the possibility of a triplet or solvated electron contribution [125, 139], yet in a spectral region and on a time scale which has no impact on the interpretation of the ring-opening and ring-closing dynamics. Hence, the observed sub-nanosecond dynamics in 6,8-dinitro BIPS do not involve triplet states. A possible explanation for the observed dynamics in Figures 4.22 and 4.24 is the existence of isomers/conformers that differ in their absorption spectrum from the completely relaxed ground state. Rotation/isomerization around the double bonds in the methine bridge would be hindered by the partial double bond character and the solvent, explaining the observed increase of the lifetime of the conformers from the 12 ps observed in the gas phase to the 34 ps in this work. Stimulated emission or excited-state absorption is not detected in Figures 4.21 and 4.22, an indication that these processes happen in the electronic ground state.

A fraction of the ring-opened product molecules can be closed back to spiropyran. This conclusion is supported by the observation that both the dynamics and the spectral shape of the bleach (Figures 4.24 and 4.25) are very similar to the bleach that results from simple excitation of the open merocyanine form. Therefore, there is a significant subensemble which does not react along a triplet route. The second nitro group has a strong effect on the relative ground-state energies of the merocyanine and spiropyran forms. In contrast to 6-dinitro BIPS, 6,8-dinitro BIPS is negatively photochromic [14]. Therefore the electronic states of 6,8-dinitro BIPS cannot be directly compared to those of 6-nitro BIPS and one cannot assume that intersystem crossing in the molecule studied here is as efficient as in 6-nitro BIPS. The time constant of 34 ps for the ring opening is furthermore in good agreement with the ring-opening speed of the unsubstituted BIPS

(28 ps [105]) for which it is known that ring opening does not proceed along a triplet pathway.

In conclusion, the fast, broad absorption observed in Figures 4.21 and 4.22 is ascribed mostly to the ground state of transient ring-open forms that are very hot and cannot be assigned to a certain isomer. Afterwards only the most stable isomers are formed and therefore the spectrum converges towards the steady-state absorption spectrum of merocyanine. During this process the absorption between 440 and 490 nm decreases whereas the absorption between 490 and 600 nm increases (Figure 4.22).

4.6 Photochemistry of 6,8-dinitro BIPS

The knowledge obtained about the possible pathways of the spiropyran–merocyanine molecular switch 6,8-dinitro BIPS is summarized in this section. Two pathways have been investigated, the electrocyclic reaction (consisting of ring closure and ring opening) and the cis/trans isomerization of the open form.

Transient-absorption experiments revealed the presence of two ring-open merocyanine isomers in solution. The isomeric separation is directly elucidated by color variations of the visible femtosecond pump pulses that rendered isolated excitation of the red-shifted isomer possible. Whereas excitation pulses centered at 550 nm resulted in a permanent bleach around 560 nm [TTC isomer, $\tau(S_1) = 98$ ps], excitation pulses centered at 625 nm were mainly responsible for merocyanine bleaching around 600 nm [TTT isomer, $\tau(S_1) = 900$ ps]. Disentanglement of the involved processes (ring closure and cis/trans isomerization), in order to extract the quantum efficiencies of both isomers and isomerization pathways, was achieved with color variations of the visible femtosecond pump pulse and a global modeling approach.

4.6.1 Insights into the electrocyclic reaction

The molecular switch (6,8-dinitro BIPS) can be switched photochemically in both directions on a picosecond time scale as shown by femtosecond pump–repump–probe experiments.

Ring opening

After ring opening of spiropyran with 267 nm femtosecond laser pulses [SP(S_0) \rightarrow MC-cis(S_0^*)] transient-absorption experiments probing in the visible spectral range revealed a mixture of isomers. The at least partial relaxation with 34 ps to the merocyanine ground state MC-TTC(S_0) (purple dashed arrows in Figure 4.26) was shown by three-color pump–repump–probe experiments. The transient-absorption experiments show that pathways to other merocyanine isomers exist. The resulting isomers of these pathways are denoted as “MC-X” since they cannot be identified any further. The overall quantum efficiency for ring opening obtained via the photostationary equilibrium is approximately 9%.

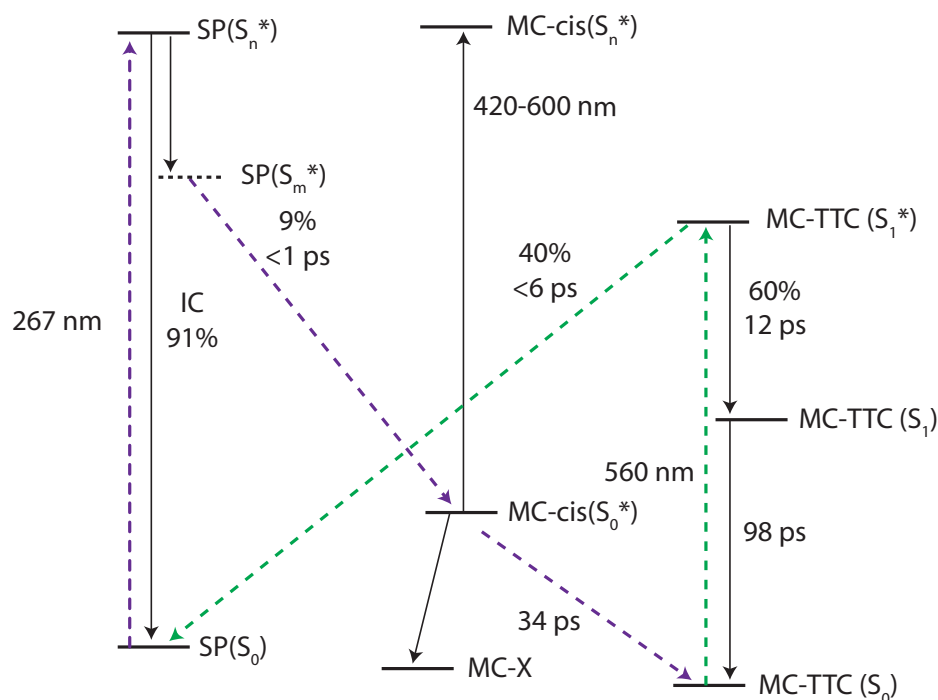


Figure 4.26: Investigated photoprocesses of 6,8-dinitro BIPS. The ring-opening pathway is depicted by the purple dashed arrows. The ring-closure pathway is depicted by the green dashed arrows. * represents a vibrationally excited state. “MC-cis” represents the reaction intermediates mentioned in the interpretation of the ultrafast-switching section, “MC-X” represents unknown isomers and pathways that MC-cis relaxes to as indicated by the UV-pump-only experiments. These isomers are converted thermally on a much longer time scale towards the MC-TTC isomer.

Ring closure

From the three-color pump–repump–probe experiments it was shown that ring closure of the generated merocyanine ground-state species MC-TTC(S_0) can be induced with 560 nm laser pulses (dashed green arrows in Figure 4.26). Transient-absorption in the visible and mid-infrared spectral range provide proof for identification of the ring-closed product. Furthermore these experiments show that the quantum efficiency for the ring-closure reaction is 40% for the major isomer (TTC) and 35% for the minor isomer (TTT). The ring closure to the spiropyran ground state completes the photocycle as shown by the dashed lines in Figure 4.26. The high speed of the ring-closure reaction (≤ 6 ps) suggests that the reaction starts from the vibrationally excited MC-TTC(S_1^*) state, because vibrational cooling to the MC-TTC(S_1) takes up to 12 ps (Figures 4.5 and 4.6).

These results demonstrate that 6,8-dinitro BIPS is a bidirectional molecular switch that can be switched back and forth on a picosecond time scale. In the cases of 6π -electrocyclic molecular switches from other families (Tab. 4.1) the open form is always present as a mixture of two isomers, of which one of the two isomers is not capable of ring closure. However, in 6,8-dinitro BIPS both isomers are capable of ring closure with

high quantum efficiency.

Whereas common molecular switches have a high quantum yield for one of the two switching directions, the other direction is often much less efficient (Tab. 4.1). For the investigated system the quantum efficiency is high for both directions. Thus the molecule possesses a high potential for a multitude of applications.

4.6.2 Insights into the cis/trans isomerization

The fate of the excited merocyanine molecules that do not proceed along the ring-closure pathway is either the return to the merocyanine ground state with a time constant of 98 ps via internal conversion/fluorescence or cis/trans isomerization to the respective other isomer.

Three temporal models were applied in the global modeling. The first one did not allow isomerization at all, the second model included isomerization via a conical intersection, and the third model described isomerization completely in the excited state. While the first model proved to be too inaccurate, the latter two models resulted in very similar quantum efficiencies of all involved reaction channels, showing that isomerization plays a role. Furthermore the model without the conical intersection seems to describe the isomerization pathway more correctly than the model involving a conical intersection. Isomerization between TTT and TTC is a minor pathway ($\Phi_{IC} = 1 - 2\%$ starting from TTC and $\Phi_{IT} = 1 - 2\%$ starting from TTT). The low quantum efficiency for the side-reaction cis/trans isomerization and vice versa the high selectivity to the ring closure pathway of the ring-open form makes 6,8-dinitro BIPS a very attractive molecular switch.

5 A sigmatropic rearrangement: The Wolff rearrangement of DMA

5.1 Introduction

In Chapter 4 an electrocyclic reaction has been investigated on the femtosecond time scale. Whereas in the electrocyclic reaction bonds are formed and broken between two reaction centers (Figure 2.24) in sigmatropic rearrangements a group of atoms migrates from one reaction center to the other (see Section 2.5.5 and Figure 2.26). As an example for such a sigmatropic rearrangement the photochemistry of DMA will be presented in this chapter. The photochemistry is also especially interesting since it offers multiple photochemical pathways, hence, it may be a good model system for a coherent control experiment in the future. The main reaction channel of DMA after photoexcitation is the Wolff rearrangement, which is widely used in photolithography for electronic microchip production and many other industrial chemistry procedures. Nevertheless DMA exhibits a much richer photochemistry due to parallel and sequential reaction channels whose understanding is a challenging task for spectroscopy. Ultrafast studies [140–143] have so far only investigated the first product of the cascade of reactions taking place after photoexcitation. However, the final products are especially important in view of the applications for DMA, e.g. high-resolution purposes as photoactive compound in deep ultraviolet (UV) lithography [144, 145] or as dopant for laser ablation in polymer matrices [140, 141, 146–148]. Furthermore, information from the final products also provides insights about the primary intermediates.

In this work, the first nanoseconds of the bimolecular photoreaction dynamics of DMA is unravelled, revealing ultrafast structural dynamics, characteristic time scales and associated emerging chemical species. The focus is thereby on the light-induced bimolecular reaction in alcohol solution, where a reaction with a solvent molecule can occur both for the ketene and the carbene species accessible after UV excitation. These bimolecular reactions also provide a contribution to the question whether and under which condition both ketene and carbene are formed for a specific compound, since subsequent reaction paths to distinct photoproducts are present which can be identified by their absorption characteristics. To reliably identify the reaction products, the transient spectra are complemented by density functional theory (DFT) calculations on the normal modes and Fourier-transform infrared (FTIR) spectroscopy of both the reactant and the products in the chemical equilibrium, thus permitting a coherent picture of the ultrafast photochemistry of DMA.

5.2 Experimental and theoretical methods

UV pump pulses Pulses in the ultraviolet spectral region (at 266 nm) were generated via SHG of the fundamental 800 nm pulses and subsequent SFG of the generated 400 nm pulses with the fundamental pulses, leading to pulse energies up to 12 μJ . The spot diameter at the place of the sample was adjusted to 350 μm .

MIR probe pulses Tunable mid-infrared probe pulses were generated by parametric processes. A homebuilt two-stage optical parametric amplifier (OPA) similar to the design in [149] is pumped by the Ti:Sa fundamental pulses (300 μJ). The OPA generates tunable signal and idler pulses. Subsequent DFG in a 1 mm thick AgGaS₂ crystal yields mid-infrared pulses with a spectral width of about 160 cm^{-1} . For the experiments in this work they were tuned between 1550 and 2250 cm^{-1} . The probe pulses were focussed into the sample to a spot diameter of 260 μm and the energy at the sample position was 350 nJ. The polarizations of pump and probe beams were set to the magic-angle configuration of 54.7° (see Section 3.1.4).

Sample The DMA sample was purchased from TCI Europe (CAS: 7270-63-5) as 5-Diazo-2,2-dimethyl-1,3-dioxane-4,6-dione. In all experiments it was used without further purification or other treatment and dissolved in spectroscopic-grade methanol, ethanol, or isopropanol. Using a peristaltic pump the sample circulated through a BaF₂ flow cell with an optical path length of 100 μm at a sufficiently high flow rate so that the sample volume is completely exchanged between successive laser shots. Due to the small extinction coefficient in the mid-infrared, high sample concentrations of 47 mmol/l were employed leading to an optical density of about 1.5 at 266 nm.

Detection After passing through the sample, the mid-infrared probe pulses were sent to a spectrograph (Chromex 250 is/sm spectrograph/monochromator), where they are dispersed by a 150 l/mm grating. They were detected by a 32-element mercury cadmium telluride photoconductive detector array (Infrared Associates, Inc.) with a spectral resolution of 10.2 nm (equivalent to about 3 – 5 cm^{-1} /pixel, depending on the probe wavelength regime). The whole experimental setup is permanently purged with dry air to minimize absorption due to air humidity. A temporal resolution of 350 fs could be achieved, as determined by observing the mid-infrared absorption rise in a thin germanium window following photoexcitation by the 266 nm pump pulse.

Steady-state spectra Steady-state infrared spectra were recorded by a Fourier transform infrared (JASCO FT/IR-4100) spectrometer with a resolution of 1 cm^{-1} . Contributions of the solvent were taken into account by measuring the solvent spectrum separately and by subtracting it from the sample spectrum. Irradiation was carried out either with a Nd:YAG laser for 350 nm excitation or with a medium-pressure UV lamp (spectrum shown in Figure 5.1) for 255 nm excitation.

DFT calculations DFT calculations of DMA in vacuum were performed using the software package GAUSSIAN 03 [150]. In our calculations the density functional Becke

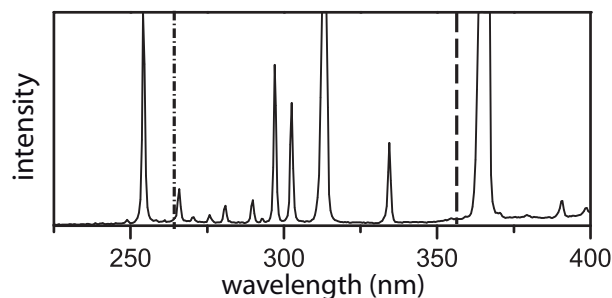


Figure 5.1: Spectrum of the UV-lamp with which the DMA was excited predominantly at 255 nm (see also Figure 5.2).

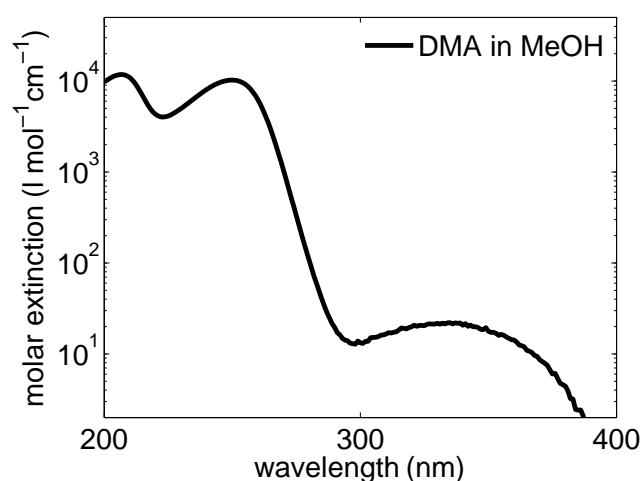


Figure 5.2: Steady-state absorption of DMA in methanol. Note the logarithmic scaling of the extinction coefficient. A strong absorption is centered at 250 nm leading to excitation into S_2 or higher. The weak S_1 excitation has its maximum absorption coefficient at 345 nm. However, this transition is weaker than the transition at 250 nm by a factor of 1000.

three-parameter hybrid method [151, 152] in combination with the Lee-Yang-Parr correlation functional (B3LYP) [153] was used. Both the molecular geometry optimization and the calculations for the normal modes and their amplitudes were carried out using the 6-311+G** basis set.

5.3 Reaction channels identification by steady-state absorption

The steady-state absorption of DMA in methanol is shown in Figure 5.2. It consists of a strong absorption at 250 nm, that corresponds to an excitation into a state higher than S_1 [154]. Furthermore a weak absorption with maximum absorption at 345 nm can be identified, which belongs to the $S_0 \rightarrow S_1$ excitation [154].

After photoexcitation a multitude of reaction pathways is accessible for DMA [140, 141, 143, 154, 155], as depicted in Figure 5.3. The initially populated electronic state is decisive for whether a Wolff rearrangement [156, 157] to the ketene (S_2 -excitation), isomerization to the diazirine [158] (S_1 -excitation) or intersystem crossing to the triplet carbene (S_1 -excitation, followed by an intersystem crossing) takes place. From these primary intermediates subsequent reactions with the solvent can take place, leading from the ketene, to the enolester and at last to the ester as product, or for the triplet carbene to a reduction to meldric acid. All these reaction steps follow first-order kinetics, or in the case of reactions with the solvent, pseudo-first-order kinetics. Hence their speed can be described by one time constant in all cases, as shown in Figure 5.3.

The dependence of the photochemistry on the excitation wavelength is confirmed by the FTIR spectra of the samples being different after irradiation with a medium-pressure UV lamp (corresponding to 255 nm excitation) and irradiation with a Nd:YAG laser (corresponding to 350 nm excitation), see Figure 5.4 top and bottom, respectively. The steady-state absorption in the mid-infrared region of DMA (top: black solid line, bottom: black dashed line) consists of combined stretching modes of the C=O groups at 1719, 1735 and 1753 cm^{-1} and the stretching vibration of the C=N=N group at 2169 cm^{-1} . Whereas for both excitation wavelengths these bands are bleached (except for the band at 1753 cm^{-1}), new bands appear at 1766 and 1808 cm^{-1} for 255 nm excitation and at 1768 and 1796 cm^{-1} for 350 nm excitation. Hence the obtained photoproducts depend strongly on the excitation wavelength.

In the next subsection the vibrational modes of the products are calculated with quantum mechanical methods to substantiate these findings. Those results also provide further information for the identification in the transient-absorption data in the section thereafter.

5.4 DFT results for the permanent products

The DFT calculations (see Figure 5.5) were able to reproduce the experiment with good agreement (see also the Method Section 5.2). However, all results tend to be slightly higher in wavenumbers than found in the FTIR data [159]. Starting with the reactant DMA (first molecule in Figure 5.5), the triple splitting of the C=O absorption could unfortunately not be reproduced. However, the stretching modes for the C=O and C=N=N group could also be found with approximately the correct relative intensity ($\epsilon_{\text{C=O}} \approx 2\epsilon_{\text{C=N=N}}$, see the experimental data in Figure 5.4).

The permanent products also observed in the FTIR data from Figure 5.4 are on the one hand the ester and on the other hand the diazirine. In case of the ester the calculated wavenumbers for the two C=O bands with almost equal intensity agree very well with the experiment (theory: second molecule in Figure 5.5; experiment: Figure 5.4 top). For the diazirine (third molecule in Figure 5.5) a blue shifted absorption band corresponding to the N=N group is found that agrees very well with the experiment regarding the spectral position (theory: 1824 cm^{-1} ; experiment: 1796 cm^{-1} , Figure 5.4 bottom) and the relative intensity ($\frac{1}{3}$ of the adjacent C=O vibration, Figure 5.4 bottom).

Following the reaction scheme in Figure 5.3 also Meldrum's acid should be observed

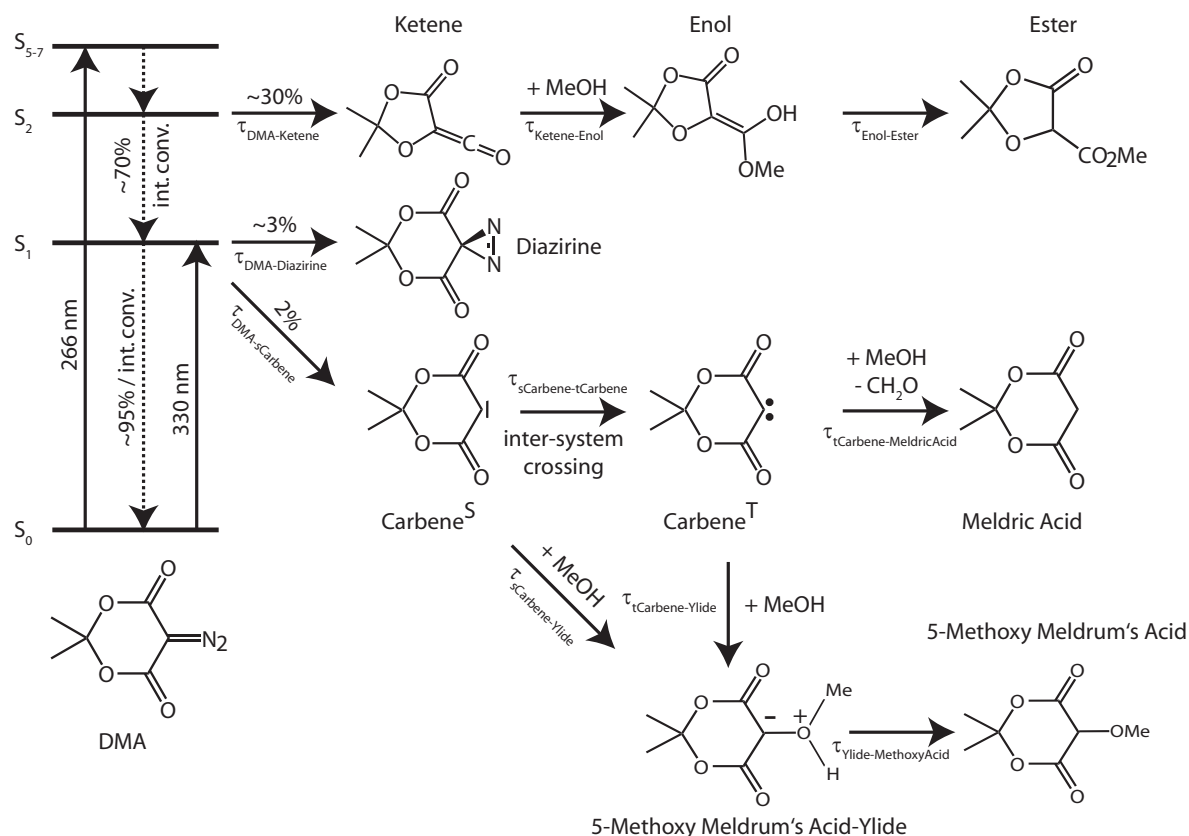


Figure 5.3: Reported photochemical pathways of DMA. After excitation into a state higher than S_2 internal conversion to the S_2 state takes place. Starting from this state 30% of the molecules undergo N_2 cleavage and rearrangement to the ketene, also called “Wolff rearrangement”. When using an alcohol as solvent, a solvent molecule can add to the ketene to form the enol and subsequently (tautomerization) the ester. The fate of the remaining 30% of the excited population is internal conversion to the S_1 state. From there, additionally to internal conversion to the ground state (95%) two reaction pathways with very low quantum efficiencies are accessible. Either a reaction towards the diazirine is possible ($\approx 3\%$) or the formation of a carbene is possible ($\approx 2\%$). It is not clear whether the pathways following the carbene formation contribute at all to the photochemistry of DMA. They are postulated due to theoretical calculations and observations in similar molecules, and depicted here only as pathways that might also be possible. The carbene might undergo intersystem crossing to the triplet carbene or addition of a solvent molecule (methanol). These reaction pathways would lead to either the Meldric acid or the 5-Methoxy Meldrum’s acid.

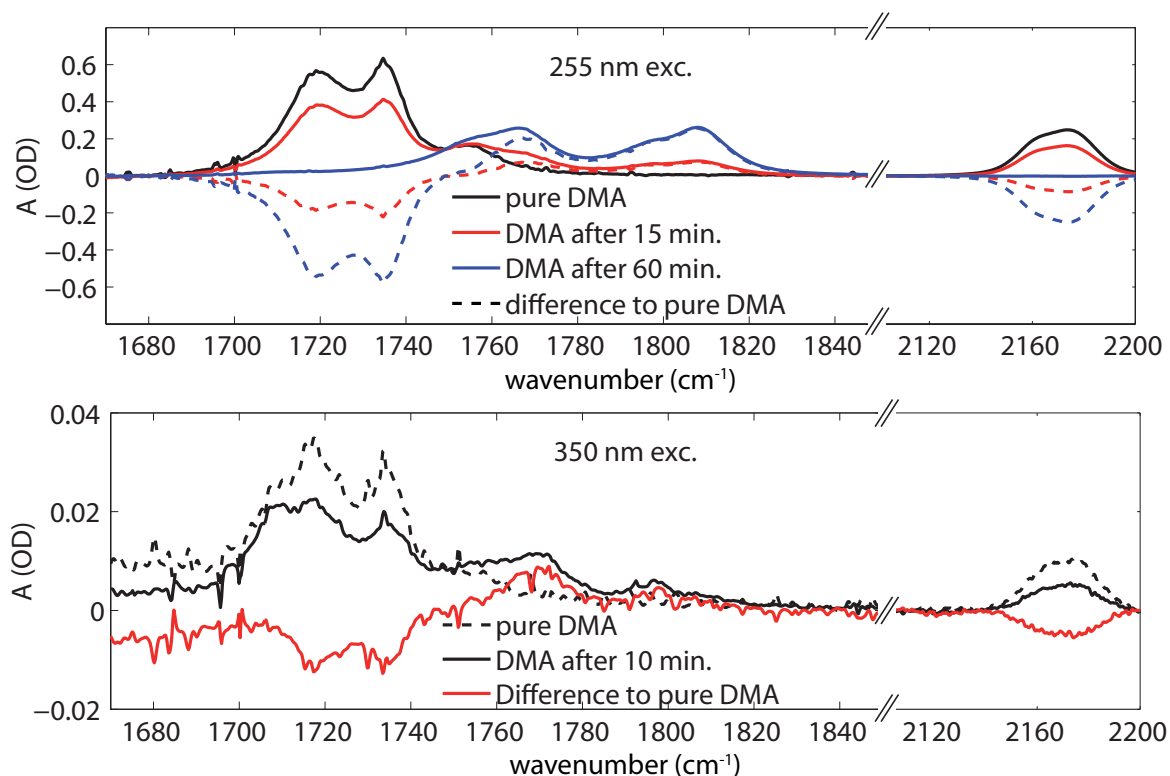


Figure 5.4: FTIR spectra of DMA dissolved in methanol after excitation with mainly 255 nm light (top) from a medium-pressure UV lamp (see lamp spectrum in Figure 5.1) and after excitation with 350 nm nanosecond pulses from a Nd:YAG laser (bottom). In both cases excitation of DMA leads to decrease of the absorption bands of the C=O groups of DMA (1719 and 1735 cm^{-1}) and the C=N=N vibration of DMA (2169 cm^{-1}). However, the product bands differ in both cases. Whereas the bands appearing after 255 nm excitation are centered at 1766 and 1808 cm^{-1} , in case of 350 nm excitation they are centered at 1768 and 1796 cm^{-1} .

in the FTIR data. However, its spectral signature (the asymmetric stretching vibration of the C=O group being red-shifted) cannot be found in the FTIR data in Figure 5.4. Hence, this reaction channel is not observed under the experimental conditions used here (255 and 350 nm excitation).

Concluding from the last two sections the strong modes at 2172 cm^{-1} for the C=N=N group and the strong absorptions of the C=O groups in the spectral region from 1700 to 1800 cm^{-1} will be used as marker modes for the reactant and products in the transient-absorption experiments in the next subsection.

5.5 Transient absorption in the mid-infrared

The photochemistry of DMA in methanol upon photoexcitation with 266 nm femtosecond laser pulses spans at least three distinguishable reaction channels some of which are of bimolecular kind (see Fig. 5.3). In order to investigate as much as possible of every

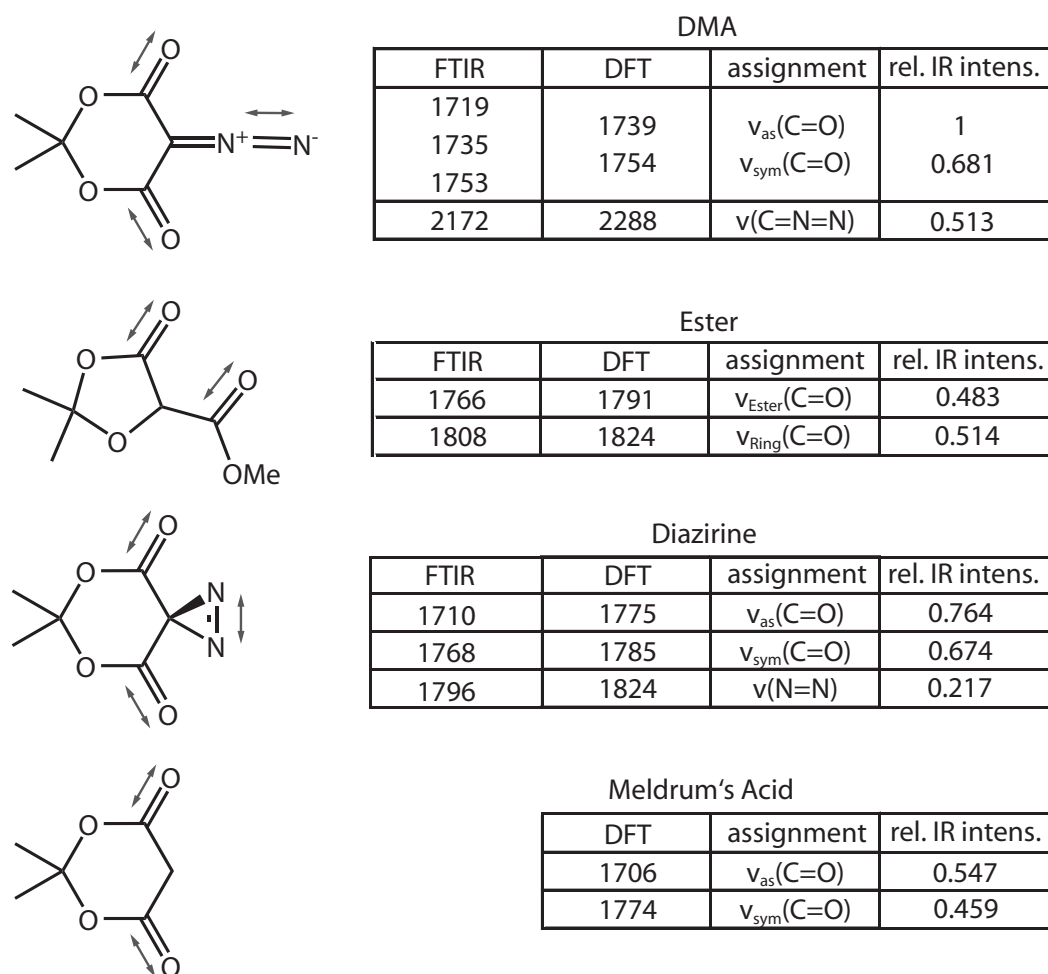


Figure 5.5: Comparison of experimental and calculated vibrational frequencies and relative intensities of the respective marker modes. Note that contrary to usual comparisons of DFT results and experimental results a correction by a factor smaller than 1 of the calculated frequencies, which are usually too high, has not been done. Meldrum's acid was not observed in Figure 5.4, hence no experimental values can be given.

occurring reaction dynamics, femtosecond vibrational spectroscopy was applied in the spectral regions from 1550 to 1900 cm^{-1} and from 2000 to 2250 cm^{-1} , whereas only data is shown that actually illustrates any kind of transient-absorption signal $\Delta A \neq 0$.

5.5.1 Experimental data

Figure 5.6 gives an overview of the whole set of spectrally and time-resolved transient-absorption signals of DMA dissolved in methanol. For the spectral region of the C=O group (1600 to 1800 cm^{-1} , top) the time delay Δt was scanned up to $\Delta t = 3400$ ps, whereas the spectral region of 2100 to 2200 cm^{-1} was only scanned up to 350 ps, since the products do not have absorption bands in that spectral region, as shown in Figure 5.4.

In the next subsections a step-by-step analysis of the reaction paths shown in Fig-

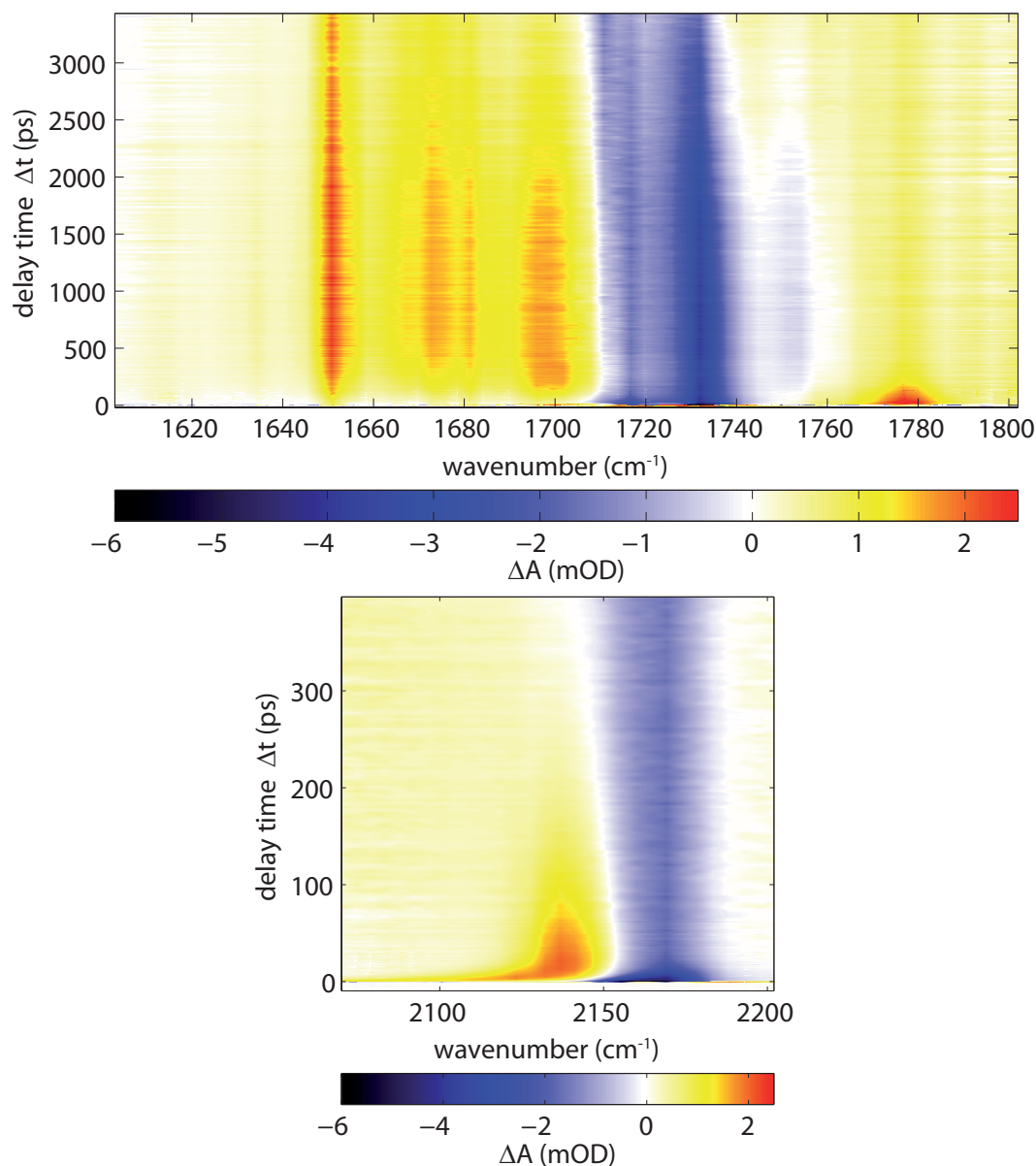


Figure 5.6: Transient absorption in the mid-infrared of DMA in methanol after excitation with 266 nm femtosecond laser pulses. In the top panel the region of the C=O marker modes (see Figure 5.4) is shown. In this region the enol as well as the ester can be observed whose dynamics take place on a longer time scale. The spectral region around the C=N=N bond ($\approx 2140 \text{ cm}^{-1}$, bottom) allows for a clearer observation of the faster dynamics (ketene formation and decay) than in the spectral region of the C=O absorption, since no spectral overlapping processes take place in that spectral region.

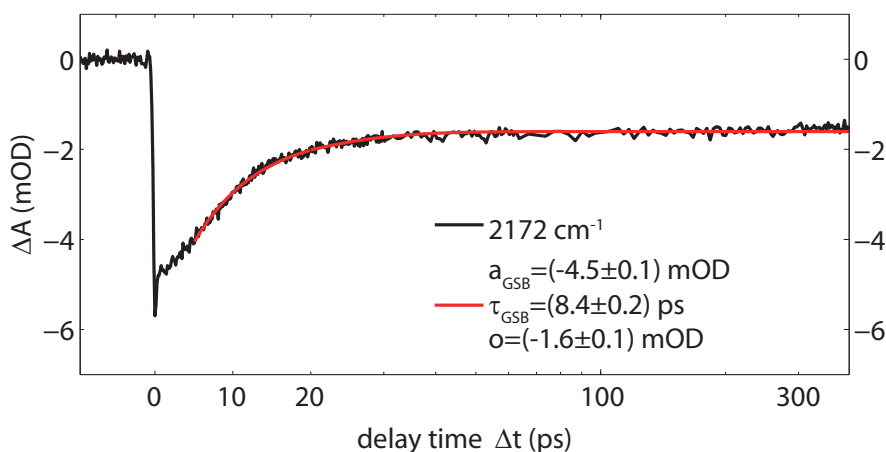


Figure 5.7: Bleach of the ground-state absorption of DMA. Initially the bleach is approximately -5.8 mOD and increases afterwards to the final bleach of approximately -1.8 mOD. However, the increase with $\tau_{GSB} = (8.4 \pm 0.2)$ ps between these two values is not due to the return to the electronic ground-state of excited DMA, but due to the repopulation of the vibrational ground-state of DMA.

ure 5.3 is given to extract the photochemical and photophysical parameters.

5.5.2 DMA bleaching

Initially after excitation the reactant is bleached (Figure 5.7), since the vibrational modes in the excited state either are spectrally shifted or possess changed oscillator strengths [160]. Afterwards a partial recovery of this bleach is observed. However, this increase of the absorption change from -4 to -2 mOD is not due to the process of DMA molecules that return to the ground state. Although this process takes place, it does almost not contribute to the dynamics shown in Figure 5.7, because the lifetime of the S_1 state is < 1 ps. Hence, these dynamics cannot be resolved. Instead the dynamics correspond to vibrational cooling (Section 2.4.4), since the hot DMA molecules that have returned to the ground state first need to dissipate their vibrational excess energy either to other internal vibrational modes or the solvent. This process is responsible for the tail of positive transient absorption at early times in Figure 5.6 (bottom). The vibrational cooling will be investigated in more detail in Section 5.5.8.

The ground-state bleach (Tab. 3.1) can be observed in both probed spectral regions of Figure 5.6 (around 1730 cm^{-1} and around 2170 cm^{-1}). However, only in the spectral region around 2170 cm^{-1} this process is not overlaid by other processes (Figure 5.7).

A monoexponential fit to the transient at 2172 cm^{-1} results in a time constant of $\tau_{GSB} = (8.4 \pm 0.2)$ ps for the arrival of excited DMA molecules back in the vibrational ground state of the C=N=N group. The summed quantum efficiency over all reaction channels (Figure 5.3) is then given by the initial bleach ($I_I \approx -5.8$ mOD) and the final bleach ($I_f \approx -1.8$ mOD) to $\frac{I_f}{I_I} = 31\%$. Hence approximately 30% of the excited molecules undergo one of the photoreactions shown in Figure 5.3.

5.5.3 Intermediate ketene

Directly adjacent to the ground-state bleach at 2170 cm^{-1} a strong additional absorption at 2140 cm^{-1} can be observed in Figure 5.6 (bottom). In agreement with the literature this band can be identified as the intermediate ketene [161, 162]. Furthermore this assignment is substantiated by DFT calculations that predict a strong absorption of the C=C=O group at 2239 cm^{-1} (Figure 5.8, right). The ketene intermediate can also be observed via its C=O vibration at 1777 cm^{-1} (Figure 5.8). Strong vibrational cooling (Section 2.4.4) effects (Figure 5.6, bottom) are visible at 2140 cm^{-1} . These can on the one hand be caused by hot ketene molecules since the rearrangement to the ketene results in excess energy in the ketene vibrational modes as it is the reaction center. On the other hand these effects can originate from hot DMA molecules that have returned to the ground state [162], since adjacent to the ketene C=C=O absorption lies the ground-state absorption of the DMA C=N=N group (Figure 5.4).

The transition induced with 266 nm occurs into a π^* orbital of the N=N group [163], hence excess energy is available after excitation in the C=N=N vibrational mode when returning to the ground state of DMA (see previous section and Section 5.5.8). These effects impede a direct kinetic analysis to obtain the ketene formation time. However, a biexponential fit to the transient at 2135 cm^{-1} results in a time constant for the initial absorption increase of $\tau_{\text{vibr.cool.}} = (1.85 \pm 0.07)\text{ ps}$, which is mostly due to vibrational cooling, and a decay of the ketene intermediate with a time constant of $\tau_{\text{Ketene-Enol}} = (125.6 \pm 3.9)\text{ ps}$ (Figure 5.8). In contrast to the transient at 2135 cm^{-1} , the transient at 1777 cm^{-1} (Figure 5.8 bottom) corresponds to the carbonyl group that does not react in the Wolff rearrangement (Figure 5.3). Hence the excess energy is not in the vibrational modes associated with this group and therefore only weak vibrational cooling effects are visible in Figure 5.6 (top). The ketene formation time obtained in a biexponential fit results in $\tau_{\text{DMA-Ketene}} = (6.0 \pm 0.3)\text{ ps}$ and in agreement with the transient at 2135 cm^{-1} a decay of the ketene intermediate with $\tau_{\text{Ketene-Enol}} = (130.7 \pm 5.0)\text{ ps}$. As will be shown in the next section the ketene continues to react to the enolester.

In view of the slower ketene formation at 1777 cm^{-1} one can safely assume that the faster initial absorption increase at 2135 cm^{-1} compared to 1777 cm^{-1} is due to hot DMA molecules in the ground state in which higher states of the C=N=N vibrational mode are populated.

5.5.4 Enol

In alcoholic solvents such as methanol that is used in these experiments, the dominating pathway of a ketene is the nucleophilic addition of a solvent molecule to the electrophilic center of the ketene, the middle carbon atom of the C=C=O group. As shown in Figure 5.3 this results in the formation of an enolester. To substantiate this assumption the solvent-dependent transient for the ketene decay in methanol, observed at the C=O group absorption around 1777 cm^{-1} ($\tau_{\text{Ketene-Enol}} = (130.7 \pm 3.86)\text{ ps}$), is shown in Figure 5.9 (top). In addition to Figure 5.8 this figure contains also a transient at 1693 cm^{-1} , where an absorption rise with the same time constant ($\tau_{\text{Ketene-Enol}} = (130.7 \pm 5.0)\text{ ps}$) can be detected at 1690 cm^{-1} . Following the DFT calculations for the enolester

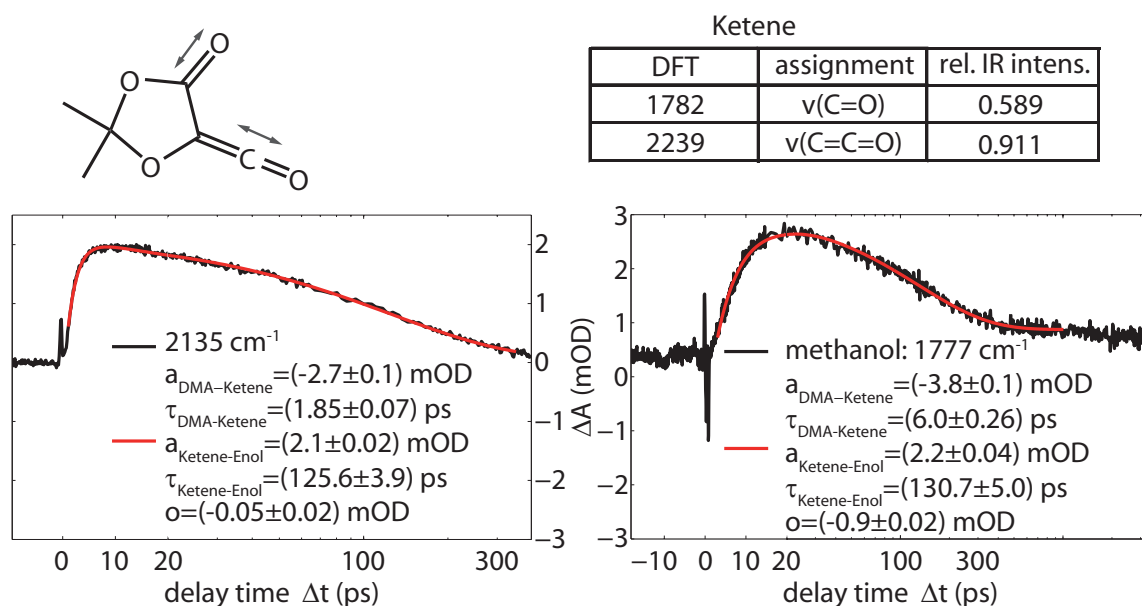


Figure 5.8: Top: DFT predictions of the C=O and C=C=O absorption bands in the ketene. Bottom: Transient-absorption dynamics at the C=C=O absorption (left) and C=O absorption (right) of ketene. The ketene has a formation time $\tau_{DMA-Ketene}$ as well as a decay time $\tau_{Ketene-Enol}$, since it is an intermediate in the Wolff rearrangement. The much shorter formation time at 2135 cm^{-1} is due to the vibrational cooling of hot DMA molecules, see previous section and Section 5.5.8.

(Figure 5.10) this additional absorption is due to the C=C bond.

The time constant $\tau_{Ketene-Enol}$ for the enol absorption rise is fitted simultaneously to the ketene absorption decay for each solvent in Figure 5.9, only the amplitude and the offset (see Tab. 3.1) are fitted individually for each transient.

By going from methanol, over ethanol to isopropanol the steric hindrance is increased drastically. If the absorption rise in Figure 5.9 were caused by the addition of the solvent to the ketene (enol formation, Figure 5.3), a higher substitution of the alcohol group of the solvent would slow this rise down due to the additional steric hindrance (Eq. 2.87) while not changing the spectral position too much [43].

Indeed the time constant for the ketene decay as well as the enol formation time increases with increasing substitution of the solvent alcohol group (see Figure 5.9). Whereas in methanol the reaction takes (130 ± 3.9) ps, it already increases by a factor of ≈ 1.6 to (224.8 ± 33.5) ps when going from the primary alcohol methanol to the primary alcohol ethanol, whose carbon chain has twice the length of methanol. In contrast to that the isopropanol is a secondary alcohol, leading to more than doubling of the time constant of ethanol to (586 ± 83.1) ps. Therefore one can conclude that the bands rising and decaying with these time constants belong to the tertiary reaction step of the DMA photoreaction, the addition of the solvent to the ketene.

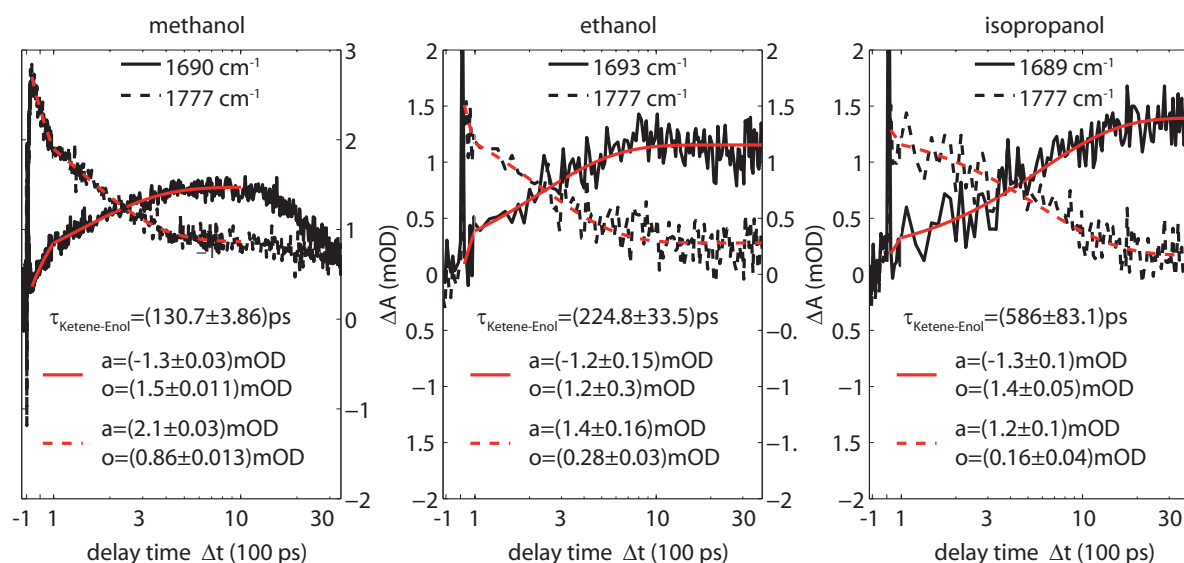
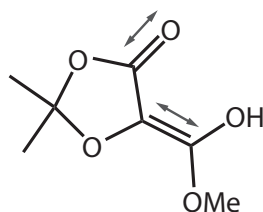


Figure 5.9: Solvent-dependent ketene decay as well as absorption increase at $\approx 1690 \text{ cm}^{-1}$. With increasing substitution of the alcoholic solvent (methanol (left) < ethanol (middle) < isopropanol (right)) the lifetime of the ketene increases and the absorption rise at 1690 cm^{-1} increases. It follows that both processes are connected and that the solvent substitution has an impact on the time constant. This substantiates the identification of the absorption rise as the enol formation. Furthermore in methanol (left) the enol decreases again on a longer time scale, whereas it is stable for the higher substituted solvents. This process may reflect the tautomerization of the enol to the ester (Section 5.5.5).



Enol		
DFT	assignment	rel. IR intens.
1704	v(C=C)	0.971
1777	v(C=O)	0.429

Figure 5.10: DFT predictions of the absorption bands in the enol.

5.5.5 Ester

The last step in the Wolff rearrangement is the tautomerization from the enolester to the ester. This process is a proton-transfer reaction and can be seen in the transient-absorption dynamics shown in Figures 5.6 and 5.9. For larger delays, it appears that the enolester contributions (around 1695 cm^{-1} in Figure 5.6 top and Figure 5.9) decrease significantly after a delay time $\Delta t > 1500 \text{ ps}$ while at the same time a new absorption appears in the region around 1750 cm^{-1} (Figure 5.6). The DFT data predict a blue-shift of the C=O absorption when going from the enol (Figure 5.10) to the ester (Figure 5.5). Looking at the transients at $\approx 1690 \text{ cm}^{-1}$ (Figure 5.9) when changing the solvent from methanol over ethanol to isopropanol the absorption decrease for delay times greater

than 1.5 ns can only be observed in methanol. Hence this process cannot be traced back to experimental reasons that are connected for example to changing pump beam sizes.

These arguments suggest that the dynamics for delay times $\Delta t > 1.5$ ns are connected to the tautomerization process from the enolester to the ester. However, a time constant for this process cannot be given, since the delay time cannot be greater than 3.4 ns due to experimental reasons.

5.5.6 Diazirine

From the FTIR data (Figure 5.4) and the reaction scheme (Figure 5.3) it was concluded previously that the diazirine is formed only in very low quantities compared to the ester. Furthermore the best chances to observe the diazirine are around 1780 to 1800 cm^{-1} (see Figure 5.4 bottom and the DFT calculations in Figure 5.5). The transient absorption in this spectral region (Figure 5.11 top) shows indeed a very small positive offset after 3 ns, indicating that a permanent product is formed.

However, also the ester absorbs in this spectral region to some degree (see Figure 5.4 top). In order to isolate a possible diazirine contribution a global fit was applied to the transient-absorption data in this spectral region. In this global fit three global time constants are fitted (diazirine formation: $\tau_{DMA-Diazirine} = (1.1 \pm 0.18)$ ps, ketene formation: $\tau_{DMA-Ketene} = (7.0 \pm 0.27)$ ps, enol formation: $\tau_{Ketene-Enol} = (128.0 \pm 4.6)$ ps), whereas the amplitudes of these decays are fitted individually to each transient. The obtained decay-associated spectra are shown in Figure 5.11 (bottom). The ketene formation component (green) is almost exactly the mirror image of the enol formation (red, ketene decay) in the decay-associated spectrum, hence these two time constants are clearly identified. They furthermore confirm again the previous findings (Figures 5.8 and 5.9) for the ketene kinetics.

The third component in Figure 5.11 (bottom), decaying with $\tau_{DMA-Diazirine}$, is spectrally different from the ketene formation and very fast. It cannot be associated with vibrational cooling of either the ketene or the DMA since it is on the one hand blue-shifted from these absorption bands (Figure 5.6). On the other hand the discussed decay-associated spectrum (blue in Figure 5.11) does not change its sign from positive to negative when crossing the responsible absorption (assumed to be the maximum of the ketene absorption, at 1777 cm^{-1}) from the red to the blue. This is necessary in vibrational cooling effects (see for example a_{vc} in Figure 4.5), since the hot molecules have a lower transition frequency (red) and decrease in population (positive amplitude) whereas the underpopulated cold molecules (blue) increase in population (negative amplitude). Instead the decay-associated spectrum is always negative, excluding a vibrational cooling of the ketene absorption band being responsible for this component.

Furthermore this component agrees very well with the absorption change induced by the 350 nm light in the FTIR measurements (Figure 5.4 bottom). In there an additional absorption can be observed that lies just below 1800 cm^{-1} similar to the transient absorption in this spectral region (Figure 5.11). The diazirine is assumed to be formed very fast, since it is a reaction starting in the excited state involving only one step. Hence the obtained time constant of $\tau_{DMA-Diazirine} = (1.1 \pm 0.18)$ ps for this absorption increase matches the diazirine formation very well. Because of this short time

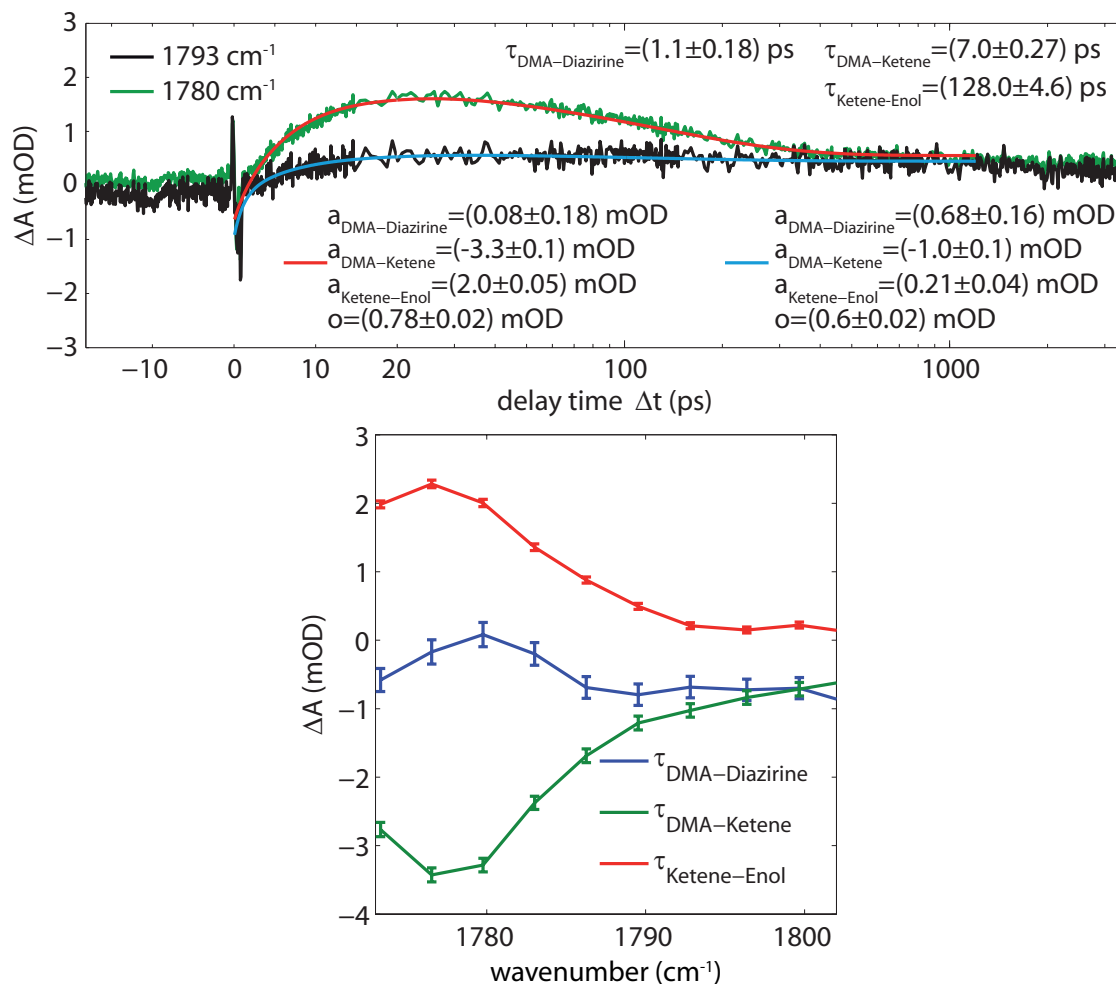


Figure 5.11: Top: Transient-absorption dynamics at 1780 and 1793 cm⁻¹. Whereas the dynamics at 1780 cm⁻¹ are partially overlapped with the ketene (identified by the time constant $\tau_{DMA-Ketene}$), the absorption rise with the time constant $\tau_{DMA-Diazirine}$ at 1793 cm⁻¹ is due to diazirine formation, in agreement with the FTIR spectra in Figure 5.4 (bottom). Bottom: Decay-associated spectra from 1780 to 1800 cm⁻¹. The intermediate ketene is responsible for the green and red curve because they are almost perfect mirror images and because the time constants match the ones found in other spectral regions (see the previous sections). However, the blue component is due to diazirine, since it cannot be vibrational cooling of neither the ketene nor the DMA (see text). Furthermore its spectral shape (considering the low signal-to-noise ratio) is in agreement with the FTIR spectra in Figure 5.4 (bottom), in which also an additional absorption in this spectral region has been found.

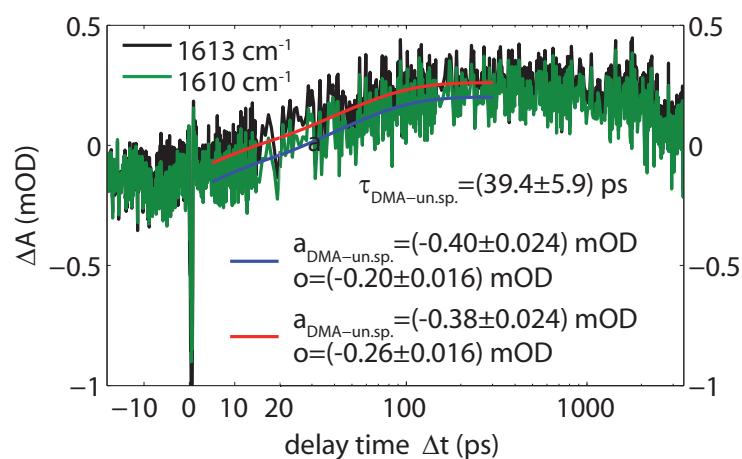


Figure 5.12: Transient-absorption dynamics at 1610 and 1613 cm^{-1} . The absorption rise with time constant $\tau_{DMA-un.sp.}$ does not match any other process identified so far. However, this unknown species seems to be an intermediate since it decreases again for later times. Possible candidates are amongst others the triplet carbene or the Ylide in Figure 5.3.

constant the ester cannot cause this absorption change, it is formed on a much longer time scale.

5.5.7 Unidentified species

A closer look at the spectral region around 1600 cm^{-1} (Figure 5.12) reveals a transient species that is formed with a time constant of $\tau_{DMA-un.sp.} = (39.4 \pm 5.9)$ ps. In the long term this absorption at 1613 cm^{-1} decreases monotonously with a time constant well beyond the maximum observation window in these experiments. The nature of this species cannot be disclosed unambiguously, however following the reaction scheme in Figure 5.3 and the literature [164] the two most promising candidates are discussed below.

Possible intermediate precursors have a decay time of 39.4 ps or maybe even much shorter, with vibrational cooling and conformational changes possibly being responsible for the 39.4 ps rise of the observed species. Because these characteristics do not fit in with any other recorded and analyzed reaction channel (i.e. the Wolff rearrangement with its subsequent photoproducts and the diazirine isomerization previously discussed), it is possibly a signature of a triplet carbene to form Meldrum's acid (Figure 5.3). The very low signal intensity (≈ 0.2 mOD) points at a low quantum efficiency for this reaction channel in agreement with the pathway for the triplet carbene in Figure 5.3.

Another assignment might be the 5-Methoxy Meldrum's acid-ylide [164]. The results from the DFT calculations in Figure 5.13 are in line with both assignments. On the one hand, the calculated vibrational modes (1662 and 1644 cm^{-1}) are closer to 1613 cm^{-1} than any other mode of all the possible reaction intermediates and products, with the deviation actually being not too far if one takes into account the general trend that the vibrational frequencies are overestimated. On the other hand, of both species (triplet

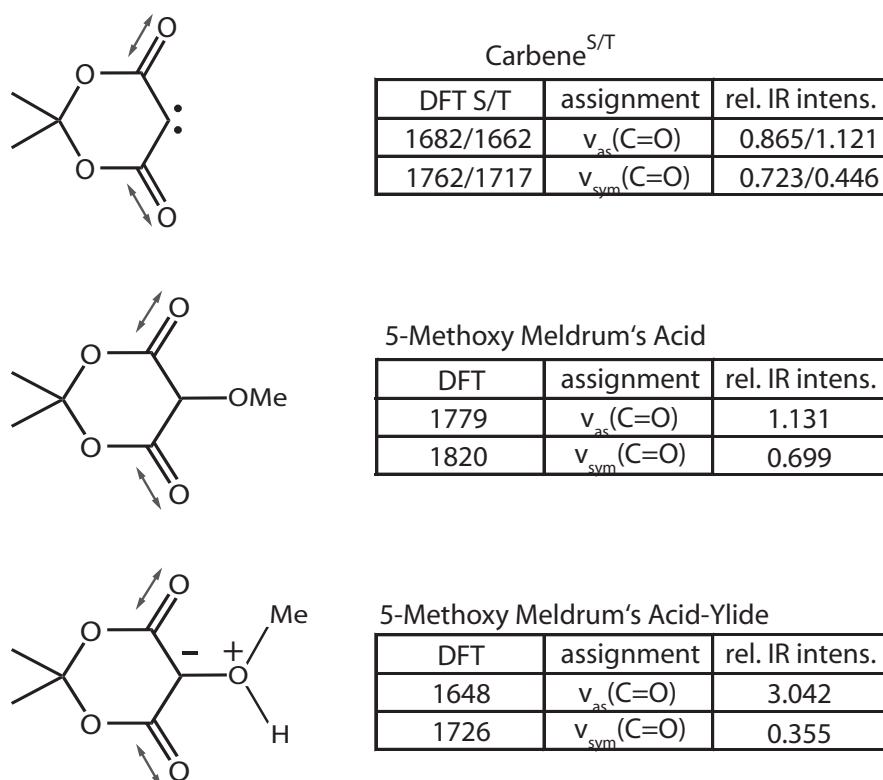


Figure 5.13: Possible candidates for the unknown species responsible for the transient absorption in Figure 5.12. Whereas the reaction scheme (Figure 5.3) suggests that the quantum efficiency for those pathways is too low ($\approx 1 - 2\%$) for observation in the transient data, the spectral position of the absorption band predicted by DFT calculations matches very well. Furthermore the relative intensity of the absorption is very high, so that observation seems not as unlikely as Figure 5.3 indicates.

carbene and 5-Methoxy Meldrum's acid-ylide) only small quantities are expected. But since the corresponding modes have the highest oscillator strength of all modes presented in this chapter (see Figure 5.13 compared to Figure 5.5, Figure 5.8 and Figure 5.10), an observation is not as unlikely as the reaction scheme in Figure 5.3 suggests.

Following this hypothesis, the composition and decomposition of the singlet carbene should be completely carried out within 39.4 ps although there is no direct evidence for it in the transient-absorption data. Other groups describing the temporal evolution of various carbene species under the very crucial impact of different solvents state lifetimes of similar magnitude [164–166]. More precisely, the singlet carbene of methyl styryldiazoacetate dissolved in methanol decays within 38 ps while the triplet state persists on a time scale of some ns [165]. Other investigations with further chemical compounds like p-biphenyl diazo species discovered upper lifetimes of the singlet carbene in the range of 700 ps [143]. However, Burdzinski *et al.* measured the lifetime of singlet carbene to be 2.3 ps (with DMA dissolved in chloroform) [167]. Water dissolved in methanol, which has an absorption band in this spectral region [168], can be excluded as source of the observed signal because no signal is observed if only methanol is used. Considering

these facts an assignment of this transient to the triplet carbene or 5-Methoxy Meldrum's Acid-Ylide is likely but ambiguous without having either detected the previous singlet species or an evidence for the subsequently formed Meldrum's Acid/5-Methoxy Meldrum's Acid. An assignment to the singlet carbene does not seem reasonable due to the slow 39 ps rise time.

The low quantum yield of the discussed transient in combination with the fact that there is neither a hint for a subsequent reaction channel in the transient data nor some indirect evidence in the transients describing the ketene dynamics, make a definite assignment of a molecular process corresponding to this spectral signature impossible.

5.5.8 Vibrational cooling

After excitation a lot of excess energy is available. Therefore the relaxed reactant (DMA) features strong vibrational cooling effects [169] in the transient-absorption data. Especially well resolved is this effect around 2140 cm^{-1} (Figure 5.6 bottom) by the tail decaying with lower wavenumbers. Furthermore this vibrational cooling process is also weakly red-shifted to the C=O group absorption of the reactant (Figure 5.6 top around 1700 cm^{-1}). With a simple model the average arrival and departure time, τ_{arrival} and $\tau_{\text{departure}}$, of the hot molecules in the quantum states can be extracted for those quantum states that do not overlap on the spectrometer pixel to a great extent with the $v = 0$ absorption. The transient-absorption dynamics can in that case be described [99] with

$$\Delta A(\tilde{\nu}, \Delta t) = a_{\text{vibr.cool.}}(\tilde{\nu}) \left(\frac{\tau_{\text{departure}}(\tilde{\nu})}{\tau_{\text{departure}}(\tilde{\nu}) - \tau_{\text{arrival}}(\tilde{\nu})} \right) \left(e^{\frac{-\Delta t}{\tau_{\text{departure}}(\tilde{\nu})}} - e^{\frac{-\Delta t}{\tau_{\text{arrival}}(\tilde{\nu})}} \right). \quad (5.1)$$

The obtained arrival times τ_{arrival} (Figure 5.14) are below 1 ps and very similar in both spectral regions (C=O absorption: $\approx 1700\text{ cm}^{-1}$, left; C=N=N absorption: $\approx 2100\text{ cm}^{-1}$, right). The departure times $\tau_{\text{departure}}$ start in both cases around 2 ps for high vibrational states and increase when approaching the $v = 0$ state. However, these values as well as the vibrational cooling amplitudes $a_{\text{vibr.cool.}}$ differ between the spectral regions, probably due to adjacent absorption bands that interfere with the vibrational cooling dynamics of the departure process. Nevertheless from these information an idea is obtained for the time dependence of the vibrational cooling process of the C=O and the C=N=N group.

5.6 Photochemistry scheme

The presented results allow for the determination of the time constants of most of the reaction pathways as shown in Figure 5.15. After excitation with 266 nm femtosecond laser pulses $\approx 30\%$ react to the ketene (Figure 5.7). The ketene appears in the transient-absorption data with a time constant of $\tau_{\text{DMA-Ketene}} = 6$ to 7 ps (Figure 5.8 or Figure 5.11), dependent on the vibrational mode investigated. However, this value serves only as an upper boundary for the ketene formation, a lower bound cannot be given, since vibrational cooling effects of the reactant are entangled in the early transient-absorption dynamics. The ketene is an intermediate product and decays with a time

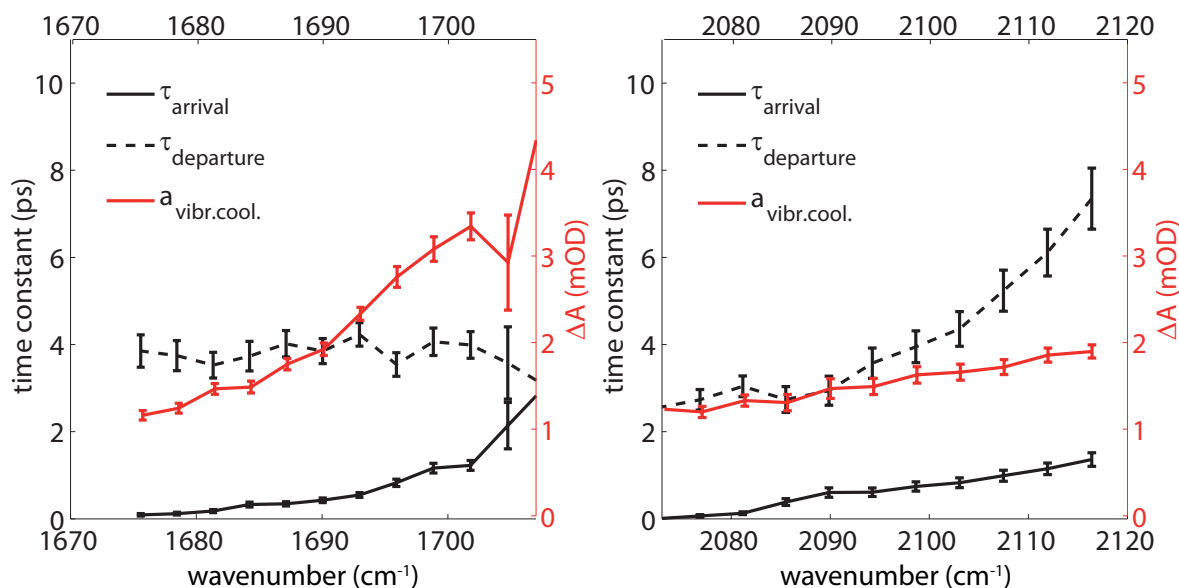


Figure 5.14: Vibrational cooling of the C=O group (left) and the C=N=N group (right) of the DMA molecules that have returned to the electronic ground state. The average arrival τ_{arrival} and departure $\tau_{\text{departure}}$ time of the vibrational states absorbing at the respective spectral position are shown to give an impression of the vibrational cooling dynamics. Note that the results are only reliable in spectral positions far away from the absorption bands of the vibrational ground state. Hence the more blue the spectral position the less reliable is the result [99].

constant of $\tau_{\text{Ketene-Enol}} \approx 130$ ps to form the enolester in methanol upon addition of a solvent molecule (Figure 5.9). However, the speed of this process is solvent dependent. At last the transient-absorption dynamics on the low-nanosecond time scale suggest that the reaction from the enolester to the ester can also be observed (Figure 5.9). The time constant of this reaction step is on the order of a few nanoseconds and cannot be measured with the transient-absorption setup used in these experiments.

After internal conversion from the S_2 state of DMA to the S_1 state a reaction to either the diazirine or the carbene can take place. From the obtained results only the diazirine pathway was confirmed by the DFT (Figure 5.5) and the FTIR results (Figure 5.4). For this pathway a time constant of $\tau_{\text{DMA-Diazirine}} = 1$ ps was obtained for the diazirine formation (Figure 5.11).

At last the transient-absorption data for the pathways involving a carbene intermediate cannot be confirmed unambiguously. Whereas a transient-absorption rise with a time constant of $\tau_{\text{DMA-un.sp.}} = 39$ ps is observed (Figure 5.12), its nature cannot be given due to missing spectroscopic information. However, the identification of this species as the triplet carbene is possible as well as the identification as the 5-Methoxy Meldrum's Acid. A 39 ps time constant seems reasonable for both molecules and furthermore the DFT calculations (Figure 5.13) predict a very strong absorption band in this spectral range. However, the singlet carbene, which would be a precursor for both species needs then to be formed on a much faster time scale ($\tau_{\text{DMA-sCarbene}} < 39$ ps).

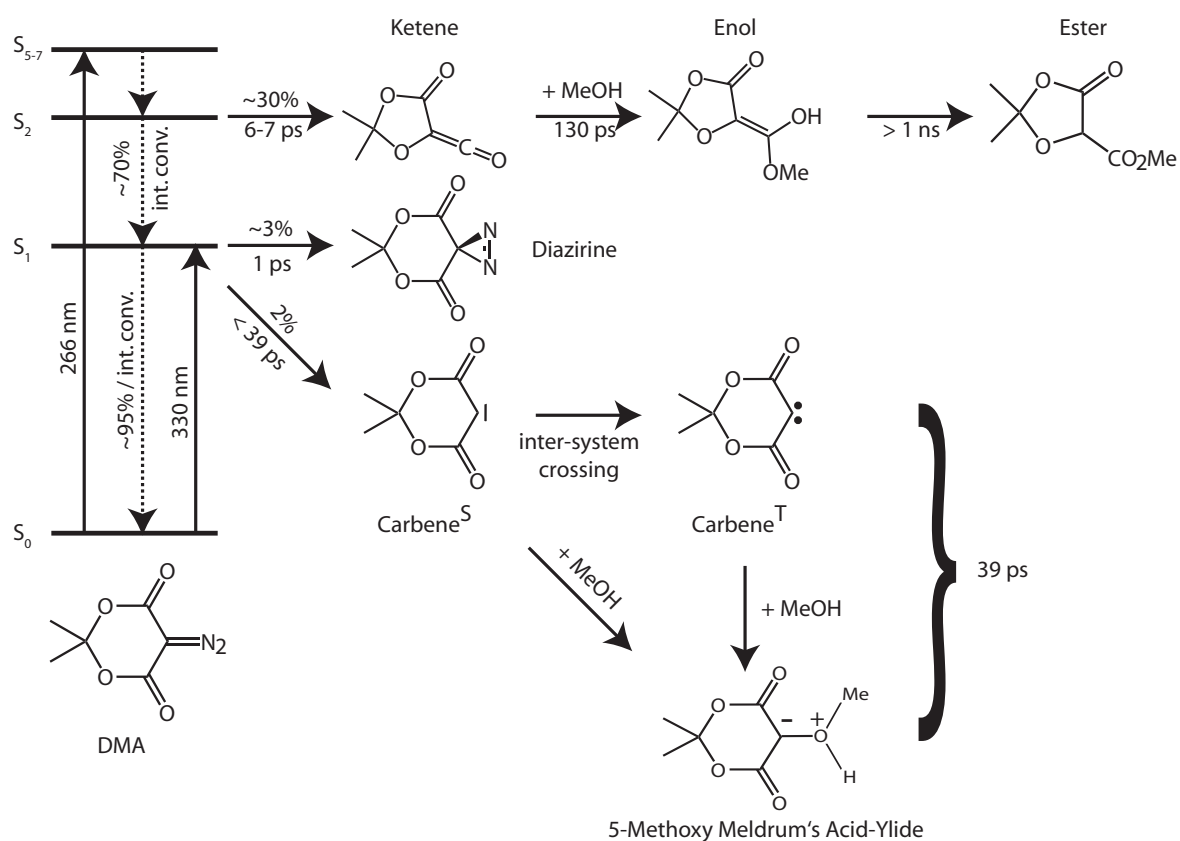


Figure 5.15: Reaction scheme of Figure 5.3 to which the findings of this chapter have been added. The Wolff rearrangement of the excited DMA to the ketene takes no more than 6–7 ps. Addition of the methanol molecule to the ketene needs 130 ps in methanol. The tautomerization step from the enol to the ester seems to occur on a time scale of a few nanoseconds. Diazirine formation from the S_1 state of DMA takes place very fast, on a time scale of 1 ps. The third pathway, the carbene formation, has not unambiguously been identified. However, the most probable interpretation of the transient-absorption data is that the singlet carbene is formed on a time scale fast than 39 ps. Subsequent reactions to the Ylide or the intersystem crossing to the carbene then proceed on a time scale of 39 ps.

5.7 Insights into the sigmatropic rearrangement

The pericyclic reaction in the photochemical pathways of DMA is the rearrangement from the DMA to the ketene. As shown in Section 2.5.5 and in Figure 5.16 (second form) this reaction is symmetry allowed if it takes place in a cationic species.

The carbene form (left), although not detected in the transient-absorption data as an intermediate with a finite lifetime, possesses a p orbital filled with two electrons (red and white orbital) and an empty p orbital. Due to the empty p orbital the carbene can be interpreted as a cationic form. The step-by-step mechanism of the ketene rearrangement is shown in Figure 5.16. The presented transient-absorption experiments of this chapter however, revealed that all these steps (including the not-shown cleavage of the C-N₂ bond preceding the carbene on the left) are so fast, that they cannot be observed within

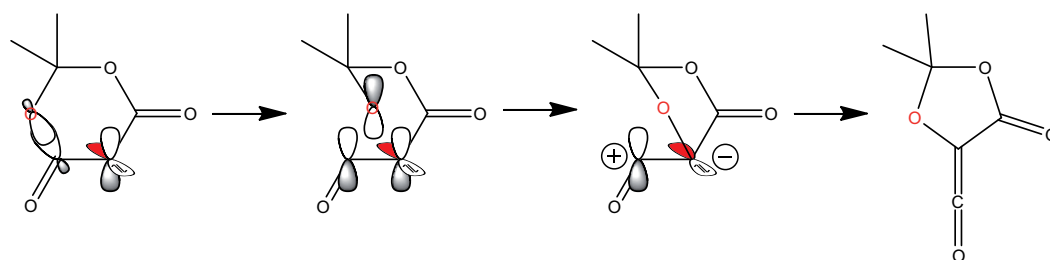


Figure 5.16: Hypothetical step-by-step mechanism of the Wolff rearrangement in DMA following Section 2.5.5. Note, that these “steps” most likely do not represent minima on the hyper-potential surface and therefore do not have a finite lifetime. Instead, as the ultrafast transient-absorption results indicate, the Wolff rearrangement proceeds simultaneously to the N_2 cleavage. These findings are also supported by the literature [167] on similar systems, that state that in cyclic diazo carbonyl compounds, such as DMA, the Wolff rearrangement is a concerted reaction.

the temporal resolution of the femtosecond spectrometer (≈ 400 fs). These results therefore suggest that the carbene species (first form in Figure 5.16) as well as all the other forms are not intermediates in the reaction but those or similar geometries are only passed during the rearrangement reaction to the ketene. These findings are in agreement with the literature [163, 167, 170] that also state that the Wolff rearrangement in cyclic diazo carbonyl compounds is a concerted reaction. Hence the ketene formation occurs simultaneously to the diazo dissociation.

6 Enantiodifferentiating photodissociation of methyl p-tolyl sulfoxide

6.1 Introduction

Chiral molecules show optical activity (Section 2.3), i.e. they rotate the polarization direction of linearly polarized light. Although this has been exploited for a long time in spectroscopy, optical rotation has hardly been used as a probing signal in femtosecond laser spectroscopy. This is due to the inherently very small effect of optical rotation. Large optical path lengths in the range of centimeters and high concentrations are conventionally employed to reach measurable optical rotation angles. Unfortunately, such conditions can hardly be met in femtosecond spectroscopy, where small volumes and short path lengths are needed to achieve high intensities for nonlinear excitations (Section 3.2.2) and to avoid pulse distortion upon propagation through the sample. Instead, commercial polarimeters have acquisition times up to a few seconds, interaction volumes of at least a few μl , and resolution down to 1 mdeg. In order to fulfill the requirements for femtosecond spectroscopy a polarimeter was assembled that allows fast and rapid detection of the optical rotation of a very small volume. In this chapter the assembly and characterization of this fast polarimeter is presented. The aim is to record a feedback signal proportional to the enantiomeric excess (see Section 2.3.3) in a fast and precise manner complying with the practical requirements (i.e. fast acquisition time and high precision) for genetic optimization algorithms [25] used in femtosecond quantum control experiments [20].

Enantio-differentiating femtosecond spectroscopy has already been demonstrated [29, 171–177] by probing the transient circular dichroism, yet the effect of circular dichroism is only reasonably large close to an absorption band. Optical rotation on the other hand is very attractive as probe signal because it is nonzero even energetically far away from the adjacent absorption. It is further directly coupled to the molecular structure [178] and enantiodifferentiating in its sign.

High-precision polarimeters generally do not have their focus on detection speed [179], since stationary products are observed with isotropic spatial distribution. Integration times up to minutes yield very high precision [180, 181], as used for example in high-performance liquid chromatography detectors. However, these cannot be used in femtosecond laser spectroscopy due to the long acquisition time. In contrast to that, polarimeters based on heterodyne detection translate the optical rotation into a phase difference, which can be detected faster. Therefore, a polarimeter based on heterodyne

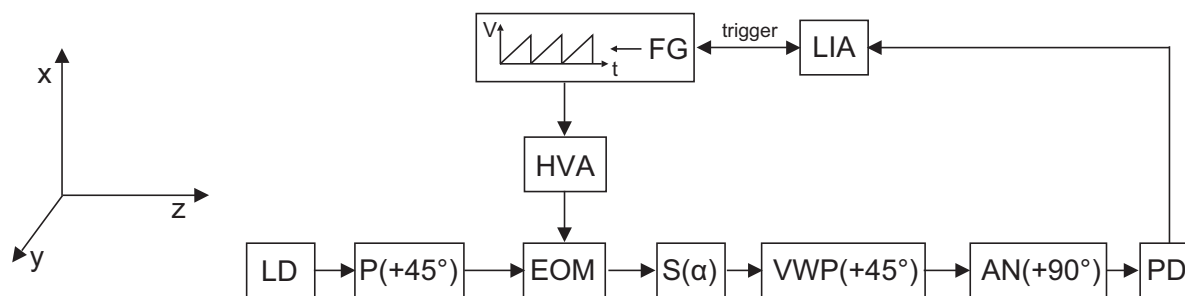


Figure 6.1: Scheme of the polarimeter setup. A laser diode *LD* is linearly polarized along $+45^\circ$ direction. One component of this polarization is retarded by an electro-optical modulator *EOM* driven by an amplified (*HVA*: high-voltage amplifier) sawtooth function from the function generator *FG*. This modulation changes the polarization of the light, see Figure 6.4. Subsequently the light passes the sample that features an optical rotation angle α . Afterwards a variable wave plate *VWP* oriented at 45° is used to translate the optical rotation angle α of the chiral sample *S* into a phase difference between the intensity modulation after the analyzer *AN* and the modulation driving the electro-optical modulator *EOM*. This phase difference is measured with a lock-in amplifier to obtain the optical rotation angle α .

detection was assembled.

The theory and practical aspects of the fast polarimeter are dealt with first. Afterwards the setup is tested in Section 6.6 with the accumulative spectroscopy (Section 3.3) of a fast change of the optical rotation angle due to the photochemically induced dissociation of chiral methyl *p*-tolyl sulfoxide. The characteristic acquisition properties (time and resolution) extracted from these accumulative experiments will be compared in Section 7.6 to a competing shot-by-shot method in order to conclude which experimental method for an enantioselective photochemistry is more promising.

6.2 Experimental setup

The experimental setup is a modification of Lee's design [182], which is based on the optical heterodyne detection, i.e. the optical rotation angle change is translated into a phase change. This phase change can be measured with great sensitivity by a lock-in amplifier [183]. The modified setup is shown schematically in Figure 6.1.

The light of a temperature controlled, pigtailed laser diode (*LD*, Thorlabs, LPS-406-FC) at 405 nm passes a thin-film polarizer (*P*, Codixx, colorPol UV405BC4) oriented at $+45^\circ$ relative to the *x* axis. An electro-optic modulator (*EOM*, Linos Photonix, LM0202) modulates the linearly polarized light with a sawtooth voltage (frequency 14.5 kHz) generated by a function generator (*FG*, Thurlby Thandar Instruments, TG4001) and amplified ($40\times$) by a high-voltage amplifier (*HVA*, FLC Electronics, A400DI) to twice the half-wave voltage of the used *EOM*. Afterwards, the light is focussed (beam diameter: 30 μm) into the sample (*S*) that rotates the linearly polarized light by the angle α . Subsequently a variable wave plate of Berek-type (*VWP*, New Focus, Model 5540), with its optical axis parallel to the polarizer (*P*), is passed before the light reaches the

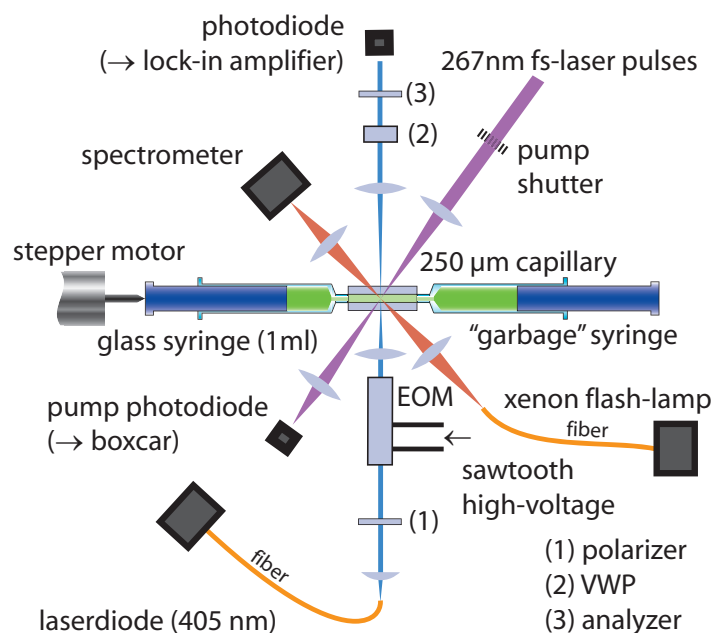


Figure 6.2: Polarimeter beam (blue, see also Figure 6.1) integrated into the setup for accumulative spectroscopy from Figure 3.9. Three beams overlap in the probe volume of the capillary. The pump beam (purple) delivers 266 nm femtosecond pulses to induce a photoreaction, whereas the red beam is used to record the absorption spectrum of the probe volume.

analyzer (AN). The analyzer is a Wollaston prism (AN, Thorlabs, WP10), oriented at $+45^\circ$ relative to the polarizer (P), hence it is oriented parallel to the y axis and only one of the two output beams is analyzed. The resulting light intensity (I) is detected with a photodiode (PD, Hamamatsu Photonics, S1337-33BQ). The phase ϕ of the signal I is determined by a lock-in-amplifier (LIA, Stanford Research Systems, SR830 DSP). The relation between ϕ , I and α is derived in Section 6.4.

The integration of the polarimeter into the experimental setup for accumulative femtosecond spectroscopy (see Figure 3.9) is shown in Figure 6.2.

In contrast to Figure 3.9 in this setup not two but three beams are spatially overlapped in the capillary:

- Purple: Pump beam representing 266 nm femtosecond laser pulses (THG, see Section 3.2.2) with a diameter of $\approx 200 \mu\text{m}$ exciting the sample. The pump beam can be blocked by the “pump shutter” before interacting with the sample volume. The time of the transition from open to close of this shutter is determined with the “pump photodiode”,
- Red: Linear-absorption probe beam representing a white-light probe (not pulsed, beam diameter: $120 \mu\text{m}$) used for recording the absorption change due to excitation with the spectrometer (Ocean Optics, HR2000+),
- Blue: Polarimeter beam representing the integration of Figure 6.1.

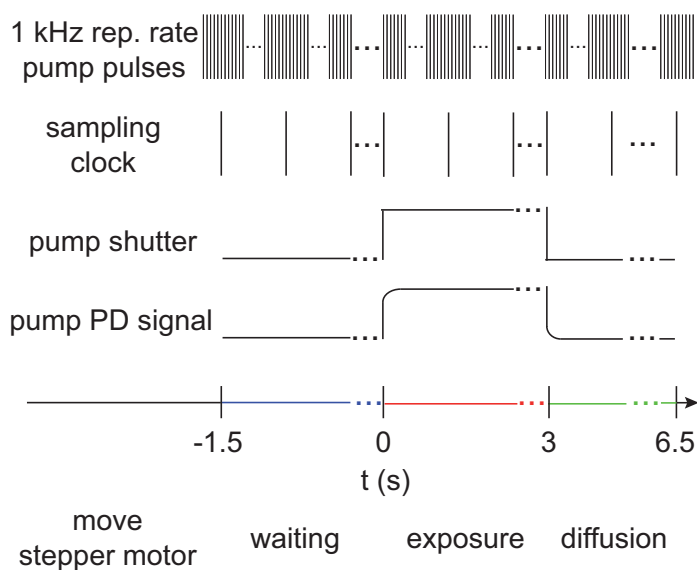


Figure 6.3: Scheme of the data acquisition of the accumulative setup. A measurement cycle consists of the four steps described in the text and shown in the bottom. Correct timing of the experimental data towards each other and respective to the count of pump pulses (first line) is achieved with one computer-generated sampling clock (second line) and the pump photodiode (pump PD signal) that counts the individual pulses exciting the sample during the accumulation process.

6.3 Data acquisition

A complete cycle of the experiment consists of the four steps depicted in the bottom of 6.3. In the first step, “move stepper motor” ($t < -1.5$ s), the sample from the previous cycle is exchanged with a fresh sample. During the “waiting step” (-1.5 s $< t < 0$ s) the measurement signals of the fresh unilluminated sample are recorded (photodiode, pump photodiode and spectrometer). Acquisition of one sample of these measurements is triggered by the “sampling clock” (either 50 or 100 Hz). After 1.5 s ($t = 0$) the opening of the pump shutter marks the beginning of the “exposure step” (0 s $< t < 3$ s) in which the sample is illuminated with the pump beam. After the closure of the pump shutter ($t = 3$ s) the “diffusion step” (3 s $< t < 4.5$ s) starts in which only diffusion of the illuminated volume into the unilluminated volume and vice versa occurs (Diffusion also takes place during the exposure step, see Section 3.3.4).

Afterwards the cycle is repeated five times and the resulting measurement signals are averaged. Whereas the absorption change due to illumination is analyzed with Eq. 3.2, the computation of the optical rotation angle α of the sample from the phase change detected by the lock-in-amplifier is given in the next section.

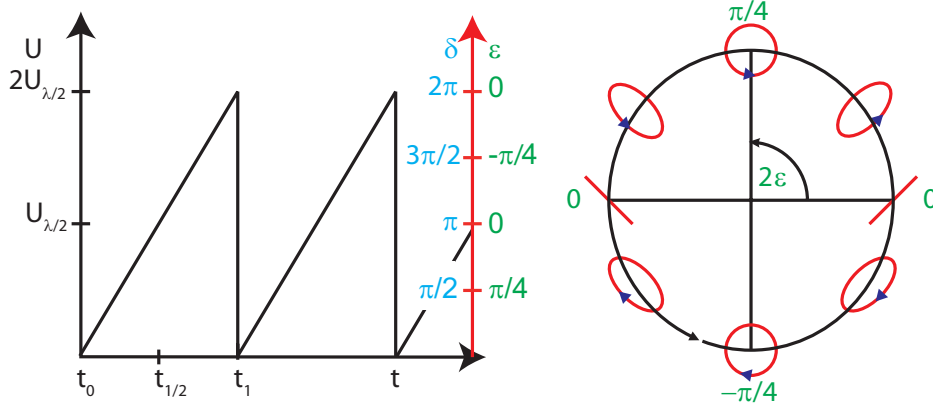


Figure 6.4: The polarization changes with the phase of the sawtooth voltage driving the electro optical modulator. Left: Polarizations passed during the modulation characterized by the retardation δ and the ellipticity ϵ . Right: Polarizations during the modulation, which can be described by a circling of the Poincaré sphere at the longitude $\theta = \pm 45^\circ$ (see Figure 2.5).

6.4 Relation of the phase to the optical rotation angle

The orientations of the optics differ from the original setup of Lee, since a quarter wave plate is left out. This is essential for the high speed and high resolution of the polarimeter since the passing of an optic under any angle other than 0° would result in a significant deviation of the signal from the calculations below due to the Fresnel coefficients (Eq. 2.53) that corrupt any polarization which is not purely s or p . In Figure 6.1 the polarization of the light of the laser diode is oriented at $+45^\circ$ due to the polarizer (P) which can be described with the Jones vector \vec{E}_{in} (see Tab. 2.1),

$$\vec{E}_{in} = \frac{1}{\sqrt{2}} \begin{pmatrix} 1 \\ 1 \end{pmatrix}. \quad (6.1)$$

Afterwards the electro-optic modulator retards the p component (oriented in the y direction) linearly by ωt , describable through the Jones matrix $EOM(\omega t)$ (see Section 2.2.2),

$$EOM(\omega t) = \begin{pmatrix} e^{\frac{i\omega t}{2}} & 0 \\ 0 & -e^{\frac{i\omega t}{2}} \end{pmatrix}. \quad (6.2)$$

This leads to the periodic circling of the Poincaré sphere (Figure 2.5) along the longitude at $\theta = \pm 45^\circ$ and therefore the alternating polarizations of the light shown in Figure 6.4. The optical rotation of the sample $S(\alpha)$ is described by the active rotation matrix (see Eq. 2.42). The variable wave plate can be described by the Jones matrix ($VWP(\delta, +45^\circ)$) of a wave plate with retardation δ and orientation $+45^\circ$,

$$VWP(\delta, +45^\circ) = Rot_p(-45^\circ) \cdot \begin{pmatrix} e^{\frac{i\delta}{2}} & 0 \\ 0 & -e^{\frac{i\delta}{2}} \end{pmatrix} Rot_p(+45^\circ), \quad (6.3)$$

with Rot_p being the passive two-dimensional rotation matrix (Eq. 2.43). The Jones matrix of the analyzer AN is given by

$$AN = \begin{pmatrix} 0 & 0 \\ 0 & 1 \end{pmatrix}. \quad (6.4)$$

The Jones vector of the light detected by the photodiode (\vec{E}_{out}) is then given by

$$\vec{E}_{out} = AN \cdot VWP(\delta, +45^\circ) \cdot S(\alpha) \cdot EOM(\omega t) \cdot \vec{E}_{in}, \quad (6.5)$$

which can be simplified to

$$\vec{E}_{out} = \begin{pmatrix} 0 & 0 \\ 0 & 1 \end{pmatrix} \cdot Rot_p(-45^\circ) \cdot \begin{pmatrix} e^{\frac{i\delta}{2}} & 0 \\ 0 & -e^{\frac{i\delta}{2}} \end{pmatrix} \cdot Rot_p(+45^\circ) \cdot Rot(\alpha) = \begin{pmatrix} e^{\frac{i\omega t}{2}} & 0 \\ 0 & -e^{\frac{i\omega t}{2}} \end{pmatrix} \cdot \frac{1}{\sqrt{2}} \begin{pmatrix} 1 \\ 1 \end{pmatrix}. \quad (6.6)$$

Hence the signal I_{out} detected by the photodiode is

$$I_{out} = |\vec{E}_{out}|^2 = \frac{1}{2}[1 + \sin(2\alpha) \cos \delta \cos(\omega t) + \sin \delta \sin(\omega t)], \quad (6.7)$$

which can be transformed into the sinusoidal form [88]

$$I_{out} = \frac{1}{2}[1 + A \sin(\omega t + \phi)], \quad (6.8)$$

with the help of the relation

$$a \sin(\omega t) + b \cos(\omega t) = \sqrt{a^2 + b^2} \sin\left(\omega t + \arctan \frac{b}{a}\right), \quad (6.9)$$

where $a = \sin \delta$ and $b = \sin(2\alpha) \cos \delta$. The amplitude A is therefore given by

$$A = \sqrt{\sin^2 \delta + [\sin^2(2\alpha) \cos \delta]^2}, \quad (6.10)$$

and the phase ϕ by

$$\phi = \arctan \frac{\sin(2\alpha)}{\tan \delta}. \quad (6.11)$$

The optical rotation angle α can then be calculated to

$$\alpha = \frac{1}{2} \arcsin(\tan \delta \tan \phi), \quad (6.12)$$

with δ being an experimental parameter and ϕ being the phase detected by the lock-in amplifier. The results in this chapter were obtained with $\delta = (2.3 \pm 0.2)^\circ$.

Considering that only small optical rotation angles α will be encountered the small-angle approximation can be applied to all terms dependent on α in Eq. 6.11 and Eq. 6.12. Equation 6.11 then becomes $\phi \approx \frac{2}{\tan(\delta)}\alpha$. For an optical rotation of $\alpha = 0.1$ deg the

error in the phase ϕ in Eq. 6.11 due to this approximation is 0.5 ‰ with $\delta = 2.3^\circ$. In respect of this approximation one can define the “angle amplification” k as

$$k = \frac{2}{\tan(\delta)}, \quad (6.13)$$

which describes the factor between the optical rotation α and the phase ϕ detected by the lock-in amplifier. Equation 6.12 then becomes

$$\alpha k \approx \phi. \quad (6.14)$$

The lock-in amplifier detects the signal I_{out} in Eq. 6.8 for a period of time (lock-in amplifier time constant T_{LIA}) and calculates values for the amplitude A of the modulation (Eq. 6.10) and the phase ϕ (Eq. 6.11). The phase is thereby relative to a reference sine oscillation. This reference can either be provided by an external signal or be internally generated. The internal reference offers higher precision of the values for A and ϕ compared to the values with external reference [183].

If the phase ϕ of the signal were zero for zero optical rotation, ϕ in Eq. 6.12 would correspond directly to the measurement value from the lock-in amplifier. However, due to the absence of a reference beam with known absolute phase it is only possible to measure a phase change $\Delta\phi$. The phase change $\Delta\phi$ relative to ϕ_0 is then the averaged phase value measured by the lock-in amplifier during the waiting step in Fig. 6.3,

$$\Delta\phi(t) = \phi(t) - \phi_0, \quad (6.15)$$

with $\phi(t)$ being the phase value determined by the lock-in amplifier at time t . With a phase ϕ_0 corresponding to a known optical rotation α_0 , e.g. the phase difference for the achiral solvent corresponding to $\alpha_0 = 0$ deg, one can directly calculate the absolute optical rotation angle α to

$$\alpha = \alpha_0 + \frac{\Delta\phi}{k}. \quad (6.16)$$

6.4.1 Angle amplification

The angle amplification depends on δ , as shown in Figure 6.5. The angle amplification k in Eq. 6.14, is infinitely large in value when δ approaches $n\pi$. At exactly $\delta = n\pi$ a phase jump occurs due to a sign change in k . At this point the amplitude therefore has to be zero in agreement with Eq. 6.10. Substituting the retardation of the variable wave plate of $\delta = (2.3 \pm 0.2)^\circ$ into Eq. 6.10 the amplitude of the sine modulation is only 3% of the total intensity.

If the beamsplitter from the original setup (placed directly after the EOM to obtain a reference beam) would still be present in this setup, the reflection and transmission coefficient would change periodically with ω , hand in hand with the polarization. Therefore real-valued transmission and reflection coefficients obeying $0.97^2 \ll \left|\frac{r_{\parallel}}{r_{\perp}}\right| \ll 1.03^2$ and $0.97^2 \ll \left|\frac{t_{\parallel}}{t_{\perp}}\right| \ll 1.03^2$ would be necessary in order to have no relevant influence on the amplitude modulation of the signal I . Whereas for the He-Ne monochromatic laser used by Lee such an optic exists, in the case of the 405 nm laser diode from this setup,

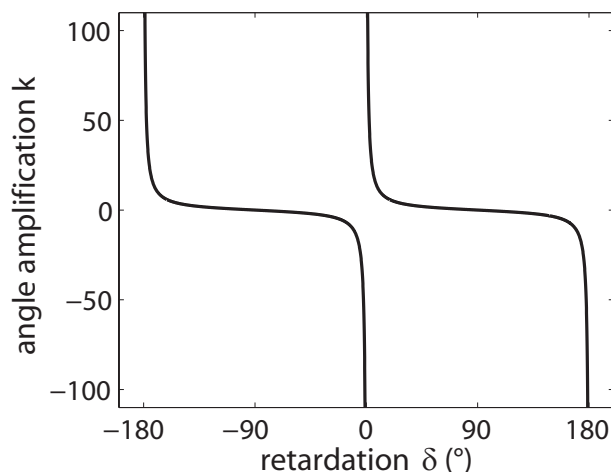


Figure 6.5: The angle amplification k changes with the retardation δ (Eq. 6.14). When δ approaches $n\pi$ the amplification approaches infinity. However, at $\delta = n\pi$ the amplitude of the modulation used to measure the optical rotation is zero (Eq. 6.10), hence no optical rotation can be measured at these retardations. The optimum amplification is $\delta = 2.3^\circ$ with an amplification of $k \approx 50$ (see Section 6.9).

such an optic is not available. However, the ultra-violet laser diode was chosen since the optical rotatory dispersion usually dictates that the specific rotation increases with shorter wavelength.

6.5 Polarimeter response function

6.5.1 Instrument response

Whereas the sample response is given by Eq. 3.26, the instrument response is determined by the lock-in amplifier. The lock-in amplifier works with a sliding Fourier window analysis, i.e. the value of the phase and amplitude at time t is calculated from the signal during $t - T_{LIA} \rightarrow t$, with T_{LIA} being the time-constant. The response function was therefore experimentally measured by changing the phase and amplitude of a sine function abruptly at one point in time. The time-resolved phase and amplitude change detected by the lock-in amplifier is then the convolution of the instrument response R_{LIA} with a step function.

The experimental data of this convolution, shown in Figure 6.6, suggest the instrument response to be an asymmetric Gaussian, consisting of two Gaussians with different widths,

$$R_{LIA}(t) = \frac{2A}{\sqrt{2\pi}(b_1 + b_2)} \left\{ \Theta(m - t) \exp \left[-\frac{(t - m)^2}{2b_1^2} \right] + \Theta(t - m) \exp \left[-\frac{(t - m)^2}{2b_2^2} \right] \right\}. \quad (6.17)$$

Here A represents the area under the curve of the asymmetric Gaussian-shaped function $R_{LIA}(t)$, the b_i^2 indicate the Gaussian variances for each side, m is the position of

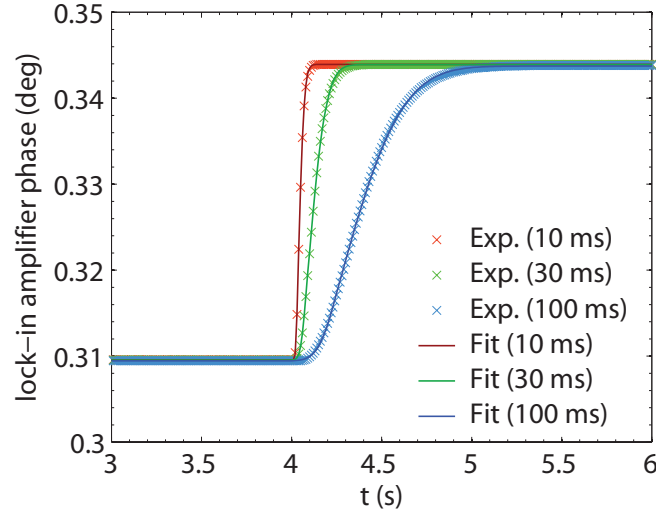


Figure 6.6: Detected phase of the lock-in amplifier after applying a sine function that abruptly changes its phase and amplitude. The curve corresponds to a step function convolved with the response function of the lock-in amplifier. The response depends on the time constant T_{LIA} of the lock-in amplifier, the smaller the time constant, the faster the response. The response function is assumed to be an asymmetric Gaussian (Eq. 6.17) and the optimal parameters to describe this asymmetric Gaussian depending on the time constant are given in Tab. 6.1. With the response function at hand, the experimental data can be deconvolved to obtain the pure sample response.

LIA time constant T_{LIA} (s)	0.010	0.030	0.100	relation with T_{LIA}
delay m (s)	0.0325	0.0801	0.2480	$\approx 2.4 T_{LIA} + 0.0084$ s
variance b_1 (s^2)	0.0075	0.0238	0.0805	≈ 0.8 s T_{LIA}
variance b_2 (s^2)	0.0280	0.0842	0.2776	≈ 2.8 s T_{LIA}

Table 6.1: Results of the fitting procedure of the response of the lock-in amplifier presented in Figure 6.6. The fit reveals a linear relationship for all parameters m , b_1 , and b_2 , with respect to the lock-in-amplifier time constant T_{LIA} as indicated by the equations in the last column.

the maximum of R_{LIA} and Θ is the Heaviside step function. The convolution of the asymmetric Gaussian $R_{LIA}(t)$ in Eq. 6.17 with a step function is given by the integration

$$\text{Erf}_{LIA}(t) = \frac{2}{\sqrt{\pi}} \int_{-\infty}^t R_{LIA}(x) dx + O \quad (6.18)$$

with O being a phase offset. Equation 6.18 corresponds directly to the data in Figure 6.6. The best fits of Eq. 6.18 to the experimental data (crosses) for three different time constants of the lock-in amplifier are shown as solid lines in Figure 6.6. The obtained fit parameters are listed in Tab. 6.1. As can be seen from the linear relationship of the fit parameters (last column in Tab. 6.1) with respect to the time constant T_{LIA} and the good

agreement of the fits with the experimental data in Figure 6.6, the model in Eq. 6.18 for the response function is satisfactory. The linear relationship is comprehensible when considering that in case that the time window length for integration is larger, i.e. the lock-in amplifier time constant T_{LIA} is larger, the final values for the amplitude and phase are reached more slowly. The parameters b_1 and b_2 describe the width of the response function linearly, therefore the linear relationship of the parameters with the time constant is a good indicator for the performance of the asymmetric Gaussian as model function for the lock-in amplifier response function.

6.5.2 Total response

The convolution of the sample response function given by Eq. 3.26 with the lock-in-amplifier instrument response function from Eq. 6.17 leads to the total response function

$$F(t, \tau) = (\alpha_{\text{pr}} * R_{\text{LIA}})(t, \tau) = \int_{-\infty}^{\infty} \alpha_{\text{pr}}(x, \tau) R_{\text{LIA}}(x - t) dx, \quad (6.19)$$

which is taken as fitting model for all experimental data from the polarimeter setup. With its help one can extract the parameters α_0 , η , d_{pu} , and d_{pr} from experimental data.

6.6 Steady-state properties and photoinduced reaction

Sulfoxides undergo a dissociation reaction, more precisely an α -cleavage reaction, after excitation with ultraviolet light [184]. As shown in Figure 6.7 for the methyl *p*-tolyl sulfoxide (**1**) investigated in this thesis during this reaction the methyl-sulfide bond is homolytically broken, leading to a methyl radical and the sulfoxide radical (middle). Whereas the reactant is chiral (the free electron pair of the sulfur atom counts as substituent, leading to the tetrahedral configuration), the two products possess mirror-plane symmetry and hence do not exhibit optical activity. With the experimental conditions of the polarimeter ($\lambda = 405$ nm, $l = 0.25$ mm) the optical rotation of a pure solution of the R and S enantiomer is 1 mdeg at a concentration of 1 mg/ml.

The steady-state absorption of methyl *p*-tolyl sulfoxide exhibits only absorption in the ultraviolet region ($\lambda < 300$ nm) as shown in Figure 6.8. At the concentration of 1 mg/ml the absorbance at 266 nm, the excitation wavelength, is ≈ 0.3 OD.

6.7 Exemplary data and their interpretation

Excitation of **1R** and probing the optical rotation angle leads to the typical data of the optical rotation change shown in Figure 6.9 on the left. During the waiting step (blue), i.e. before illumination, a constant signal is acquired, referring to zero optical rotation change. At $t = 0$ (left vertical line in Figure 6.9, left) the pump shutter opens and the illumination with 267 nm femtosecond laser pulses starts. During this exposure step (red) the optical rotation decreases rapidly due to the photodecomposition

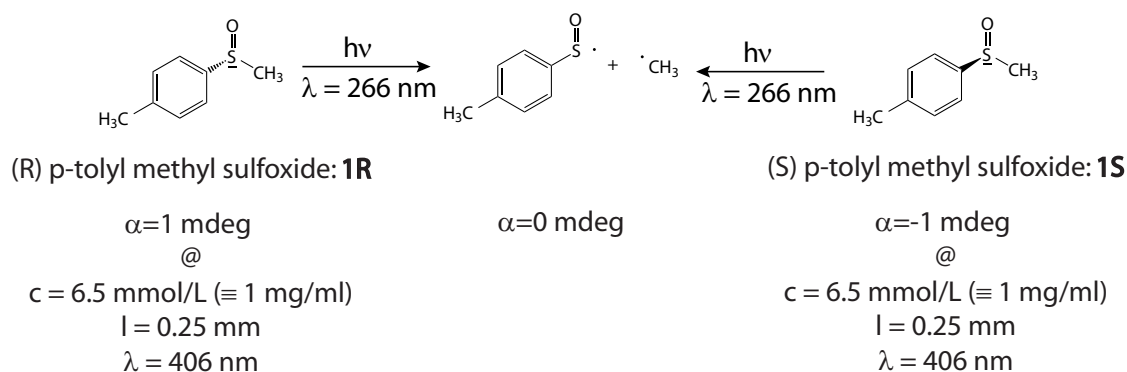


Figure 6.7: After ultraviolet excitation, here 266 nm, methyl *p*-tolyl sulfoxide undergoes α -cleavage leading to the methyl and sulfoxide radical. Whereas the reactants are optically active the products possess mirror-plane symmetry and hence feature no optical rotation. The optical rotation angle is +1 mdeg and –1 mdeg for the R and S enantiomer at the chosen experimental conditions, respectively (see Eq. 2.73).

of the chiral reactant taking place (going from a positive optical rotation towards zero optical rotation). After the end of illumination (the pump shutter is closed at the right vertical line), i.e. during the diffusion step (green), reactant molecules diffuse into the probe volume, and product molecules diffuse out of the probe volume. This process increases the optical rotation angle again, see Section 3.3.4. The final value of the exposure step ($t = 3 \text{ s}$) refers to an equilibrium between the diffusion and the destruction of reactant molecules by the femtosecond laser pulses. The value at the end of the diffusion step ($t = 6.5 \text{ s}$) would be close to the initial optical rotation value due to diffusion, if the waiting time after illumination were long enough and if the pump volume were in contact with an infinite reservoir of the intact reactant. Steady-state optical rotation measurements give an optical rotation angle of $\alpha_0 = +x \text{ mdeg}/(\text{mg ml}^{-1})$ for the experimental conditions of the data in Figure 6.9 (405 nm, 250 μm path length), with $x = 2 \text{ mg/ml}$ being the concentration of **1R**. The observed value for the optical rotation change does not reach complete photodestruction ($\Delta\alpha = -2.0 \text{ mdeg}$), instead only an optical rotation change of $\Delta\alpha = -1.7 \text{ mdeg}$ can be achieved. This deviation is due to the diffusion of undestroyed molecules into the probe volume as explained in Section 3.3.4.

As an example the resulting fit of Eq. 6.19 to the experimental data for **1R** (left in Figure 6.9) is shown as black dashed curve. The optimal parameters are $\alpha_0 = 2.13 \text{ mdeg}$, $\eta = 2.39 \times 10^{-3}/\text{pulse}$, $d_{\text{pu}} = 3.58 \text{ s}^{-1}$, and $d_{\text{pr}} = 4.69 \text{ s}^{-1}$. The agreement of the fit with the experimental data is excellent, validating the assumed model for the response function of the lock-in amplifier and the diffusion model in Section 3.3.4. The deconvolution of the fit leads to the pure sample response, shown as brown solid curve in Figure 6.9. The deviation of the value α_0 with respect to the expected value 2.0 mdeg might originate from the retardation setting δ , which is not known exactly, and hence might cause a small deviation (see Eq. 6.16).

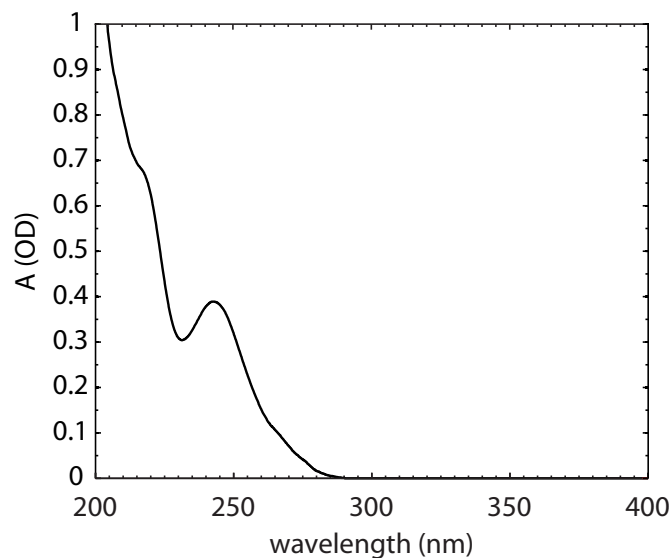


Figure 6.8: Steady-state absorption of methyl *p*-tolyl sulfoxide ($c = 0.5$ mg/ml) in acetonitrile (path length: 250 μm).

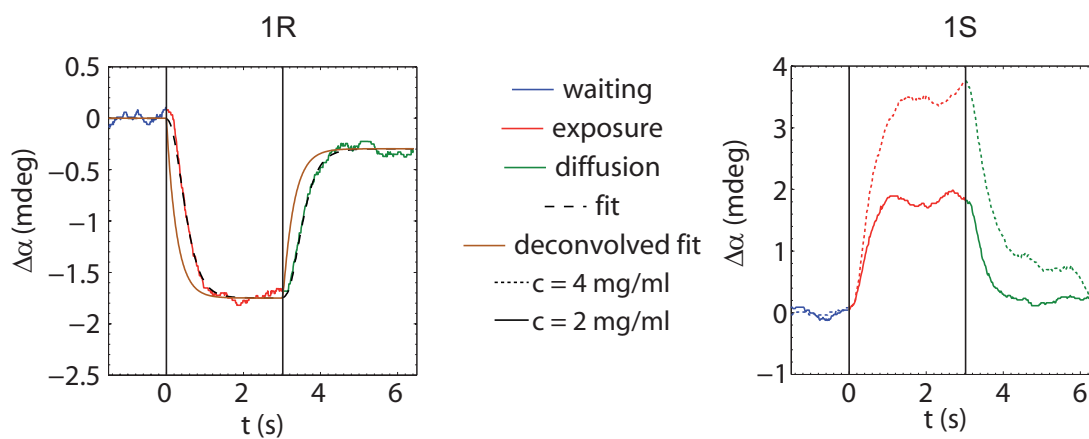


Figure 6.9: Exemplary experimental data and the fit of Eq. 6.19 to these data of the enantiodifferentiating photodissociation of **1**. In the case of **1R** (left) the optical rotation changes from positive to zero ($\Delta\alpha < 0$) during exposure (red) to the 266 nm pump pulses, vice versa for the other enantiomer **2** (right) the optical rotation changes from negative to zero ($\Delta\alpha > 0$) during irradiation with the pump pulses (red). Before exposure (blue) the optical rotation angle change is zero for both enantiomers since the stereogenic center is stable, whereas after exposure (green) diffusion leads to a return to almost the initial optical rotation angle. The fit of the parameters to the experimental data of **1R** is in very good agreement (black dashed line). Due to the knowledge of the Lock-in amplifier response function the deconvolution to obtain the pure sample response is possible (orange).

6.8 Influence of experimental parameters

6.8.1 Enantiomer

In order to prove the enantiodifferentiating character of the signal the results for the same experiment with **1S** is shown on the right of Figure 6.9. The data show now an increase in optical rotation due to photodestruction, since $\alpha_0 = -x \text{ mdeg}/(\text{mg ml}^{-1})$ for the S-enantiomer. Concluding the same features during the experimental steps can be observed for the S-enantiomer and R-enantiomer only with opposite sign, as theoretically predicted in Eq. 6.16.

6.8.2 Concentration

Furthermore the proportionality of $\Delta\alpha$ with the concentration of the enantiomer is demonstrated by the dashed-curve that was recorded with $x = 4 \text{ mg/ml}$ instead of 2 mg/ml (solid curve). In this case the change in optical rotation also doubles and reaches almost $\Delta\alpha \approx 4 \text{ mdeg}$.

6.8.3 Pulse energy

Pulse energy variation leads to the experimental data shown on the left in Figure 6.10.

In this case a concentration of 6 mg/ml was used. As can be seen the optical rotation change scales almost linearly with the pulse energy. The optimal parameters of the total response function were obtained in a global fit (shown as solid lines), so that the parameters for diffusion (d_{pu} only, since d_{pr} is only relevant during the diffusion part that has not been recorded for these curves) were optimized for all four curves simultaneously. The increasing pulse energy is expressed in this fit by an increasing η , the photoconversion efficiency parameter in the diffusion model (Section 3.3.4), as shown on the right of Figure 6.10. Whereas η scales linearly with the pulse energy, the small negative curvature of $\Delta\alpha$ (right axes on the right in Figure 6.10) with increasing pulse energy is a saturation effect, since $\Delta\alpha$ can at most be $-\alpha_0 = 6 \text{ mdeg}$. This is also expressed by the inset of Figure 6.10 (right), which should be constant if no saturation effect were present, because η as well as $\Delta\alpha$ are zero if the pulse energy is zero. Both quantities can therefore be described as lines through the origin.

6.8.4 Solvent

The use of acetonitrile and isopropanol as solvents results in similar optical rotation changes (concentration of **1R**: 2 mg/ml) but different diffusion parameters d_{pu} and d_{pr} due to their difference in viscosity (acetonitrile: 0.369 mPa s ; isopropanol: 2.038 mPa s) [185]. For best comparison all experimental parameters (e.g. spatial overlap of the pump and probe beam) in this comparison were the same except for the solvent. The resulting optimal diffusion parameters are shown in Tab. 6.2 and confirm the total response function: In a solvent with higher viscosity, diffusion processes are slower, i.e. the diffusion parameters for isopropanol are slower than the diffusion parameters of acetonitrile. However, these diffusion parameters depend not only on the viscosity of

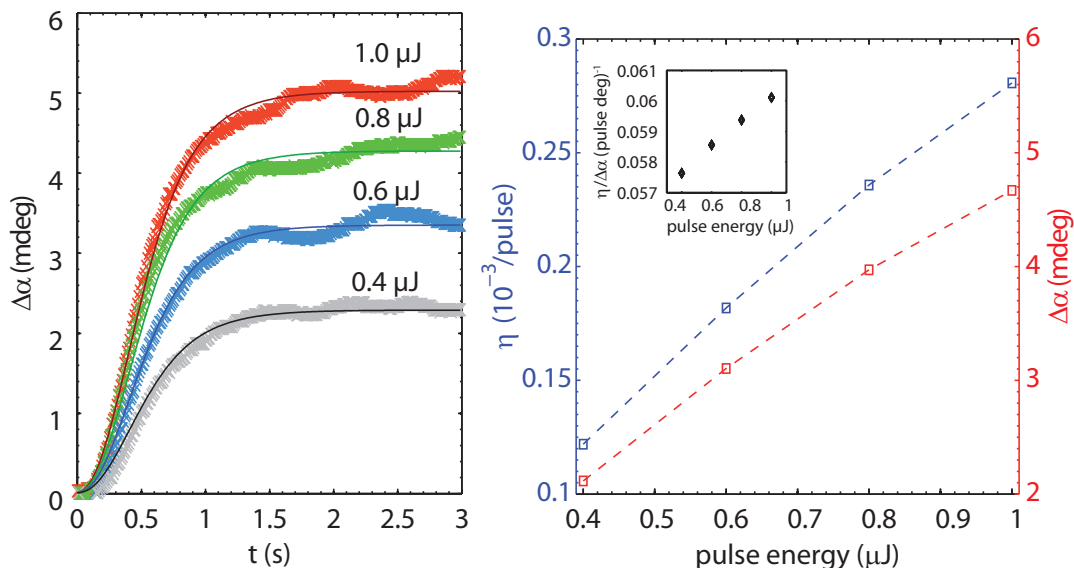


Figure 6.10: Experimental data obtained with different pulse energies (left) ($c_{1R} = 6$ mg/ml). With increasing pulse energy the achieved optical rotation angle change $\Delta\alpha$ increases from ≈ 2 mdeg for $0.4 \mu\text{J}$ to ≈ 5 mdeg for $1.0 \mu\text{J}$. A global fit (left, solid lines) in which only the conversion efficiency η is fitted individually to each experiment, whereas the diffusion constants are the same for all curves, results in the conversion efficiencies dependent on the pump energy on the right (blue). The increase in optical rotation angle change $\Delta\alpha$ with pump energy is shown in red. Both curves pass through the origin, therefore the negative curvature of $\frac{\eta}{\Delta\alpha}$, shown as inset, indicates that the optical rotation change cannot be infinitely large. This is in agreement with the experimental conditions since the maximum optical rotation angle change is the negative of the optical rotation angle of the unirradiated solution.

the solvent but also on the dimensions and the spatial overlap of the pump and probe beam. Therefore these diffusion parameters are not exactly the same for all experiments with the same solvent. The calibration process (Section 3.3.4) should thus be carried out for each arrangement such that the desired photoconversion efficiency can always be extracted from an experiment.

solvent	d_{pu} [s ⁻¹]	d_{pr} [s ⁻¹]
acetonitrile	3.5739	4.4795
isopropanol	1.9789	1.8191

Table 6.2: Dependence of the diffusion constants d_{pu} and d_{pr} on the solvent.

6.9 Optical rotation angle and time resolution

With the desire to implement optical rotation as a probe in femtosecond spectroscopy, two decisive characteristics of the polarimeter setup are rotatory resolution and acqui-

sition time.

The theoretical limit in the time domain is set by the time constant of the lock-in amplifier, since one has to wait approximately three to five times the time constant to reveal a reliable phase value (see Fig. 6.6). The resolution in optical rotation is more complicated to determine. Theoretically it is given by the angular phase resolution of the lock-in amplifier. In our case the lock-in amplifier has an angular phase resolution of 8 mdeg [183], which would lead to a resolution of the optical rotation of 0.16 mdeg for a retardation setting of the variable wave plate of $\delta = 2.3^\circ$ (Eq. 6.12), which will be shown to be optimal below.

Lee et al. have calculated a theoretical resolution limit of 0.035 mdeg considering besides the angular resolution of the lock-in amplifier also the second-harmonic error, and the polarization-mixing error [182]. However, this value is not reached in an actual experiment due to effects like electronic noise, scattering in the sample solution or intensity fluctuations of the laser diode, to mention just a few examples. Therefore the true resolution of the polarimeter is determined experimentally here.

For this purpose, the capillary is filled with solvent only (acetonitrile) and the measurement procedure of the previous section is repeated. Thus, all noise effects of the measurement including the pump pulses are included in this analysis. The data should be basically a horizontal flat line as no change in rotation angle should occur upon irradiation with the femtosecond pulse train. The recorded fluctuations due to noise are assumed to be Gaussian distributed, which was confirmed by statistical analysis of the distribution of the data points. A step change in such data can be resolved if it is greater than two times the standard deviation of the noise. Hence, the rotatory resolution of the polarimeter is calculated by the standard deviation of the solvent data and multiplied by two.

The result of this noise analysis can be seen in Fig. 6.11 for different settings of the retardation δ of the variable wave plate and different time constants of the lock-in amplifier T_{LIA} . The resolution gets better with longer time constants. Concerning the retardation δ of the variable wave plate, a setting of $\delta = 2.3^\circ$ is optimal, revealing a resolution of 0.12 mdeg within only 1 s of measuring time ($T_{LIA} = 100$ ms). This value of 0.12 mdeg is smaller than the value of 0.16 mdeg determined by the resolution of the lock-in amplifier because of data averaging. On the other hand it is somewhat larger than the purely theoretical value of 0.035 mdeg by Lee et al. because all experimental noise sources are included.

Theoretically, the angle amplification k should get infinitesimally large when approaching a retardation setting of $\delta = 0^\circ$ according to Eq. 6.12, which should result in an infinitesimally small resolution, see Figure 6.5. However, the amplitude A of the modulation given by Eq. 6.10 for such small retardations would be very small (zero in the case of $\delta = 0^\circ$). Since the lock-in amplifier reveals a higher noise level for smaller signal amplitudes, the effect of the optimal retardation setting should feature a local minimum. Figure 6.11 shows that the resolution for a retardation value of $\delta = 1.3^\circ$ is worse than for $\delta = 2.3^\circ$, which is a direct consequence from this relationship.

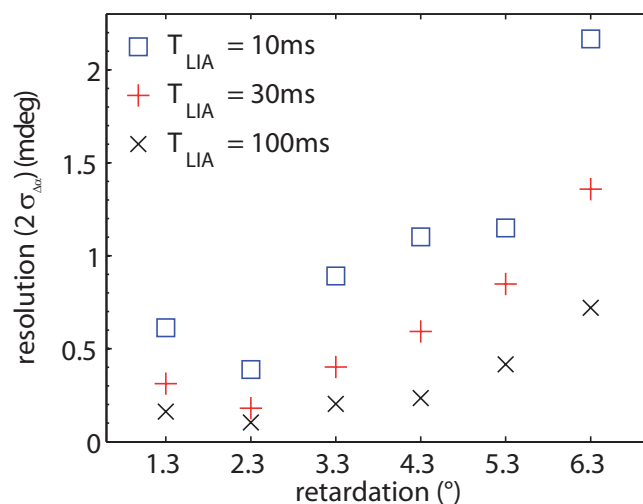


Figure 6.11: Optical rotation angle error after averaging 1 s versus the retardation of the variable wave plate (see Figure 6.1). With increasing time constant T_{LIA} of the lock-in amplifier the optical rotation angle resolution decreases. An optimum can be found for the retardation of the variable wave plate ($\delta = 2.3^\circ$) which is a compromise between decreasing amplitude A of the modulation (Eq. 6.10) and increasing the angle amplification k (see Figure 6.5 and Eq. 6.13). In the optimum the optical rotation angle resolution is ≈ 0.12 mdeg for a time constant of 100 ms.

6.10 Summary

In this chapter optical rotation as a probe signal for femtosecond spectroscopy was introduced. A polarimeter based on the common-path optical heterodyne interferometry was combined with the accumulative technique for femtosecond laser spectroscopy (Section 3.3) to measure small changes in optical rotatory power. The functionality of the technique was demonstrated with a photoreaction of chiral sulfoxides. Optical rotation is an attractive signal for monitoring chemical reactions involving enantiomers that exhibit only weak absorption changes. The presented setup has an experimentally determined angular resolution of 0.12 mdeg including all noise sources, which is better than most commercial devices. On top of that, here a measurement time of only one second, an interaction length of only 250 μm and a probe volume of ≈ 2 nl is needed. Hence, this polarimeter offers rapid and precise detection of optical rotation changes of small volumes making it applicable for spectroscopy of ultrafast reactions including enantiomers.

7 Polarization-shaped pump–probe experiments for chiral control

7.1 Introduction

The enantioselective synthesis of chemical compounds is one of the main tasks for chemists. The chiral information is indispensable for example in pharmaceutical compounds, whose effect on the human body depends on the chirality. Nowadays, asymmetric synthesis, the chemical division developing enantioselective reaction pathways, allows for most target molecules the selective synthesis, amongst other ways, via chiral catalysts. In contrast to that, conventional photochemistry lacks a possibility to introduce chiral information into a reaction (excluding the conventional circular dichroism and excluding the photoreactions that occur via the excitation of chiral catalysts, a field called “photochirogenesis” [186]). Chiral control aims at introducing the chiral information into a photochemical reaction through either a chiral electric field or a circular-dichroism effect, that exceeds the conventional 1-photon circular dichroism (Section 2.3). For an electric field to introduce chiral information into an isotropic mixture of molecules via the electrostatic interaction (Eq. 2.70) at least two electric fields with non-coplanar polarization state and stable phase relation are necessary to allow for three polarization directions [187] of the electric field \vec{E} . The circular dichroism on the other hand is based on the magnetic interaction (Eq. 2.71) and is a very weak effect and hence at first no good enantiomer excesses are to be expected on its basis.

Up to now circular dichroism in combination with femtosecond laser pulses was mostly used for spectroscopic purposes (exceptions are described below), meaning that a solution containing only one enantiomer is excited and its time-dependent circular-dichroitic dynamics are investigated. In these experiments, that are all based on the pump–probe principle (Section 3.1.1), the pump pulse is a linearly polarized pulse and the probe pulse is either switched between the two circular polarizations to determine ϵ_l and ϵ_r (Figure 2.8) or the circular part of a previously linearly polarized pulse after interaction with the circular-dichroitic media is measured. Experiments on time-dependent circular dichroism have already been demonstrated in the literature [29, 172, 173]. In all these experiments the weakness of the circular-dichroism effect and the consequential very low signal-to-noise ratio despite long integration times becomes apparent.

As mentioned before, chiral control aims at inducing chirality into achiral solutions (racemates or achiral molecules) instead of measuring it. Theoretical suggestions [188, 189] for experiments in which the chirality of the electric field interaction with the molecule (Eq. 2.71) introduces the chiral information assume many experimental conditions that are very hard or even impossible to achieve, e.g. the intensity profile in

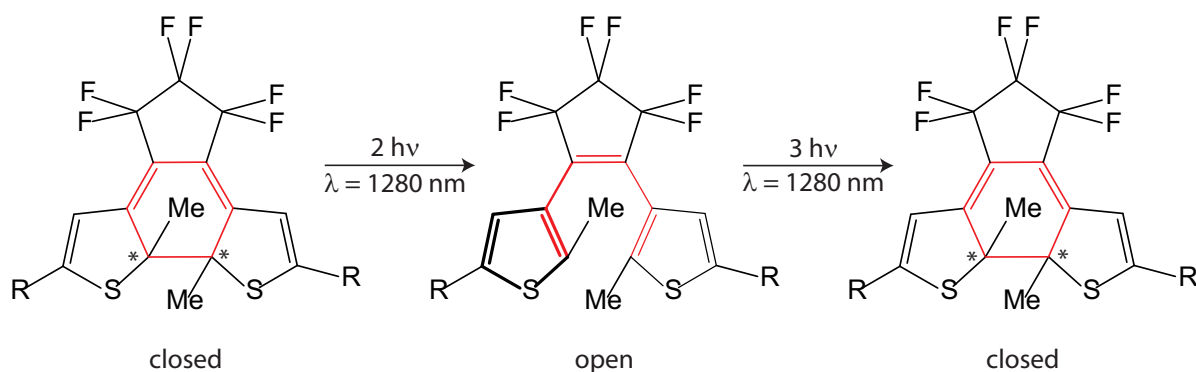


Figure 7.1: Multiphoton bidirectional switching in a diarylethene, adapted from Ref. [192]. The closed form (left and right) is chiral if the two stereogenic centers, denoted by the star, are not mirror image of each other (meso form). The open form (middle) is helically chiral dependent on the steric demand of the substituents, here Me and R. Ring opening can be induced via 2-photon absorption of 1280 nm pulses or with visible light. After the complete shift towards the open form, ring closure can be induced via 3-photon absorption of 1280 nm pulses.

time has to follow a square function. Therefore a more practical first step is to use the circular-dichroism effect as basis for chiral-control experiments. Also from the practical standpoint a detection of a circular-dichroism effect is the minimum sensitivity that should be achieved to start with a chiral-control optimization, since any optimization needs to start at a clearly identified signal.

Some scenarios are conceivable, and have been realized in the gas phase, in which the combination of femtosecond laser pulses with circular dichroism might increase the effect of the usual linear circular dichroism [190, 191]. Whereas in these experiments the circular-dichroitic process is a nonresonant multiphoton absorption, a step-wise process may also give access to an increased circular-dichroism effect. Assume for example an achiral molecule reacts in a photoreaction towards a chiral molecule, e.g. merocyanine ring closure to chiral spiropyran. The decision about the chirality of the product is met at some point during the reaction. Consider now a system in which the photoreaction proceeds with much higher quantum efficiency if the excited state is excited again, hence two interactions with the electric field take place. In that case the first interaction, excitation from the ground state to the excited state, as well as the second interaction with the electric field, excitation from the excited state to the hyperpotential surface from which the reaction proceeds with high quantum efficiency, have both their unique circular-dichroitic properties. A femtosecond polarization-shaped laser pulse is then able to reproduce the circular-dichroitic property of both transitions in an optimal way to exceed the linear circular-dichroism effect.

A promising system for such a control scheme is the photochromic switch diarylethene [106] (see Figure 7.1). Similar to the merocyanine–spiropyran system from Chapter 4 it can be switched between an open and a closed form [193] in an electrocyclic reaction on an ultrafast time scale [96, 192, 194]. Whereas in diarylethenes the closed form is always chiral (except for meso substitution), the stability of stereogenic centers in the

open form depends on steric hindrance of the substituents [106]. Additionally to their unique features of photochromic switching these molecules due to the helical structure of their π system have huge specific rotation angles [195] exceeding the usual ones by a factor of more than 10.

It has been shown for diarylethenes that the ring-opening reaction proceeds from higher-lying excited states with much greater efficiency [96]. The population of this state may be generated via two pump pulses (similar to the pump–repump–probe experiment in Section 4.5) which are both optimized in their polarization for the respective transition. In such a resonant multiphoton process each transition features its own circular dichroism leading perhaps to a greater circular dichroism than the conventional 1-photon circular dichroism.

In case of non-resonant excitation, the circular-dichroism effect increases with the order of the process [191]. The complete switching cycle given in Figure 7.1 can be fulfilled with two non-resonant excitations (opening: 2-photon process; closure: 3-photon process). Hence, a molecule reacting along the complete switching cycle senses on top of the circular dichroism of each reaction step also the non-resonant multiphoton circular dichroism. Applying a distillation scheme to this reaction, so that this switching cycle is repeated until an equilibrium is reached, a cumulative circular-dichroism effect [190, 191] might be detectable.

In a distillation experiment an accumulative scheme needs to be employed (Section 3.3), whereas in a pump–probe experiment special attention on the experimental realization has to be paid, since anisotropy artefacts (Section 3.1.4) might dominate the weak circular-dichroism effect. In an accumulation experiment a larger signal is possible, since all molecules in solution are converted and not just the small part that reacts with the first pump pulse. This scheme is therefore very attractive for step-wise mechanisms, in which the molecules that do not interact with all pump pulses reform the reactant. On the other side in the accumulative scheme all transient signals cannot be used for analysis since they are usually not recorded.

In this chapter a setup and an experiment are presented that allow the combination of chiral control on the basis of circular dichroism with polarization-shaped femtosecond laser pulses and the pump–probe principle. In the next section a concept that affords switching between the exact mirror images of laser pulses is introduced. In the third section the anisotropy artefacts that appear when polarization-shaped pulses are used in a pump–probe experiment are presented as well as an experimental arrangement in which these anisotropy effects are cancelled. The fourth section gives a simulation of an experiment including many experimental errors that can be accounted for by simple calculations in order to estimate the feasibility of a pump–probe experiment that seeks to prove a circular dichroitic effect of the pump pulse onto the transient dynamics. The section thereafter shows how the experimental setup can also be used for transient circular dichroism as well as transient optical rotatory dispersion measurements. The chapter closes with a comparison of the accumulative scheme versus the pump–probe scheme for proving a circular-dichroism effect of a pump pulse.

7.2 Setup for polarization mirroring

In this section a setup for polarization mirroring is presented. In the first subsection it is described what happens upon mirroring with the polarization. The basic idea of the setup is explained thereafter. In the third subsection a simple version of the setup is given, which does not fulfill the pretense that the incident and outgoing polarization of the setup need to be the same or the exact mirror image. The inclusion of the rotating periscopes from the fourth subsection results in the setup of the fifth subsection which also fulfills the previous requirement that incident and outgoing polarization are the same.

7.2.1 Mirror image of a polarization state

In order to understand the concept of the mirror image of a polarization state it is helpful to remember that any polarization state can be separated into a circular and linear part (see Section 2.2.1 and [29]). Upon reflection at an ideal surface, i.e. no intensity change and no phase offset, the transformation $rcpl \rightarrow lcpl$ and vice versa is performed, whereas the relative phase δ does not change its sign, leading to the transformed Jones vector E_t of an arbitrary input polarization state,

$$\vec{E}_t = \text{transform} \left(A_1 \begin{pmatrix} 1 \\ i \end{pmatrix} + A_2 \begin{pmatrix} 1 \\ -i \end{pmatrix} e^{i\delta} \right) = A_1 \begin{pmatrix} 1 \\ -i \end{pmatrix} + A_2 \begin{pmatrix} 1 \\ i \end{pmatrix} e^{i\delta}, \quad (7.1)$$

since the handedness of circularly polarized light is defined by the wave vector and the rotation direction. While the rotation direction does not change its sign upon reflection, the wave vector does (“a mirror exchanges front and rear”). Therefore the handedness also changes while the relative phase between the components is preserved.

The circular part of a polarization state can be described on the Poincaré sphere as a pure circular polarization $\begin{pmatrix} a \\ b \\ c \end{pmatrix} = \begin{pmatrix} a_p = 0 \\ b_p = 0 \\ c_p \neq 0 \end{pmatrix}$, with a_p , b_p and c_p being the projection onto the respective axes of the Poincaré sphere in Figure 2.5. Upon reflection this polarization state is transformed into $\begin{pmatrix} 0 \\ 0 \\ -c_p \end{pmatrix}$.

While the transformation is straightforward for the circular part, attention has to be paid to the linear part. Linear polarization can be separated into two circularly polarized components with a relative phase δ_{rcpl} (Eq. 2.56) that determines the orientation θ of the polarization. When the transformation $rcpl \rightarrow lcpl$ and vice versa is applied the relative phase δ_{rcpl} of the $rcpl$ component changes its sign,

$$\text{transform} \left(\begin{pmatrix} 1 \\ i \end{pmatrix} + \begin{pmatrix} 1 \\ -i \end{pmatrix} e^{i\delta_{rcpl}} \right) = \begin{pmatrix} 1 \\ -i \end{pmatrix} + \begin{pmatrix} 1 \\ i \end{pmatrix} e^{i\delta_{rcpl}} \quad (7.2)$$

$$= \left(\begin{pmatrix} 1 \\ -i \end{pmatrix} e^{-i\delta_{rcpl}} + \begin{pmatrix} 1 \\ i \end{pmatrix} \right) e^{i\delta_{rcpl}}, \quad (7.3)$$

hence the orientation $\theta = \frac{\delta_{rcpl}}{2}$ (see Eq. 2.56) also changes its sign. On the Poincaré sphere (Figure 2.5) the linear polarization direction in the mirror image is therefore obtained by mirroring the point at the axis of the principal directions of the Jones vector, i.e. a linear polarization $\begin{pmatrix} a_p \\ b_p \\ 0 \end{pmatrix}$ is transformed into $\begin{pmatrix} a_p \\ -b_p \\ 0 \end{pmatrix}$, with a direction corresponding to the direction of the first element of the Jones vector and $-a$ corresponding to the direction of the second element of the Jones vector. These directions are given by the reference system of the Jones vector in which the transformation occurs, i.e. the orientation of the mirror.

Combining the movement on the Poincaré sphere of the circular part and the linear part, one obtains on the Poincaré sphere upon mirroring of the polarization $\begin{pmatrix} a_b \\ b_p \\ c_p \end{pmatrix}$ the polarization $\begin{pmatrix} a_b \\ -b_p \\ -c_p \end{pmatrix}$. This can in a simpler way be perceived as a rotation of the polarization state on the Poincaré sphere around the principal direction axis of the Jones vector by π when being mirrored.

7.2.2 Principle idea

The basic idea for a setup that performs the transformation $rcpl \rightarrow lcpl$ and vice versa on a polarization state has as central element a 0° mirror, because upon reflection on top of the transformation $rcpl \rightarrow lcpl$ at such a mirror s and p direction is not defined and hence the polarization state is not altered in any other way by intensity effects or phase offset effects. However, a simple reflection to obtain the mirror image does not suffice, because the obtained mirror image has somehow to be recombined with the original polarization so that they propagate collinearly, whereas after the reflection they first propagate anticollinearly. A further requirement of the setup is that the original polarization state is not changed in the course of mirroring. The next subsection describes the solution to recombine original and mirror polarization. Afterwards the modifications necessary to fulfill the pretense of not changing the original polarization are described.

7.2.3 Collinear recombination

To achieve collinear recombination of the mirrored (m) and the original (o) polarization a Mach-Zehnder interferometer is employed in which one mirror is replaced with a beamsplitter and a subsequent 0° mirror, as shown in Figure 7.2.

In this figure the mirrors and beamsplitters are framed by black and blue circles, respectively. After passing the first beamsplitter (bottom left) and several more optical elements, the green path passes a 0° mirror (second mirror), whereas the red path does not. The green path is reflected five times, whereas the red path is reflected only four times. Hence the number of $rcpl \rightarrow lcpl$ transformations is odd for the green path which

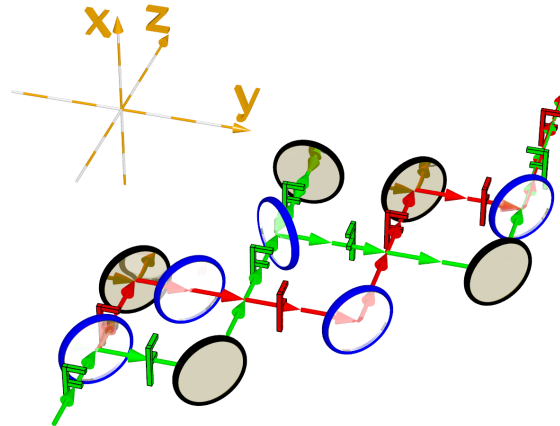


Figure 7.2: Basic idea of the setup that generates the mirror image of a polarization. In a Mach-Zehnder interferometer (mirrors are framed black, beamsplitters are framed blue, “F” indicates the current state of the polarization compared to the original polarization after every mirror) one mirror is substituted in the green path by a beamsplitter and a 0° mirror (middle, second mirror) to generate the mirror image. The red path has one reflection less, hence green and red path are mirror images of each other while propagating collinearly. With the assumption that the reflection and transmission coefficients of the optics are the same for the s and p component (except for the sign), the original polarization is maintained for the red path (original: o), since the number of reflections is even (4). The mirrored polarization is obtained via the green path (mirrored: m), since the number of reflections is odd (5). This can be verified by the “F” when using the right-hand rule with the thumb showing towards the top of the initial “F” and the forefinger showing in direction of the horizontal bars. In case of original polarization the middle finger should show in the propagation direction, otherwise opposite to the propagation direction. Two additional beamsplitters have to be inserted into the red path to account for the beamsplitter before the 0° mirror in the green path. However, the polarization of the incident light (green, bottom left) is different from the outgoing polarization (green/red, top right), since all the mirrors interact with the polarization with their respective Jones matrix.

results in the mirrored polarization m compared to the incident polarization (see green “F” after the last beamsplitter), if it is assumed that the coefficients for s and p polarized light are the same except for the sign. With this assumption the polarization after the red path would correspond to the original polarization o (see red “F” after the recombination mirror). Both paths are recombined at the last beamsplitter and propagate collinearly afterwards. Additionally, a beamsplitter of which only the transmitted portion is used is inserted into the red path and one mirror in the red path is replaced by a beamsplitter of which only the reflected portion is used. Therefore the total number of reflections and transmission at a beamsplitter amount to two, respectively, for both paths.

When neglecting the intensity effect of the 0° mirror (which is very small, $< 1\%$ when choosing a good mirror), the two polarizations o and m leaving the recombination beamsplitter are exactly mirror images with respect to each other. However, the polarization

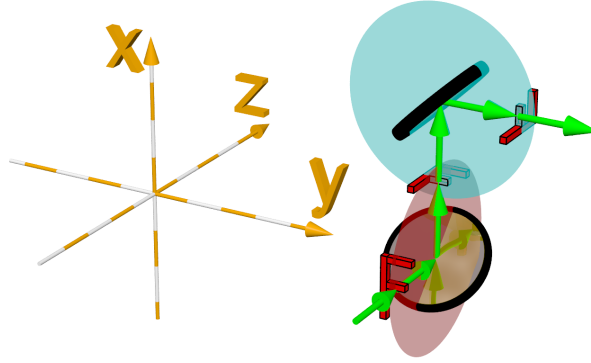


Figure 7.3: In a rotating periscope the polarization of the incoming beam is preserved while changing the wave vector of the light, because the plane of incidences of the two mirrors (first: red, second: cyan) enclose an angle of 90° . Therefore the s component of the first mirror is the p component of the second mirror and vice versa. After passing the periscope, the polarization of the original beam is rotated by 90° towards the laboratory reference system (left), as can be seen directly when looking at the “F”.

is not the same as the incoming beam, because at every mirror the Jones matrix leads to different attenuation of the s and p component as well as different phase offsets for mirrors possessing partly imaginary indices of refraction (Section 2.2.2). The same applies to the beamsplitters, whose indices of refraction and transmission differ usually much stronger for the s and p component. In the next subsections a solution to this issue is presented.

7.2.4 Polarization independence

In a perfect rotating periscope as shown in Figure 7.3 the planes of incidence of mirror 1 (red) and mirror 2 (cyan) enclose an angle of $\alpha = 90^\circ$.

With both mirrors being of the same material they possess the same Jones matrix $E_m = \begin{pmatrix} r_\perp & 0 \\ 0 & r_\parallel \end{pmatrix}$ (Section 2.2.2). An incident polarization $\vec{E}_i = \begin{pmatrix} s \\ p \end{pmatrix}$ ($s \rightarrow x$, $p \rightarrow y$) leaves the rotating periscope then with the polarization \vec{E}_o ,

$$\vec{E}_o = E_m \cdot Rot_p(\alpha) \cdot E_m \cdot \vec{E}_i = \begin{pmatrix} -r_\perp r_\parallel p \\ r_\perp r_\parallel s \end{pmatrix}. \quad (7.4)$$

The directions s and p are also rotated by 90° from their initial meaning after leaving the last mirror. A rotation back to $s \rightarrow x$, $p \rightarrow y$ yields for \vec{E}_o the original polarization since both components are attenuated (and phase-shifted in case of partly imaginary indices of refraction) by $r_\perp r_\parallel$. Hence, the polarization is maintained [196], while acting on the propagation wave vector like a mirror that changes the wave vector only.

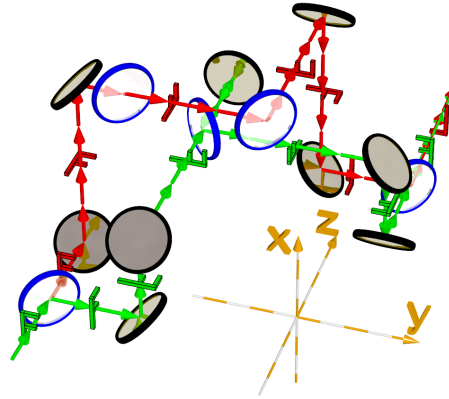


Figure 7.4: Combination of Figure 7.2 and Figure 7.3 to achieve a setup that generates the mirror image while also preserving the original polarization. All mirrors (framed black) from Figure 7.2 are thereby substituted with rotating periscopes (Figure 7.3). Furthermore, the positions of the beamsplitters (framed blue) lead to reflection and transmission of both components once in each beam path, hence the effects due to different Jones matrices of the beamsplitters are cancelled. Similar to Figure 7.2 the original polarization o is obtained via the red path and the mirrored polarization m via the green path, which can be verified by the “F”s and the right-hand rule (see Caption of Figure 7.2).

7.2.5 Setup

Substitution of all mirrors (except the 0° mirror) in Figure 7.2 by rotating periscopes (Figure 7.3) results in the setup shown in Figure 7.4. Two issues need to be addressed, the different path lengths of the red and green path and the position of the beamsplitters (framed blue in Figure 7.4).

The different path lengths can be elegantly solved by different heights (x direction) of the red and green path, hence additional mirrors for delay paths are not necessary. The red path must be higher than the green path by the distance from the beamsplitter and the 0° mirror in the green path to achieve equal path lengths for both paths.

The beamsplitters must be positioned such that the initial s and p component are both once reflected and transmitted, which is fulfilled by the positions chosen in Figure 7.4. In that case their effects also cancel, similar to Eq. 7.4. Furthermore the beamsplitters need to be symmetric [37], meaning their Jones matrix should be invariant to the direction in which they are passed. This condition is fulfilled by metallic cubic beamsplitters, furthermore they offer very good beamsplitter properties ($r_\perp \approx -r_\parallel \approx t_\perp \approx t_\parallel \approx \frac{1}{\sqrt{2}}$) over a wide spectral range with low absorption (see Appendix C).

However, they introduce an additional wavelength-dependent retardation, but since the application of this setup is the combination with a pulse shaper, this additional phase can easily be corrected by the pulse shaper. Furthermore this additional phase is an instrument constant, therefore it only needs to be measured once to correct this effect later-on.

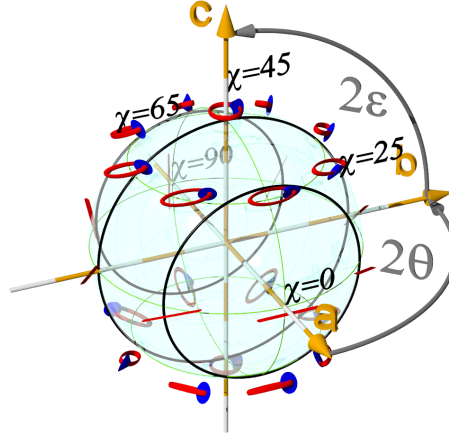


Figure 7.5: Limitation of accessible ellipticities dependent on χ according to Eq. 7.5. All ellipticities available at a given χ lie on the corresponding black circle. All ellipticities ($-\frac{\pi}{4} \leq \epsilon \leq \frac{\pi}{4}$) are only available when $\chi = 45^\circ$ which encloses the poles. If $\chi = 90^\circ$ or $\chi = 0^\circ$ only linear polarization in $\theta = 90^\circ$ and $\theta = 0^\circ$ direction is possible, respectively.

7.3 Anisotropy dependent on polarization

The magic-angle conditions in Section 3.1.4 can only be applied to linearly polarized pump pulses to achieve that the pump–probe signal is independent of the angle α between the pump and probe transition dipole moment. This independence of α is called from now on “anisotropy-free” condition. In order to allow for anisotropy-free conditions with arbitrarily polarized pump pulses a different approach than the magic angle has to be taken as shown in this section. Anisotropy-free conditions are necessary when using a polarization-shaped pump pulse in a pump–probe experiment in order to probe only the transient populations while cancelling anisotropy contributions.

Any polarization state \vec{E} can be expressed by

$$\vec{E} = A \begin{pmatrix} \cos \chi e^{i\delta_1} \\ \sin \chi e^{i\delta_2} \end{pmatrix} = A \begin{pmatrix} \cos \chi \\ \sin \chi e^{i\delta} \end{pmatrix} e^{i\delta_1}, \quad (7.5)$$

with A being the real-valued amplitude (see Eq. 2.35) and δ being the relative phase $\delta = \delta_2 - \delta_1$. The angle χ thereby corresponds to the orientation θ of the Poincaré sphere (Figure 2.5) in case of $\delta = 0^\circ$. The expressible polarizations with one fixed χ correspond to one of the black circles in Figure 7.5. As can be seen all ellipticities are only available when $\chi = 45^\circ$, whereas if $\chi = 0^\circ$ or $\chi = 90^\circ$ only linear polarization in $\theta = 0^\circ$ and $\theta = 90^\circ$ is possible, respectively.

The expression in Eq. 7.5 is directly related to polarization shaping with liquid-crystal spatial-light modulators [22]. In this technique the spectral components of the two components of the Jones vector are independently retarded (δ_1 and δ_2 in Eq. 7.5). Hence, the relative phase δ between the components in Eq. 2.40 is varied, whereas χ cannot be changed. Changing χ requires the use of vector-field synthesizers [197]. However,

as will be shown in Section 7.3.3, this is not necessary to allow for an anisotropy-free pump-probe experiment in which the pump process is a 1-photon process and the pump polarization has been shaped with a two-layer pulse shaper. Similar to before, χ is also an instrument constant (of the laser system and the pulse shaper) and needs to be accounted for always in the same way later-on once being determined.

7.3.1 Pumped distribution

The distribution $P3(\theta, \phi, \alpha, \chi_{pu}, \delta_{pu})$ (see Appendix for derivation, Eq. B.11) describes the probability to find the probe transition dipole moment of one molecule in direction (θ, ϕ) whose corresponding pump transition dipole moment (both enclose the angle α) has been excited by the electric field propagating in z direction with the Jones vector $\begin{pmatrix} \cos \chi_{Pu} \\ \sin \chi_{Pu} e^{i\delta_{Pu}} \end{pmatrix}$. Six examples of the distribution resulting from this equation are presented in Figure 7.6 and Figure 7.7 to illustrate the effect of the pump polarization and α onto the distribution that can be probed. Note that for this calculation the molecule is assumed to be immobile, i.e. it does not rotate. The influence of the rotational degrees of freedom, as well as alignment and orientation, are discussed shortly in Appendix B.2.

In the top-left of Figure 7.6 $P3(\theta, \phi, \alpha = 0^\circ, \chi_{Pu} = 90^\circ, \delta_{Pu} = 0)$ is shown, hence pump and probe transition dipole moment are parallel and the pump pulse is polarized linearly in y direction (blue arrow) and propagates in z direction (to the top, green arrow). It follows the commonly known \cos^2 distribution indicating that the highest probability to find a probe transition dipole moment that can be probed due to excitation of the corresponding pump transition dipole moment is oriented in the direction $(\theta = 90^\circ, \phi = 90^\circ)$ with $x \rightarrow (\theta = 90^\circ, \phi = 0^\circ)$, $y \rightarrow (\theta = 90^\circ, \phi = 90^\circ)$ and $z \rightarrow (\theta = 0^\circ)$. Note that it is necessary that the distribution has rotational symmetry around the pump-polarization axis, in this case the y axis. Furthermore note also that the distribution possesses mirror image symmetry towards the plane normal to the polarization direction, here the x - z plane. Independent of α both symmetry conditions need to be fulfilled for $P3$ for linearly polarized pulses since the pump polarization also possesses this symmetry. However, the distribution is not symmetric towards rotation around the propagation axis (green arrow).

In the top-right figure [$P3(\theta, \phi, \alpha = 90^\circ, \chi_{Pu} = 90^\circ, \delta_{Pu} = 0)$] the pump polarization is the same as on the left, but $\alpha = 90^\circ$. Now the distribution is a torus, which can easily be understood because of the previously two mentioned conditions for linearly polarized pump. Note that in this case the propagation vector also runs from bottom to top and as before the distribution is not symmetric towards rotation around the propagation axis.

This changes in the two figures in the bottom of Figure 7.6 [right: $P3(\theta, \phi, 0^\circ, 45^\circ, \frac{\pi}{2})$, left: $P3(\theta, \phi, 90^\circ, 45^\circ, \frac{\pi}{2})$], in which a circularly polarized pump is used as indicated by the blue disk. Now the distribution needs to be symmetric towards rotation around the propagation axis (green arrow), because the pump polarization also possesses this symmetry.

In case of elliptically polarized light ($\delta_{Pu} = 70^\circ$ in Figure 7.7) no rotation symmetry, except rotation by 180° , remains. As shown in the next section and in the Appendix B.1

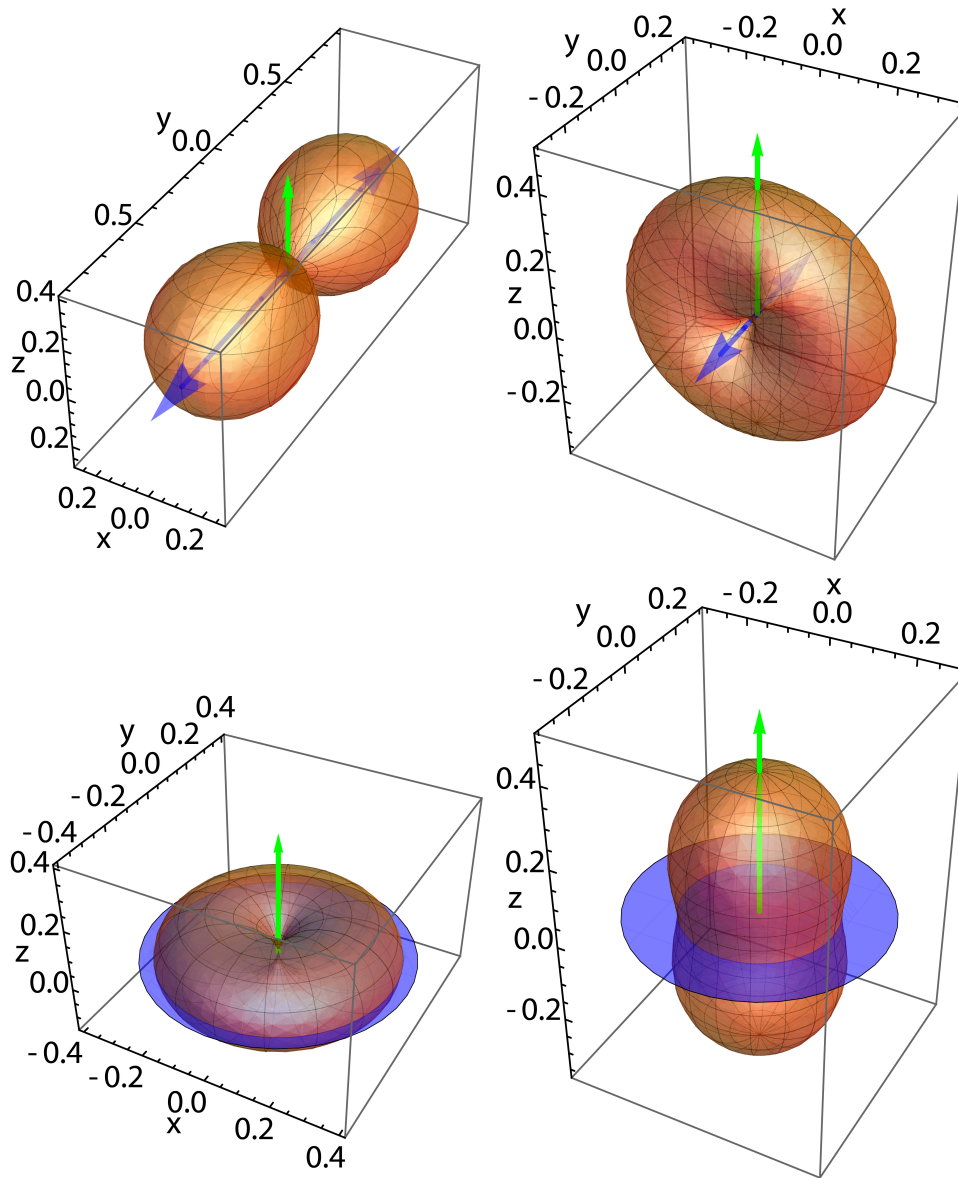


Figure 7.6: Distribution P_3 (Eq. B.11) describing the probability to find the probe transition dipole moment of one molecule in the direction (θ, ϕ) whose corresponding pump transition dipole moment (both enclose the angle α) has been excited. The coordinate system of the distribution is thereby given in cartesian coordinates (see text). Beam propagation occurs along the z axis (green arrow) and pump excitation is indicated by the blue arrow (linear polarization) or disk (circular polarization). Top left: Linearly polarized pump in y direction with $\alpha = 0^\circ$ gives the well-known \cos^2 distribution in y direction. Top right: Linearly polarized light in y direction with $\alpha = 90^\circ$ gives a torus. Note that in these two cases the distribution is symmetric towards rotation around the polarization axis, affording that the differences in the distribution described by P_3 caused by α can be cancelled in the pump–probe signal by adjusting the magic angle between linear pump and linear probe polarization (Section 3.1.4). Bottom: Circularly polarized light (left: $\alpha = 0^\circ$, right: $\alpha = 90^\circ$) leads to a distribution which is not symmetric around the polarization axis (circularly polarized light does not have an orientation). To eliminate the α dependence on the pump–probe signal for polarizations with $\delta_{Pu} \neq 0$ an approach different to the magic angle needs to be found (Section 7.3.3).

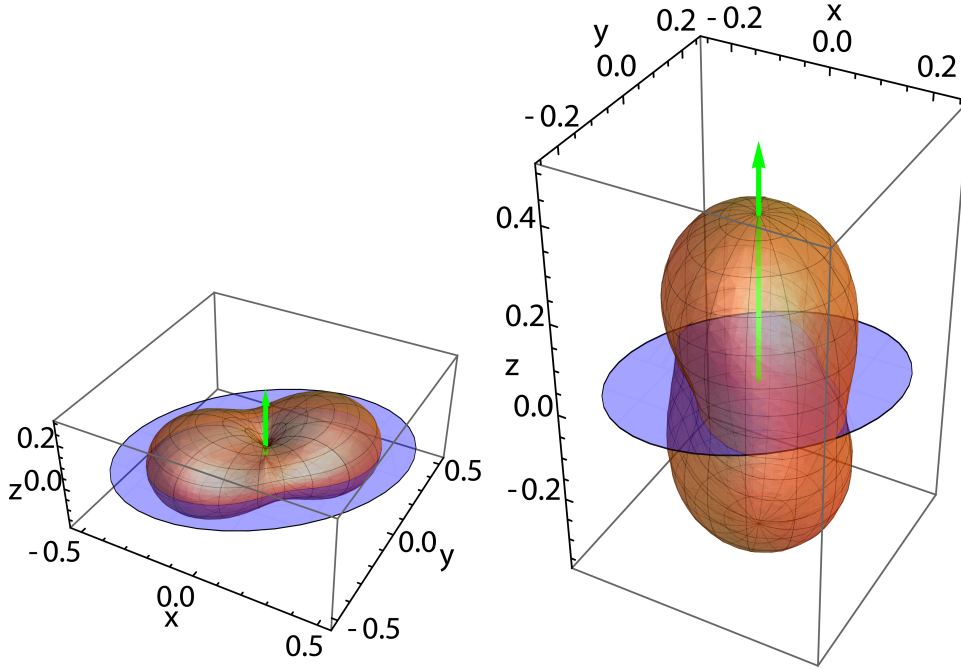


Figure 7.7: Distribution $P3$ (Eq. B.11) describing the probability to find a probe transition dipole moment in the direction (θ, ϕ) whose corresponding pump transition dipole moment (both enclose the angle $\alpha = 0^\circ$ (left) and $\alpha = 90^\circ$ (right)) has been excited with elliptically polarized light (with the blue ellipse describing the polarization state of the pump) with a relative phase of $\delta_{P_u} = 70^\circ$ propagating in z direction (green arrow). In this case no rotation symmetry exists in contrast to linearly and circularly polarized light (see Figure 7.6).

the loss of symmetry due to elliptically polarized light leads to a completely different solution to circumvent the anisotropy for any polarization expressed by Eq. 7.5 (for the special case of circularly polarized light see [198]).

7.3.2 Probing probability

The probability distribution $P3$ needs to be multiplied with the distribution $P4$ that a probe pulse with arbitrary polarization can query in an isotropic medium to obtain the probability distribution that an excited molecule is probed in a pump–probe experiment as shown in the Appendix (Eq. B.12 to Eq. B.17, called $P5$). The probed distribution ($P5$) is a function of the Jones vector of the pump $\vec{E}_{P_u} = \begin{pmatrix} \cos \chi_{P_u} \\ \sin \chi_{P_u} e^{i\delta_{P_u}} \end{pmatrix}$ and probe $\vec{E}_{P_r} = \begin{pmatrix} \cos \chi_{P_r} \\ \sin \chi_{P_r} e^{i\delta_{P_r}} \end{pmatrix}$, the angle α between pump and probe transition dipole moment, the angle β describing the angle between the wave vectors of the pump and probe electric field (see Figure 7.8), and the spherical coordinates θ and ϕ .

However, this distribution is not intuitive to understand. Nevertheless, the integral

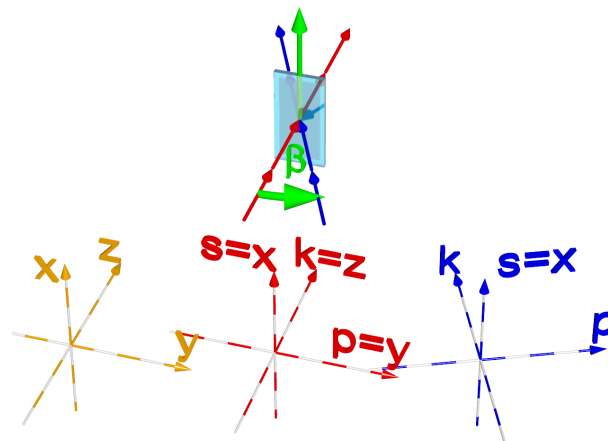


Figure 7.8: Definition of the angle β (rotation axis: green arrow) describing the angle of the wave vector of the pump (red) and probe (blue) beam (which are spatially overlapped in the sample, the blue flow cell) in the laboratory coordinate system (bottom left, yellow). As can be seen by the coordinate systems of the pump (bottom middle, red) and the probe (bottom right, blue) the s direction of pump and probe does not change upon rotation along the angle β , only the direction of the p component and the wave vector (k) of the probe changes with β .

P_{Pr} over the spherical coordinates

$$P_{Pr}(\alpha, \chi_{Pu}, \delta_{Pu}, \chi_{Pr}, \delta_{Pr}, \beta) = \int_{\phi=0}^{2\pi} \int_{\theta=0}^{\pi} P5(\theta, \phi, \alpha, \chi_{pu}, \delta_{pu}, \chi_{pr}, \delta_{pr}, \beta) \sin \theta d\theta d\phi \quad (7.6)$$

of this probability distribution is proportional to the transient-absorption signal ΔA (see Appendix B.1, especially Eq. B.24), the decisive property in transient-absorption pump-probe experiments.

7.3.3 Anisotropy-free conditions

As shown in Section 3.1.4 taking the correct parameters the magic angle is readily obtained by setting the differentiated probing probability P_{Pr} with respect to α zero,

$$\frac{\partial P_{Pr}(\alpha, 0, 0, \chi_{Pr}, 0, 0)}{\partial \alpha} = 0, \quad (7.7)$$

and solving for χ_{Pr} . Differentiation has to occur with respect to α because the independence of the pump-probe signal on the angle between pump and probe transition dipole moment is the aim.

However, extending the pump polarization with a relative phase (Eq. 7.5) ($\delta_{Pu} \neq 0$ and $\chi_{Pu} \neq n\frac{\pi}{2}$) it is no more possible to find a solution to this equation. Instead a solution (see Appendix B.4.3) can be found for

$$\frac{\partial P_{Pr}(\alpha, \chi_{Pu}, \delta_{Pu}, \chi_{Pr} = 90^\circ, 0, \beta)}{\partial \alpha} = 0. \quad (7.8)$$

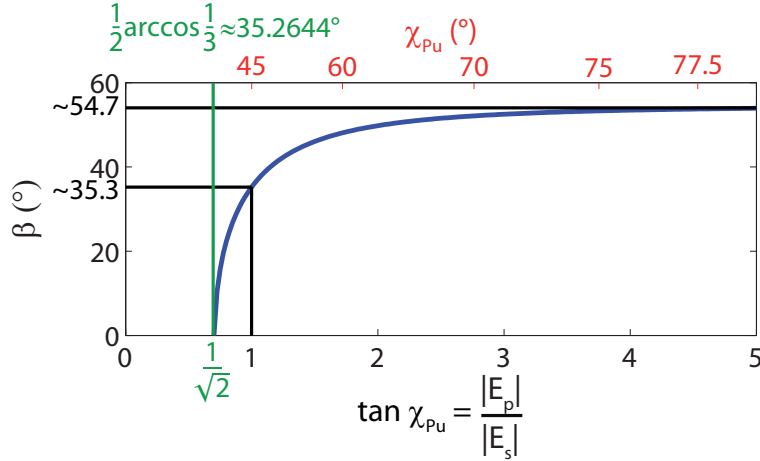


Figure 7.9: Condition for β (Eq. 7.9, see also Figure 7.8) to result in a pump–probe signal that is independent of α (the angle between pump and probe transition dipole moment) and δ_{Pu} (the relative phase between the components of the pump electric field) but still depends on χ_{Pu} (Eq. 7.5). The angle β does not depend on the sign of χ_{Pu} , therefore polarization mirroring as described in Section 7.2.1 results in the same β for original and mirror-image polarization (Figure 7.11).

It is crucial that the polarization of the probe is p (see Eq. B.17 and Figure 7.8). In case of an s polarized probe pulse, β would have no influence at all and an anisotropy-free condition would be impossible to reach by altering β . The condition that is derived for β with p polarized light (Appendix B.4.3),

$$\beta = \pm \arccos \left(\pm \frac{1}{\sqrt{3} |\sin \chi_{Pu}|} \right), \quad (7.9)$$

to obtain an anisotropy-free pump–probe signal depends on χ_{Pu} as shown in Figure 7.9. Note, that in case of $\chi_{Pu} = 90^\circ$ the pump is linearly polarized in $p = y$ direction, see Figure 7.8. With the probe being oriented in p direction and $\beta \approx 54.735^\circ$, following Eq. 7.9, the situation is exactly the same as met under the conventional magic-angle conditions: pump and probe polarization enclose the angle $\approx 54.735^\circ$. Assuming linearly polarized pump pulses ($\delta_{Pu} = 0$), the angle between the pump and probe polarization is always the magic angle ($\approx 54.735^\circ$) when Eq. 7.9 is fulfilled, remember that the probe

is linearly polarized in $\begin{pmatrix} 0 \\ \cos \beta \\ \sin \beta \end{pmatrix}$ direction (Figure 7.8). Thus, it is obvious that for $\chi_{Pu} \leq 90^\circ - 54.735^\circ \approx 35.264^\circ$ it is impossible that linear pump and probe polarization enclose an angle of $\approx 54.735^\circ$ by only adjusting β (see Figure 7.9), since the probe polarization lies in the y – z plane for any β .

Translated back into the Poincaré sphere from Figure 7.5 in the two-dimensional representation from Figure 2.6 this means that for any polarization that is not contained within the gray area of the Poincaré sphere shown in Figure 7.10, which includes the portion fulfilling $\chi_{Pu} \geq 35.2644^\circ$, there exists an angle β that allows anisotropy-free

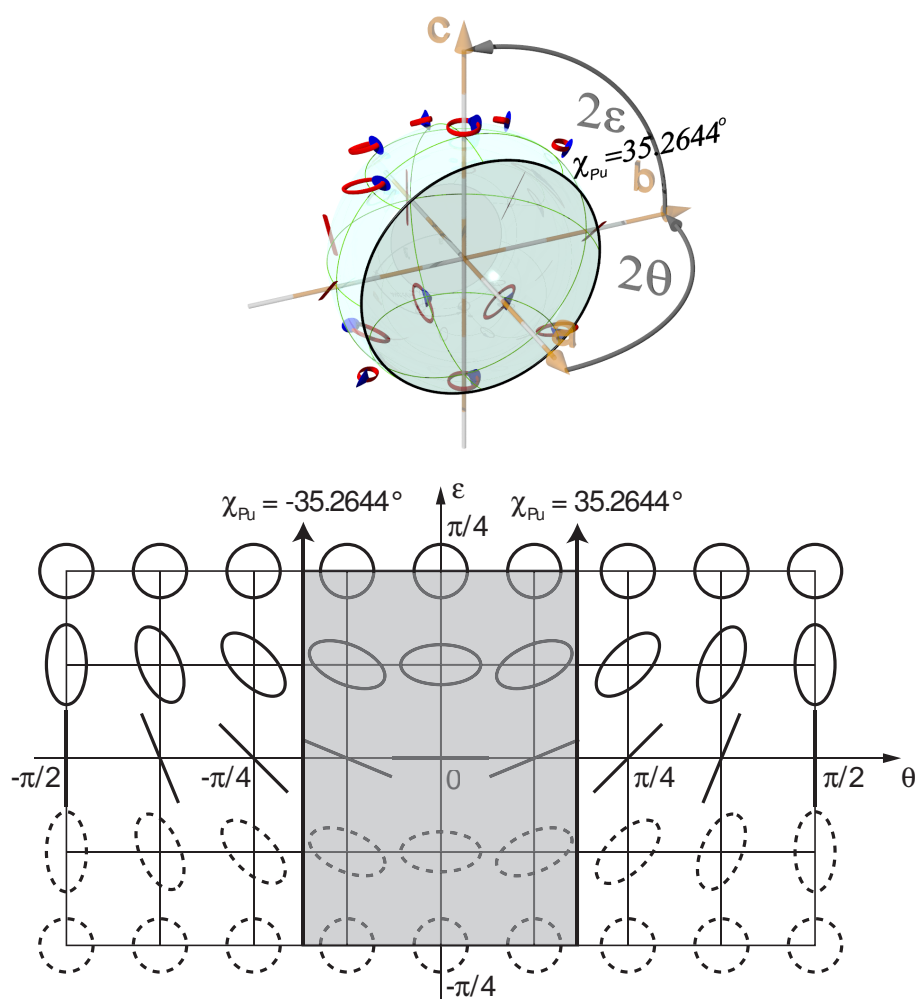


Figure 7.10: Anisotropy-free measurements are possible for any pump polarization that lie inside the section of the Poincaré sphere (top), or, in the two-dimensional representation of Figure 2.6, outside of the grey area (bottom). Note, that the poles do not lie within the grey area. Anisotropy-free conditions are achieved by adjusting the angle β according to Eq. 7.9 dependent on χ_{Pu} , see also Figure 7.9. Also note, that $\theta = 0^\circ$ corresponds to the x direction in Figure 7.8.

measurements.

7.3.4 Anisotropy-free conditions combined with pulse shaping and polarization mirroring

As shown in Section 7.2.1 upon generating the mirror image of the polarization a rotation by 180° around the $\theta = 0^\circ$ axis takes place on the Poincaré sphere. The direction of $\theta = 0^\circ$ is thereby assumed to be on the one hand in x direction in the laboratory frame, as this is one principal direction of the Jones matrices of the optical elements in the

polarization-mirroring setup (see Figure 7.4), and on the other hand in $+a$ direction in the Poincaré sphere. From Eq. 7.9 it follows that the sign of χ_{Pu} is irrelevant for the condition for β in Eq. 7.9.

In order to investigate whether polarization mirroring changes the condition for β it is sufficient to concentrate only on linear polarizations ($\delta_{Pu} = 0$), since δ_{Pu} does not have an influence on β (Eq. 7.9). Two cases will be investigated.

In the first case it is assumed that the angle χ_{Pu} from Eq. 7.5 is defined in the same coordinate system as the orientation θ from the Poincaré sphere, with $\theta = \chi_{Pu} = 0$ corresponding to linear polarization in x direction (see Figure 7.5 and blue circles and arrows in Figure 7.11). In this case the mirroring of the original linear polarization in $\theta = 30^\circ$ direction (solid blue arrow) leads to polarization in $\theta = -30^\circ$ direction, shown as the dashed blue arrow, due to 180° rotation around the a axis. This polarization can be described by $\chi_{Pu} = -30^\circ$ with a relative phase of $\delta_{Pu} = 0$ or $\chi_{Pu} = 30^\circ$ with a relative phase of $\delta_{Pu} = \pi$. Hence, the condition for β does not change.

In the second case χ_{Pu} of Eq. 7.5 is defined in another coordinate system, e.g. rotated by $\theta_c = +45^\circ$ as usually is the case in two-layer liquid-crystal pulse shapers, hence, $\theta \neq \chi_r$ even for linearly polarized pulses, with χ_r being defined in the rotated coordinate system and χ_u being defined in the unrotated coordinate system. For the case of $\theta_c = +45^\circ$, the polarizations that can be achieved with $\chi_r = 30^\circ$ by changing the relative phase δ are described by the red solid circle (Figure 7.11). Upon mirroring one of these polarizations, i.e. 180° rotation of the solid red arrow around the a axis, one obtains the dashed red arrow as polarization. This polarization lies on the dashed red circle $\chi_r = 90^\circ - 30^\circ = 60^\circ$. Whereas both red arrows can still be connected by the dashed blue circle with $\chi_u = 45^\circ - 30^\circ = 15^\circ$ allowing for polarization mirroring, this is only valid for one fixed value of δ_{Pu} . As can be seen the change of δ_{Pu} in the rotated coordinate system, a motion along a red circle, leads to a change in the value of χ_u that connects the original and the mirrored polarization in the unrotated coordinate system (blue circles). The change of χ_u means a change in the condition for β in Eq. 7.9. Generally no condition for β can be found that allows anisotropy-free pump-probe signals independent of δ_{Pu} (see Appendix B.4.3) for any coordinate system except the coordinate system of the polarization-mirroring setup. However, in an experimental setup this can easily be corrected by inserting a $\frac{\lambda}{2}$ plate just before the sample that rotates the coordinate system back by $-\theta_c$.

In a two-layer pulse shaper for femtosecond polarization shaping the retardation is introduced between the components oriented at $\theta = +45^\circ$ and $\theta = -45^\circ$ of the laboratory reference system [$\theta = 0^\circ = \vec{e}_x$ corresponding to a direction parallel to the table surface (horizontal) and $\theta = 90^\circ = \vec{e}_y$ corresponding to the perpendicular direction of the table (vertical), see for example Figure 7.8]. Therefore in a two-layer pulse shaper χ_{Pu} is in the ideal case fixed and $\theta_c \neq 0$, necessitating the mentioned $\frac{\lambda}{2}$ plate. When using vector-field synthesizers [197] the pulse shaper is able to introduce the relative phase δ_{Pu} in any coordinate system, thus also in the coordinate system given by $\theta_c = 0^\circ$.

Hence, χ_{Pu} only has to be determined once to find the correct angle β for the experimental setup. Depending on the pulse shaper an additional wave plate has to be inserted to correct for a rotation of the coordinate system of the pulse shaper against the coordinate system of the polarization-mirroring setup, but in principal any value of

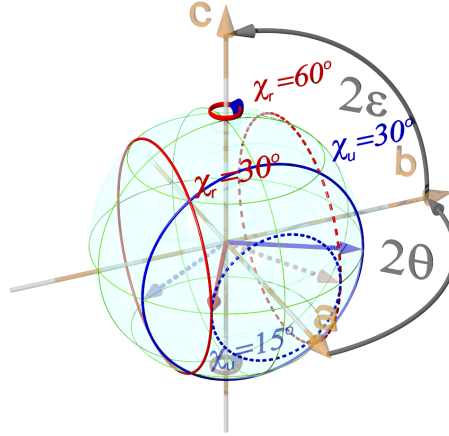


Figure 7.11: Polarization mirroring corresponds to a rotation around the principal axis of the Jones vector on the Poincaré sphere, this axis is determined by the polarization-mirroring setup and defined here to be the a axis. If χ_{Pu} in Eq. 7.5 is defined in the same coordinate system as θ , i.e. for linearly polarized pulses $\theta = \chi_{Pu}$, the blue circles represent the possible polarizations with changing relative phase δ_{Pu} for a fixed value of $\chi_u = \chi_{Pu}$ (with χ_u being defined in this coordinate system). Upon mirroring a polarization, e.g. the solid blue arrow, the obtained polarization, i.e. the dashed blue arrow, still lies on the same circle, hence, the value of χ_u does not change and therefore the condition for β (Eq. 7.9) also does not change making anisotropy-free measurements possible independent of the relative phase δ_{Pu} . The situation changes when χ_{Pu} of Eq. 7.5 is not defined in the same coordinate system as θ , i.e. $\theta \neq \chi_{Pu}$. For example in case of a rotated coordinate system by 45° (the χ_{Pu} values defined in this system are labeled χ_r), polarization mirroring still allows for an anisotropy-free measurement, because both red arrows lie on the $\chi_u = 45^\circ - 30^\circ = 15^\circ$ circle and therefore do not change the condition for β . But the change of δ_{Pu} in the rotated coordinate system corresponds to a motion along one of the red circles, which incorporates a change of the χ_u circle describing the polarization in the unrotated coordinate system. The change of χ_u leads to a changed condition for β and hence anisotropy-free condition independent of δ_{Pu} cannot be found if χ_{Pu} is not defined in the same coordinate system as the polarization-mirroring setup.

χ_{Pu} allows for a pump–probe signal independent of the relative phase δ_{Pu} and the angle between pump and probe transition dipole moment α .

However, for multiphoton processes χ_{Pu} needs to be 45° , else small errors are introduced due to anisotropy effects, as will be shown in Section 7.4.3. Furthermore when performing pump–repump experiments (see Section 4.5) anisotropy is much more complicated. A definite answer whether anisotropy-free measurements, where the relative phases of pump and repump are arbitrary, are possible cannot be given so far. However, in any case the original and the mirror-image polarization introduce the same anisotropy in a sample.

7.3.5 Suggestion for experimental realization

In a two-layer pulse shaper the principal axes are oriented in $+45^\circ$ and -45° direction. Since all mirrors usually do not change the height of the beam, the two components in $+45^\circ$ and -45° have the same Jones matrices on all mirrors after and before the pulse shaper, so that intensity changes dependent on the polarization can be neglected for the experiment.

As shown in the previous subsection, polarization mirroring (Section 7.2.1), can only be combined with femtosecond polarization shaping if the principal axes of the pulse shaper, as defined by Eq. 7.5, are parallel to the axes of the polarization-mirroring setup, which are assumed to be the horizontal and the vertical direction. This can be achieved with a $\frac{\lambda}{2}$ plate in the pump beam.

The coordinate system of the polarization-mirroring setup dictates the orientation and polarization of the probe pulse. In the following it is defined that the s direction of the probe is oriented along the x direction. In the definition of β (Figure 7.8) it was assumed that the s polarization of pump and probe are always parallel (see also Appendix B.1). Furthermore, the p direction of the probe encloses an angle of 90° with the s polarization. In case of $\beta = 0^\circ$ or $\beta = 90^\circ$ the p direction of the probe is the p direction of the pump or the propagation direction of the pump, respectively (see Figure 7.8).

It is desirable from the practical view that a change of χ_{Pu} does not incorporate new beam propagation directions of the probe but can be adjusted without the need to adjust any mirror. Hence, the setup in Figure 7.12 is proposed that allows to rotate the polarization of the probe such that it is parallel to the propagation direction of the pump.

Anisotropy-free conditions for this sample setup can be derived analogously to Appendix B.1 by substituting the three-dimensional probe polarization \vec{E}_{3Pr} in Eq. B.13 by

$$\vec{E}_{3Pr}(\chi_{Pr}, \beta_2) = \begin{pmatrix} \sin \beta_2 \\ 0 \\ \cos \beta_2 \end{pmatrix}. \quad (7.10)$$

Due to this definition of β_2 in Figure 7.12 ($\beta_2 = 0^\circ$: p direction of the probe equals the wave vector of the pump, s direction of the probe equals s direction of the pump; $\beta_2 = 90^\circ$: p direction of the probe equals the s direction of the pump, s direction of the probe equals the wave vector of the pump) compared to the definition in Figure 7.8 ($\beta = 0^\circ$: p direction of the probe equals the p direction of the pump, s direction of the probe equals the s direction of the pump; $\beta = 90^\circ$: p direction of the probe equals the wave vector of the pump, s direction equals the s direction of the pump), slightly changed conditions for β_2 result to allow for an anisotropy-free measurement. Note, that the probe is assumed to be linearly polarized ($\delta_{Pr} = 0$). One obtains for the anisotropy-free condition for β_2 ,

$$\beta_2 = \pm \arccos \left(\pm \frac{\sqrt{1 + 3 \cos(2\chi_{Pu})}}{\sqrt{6} |\cos \chi_{Pu}|} \right), \quad (7.11)$$

where $\beta_2 = 0^\circ$ corresponds to a probe polarization in z direction (Figure 7.12).

This setup has many practical advantages compared to the setup in Figure 7.8:

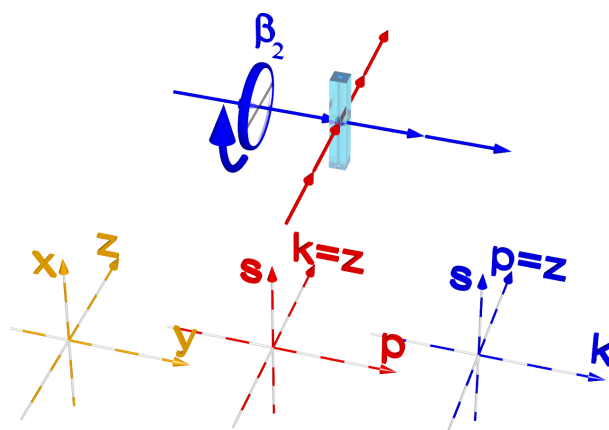


Figure 7.12: Exemplary setup in which all the requirements for anisotropy-free polarization-shaped pump-probe experiments are fulfilled. Pump and probe beam are spatially overlapped in a capillary that allows perpendicular excitation and probing (Section 3.3 and Chapter 6). This capillary is mounted in the direction of one axis of the mirroring setup (usually one of the laboratory axis, e.g. vertical). Directions of pump (red) and probe (blue) components and the respective wave vector (k) relative to the laboratory frame are given in the bottom. This setup avoids any effects that might differ for s and p component, since the incident angles for pump and probe are 0° in both cases. Furthermore a $\frac{\lambda}{2}$ plate or a linear polarizer (framed blue) in the probe beam allows for an easy adjustment of β_2 without the need to align any beampaths. However, for a polarization shaper with its principal axes rotated against the laboratory axes, an additional wave plate in the pump beam (see Section 7.3.4) just before the capillary is necessary (not shown here).

- A change of χ_{Pu} can be compensated by rotating the linear polarization of the probe into the wave vector direction of the pump. With the arrangement shown in Figure 7.12 the rotation of the probe beam (blue) polarization into the wave vector of the pump (red) is performed via a rotation of a $\frac{\lambda}{2}$ plate (or equivalently a linear polarizer) without the need to realign any of the beams after changing χ_{Pu} . However, the definition of β (Figure 7.8) cannot be applied here anymore, since it corresponds to a rotation around the s direction of the probe whereas the use of a wave plate or a linear polarizer corresponds to a rotation around the wave vector of the probe. Nevertheless for the arrangement in Figure 7.12 a condition for β_2 , the orientation of the linear polarization of the probe, can be found that also allows anisotropy-free measurements (Eq. 7.11).
- The sample needs to be in a capillary (in the middle of Figure 7.12) as used in Section 3.3 and Section 6 in which probing orthogonally to excitation direction is possible. Probing orthogonally further avoids any effect that might arise due to different Fresnel coefficients for the s and p component of either pump and probe because both hit the surface at an angle of 0° to the surface normal. Especially when looking at Figure 7.9 the internal total reflection on the rear-surface of the

capillary prohibits to have an incident angle larger than $\approx 45^\circ$ (dependent on the wavelength and the material) on the capillary surface for the probe beam. Furthermore refraction also does not take place in this arrangement when pump or probe enter the capillary.

- The bottom of Figure 7.12 shows the laboratory reference axes (yellow) and the orientation of s and p direction in this reference system of the pump (red) and the probe beam (blue) before the wave plate. Note that the s direction is the same for pump and probe. The wave vector of the probe beam is easily adjusted by the back reflection of the capillary, offering an easy and exact adjustment.

It should be noted, that the perpendicular propagation of pump and probe decreases the time resolution compared to a collinear propagation. The time resolution is in a good approximation, in which the pump pulse is assumed to be infinitely short in time, as small as the time necessary for the pump to propagate completely through the probe beam. Assuming a probe beam diameter of $50\ \mu\text{m}$, the time resolution decreases to $\Delta t \approx \frac{50\ \mu\text{m}}{c/n} \approx 250\ \text{fs}$ due to the sample setup, with c being the speed of light and n being the index of refraction in solution assumed to be 1.5 here. Note however, that a similar decrease in time resolution applies also to the sample setup shown in Figure 7.8 due to the collinearity angle between the pump and probe wave vector $\beta \neq 0$ (Figure 7.9). In that case the decrease of the time resolution depends on β .

Nevertheless for all the practical reasons given above the setup in Figure 7.12 should be chosen in a first attempt to realize anisotropy-free polarization-shaped pump–probe experiments in solution.

7.4 Ground-state circular-dichroism experiment

In the first subsection below an exemplary experiment is simulated in which the sample setup (Figure 7.12) and the polarization-mirroring setup (Figure 7.4) from the previous sections are combined to determine the ground-state circular dichroism via femtosecond pump–probe transient-absorption experiments. This allows to calculate how adjustment errors in the alignment of the polarization-mirroring setup and the sample setup corrupt the pure circular-dichroism effect measurement in the second subsection.

7.4.1 Simulation description

In the simulated experimental arrangement (see Figure 7.13) linearly polarized light in $\theta = +45^\circ$ direction passes the polarization-mirroring setup and an additional $\frac{\lambda}{4}$ plate (the retardation δ_{WP} of this wave plate will be varied from $\delta_{\frac{\lambda}{4}} = \frac{\pi}{2}$ in further discussions), oriented with its fast axis in the vertical direction ($\theta_{WP} = 90^\circ$, the orientation θ_{WP} of the wave plate will also be varied below), before entering the sample setup as pump light (blue beam in Figure 7.12). The two mirror images of the polarization state of the pump light are therefore *lcpl* and *rcpl* in case of $\delta_{WP} = \frac{\pi}{2}$. In the simulation all optical elements (mirrors, beamsplitters, wave plates) are characterized by their surface

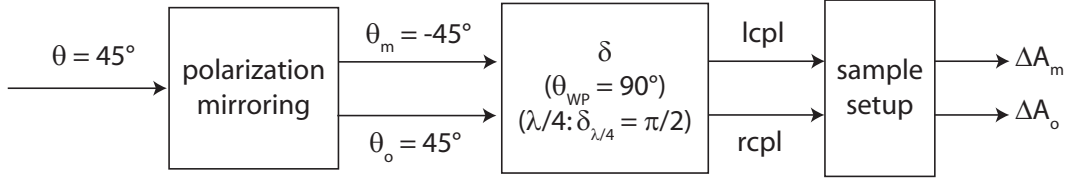


Figure 7.13: Experiment that combines the polarization-mirroring setup (Figure 7.4) with the exemplary setup (Figure 7.12) to record the ground-state circular dichroism of a sample. Linearly polarized light in $\theta = +45^\circ$ direction leads to original (o , red path in Figure 7.4) and mirrored polarization (m , green path) of $\theta_o = +45^\circ$ and $\theta_m = -45^\circ$ direction, respectively. A subsequent $\frac{\lambda}{4}$ plate that introduces a retardation of $\delta_{\frac{\lambda}{4}} = \frac{\pi}{2}$ oriented with its fast axis in the direction $\theta_{WP} = 90^\circ$ changes these polarizations to $lcpl$ and $rcpl$, respectively. With these two polarizations, when being used as pump for a chiral sample, one can determine the ground-state circular dichroism of the sample via the induced transient-absorption signals ΔA_o and ΔA_m .

normal. The effect of the sequence of the optical elements, given by the polarization-mirroring setups of Figure 7.2 or Figure 7.4 plus the additional waveplate, on the input polarization is calculated with the approach given in Section 2.2.4 to obtain the Jones vector \vec{E}_{Pu} of the pump light before the sample.

The linearly polarized probe beam propagates perpendicular to the pump beam (see Figure 7.12). The linear polarization direction of the probe is adjusted with the $\frac{\lambda}{2}$ plate in Figure 7.12 according to Eq. 7.11 to $\beta_2 \approx 54.735^\circ$, with 0° corresponding to polarization in the wave vector direction of the pump and 90° corresponding to polarization in s direction of the pump. Note, that this arrangement does not correspond to the magic angle but to the condition derived by Eq. 7.11 for circularly polarized pump pulses ($\chi_{Pu} = 45^\circ$, see Figure 7.5).

The pump intensity (\vec{E}_{Pu}) is adjusted to lead to a simulated mean transient absorption of $\Delta A_{ma} \approx 8.45$ mOD in magic-angle configuration between ΔA_o and ΔA_m , corresponding to an excitation of 8.6% of the present molecules, following the calculation given in Appendix A. This necessitates an intensity I before the polarization-mirroring setup of $I = 1$ μ J, with the other parameters, such as extinction coefficient or beam size, given in Appendix A. The transient absorption is calculated from the extinction coefficient ϵ and the circular dichroism $\Delta\epsilon$ of the sample as described in Appendix A. The circular dichroism is set to $\Delta\epsilon = \frac{\epsilon}{1000}$.

The dependence of the transient-absorption signal on the retardation δ_{WP} of the wave plate leads to a sine modulation that is caused by the circular-dichroism effect as shown in Figure 7.14. It is independent of α since the condition of Eq. 7.11 for anisotropy-free measurements is fulfilled.

The circular-dichroism signal has its minimum and maximum at a retardation of $\delta_{WP} = \frac{\pi}{2} = \frac{\lambda}{4}$ and $\delta_{WP} = 3\frac{\pi}{2} = \frac{3\lambda}{4}$, respectively, where the circular part of the pump light is maximum and the measurable circular dichroism is $\Delta A_o - \Delta A_m \approx 15$ μ OD. ΔA_o and ΔA_m are therein the absorbance changes due to the pump from the red (original polarization o) and green path (mirrored polarization m) of the polarization-mirroring

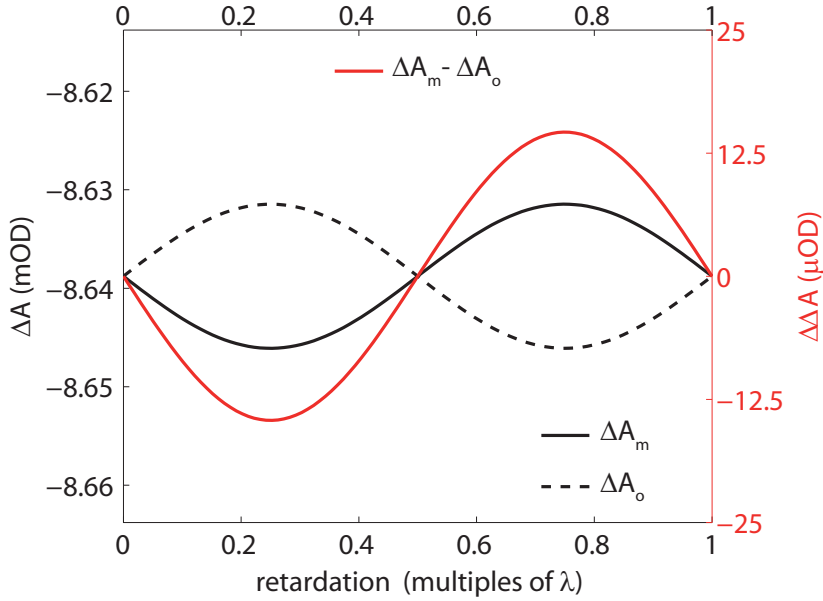


Figure 7.14: Simulated data of the exemplary experiment with the 0° mirror of Figure 7.4 assumed to be an ideal mirror. Upon changing the retardation δ_{WP} of the wave plate (Figure 7.13) the polarization of the pump changes according to the black circle with $\chi = 45^\circ$ in Figure 7.10. The ellipticity has its maximum at $0.25\lambda = 0.5\pi$ (*lcpl*) and $0.75\lambda = 1.5\pi$ (*rcpl*), leading to a maximum and minimum due to the circular-dichroism effect, respectively, for ΔA_o and vice versa for ΔA_m . Subtraction of $\Delta A_o - \Delta A_m$ gives the circular-dichroism signal (red).

setup, respectively (see Figure 7.13). These data were obtained when substituting the 0° mirror of the polarization-mirroring setup by an ideal mirror with $r_\perp = 1$ and $r_\parallel = -1$, hence the transient-absorption signal ΔA_m is slightly higher than 8.45 mOD.

When using a silver mirror with the literature index of refraction of silver one can see the influence of the change in intensity due to the additional reflection in the green path (m). The pump wavelength is assumed to be centered at $\lambda_p = 550$ nm, with the Jones matrix of the 0° mirror being $\begin{pmatrix} 0.97965e^{-0.581i} & 0 \\ 0 & 0.97965e^{2.560i} \end{pmatrix}$ [199]. Therefore the intensity of the green beam (mirrored polarization m) in Figure 7.4 is reduced by $R \approx 0.97965^2 \approx 0.959$ compared to the red beam (original polarization o). Note that the value of $R \approx 0.959$ is very pessimistic, values of $R \approx 0.99$ are much more realistic. Therefore ΔA_m in Figure 7.15 is decreased by this factor $R \approx 0.959$ compared to ΔA_o and the measured difference $\Delta A_m - \Delta A_o$ increases to 0.35 mOD.

As can be seen in Figure 7.15 (red line) the decrease in intensity due to one additional silver mirror leads to a signal that is $\approx 25\times$ higher than the circular dichroism $\Delta A_m - \Delta A_o$ in Figure 7.14. To account for this effect from now on for the simulation the data analysis shown in Figure 7.16 is performed. First the transient-absorption signals $\Delta\Delta A_{90^\circ}$ and $\Delta\Delta A_{0^\circ}$ (see Figure 7.17, black and black dashed line, respectively), calculated via the difference between $\Delta A_m - \Delta A_o$ at an orientation of the wave plate (Figure 7.13) of $\theta_{WP} = 90^\circ$ ($\Delta\Delta A_{90^\circ}$) and $\theta_{WP} = 0^\circ$ ($\Delta\Delta A_{0^\circ}$), are used to calculate

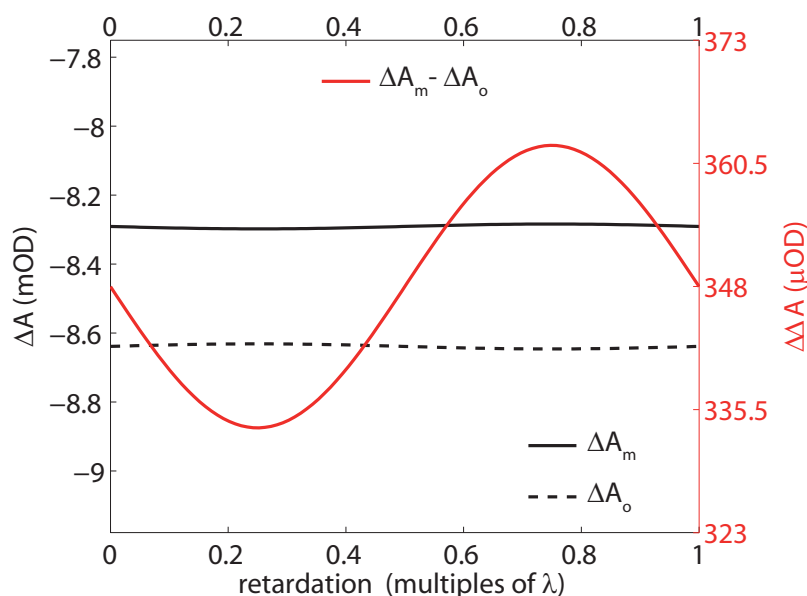


Figure 7.15: Simulated data in the exemplary experiment with the 0° mirror of Figure 7.4 assumed to be a silver mirror. The decrease in intensity in ΔA_m results in an offset of the circular-dichroism signal $\Delta A_m - \Delta A_o$, with the modulation due to the circular-dichroism effect maintained.

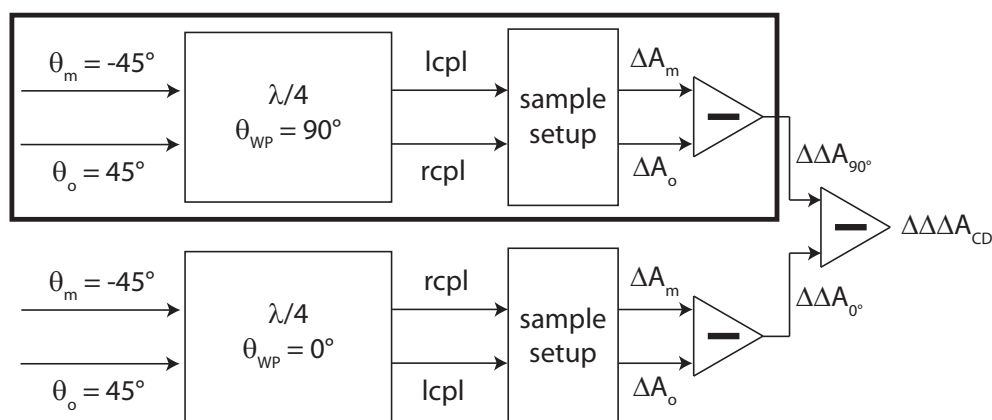


Figure 7.16: The intensity loss due to the additional reflection at the 0° mirror in the green path of Figure 7.4 is corrected by subtracting the transient-absorption signals of the individual paths, ΔA_o and ΔA_m , once with the $\frac{\lambda}{4}$ plate oriented with its fast axis in $\theta = 90^\circ$ direction (top) and once in $\theta = 0^\circ$ direction (bottom), resulting in $\Delta\Delta A_{90^\circ}$ and $\Delta\Delta A_{0^\circ}$, respectively. The difference between these two values is the pure circular-dichroism signal $\Delta\Delta\Delta A_{CD}$ also labeled ΔA_{CD} in the text. Note that with a proper intensity calibration of the pump ΔA_{CD} can be directly obtained in shot-to-shot measurement when assuming only 1-photon processes. In this case ΔA_m is always smaller than ΔA_o by a known factor, and only the experimental procedure in the black box needs to be done to obtain ΔA_{CD} .

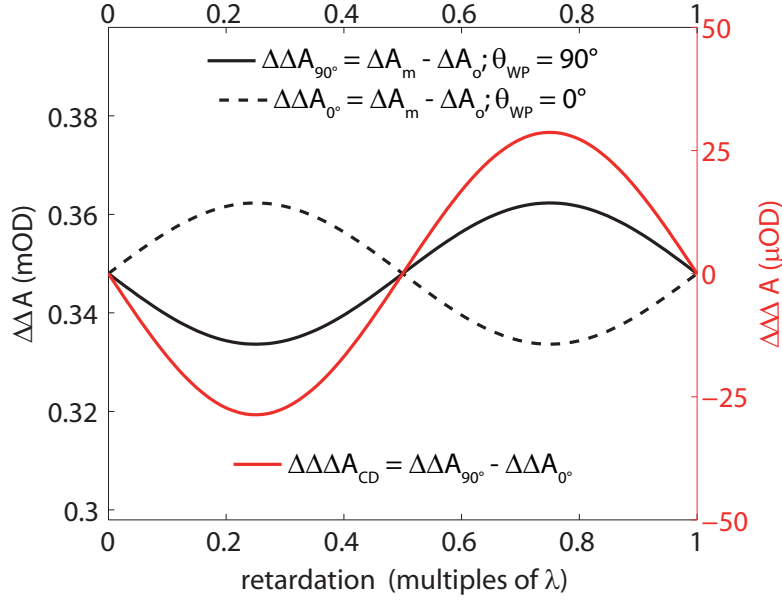


Figure 7.17: Simulated data in the exemplary experiment with the 0° mirror of Figure 7.4 assumed to be a silver mirror. $\Delta\Delta A_{90^\circ}$ and $\Delta\Delta A_{0^\circ}$ are defined as the signals $\Delta A_m - \Delta A_o$ at an orientation of the wave plate of $\theta_{WP} = 90^\circ$ and $\theta_{WP} = 0^\circ$, respectively (see also Figure 7.16). The circular-dichroism signal $\Delta\Delta\Delta A_{CD}$ is given by $\Delta\Delta A_{90^\circ} - \Delta\Delta A_{0^\circ}$ and is the pure circular-dichroism signal without the intensity change due to the additional mirror in one beam of Figure 7.4 (Figure 7.15).

the circular dichroism $\Delta\Delta\Delta A_{CD}$ with $\Delta\Delta\Delta A_{CD} = \Delta\Delta A_{90^\circ} - \Delta\Delta A_{0^\circ}$ (red line in Figure 7.17). In this approach the intensity change due to the additional mirror in one beam is canceled, whereas the circular-dichroism signal is increased by a factor of 2 compared to Figure 7.14. Note, that when assuming that only 1-photon processes occur, ΔA_m is always smaller by a known factor than ΔA_o due to the intensity reduction. Therefore only the steps in the black box of Figure 7.16 need to be performed with a proper intensity calibration to obtain the circular-dichroism signal ΔA_{CD} , which can be done in a shot-to-shot manner. In the following the circular dichroism $\Delta\Delta\Delta A_{CD} = \Delta A_{CD}$ is simulated if not stated otherwise.

After the experiment being introduced, in the next subsection alignment errors and their influence on the circular-dichroism signal ΔA_{CD} are investigated.

7.4.2 Alignment errors

In this subsection the influence of alignment errors of the polarization-mirroring setup (Figure 7.4), the sample setup (Figure 7.12), and the $\frac{\lambda}{4}$ plate in the exemplary experiment (Figure 7.13) on the circular-dichroism signal ΔA_{CD} is calculated.

The benchmark for the invariance of the circular-dichroism signal towards an alignment error has been chosen here to be on the one hand the peak-to-peak deviation of ΔA_{CD} , with α (the angle between the pump and probe transition dipole moment) varied from $\alpha = 0^\circ \rightarrow 90^\circ$ (see the example in Figure 7.18). In an anisotropy-free signal, ΔA_{CD}

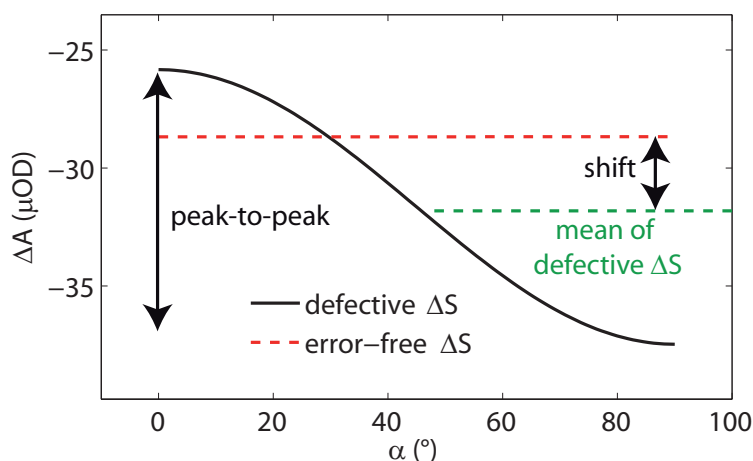


Figure 7.18: Two benchmarks are used to estimate the influence of an alignment error on the circular-dichroism signal ΔA_{CD} . The first (peak-to-peak) gives the minimum to maximum deviation of the circular-dichroism signal ΔA_{CD} upon changing the angle α between the pump and probe transition dipole moment. In an error-free experiment (red dashed line) anisotropy-free conditions are present, leading to a value of zero for the peak-to-peak deviation (numerical error < 4 nOD). In case of a defective alignment, anisotropy-free condition is not present and hence a dependence of ΔA_{CD} on α can be observed (black line) leading to a peak-to-peak value on the order of μOD . This benchmark is relevant prior to rotational diffusion taking place. The second benchmark is the shift of the mean of the circular-dichroism signal (green dashed line) compared to the error-free experiment (red dashed line). This benchmark is relevant after rotational diffusion has occurred.

should be independent of α . On the other hand the shift of the mean circular-dichroism signal (Figure 7.18) is taken as a benchmark. The first benchmark (“peak-to-peak”) is relevant prior to rotational diffusion of the excited population (see Appendix B.2.1), whereas the second benchmark (“mean shift”) is relevant after rotational diffusional of the excited population because then any anisotropy of the pumped distribution, which has been introduced due to α , is lost.

Exemplary experiment

In the exemplary experiment circularly polarized light is obtained with a $\frac{\lambda}{4}$ plate (Figure 7.13). As alignment errors the orientation θ_{WP} , the retardation δ_{WP} , and an incident polarization different from linear in $+45^\circ$ direction (Figure 7.13) are conceivable.

Since it has been shown in Section 7.3.3 that the transient-absorption signal (Eq. 7.9) does not depend on δ_{Pu} (Eq. 7.5) the only thing that changes ΔA_o and ΔA_m due to a retardation $\delta_{WP} \neq \frac{\pi}{2}$ and $\delta_{WP} \neq 3\frac{\pi}{2}$ is the decreasing circular part of the polarization. (Note that $\delta_{Pu} = \pm\delta_{WP}$ after the wave plate if the incident light is linearly polarized in $+45^\circ$ direction. The orientation θ_{WP} determines the sign of the retardation.)

Since the sample is circular dichroitic, the extinction coefficients for circularly and linearly polarized light are different. Therefore the anisotropy-free attribute of ΔA_{CD} is not influenced but only a shift to a lower circular-dichroism signal is observed. In case

of $\delta_{WP} = 0.2\lambda$ and $\delta_{WP} = 0.3\lambda$ the circular-dichroism signal decreases from 28.7 μOD ($\delta_{WP} = 0.25\lambda$) to 27.3 μOD .

The wave plate orientation θ_{WP} leads to a sine modulation of the circular-dichroism signal between 28.7 μOD and $-28.7 \mu\text{OD}$ when going from $\theta = 0^\circ \rightarrow 90^\circ$, whereas an error in the orientation of 2° corresponds only to an increase of the peak-to-peak deviation (see Figure 7.18) to 1.2 μOD .

Similarly, a polarization different from linear in $+45^\circ$ direction leads to a decreased circular part and an increased linear part after the $\frac{\lambda}{4}$ plate, i.e. elliptical polarization. Due to the subtraction of the polarization-mirrored signal, only the circular part, for which the extinction coefficients differ ($\epsilon_l \neq \epsilon_r$), can contribute to the circular-dichroism signal ΔA_{CD} . The linear part is canceled in the subtraction (see also Figure 7.11 in which original and mirrored polarization are elements of one blue circle). Hence, the circular-dichroism signal decreases with increasing deviation from $+45^\circ$ direction similarly to an error in the orientation θ_{WP} of the wave plate.

Polarization-mirroring setup

In the polarization-mirroring setup the orientation of every mirror is given by its surface normal. Taking Figure 7.4 these orientations are described in spherical coordinates, with the x direction corresponding to $\theta = 0^\circ$, z direction corresponding to $\theta = 90^\circ$ and $\phi = 90^\circ$ and the y direction being $\theta = 90^\circ$ and $\phi = 0^\circ$. The beamsplitters are assumed to be metallic cubic beamsplitters as suggested in Section 7.2.5 and are assumed to be describable by the Jones matrix derived in Appendix C. Every optic has two degrees of freedom, the polar angle θ and the azimuth angle ϕ . Alignment errors of an optic are simulated such that the subsequent reflection at next reflecting optic (which does not necessarily have to be the next optic, e.g. a beamsplitter of which the transmitted portion is used) leads to the same wave vector as without the alignment error. This approach is in step with actual practice because mirrors are usually aligned by the wave vector to show in a certain direction. The simulation is carried out by manually misaligning the corresponding optical element by the introduced error in the sequence of the optical elements. This changes the obtained polarization of the pump \vec{E}_{Pu} and subsequently the obtained transient-absorption signals.

If the specific alignment error does not have a strong influence the deviation should be close to zero (compared to the $-28.7 \mu\text{OD}$ of Figure 7.17), else the deviation should be on the order of $-28.7 \mu\text{OD}$ or greater. Any alignment error that leads to a deviation that is greater than the circular-dichroism signal itself must not exist.

As can be seen from Tab. 7.1 an alignment precise to 0.01° at every mirror allows for a circular-dichroism signal to be recorded. But even at this small angle also substantial influence of ΔA_{CD} on alignment errors should be observable which underlines the smallness of the circular-dichroism effect. Nevertheless, especially with the help of beam positioners that allow resolutions well below 1 mm for the beam position, it should be feasible to adjust a beam to a precision of $\sin(0.02) 3 \text{ m} \approx 1 \text{ mm}$ (incident angle = emergent angle) at a distance from the mirror of 3 m.

For the sake of completeness the polarization-mirroring setup without rotating periscopes (Figure 7.2) is investigated in the following to be able to conclude whether the

element	function	angle	alignment error ($^{\circ}$)	peak-to-peak (μOD)	mean shift (μOD)
original polarization: red beam					
0	BST	azimuth	± 0.01	< 1	< 1
0	BST	polar	± 0.01	2.4	± 1.3
1	SM	azimuth	± 0.01	1.7	< 1
1	SM	polar	± 0.01	3.4	± 2.0
2	SM	azimuth	± 0.01	< 1	< 1
2	SM	polar	± 0.01	7.0(3.7) ^a	$\pm 4(1.5)$
3	BST	azimuth	± 0.01	< 1	< 1
3	BST	polar	± 0.01	2.4	± 1.3
4	BSR	azimuth	± 0.01	< 1	< 1
4	BSR	polar	± 0.01	3.7	< 1
5	SM	azimuth	± 0.01	1.7	∓ 1.1
5	SM	polar	± 0.01	3.5	± 2.0
6	SM	azimuth	± 0.01	< 1	< 1
6	SM	polar	± 0.01	< 1	< 1
mirrored polarization: green beam					
0	BSR	azimuth	± 0.01	< 1	< 1
0	BSR	polar	± 0.01	< 1	< 1
1	SM	azimuth	± 0.01	1.7	< 1
1	SM	polar	± 0.01	3.4	± 1.1
2	SM	azimuth	± 0.01	< 1	< 1
2	SM	polar	± 0.01	3.4	∓ 1
3	BST	azimuth	± 0.01	< 1	< 1
3	BST	polar	± 0.01	2.3	< 1
4	OSM	azimuth	± 0.01	< 1	< 1
4	OSM	polar	± 0.01	3.3	< 1
5	BSR	azimuth	± 0.01	< 1	< 1
5	BSR	polar	± 0.01	< 1	< 1
6	SM	azimuth	± 0.01	3.3	< 1
6	SM	polar	± 0.01	2.8	< 1
7	SM	azimuth	± 0.01	< 1	< 1
7	SM	polar	± 0.01	3.9	< 1

Table 7.1: Influence of alignment errors of the optical elements in Figure 7.4 on the circular-dichroism signal ΔA_{CD} . The function abbreviations are: BSR = beamsplitter reflective; SM: silver mirror; BST: beamsplitter transmissive; OSM = 0° silver mirror.

^avalues in brackets are obtained when the subsequent beamsplitter, which is used in transmission, is oriented in such a way that the not-used reflected portion would propagate parallel to the y - z plane, as is the case in an error-free alignment

additional effort to use rotating periscopes is worth the trouble. As before, the incoming beam is assumed to be linearly polarized in $\theta = +45^{\circ}$ direction (ellipticity: $\epsilon = 0$). Due

to polarization changing effects, different index of reflection and transmission and phase offsets for the s and p component at every silver mirror, the polarization leaving the polarization-mirroring setup is for the red beam $\epsilon_{o-Pu} = 10.8^\circ$ and $\theta_{o-Pu} = -47.45^\circ$, whereas the polarization of the green beam is $\epsilon_{m-Pu} = -10.8^\circ$ and $\theta_{m-Pu} = 47.45^\circ$. While both polarizations are mirror images of each other, the original linear polarization is not maintained. Nevertheless an anisotropy-free signal of the individual signals ΔA_o and ΔA_m can still be achieved when fulfilling Eq. 7.11 for the angle β_2 (Figure 7.12). Incorporating Eq. 2.36 solved for δ_{Pu} in Eq. 2.34 one obtains for χ_{Pu}

$$\chi_{Pu}(\tilde{\theta}_{Pu}, \epsilon_{Pu}) = -\frac{1}{2} \arcsin \sqrt{1 - \frac{1 - \sin(2\epsilon_{Pu})^2}{1 + \tan(2\tilde{\theta}_{Pu})^2}}. \quad (7.12)$$

With the parameters $\epsilon_{Pu} = \pm 10.8^\circ$ and $\theta_{Pu} = \mp 47.45^\circ$ one obtains $\chi_{Pu} = 42.72^\circ$ and as anisotropy-free condition the angle $\beta_2 = 51.80^\circ$ (Eq. 7.11). Note that the corresponding value for the definition of β in Figure 7.8 would be $\beta = 31.68^\circ$, as given by Eq. 7.9.

As explained in the section concerning the exemplary experiment, in case of an alignment error of the $\frac{\lambda}{4}$ plate, due to the decreased ellipticity, the mean of the circular-dichroism signal ΔA_{CD} decreases. In the example of the polarization-mirroring setup of Figure 7.2, ΔA_{CD} decreases from 28.7 μOD to 26.5 μOD when adjusting the intensity to an absorption change $\Delta A = 8.45 \text{ mOD}$ ($I = 0.915 \mu\text{J}$) as for the previous polarization-mirroring setup. The values given in Tab. 7.2 are obtained in case of anisotropy-free condition of the circular-dichroism signal ΔA_{CD} ($\beta_2 = 51.80^\circ$).

As can be seen in Tab. 7.2 an error in the azimuth angles does not influence the circular-dichroism signal when not using rotating periscopes, whereas an error in the polar angles obscures the circular-dichroism signal. Especially the optics in the vicinity of the 0° mirror have a strong influence on the signal. The setup with rotating periscopes offers smaller deviations due to alignment errors (the highest peak-to-peak deviation being $\frac{\Delta A_{CD}}{7}$ and the highest mean shift being $\frac{\Delta A_{CD}}{15}$) compared to the setup without rotating periscopes (highest peak-to-peak deviation $\frac{\Delta A_{CD}}{3}$ and highest mean shift being $\frac{\Delta A_{CD}}{6}$). However, since the polar angle, that determines the x component of the wave vector in Figure 7.2, is adjusted very easily in practice, probably to an accuracy even better than 0.01° , both setups seem to be promising. Note also, that the simulation is not fully general, for example it has not been taken care, if not stated otherwise, that the reflected part of a beamsplitter travels in the right direction if the transmitted part is used. Furthermore, in the simulation the beamsplitter in front of the 0° mirror, which is used two times, is simulated as one individual beamsplitter for every interaction.

Sample setup

In the sample setup the angle β_2 can be misaligned. Following the sample setup of Figure 7.12, β_2 is adjusted by a $\frac{\lambda}{2}$ plate or a linear polarizer. The influence of an elliptical polarization is not investigated here, since it can be circumvented by a linear polarizer.

Due to the subtraction of the signals as described in Section 7.4.1 a misalignment in the angle β_2 leads mostly to a change in ΔA_o and ΔA_m but not to a large change

element	function	angle	alignment error ($^{\circ}$)	peak-to-peak (μOD)	mean shift (μOD)
original polarization: red beam					
0	BST	azimuth	± 0.01	< 1	< 1
0	BST	polar	± 0.01	1.3	∓ 1.9
1	SM	azimuth	± 0.01	< 1	< 1
1	SM	polar	± 0.01	6.0	± 5.0
2	BST	azimuth	± 0.01	< 1	< 1
2	BST	polar	± 0.01	3.1	± 3.3
3	BSR	azimuth	± 0.01	< 1	< 1
3	BSR	polar	± 0.01	3.2	± 3.6
4	SM	azimuth	± 0.01	< 1	< 1
4	SM	polar	± 0.01	6.9	± 3.5
mirrored polarization: green beam					
0	BSR	azimuth	± 0.01	< 1	< 1
0	BSR	polar	± 0.01	5.7	< 1
1	SM	azimuth	± 0.01	< 1	< 1
1	SM	polar	± 0.01	8.2	∓ 1
2	BST	azimuth	± 0.01	< 1	< 1
2	BST	polar	± 0.01	10.9	< 1
3	OSM	azimuth	± 0.01	< 1	< 1
3	OSM	polar	± 0.01	8.8	∓ 1.5
4	BSR	azimuth	± 0.01	< 1	< 1
4	BSR	polar	± 0.01	< 1	∓ 2.1
5	SM	azimuth	± 0.01	< 1	< 1
5	SM	polar	± 0.01	10.8	∓ 2.0

Table 7.2: Influence of alignment errors of the mirrors in Figure 7.2 on the circular-dichroism signal ΔA_{CD} . The function abbreviations are: BSR = beamsplitter reflective; SM: silver mirror; BST: beamsplitter transmissive; OSM = 0° silver mirror.

in the circular-dichroism signal ΔA_{CD} . When tuning β_2 from $50^{\circ} \rightarrow 60^{\circ}$ the peak-to-peak deviation due to anisotropy effects is $2.0 \mu\text{OD}$ and the mean of the circular-dichroism signal shifts by $0.3 \mu\text{OD}$ in case of the polarization-mirroring setup with rotating periscopes.

Summary

Summarizing, one can state that the circular-dichroism signal is very sensitive to alignments errors of the polarization-mirroring setup. Nevertheless a careful adjustment of every optical element to a precision of 0.01° , corresponding to a misalignment of 1 mm at a path length of 3 m, should be possible. Alignment errors of the sample setup as well as the exemplary experiment setup are very low. Therefore the proposed experiment that is based on the ground-state circular dichroism seems to be possible. This section

does not claim to be complete or exact in its simulations. A lot of degrees of freedom are yet unaccounted for in the alignment error section. Furthermore the simulations are based on literature data for the refractive index of silver. Comparing those with data from commercial silver mirrors allows to classify the results presented as a “worst-case scenario”.

7.4.3 Multiphoton processes

In multiphoton processes multiple photons are absorbed by the quantum-mechanical system. The energy due to combination of multiple photons allows to reach a state of the system that is not accessible by the energy of an individual photon. In this subsection first non-resonant multiphoton processes in which multiple photons are absorbed simultaneously, and afterwards resonant multiphoton processes involving an intermediate resonant state will be discussed.

Non-resonant multiphoton processes

The derivation of the anisotropy in multiphoton processes can in principle be obtained by substitution of the exponent 2 in Eq. B.8 by $2n$, with n being the order of the process (see Appendix B.3). Due to the analytical complexity only the case of a 2-photon process is treated in the following. The anisotropy and circular-dichroism effect increases when going from a 1-photon process to a 2-photon process. An analytical treatment of the increase necessitates the inclusion of many additional parameters.

Intensity For instance the extinction coefficient in a multiphoton process in contrast to the linear extinction coefficient depends on the intensity of the electromagnetic wave itself. Instead of the Beer–Lambert law, the drop in intensity I due to 2-photon process is described by

$$I = \frac{I_0}{1 + \beta cl I_0}, \quad (7.13)$$

with β being two-photon absorption cross section with the unit “Göppert-Mayer” [200], l being the optical path length, c being the concentration of the absorbing molecule and I_0 being the incident intensity. This also invalidates the relation of the maximum pump-probe signal with the extinction coefficient given in Appendix A. However, a similar calculation for 2-photon processes should be feasible.

In order to integrate the continuous change of the intensity I and subsequently the change of the extinction, the Jones vector of the pump pulse needs to be developed as a function dependent on the time t that describes the intensity and extinction in a time-dependent way. The calculation of the anisotropy would then be performed over an infinitesimal small time interval $t + \Delta t$ to be able to calculate the extinction coefficient which itself depends on the intensity of Jones vector in the time interval $t + \Delta t$. The excited population would then be given by integration over the time of the laser pulse. One could assume simple models for the laser pulse with a reduced set of parameters, e.g. Gaussian in the time-domain and linearly polarized, and calculate the anisotropy induced by such laser pulses. However, the purpose of this chapter is to find general

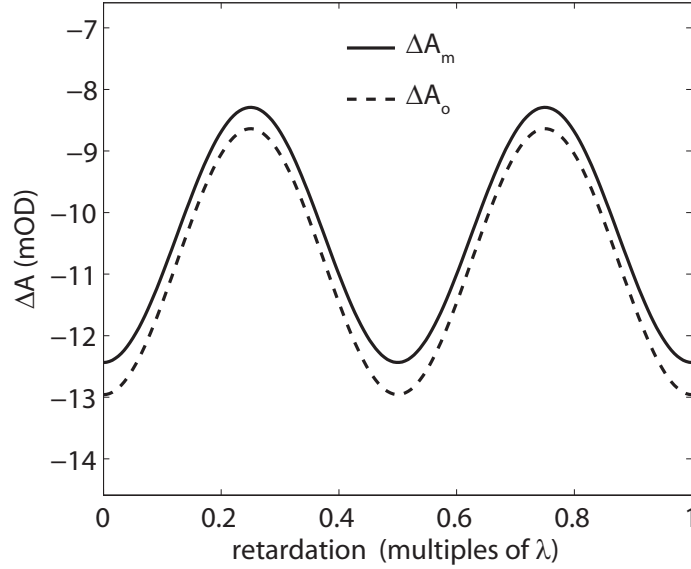


Figure 7.19: Dependence of the individual signals ΔA_o and ΔA_m on the polarization in a 2-photon process. Due to the electric field in direction \vec{m} in case of circular polarization being smaller by $\sqrt{2}$ compared to linear polarization in \vec{m} direction the transient-absorption signal is lower in case of circular polarization (0.25λ and 0.75λ) compared to linear polarization (0λ , 0.5λ and 1λ).

rules for anisotropy-free polarization-shaped-pump-probe spectroscopy, which cannot be obtained by such an approach. Therefore multiphoton processes cannot be modelled correctly in a simple approach.

Polarization A second phenomenon when dealing with multiphoton processes is the dependence of the pump-probe signal on the polarization (see for example [201]). In the following it is assumed that the intensity of the Jones vector does not change in the simulation of the examined time interval. In the simulation the pump intensity is adjusted to a pump-probe signal of the 2-photon process (circularly polarized pump) in magic-angle configuration of 8.45 mOD under anisotropy-free conditions ($\chi_{Pu} = 45^\circ$ and $\beta_2 = 54.735^\circ$, see Appendix B.3). The difference between ΔA_o and ΔA_m (Figure 7.19) thereby increases compared to the 1-photon process (Figure 7.15). Furthermore one obtains a strong dependence on the retardance δ_{WP} of the wave plate of the exemplary experiment (Figure 7.13), i.e. the polarization of the pump, which is clearly different (2 modulations per λ retardation) from the modulation one would expect from the circular-dichroism signal (1 modulation per λ retardation, see for example Figure 7.14).

The strong modulation of ΔA_o and ΔA_m with the retardation is due to the lower amplitude of the electric field in a certain direction with increasing ellipticity, e.g. the amplitude in a direction \vec{m} in case of circular polarization is smaller by a factor of $\sqrt{2}$ compared to linear polarization in \vec{m} direction. Hence, the effect of the polarization is much stronger than in the linear regime.

Concluding, multiphoton processes can in principle be modelled, but due to the in-

creased complexity it is not shown here. The dependence of the extinction coefficient on the intensity requires an additional time-dependent treatment of the Jones vector, which lies beyond the scope of this chapter.

Multiphoton processes with intermediate states

Photochemical reaction pathways that proceed via two separate absorption processes, such as the bidirectional switching in Section 4.5, possess characteristic anisotropy. Taking the example of Section 4.5, the first step of the switching (purple in Figure 4.26) is the opening, induced by absorption of a UV photon (pump), and the second step is the closure (green in Figure 4.26), induced by absorption of a VIS photon (repump). The third interaction of the sample is the probe (see Figure B.2). All three processes are 1-photon processes. In this example three polarizations as well as their wave vectors need to be managed: Pump, repump and probe (Figure 4.23). Neglecting rotational diffusion, the anisotropy is much more complicated than in usual pump–probe experiments. On the one hand the additional degrees of freedom due to three polarizations impede an easy analysis as given by Eq. 3.9, on the other hand they offer a much more detailed analysis of the relative orientation of the transition dipole moments contributing to the transient-absorption signal (see Appendix B.6).

The solution cannot be calculated analytically but nevertheless one can calculate the pump–repump–probe probability numerically. The result of this calculation depends on a lot of parameters which can be classified as experimental (wave vectors and Jones vectors of pump, repump and probe) and molecular (angles between the transition dipole moments). Recording a set of transient-absorption data with varied experimental parameters one therefore can in principle determine the molecular parameters. In view of this approach even the polarization-shaping of the probe might be an attractive degree of freedom to simultaneously determine the anisotropy spectrally-resolved without having to pay attention towards intensity dependence of the shaped probe pulse (Eq. 3.2).

Concluding, the anisotropy of multiphoton processes that proceed via multiple individual absorption processes can numerically be modelled. However, the large number of experimental degrees of freedom, e.g. the number of pump pulses, do not allow a general analytical solution to all situations. Instead, with the experimental conditions known, the molecular parameters might be accessible in much more detail, e.g. determining also the relative orientation between molecular transition dipole moments, compared to the usual anisotropy measurements.

7.5 Transient enantiosensitive signals

The steady-state enantiosensitive optical signals circular dichroism and optical rotatory dispersion have proven especially useful for the determination of secondary structures [202]. Therefore the ability to determine these signals in a time-resolved manner would open the possibility to follow these changes of the secondary structures [203]. As already mentioned before, the circular dichroism and the optical rotatory dispersion are very small signals, thus their experimental measurement in a time-resolved experiment, in which only a fraction of the molecules undergoes the structure change, is therefore

far more difficult compared to steady-state measurements. However, with great effort a few groups [29, 172, 173] have achieved to record such a “transient” circular dichroism and “transient” optical rotatory dispersion. These experiments are extremely time consuming [172], due to the long-time averaging, and the obtained results generally show low signal-to-noise ratios. With the setup presented in Section 7.2.1 the measurement of a transient circular dichroism as well as a transient optical rotatory dispersion are also possible, as explained in the next two subsections.

7.5.1 Transient circular dichroism

The transient-absorption dynamics in a chiral molecule after excitation possess a certain transient circular dichroism in most cases. Especially in the mid-infrared spectral region, the spectral region of the vibrational modes, the transient circular dichroism can be used to determine the structural changes [29].

In contrast to the exemplary experiment in Section 7.4.1, where the pump is sent through the polarization-mirroring setup to switch the polarization, in a transient circular-dichroism experiment the probe needs to be sent through the polarization-mirroring setup to switch between *rcpl* and *lcpl*. Note that in the methods described in the literature this modulation between *rcpl* and *lcpl* is achieved with optical modulators, which are not suited for broadband pulses, hence those methods are only able to probe a very small spectral window in one experiment [172].

Nevertheless, when measuring the transient circular dichroism with the help of the polarization-mirroring setup anisotropy-free conditions are necessary, i.e. the angle α between pump and probe transition must not influence the signal. In this case one therefore has to find a solution to

$$\frac{\partial P_{Pr}(\alpha, \chi_{Pu} = 90^\circ, \delta_{Pu} = 0^\circ, \chi_{Pr}, \delta_{Pr}, \beta_3)}{\partial \alpha} = 0, \quad (7.14)$$

with the definitions of the directions of pump and probe used in Figure 7.8 (β_3 corresponds to β) and the probe having the Jones vector $\begin{pmatrix} \cos \chi_{Pr} \\ \sin \chi_{Pr} e^{i\delta_{Pr}} \end{pmatrix}$. The solution for β_3 is similar to the one found in Appendix B.4.3 and Eq. 7.9,

$$\beta_3(\chi_{Pr}) = \pm \arccos \left(\pm \frac{1}{\sqrt{3} |\sin \chi_{Pr}|} \right). \quad (7.15)$$

In that case the pump–probe signal is independent of α and δ_{Pr} . The absence of a δ_{Pr} dependence is especially important for transient circular-dichroism experiments, since then an “achromatic” $\frac{\lambda}{4}$ plate can be used to generate the circular polarization. The achromatism of those wave plates is not perfect, because the introduced retardation is not precisely $\delta_{Pr} \approx 0.25\lambda$ (but χ_{Pr} is not changed). With β_3 being adjusted to the right condition, the defective polarization (elliptical instead of circular) does not cause anisotropy effects, but the strength of the desired signal is decreased. The condition for β_3 is invariant to a sign change of χ_{Pr} , which is the decisive property to be able to mirror the polarization without effecting the condition for β_3 (Section 7.3.4). Therefore, the

polarization-mirroring setup allows for broadband probing in contrast to the methods presented so far in the literature.

The setup shown in Figure 7.12 cannot be used to record a transient circular dichroism, because a change of β_2 would not change the three-dimensional polarization of the probe in case of circular polarization. However, the limitation to the setup shown in Figure 7.8 is not dramatic, because χ_{Pr} can simply be set once by a linear polarizer in front of the $\frac{\lambda}{4}$ plate. Because the intensity of the probe is not important, there is never the necessity to change the orientation of the linear polarizer (and subsequently χ_{Pr}) and therefore there is never the necessity to change β_3 .

When recording transient circular dichroism especially the laser-induced linear dichroism leads to artifacts that are much stronger than the pure circular-dichroism signal. When the probe polarization states are exact mirror images of each other the laser-induced linear dichroism is cancelled [29]. Experimentally, the challenge to generate perfect mirror images of the probe polarization state with modulators has so far only been solved with great effort [29, 204]. In contrast to that, the perfect mirror-image symmetry of the polarization state is a given when using the polarization-mirroring setup of Figure 7.4, thus it might be an attractive alternative approach to measure a transient circular dichroism. In that case the signal-to-noise ratio would only be limited by the ability to measure small intensity changes of the probe. Literature results [29, 172, 173] so far show absorption changes $\Delta A > 20 \mu\text{OD}$ due to a transient circular dichroism which should be readily detectable [205]. Furthermore the polarization-mirroring setup can also be combined with highly repetitive laser sources, e.g. with 100 kHz pulse rate, leading to a much better signal-to-noise ratios and much lower data acquisition times compared to conventional 1 kHz laser systems [75]. Such a high-speed switching may not be possible with the Pockels cell of [172] or the photoelastic modulator of [173].

7.5.2 Transient optical rotatory dispersion

In transient optical rotatory dispersion the real part of the refractive index of a chiral molecule for circularly polarized light changes during the dynamics of a reaction. These changes can be made visible in transient optical rotation experiments similar to the transient circular dichroism from the previous subsection. The polarimeter in Chapter 6 does not measure a transient optical rotation but the steady-state optical rotation, i.e. after complete decay of the transient dynamics. The setup shown in this chapter (Figure 7.4) can in principle be used to measure a transient optical rotatory dispersion.

In this case one needs to switch between two linearly polarized probe beams with known orientation $+\theta$ and $-\theta$, which is done by the polarization-mirroring setup (Section 7.2.1). In the sample the orientation of the linear polarization is rotated by a small angle α_{or} whose sign does not depend on the orientation of the linear polarization. Hence, one obtains after the sample the two orientations

$$\theta_1 = +\theta + \alpha_{or} \quad (7.16)$$

$$\theta_2 = -\theta + \alpha_{or}, \quad (7.17)$$

of the linear orientations of the original and mirrored polarization as shown in Figure 7.20.

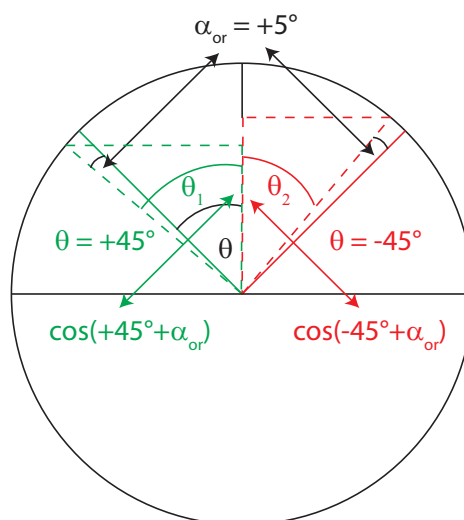


Figure 7.20: To record a transient optical rotatory dispersion signal the setup from Figure 7.4 needs to switch between linear polarizations in $\theta = +45^\circ$ direction (green) and $\theta = -45^\circ$ direction (red). The sample rotates both linear polarizations by the angle α_{or} in the same direction (dashed lines). The intensity measured after a subsequent analyzer which only transmits light in $\theta = 0^\circ$ direction (vertical) differs for the two incident linear polarizations (vertically colored dashed lines). Recording the optical density change of the system “sample+analyzer” it is therefore possible to calculate α_{or} (Eq. 7.20).

After a subsequent linear analyzer that transmits only in direction $\theta = 0$ (vertical direction in Figure 7.20), the optical rotatory dispersion, in case of linear polarization oriented in $-\theta$ direction, leads to a positive change of the intensity measured after the analyzer if $\alpha_{or} > 0$ or to decrease if $\alpha_{or} < 0$. The contrary is true for the linear polarization oriented in $+\theta$ direction. The ratio of the intensities of the two polarizations (I_o : $\theta = +45^\circ$ and I_m : $\theta = -45^\circ$ in Figure 7.20) after having passed the optically active sample is therefore given by

$$\frac{I_m}{I_o} = \frac{\cos^2(-45^\circ + \alpha_{or})}{\cos^2(+45^\circ + \alpha_{or})}, \quad (7.18)$$

and hence the optical density change of the system “sample+analyzer” by

$$\Delta A = \log \frac{I_m}{I_o}. \quad (7.19)$$

The optical rotation angle α_{or} then becomes

$$\alpha_{or} = \frac{1}{4}[-\pi + 4\arctan(10^{\frac{\Delta A}{2}})]. \quad (7.20)$$

An optical rotation angle of $\alpha_{or} = 0.12$ mdeg, which is the resolution of the polarimeter in Chapter 6, leads to an optical density change of only 3.6 μ OD, which is very small. The polarimeter presented in Chapter 6 is therefore much better suited to record an optical rotation. Unfortunately it is not capable of recording a transient optical rotation in its current implementation but only steady-state optical rotation.

7.6 Field of application of the accumulative and the pump–probe scheme

A polarimeter based on the accumulative scheme (Section 3.3) was presented in Chapter 6. It affords detection of optical rotation angles down to 0.12 mdeg in less than 3 seconds acquisition time and hence is a very attractive tool to measure chiral systems. However, it does not give access to the transient dynamics of a photoreaction, excluding the use of pump multipulses.

In this chapter a way to record in a pump–probe manner the enantiosensitive transient dynamics of a photoreaction, i.e. transient circular dichroism, transient optical rotatory dispersion as well as ground-state and intermediate circular dichroism, was proposed. In these experiments the enantiosensitive signal is translated into a probe intensity change which is measured by a fast CCD camera. The attractiveness of this approach depends strongly on the achievable resolution which is given by the ability of the CCD camera to measure small intensity changes. The detection electronics of the CCD camera used in this thesis have a dynamic range of $\approx 1 : 65000$. The smallest intensity change measurable with one shot in the ideal case is therefore given by $-\log \frac{64999}{65000} = 15 \mu\text{OD}$. Averaging over many shots it is probably possible to achieve resolutions down to 1 μOD as shown by other authors that use detection electronics with similar dynamic range [205]. The high repetition rate of the femtosecond laser system (1 kHz) allows to measure signals with a standard deviation of around 20 μOD in just a few seconds. Hence, a signal as the one calculated for the ground-state circular dichroism in Section 7.4.1 (17 μOD) should be detectable.

Whether the accumulative setup or the pump–probe setup is to be preferred in an experiment depends on the aim of the experiment. When doing spectroscopy on transient species the pump–probe setup is much more attractive because the transient dynamics are directly accessible therein, whereas in the accumulative scheme only multipulses allow the detection of the transient dynamics. However, the probability for a multipulse process is much smaller compared to the 1-photon process. Therefore the bigger part of the detected signal will be the pure 1-photon process signal.

In contrast to that when doing optimal control, i.e. when parameters of the pump pulse are optimized to maximize the enantiomeric excess, which is in a good approximation given by the steady-state optical rotation (Eq. 2.73), the accumulative setup is preferred. Its data acquisition times of only a few seconds to obtain a standard deviation of 0.12 mdeg exceed the ones achievable by the pump–probe setup ($\approx 3.6 \mu\text{OD}$ for $\alpha_{or} = 0.12$ mdeg, i.e. a few minutes acquisition times). Furthermore anisotropy effects do not influence the signal because rotational diffusion is much faster than the response function of the setup (Section 6.9).

Therefore both setups serve their purpose and complement one another when doing either control or spectroscopy experiments.

8 Summary and Outlook

From a mechanistic point of view all steps of a chemical reaction proceed on the time scale of a few femtoseconds. Femtosecond spectroscopy affords the direct observation of these steps and has been established as a versatile tool to determine for example lifetimes, quantum efficiencies or molecular geometries and also serves as a means to determine reaction mechanisms by observing directly the sequential or parallel photochemical and photophysical pathways.

An example for a parallel and sequential photochemistry is given in this thesis with the Diazo Meldrum's Acid (DMA). Upon UV excitation of DMA in solution two parallel photochemical pathways, Wolff rearrangement and diazirine formation, could be identified by time-resolved probing of the absorption in the mid-infrared spectral range. On top of that, the sequential mechanism of the Wolff rearrangement from the ketene over the enolester to the final ester product was observed. Solvent-dependent time constants of the nucleophilic addition of an alcoholic solvent to the ketene as well as DFT calculations of the decisive marker modes in the mid-infrared spectral range completed the analysis and allowed for an unambiguous assignment of the transient-absorption signals.

In most femtosecond experiments, including the previous one, the aim is the determination of either the reaction mechanism or molecular quantities. With advancing technology to generate and manipulate femtosecond laser pulses, a more active role of the light is conceivable, wherein the electric field steers the photoreaction into a certain direction. Two approaches to obtain the optimal field exist. Either experimental, in the "adaptive" control, via optimization of an experimental feedback signal, or theoretically, in the "optimum" control, via the computation of the optimum field based on the knowledge of the complete wavefunction of the system. In either case an experimental feedback signal is indispensable to determine the success of an applied electric field. For example the obtained knowledge of the photochemistry of DMA will serve in the near future as basis to choose an appropriate feedback signal to control the ratio of the population of the two parallel pathways via the excitation.

A complete example for a control of a molecule, from the spectroscopy of the individual reaction steps to the steering of the molecule, is given in this thesis by the molecular switch 6,8-dinitro-1',3',3'-trimethylspiro[2H-1-benzopyran-2,2'-indoline] (6,8-dinitro BIPS). 6,8-dinitro BIPS belongs to the family of the merocyanine-spiropyran and is stable in an open form (merocyanine) as well as a closed form (spiropyran). Whereas these molecules are commonly known as attractive molecular switches, the ultrafast ring closure was proven directly for the first time in this thesis by probing in the mid-infrared spectral region. Furthermore, the existence of two ring-open isomers with different photochemistry and photophysics was shown. Variation of the excitation wavelengths and a global fit of multiple spectrotemporal transient-absorption datasets simultaneously with a specially devised algorithm afforded the determination of all par-

ticipating quantum efficiencies. Whereas the interconversion of the isomers (cis/trans isomerization) does not contribute strongly to the photochemistry of the merocyanines, the ring-closure pathway has a very high quantum efficiency ($\approx 40\%$) after excitation in the visible spectral range.

The extension of the pump–probe experiment by a second pump pulse (repump) allowed to prove that upon UV excitation of the closed form (spiropyran) generation of the open form (merocyanine) is possible. In this pump–repump–probe experiment an active control of a subensemble took place by switching between the open and the closed form within less than 40 ps via a two-color multipulse sequence. A sophisticated data acquisition as well as a suitable selection of the temporal delays between the three pulses (pump, repump and probe) enabled on the one hand the determination of the reaction times for both switching directions (opening: 36 ps and closure: < 6 ps). On the other hand, bidirectional switching was shown, i.e. both switching cycles, open–closed–open as well as closed–open–closed, were directly observed. Several control experiments are planned that seek to take influence on the quantum efficiency for the ring-closure pathway in order to gain a deeper understanding of the shapes of the participating potential surfaces.

In the bidirectional switching experiment the time delay between pump and repump pulse was the control parameter. More complex systems may need more complex control parameters. In those cases pulse shaping is an attractive tool and found its way into many control experiments. With the advancement of pulse shaping technologies, the ability to change the polarization on the femtosecond time scale has emerged hand in hand with the desire to control the molecular chirality (“chiral control”) via the femtosecond polarization during the excitation. However, in such an experiment, the enantiosensitive optical signals conceivable for probing, e.g. circular dichroism and optical rotatory dispersion, are very small and hence necessitate a very sensitive detection as well as an experimental arrangement in which experimental artefacts cannot obscure the signal.

Before doing a control experiment, spectroscopy of the reaction in question needs to be performed, for example to identify an attractive feedback signal. However, pump–probe spectroscopy with a polarization-shaped pump pulse, the method of choice to stamp the chiral information on the laser pulse, was hitherto impossible. The spatial distribution of the transition dipole moments that can be probed depends strongly on the pump polarization. Thus, the probed signal also depends strongly on the pump polarization and not only on the population of states. Although experimental three-dimensional arrangements for the two limiting cases of linear and circular pump polarization exist, a general solution to probe only the population of states in case of arbitrary pump polarization was hitherto unknown.

In this thesis a theoretical approach was developed that describes the anisotropy dependent on the three-dimensional polarization of the pump and probe pulse. With the help of this approach a possibility was identified that allows indeed to perform pump–probe spectroscopy with arbitrary pump polarization while probing only the population. The previous two limiting cases of linear and circular polarization are only two elements of this solution. On top of that, it has been found that the new approach offers exciting new possibilities exceeding all other known approaches. For example, it allows to

simulate numerically the anisotropy of more complex pump–probe experiments, such as a pump–repump–probe experiment, with arbitrary three-dimensional polarization of all entering pulses. This simulation gives access to molecular quantities such as the relative orientation of the three transition dipole moments participating in a pump–repump–probe experiment, which was not obtainable beforehand. This aspect alone opens new fascinating possibilities to pump–probe spectroscopy, for example to obtain more information via anisotropy measurements or to investigate the femtoseconds dynamics dependent on the pump polarization.

Of great importance for pump–probe spectroscopy of chiral molecules is the possibility to generate the exact mirror images of polarization states, because chiral molecules differentiate between the circular part of a polarization state. In the context of pump–probe spectroscopy a polarization-shaped pump as well as a polarization-shaped probe are conceivable. The former leads to an experiment in which the quantum efficiency dependent on the pump pulse polarization is investigated. Here, the use of femtosecond laser pulses can for example lead to a cumulative, and thus greater, circular dichroism, because due to the high intensity of the electric field multiple interactions with the chiral excitation field occur. A polarization-shaped probe pulse on the other hand has applications in the detection of a transient circular dichroism or a transient optical rotatory dispersion. Both experiments have in principle already been implemented in the literature with the help of acousto-optical or electro-optical modulators, but the very low signal-to-noise ratio of these experiments is reason enough to follow new ideas.

In this thesis a setup was developed that performs exactly this mirror-image generation of polarization states, independent of the wavelength and the polarization. Analogous to conventional pump–probe spectroscopy, the setup allows a shot-to-shot alternating switching between original and mirror image of the pump or probe polarization. Especially the achromatism of the setup, a feature not shared with acousto-optical and electro-optical modulators, allows for a better signal-to-noise ratio, because simultaneous probing at many spectral positions is possible and hence data acquisition time is reduced drastically. The extensive simulations in this thesis of a polarization-shaped pump–probe experiment allow to predict that the necessary precision of the alignment should be achievable in practice.

The results of this thesis, on the one hand the approach to describe the anisotropy dependent on the polarization and on the other hand the possibility to generate exact mirror images of polarization states on a shot-to-shot basis, enable polarization-shaped pump–probe spectroscopy. On top of that, the polarization of the pump pulse can be shaped while not introducing anisotropy effects, which allows to perform control experiments that seek to optimize the polarization of the pump pulse to maximize certain transient signals.

The signal-to-noise ratio of the employed detection method in these experiments might be too low for control experiments that often feature a low degree of control. Especially for control experiments a polarimeter was developed, simulated and set up. The combination of the polarimeter with femtosecond laser pulses was the primary focus, hence, it has a very small interaction volume (< 10 nl) while being very sensitive ($\sigma_\alpha \approx 0.12$ mdeg) and fast (data acquisition time: < 1 s). All three specifications can hardly be met individually by commercial polarimeters, let alone in combination. Said specifications

were shown by the photodissociation of chiral methyl *p*-tolyl sulfoxide. It was possible to determine quantitative values of the efficiency of the dissociation pathway via the detection of the optical rotation angle only, on an optical path length of 250 μm .

Chapter 6 and Chapter 7 of this thesis give a set of tools, theoretical as well as practical, that aim on the one hand at the spectroscopy of chiral molecules, either with polarization-shaped pump or polarization-shaped probe pulses in pump–probe experiments. On the other hand this thesis delivers a possibility to realize chiral control, meeting the demand to reliably detect a low enantiomeric excess. Both approaches promise success and allow many new experiments.

The spectroscopic results of Chapter 4 and Chapter 5 may serve as a basis for these experiments. The parallel and sequential photochemical pathways of DMA and the feasibility of the bidirectional switching of 6,8-dinitro BIPS in a pump–repump experiment on the one hand offer a playground to test the relation of the anisotropy with the polarization of the pump, repump and probe pulse. On the other hand control experiments with varying pump and repump polarization may be able to take influence on the dynamics after excitation. Especially interesting is the combination of the 6,8-dinitro BIPS with the polarization-mirroring setup, because the closed form (spiropyran) is chiral. Perhaps in the future it will be possible to prove a cumulative circular-dichroism effect or even a chiral control with this system.

9 Zusammenfassung und Ausblick

Aus mechanistischer Sicht laufen alle Teilschritte chemischer Reaktionen auf der Zeitskala von einigen Femtosekunden ab. Die Femtosekundenspektroskopie ermöglicht, diese Schritte sichtbar zu machen, und hat sich mittlerweile als Methode etabliert, um zum Beispiel Lebenszeiten, Quantenausbeuten und molekulare Geometrien zu bestimmen sowie parallele und zugleich sequentielle Photoreaktionskanäle direkt zu verfolgen. Ein Beispiel für die Untersuchung einer parallelen und sequentiellen Photochemie wurde in dieser Arbeit anhand der Diazo Meldrumsäure (DMA) gezeigt. Nach Anregung der DMA mit UV-Femtosekundenpulsen konnten durch zeitaufgelöste Abfrage der Absorption im mittleren Infrarotbereich zwei parallele Reaktionskanäle, die Wolff-Umlagerung und die Diazirinbildung, nachgewiesen werden. Zudem konnte der sequentielle Mechanismus der Wolff-Umlagerung vom Keten über den Enolester bis hin zum Ester verfolgt werden. Sowohl die lösungsmittelabhängigen Zeitkonstanten der Addition eines Alkohols an das Keten als auch DFT-Rechnungen komplettierten die Analyse und ermöglichten so eindeutige Zurechnungen der transienten Absorptionssignale.

In den meisten Femtosekundenexperimenten, wie auch in dem zuvor erwähnten, ist der Zweck des Experiments die Bestimmung von molekularen Größen. Prinzipiell ist jedoch auch eine aktivere Rolle des Lichts denkbar, in der das elektrische Feld die Photoreaktion in bestimmte Richtungen lenkt. Hierbei gibt es zwei grundlegend verschiedene Wege, die optimalen Felder zu finden. Einerseits, in der „adaptiven“ Kontrolle, durch Optimierung eines experimentellen Rückkopplungssignals, und andererseits theoretisch in der „optimalen“ Kontrolle durch Berechnung der optimalen Pulsform basierend auf dem Kenntnis der Wellenfunktion des Systems. Unabhängig vom gewählten Kontrollansatz ist immer ein eindeutig identifiziertes Rückkopplungssignal vonnöten, das Aufschluss über den Erfolg einer bestimmten Pulsform für das Kontrollziel gibt. So dient zum Beispiel das erlangte Wissen über die Photochemie der DMA als Grundlage, um in der nahen Zukunft geeignete Rückkopplungssignale auszuwählen, um die Bevölkerung der parallelen Reaktionskanäle der DMA durch die Anregung zu kontrollieren.

Ein komplettes Beispiel einer solchen Kontrolle, von der Spektroskopie der Einzelschritte hin zu einer Steuerung des molekularen Systems, wurde in dieser Arbeit für den molekularen Schalter 6,8-dinitro-1',3',3'-trimethylspiro [2H-1-benzopyran-2,2'-indoline], „6,8-dinitro BIPS“, vorgestellt, der zur Familie der Merocyanin-Spiropyranen gehört. Dieses Molekül ist stabil sowohl in der offenen Form (Merocyanin) als auch der geschlossenen Form (Spiropyran). Obwohl diese Moleküle eine weite Verbreitung haben, wurde der ultraschnelle elektrocyclische Ringschluss eines Merocyanins zum Spiropyran zum ersten Mal in dieser Arbeit durch Abfrage im mittleren Infrarotbereich direkt nachgewiesen. Zudem wurde die Existenz von zwei Merocyaninen mit unterschiedlicher Photochemie und Photophysik gezeigt. Durch Variation der Anregungswellenlänge und einen globalen Fit mehrerer spektrottemporaler transientser Absorptionsdatensätze gleichzeitig mit einem

speziell dafür entwickelten Algorithmus konnte die Quanteneffizienz der verschiedenen Reaktionskanäle bestimmt werden. Während die Interkonversion der Isomere (cis/trans Isomerisierung) keinen großen Beitrag zur Photochemie der Merocyanine liefert, haben beide ringoffenen Isomere eine sehr große Quanteneffizienz ($\approx 40\%$) für den elektrocyclischen Ringschluss.

Durch Erweiterung des Anrege-Abfrage-Experiments um einen zweiten Anregepuls (Wiederanregepuls) konnte zudem nachgewiesen werden, dass aus der geschlossenen Form (Spiropyran) durch UV-Anregung mit Femtosekundenpulsen wieder die geöffnete Form (Merocyanin) generiert werden kann. In diesem Anrege-Wiederanrege-Abfrage-Experiment wird somit ein Subensemble der Moleküle durch einen zweifarbigen Mehrfachpuls aktiv so gesteuert, dass zwischen der offenen und der geschlossenen Form innerhalb von weniger als 40 ps hin- und hergeschaltet wird. Durch eine geschickte Einstellung des Anrege-Wiederanrege-Zeitabstands und der Datenaufnahme konnte so einerseits sowohl die Ringöffnungs- (≈ 36 ps) als auch die Ringschlussreaktionszeit (< 6 ps) bestimmt werden. Andererseits konnte bidirektionales Schalten nachgewiesen werden, das heißt sowohl der Zyklus offen-geschlossen-offen als auch der Zyklus geschlossen-offen-geschlossen konnte verfolgt werden. Für die Zukunft sind Kontrollexperimente geplant, in denen die Quanteneffizienz des Ringschlusses beeinflusst werden soll, was zu einem tieferen Verständnis über die am Ringschluss beteiligten Potentialflächen führen könnte.

Für das bidirektionale Schaltexperiment wurde als Steuerungsparameter der Zeitabstand zwischen Anrege- und Wiederanregepuls benutzt. Für andere Systeme mag der Mechanismus jedoch komplizierter sein. In diesen Fällen hat sich besonders die Pulsformung als attraktive Möglichkeit hervorgetan und bereits in vielen Kontrollexperimenten Anwendung gefunden. Mit Aufkommen der Polarisationspulsformung, also der Kontrolle der Polarisations-eigenschaften des Lichts auf der Femtosekundenzeitskala, hat sich der Wunsch einer chiralen Kontrolle entwickelt, das heißt die Chiralität eines Moleküls mit Hilfe der Chiralität der Femtosekundenpolarisation zu kontrollieren. In einem solchen Experiment bedürfen die sehr kleinen enantiosensitiven optischen Signale, zum Beispiel optische Rotationsdispersion und Zirkulardichroismus, einerseits einer sehr genauen Detektion und andererseits eines experimentellen Aufbaus, der eine Verfälschung dieser Detektion aufgrund experimenteller Artefakte ausschließt.

Bevor eine Reaktion kontrolliert werden kann, muss diese jedoch spektroskopiert werden, z.B. um ein geeignetes Rückkopplungssignal zu identifizieren. Die Spektroskopie einer Reaktion in Anrege-Abfrage-Experimenten mit polarisationsgeformten Anregepulsen, dem Mittel der Wahl um einem Laserpuls chirale Informationen aufzuprägen, war jedoch bisher nicht möglich. Die räumliche Verteilung der abfragbaren Übergangsdipolmomente ist stark abhängig von der Polarisation des Anregepulses, womit das abgefragte Signal prinzipiell auch stark abhängig ist von der Polarisation des Anregepulses und nicht nur von der Population der Zustände. Zwar gibt es für die beiden Grenzfälle linear und zirkular polarisiertes Licht jeweils eine Lösung, in der sich die Anisotropie durch geschickte experimentelle dreidimensionale Anordnung der Polarisation des Abfragepulses aufhebt, eine allgemeingültige Lösung war bisher jedoch unbekannt.

In dieser Arbeit wurde eine theoretische Beschreibung der Anisotropie abhängig von der dreidimensionalen Anrege- und Abfragepolarisation aufgestellt. Anhand dieser Beschreibung wurde eine Möglichkeit identifiziert, die es tatsächlich erlaubt, Anrege-Abfra-

ge-Spektroskopie mit beliebiger Polarisation des Anregepulses durchzuführen. Die beiden vorher bekannten Einzelfälle für linear und zirkulare Polarisation sind nur zwei Elemente dieser Lösung. Es hat sich zudem herausgestellt, dass die allgemeingültige Beschreibung der Anisotropie in dem neuen Ansatz sehr viel mehr zu leisten vermag als bisherige Ansätze. So erlaubt dieser Weg zum Beispiel sogar die Anisotropie komplexerer Experimente, wie zum Beispiel eines Anrege-Wiederanrege-Abfrage-Experiments mit beliebiger dreidimensionaler Polarisation aller beteiligten Pulse, numerisch zu simulieren und daraus Zugriff auf molekulare Größen zu erhalten, die vorher nicht messbar waren, wie zum Beispiel die relative Orientierung der drei beteiligten Übergangsdipolmomente im Anrege-Wiederanrege-Abfrage-Experiment. Dieser Aspekt, vollkommen losgelöst von der chiralen Kontrolle an sich, eröffnet faszinierende Möglichkeiten für neue Spektroskopieexperimente, in denen die Femtosekundendynamik abhängig von der Polarisation des Anrege- und Abfragepulses untersucht werden kann.

Besonders wichtig für die Anrege-Abfrage-Spektroskopie von chiralen Molekülen ist darüber hinaus die Fähigkeit, exakte Spiegelbilder von Polarisationszuständen herzustellen, da chirale Moleküle zwischen den zirkularen Anteilen dieser differenzieren. Denkbar ist in diesem Zusammenhang einerseits ein polarisationsgeformter Anrege- aber auch ein polarisationsgeformter Abfragepuls. Ersteres führt zu einem Experiment, das die Quanteneffizienz abhängig von der Polarisation des Anregepulses spektroskopiert. Die Kombination mit Femtosekundenpulsen könnte in diesem Zusammenhang zum Beispiel zu einem kumulativen, und somit größeren, Zirkulardichroismus führen, da mehrere Wechselwirkungen mit dem chiralen Feld des Anregepulses stattfinden können. Ein polarisationsgeformter Abfragepuls hat hingegen Anwendung zum Beispiel bei der Detektion des transienten Zirkulardichroismus oder der transienten optischen Rotationsdispersion. Beides sind Experimente, die im Moment für einige wenige Spezialfälle mit Hilfe von akusto-optischen oder elektro-optischen Modulatoren schon durchgeführt wurden, das allgemein sehr schlechte Signal-Rausch-Verhältnis in diesen Experimenten gibt jedoch Anlass, auch hier neue Wege zu beschreiten.

In dieser Arbeit wurde ein Aufbau entwickelt, der genau diese Erstellung spiegelbildlicher Polarisationszustände, unabhängig von Wellenlänge und Polarisation, ermöglicht. Analog zu der normalen Anrege-Abfrage-Spektroskopie erlaubt es der Aufbau auf der Schuss-zu-Schuss-Basis zwischen den spiegelbildlichen Polarisationszuständen, sei dies in Funktion als Anrege- oder Abfragepuls, hin- und herzuschalten. Besonders die Unabhängigkeit von der Wellenlänge, die akusto-optische oder elektro-optische Modulatoren zum Beispiel nicht aufweisen, ermöglicht ein sehr gutes Signal-Rausch-Verhältnis für Anrege-Abfrage-Experimente, da gleichzeitig bei vielen Wellenlängen abgefragt werden kann. Die ausführlichen Simulationen in dieser Arbeit am Beispiel der Kombination eines geformten Anregepulses mit diesem Aufbau in einem Anrege-Abfrage-Experiment haben ergeben, dass die notwendige Genauigkeit der Justage für die genannten Experimente umgesetzt werden kann.

Die vorgestellten neuen Erkenntnisse dieser Arbeit, einerseits die mächtige Beschreibung der Anisotropie abhängig von der Polarisation und andererseits die Möglichkeit, exakte Spiegelbilder von Polarisationszuständen zu erstellen, ermöglichen somit polarisationsgeformte Anrege-Abfragespektroskopie. Darüber hinaus ist sogar die Formung des Anregepulses möglich, ohne Anisotropieeffekte einzuführen und somit Kontrollexp-

perimente durchzuführen, in denen zum Beispiel die Polarisation des Anregepulses optimiert wird, um bestimmte, auch transiente, Signale zu maximieren.

Das Signal-Rausch-Verhältnis der verwendeten Detektionsmethode bei diesen Experimenten könnte jedoch besonders in Kontrollexperimenten, in denen der Grad der Kontrolle oft nur gering ist, ein begrenzender Faktor sein. Speziell dafür wurde ein Polarimeter entwickelt, simuliert und aufgebaut. Es wurde besonders auf die Kombination des Polarimeters mit Femtosekundenpulsen geachtet, so hat das Polarimeter ein sehr kleines Wechselwirkungsvolumen (< 10 nL) bei gleichzeitig sehr hoher Auflösung (≈ 0.12 mdeg) und kurzer Datenaufnahmezeit (< 1 s). Alle drei Eigenschaften allein können kaum von kommerziellen Geräten erreicht werden, geschweige denn in Kombination. Die genannten Spezifikationen des selbstgebauten Polarimeters wurden anhand der Photodissoziation von chiralem methyl-*p*-tolyl Sulfoxid nachgewiesen. Aus diesen Experimenten lassen sich allein durch Detektion der optischen Aktivität auf einer optische Weglänge von nur 250 μm quantitative Werte für die Effizienz des Dissoziationskanals extrahieren.

Kapitel 6 und Kapitel 7 dieser Arbeit liefern somit einen Bausatz an theoretischen und experimentellen Vorschlägen, die einerseits auf die Spektroskopie chiraler Moleküle abzielen, sei es durch polarisationsgeformte Anrege- oder Abfragepulse für Anrege-Abfrage-Experimente. Andererseits zeigt sie eine Realisierungsmöglichkeit chiraler Kontrolle, die der Anforderung, einem extrem geringen Enantiomerenüberschuss nachzuweisen, gerecht wird. Beide Ansätze sind erfolgsversprechend und lassen auf viele aufregende Experimente hoffen.

Die spektroskopischen Untersuchungen von Kapitel 4 und Kapitel 5 können als Basis für solche Experimente dienen. Die parallelen und sequentiellen Reaktionskanäle des DMA sowie die Möglichkeit des Anrege-Wiederanrege-Abfrage-Experiments beim 6,8-dinitro BIPS bieten viele Möglichkeiten, um die Zusammenhänge der Anisotropie mit der Polarisation des Anrege-, Wiederanrege- und Abfragepulses zu überprüfen oder die Dynamik durch die Polarisation des Anregepulses zu beeinflussen. Ein zusätzlicher Reiz ist die Tatsache, dass die geschlossene Form des 6,8-dinitro BIPS (Spiropyran) chiral ist und somit die Kombination mit dem Aufbau zur Erzeugung spiegelbildlicher Polarisationszustände besonders attraktiv ist, um vielleicht in der Zukunft tatsächlich einen kumulativen Zirkulardichroismus oder sogar eine chirale Kontrolle nachzuweisen.

A Relation of extinction coefficient and maximum pump–probe signal

When performing pump–probe transient-absorption experiments, the detected absorption change ΔA depends on many parameters. Basically one is interested in the probability P for a successful pumping and probing. This can be separated into two probabilities $P = P_{P_u}P_{P_r}$, with the probability P_{P_u} for successful pumping, i.e. excitation, and the probability P_{P_r} for successful probing. The first probability is the topic of this chapter, whereas the latter probability is treated in Appendix B.1.

When determining the probability for successful excitation, one can calculate directly the relation between the maximum pump–probe signal $\Delta A_{max} = \frac{\Delta A}{P_{P_r}}$ and the linear extinction coefficient at the pump wavelength. The derived pump–probe signal ΔA_{max} is the highest in its value because it is assumed that every excited molecule is probed ($P_{P_r} = 1$) (even the molecules having its probe transition dipole moment in the pump wave vector direction), i.e. the anisotropy of the excited population is not included at all.

In such an isotropic system the intensity of the pump I_0 is decreased due to absorption in the sample by $10^{-\epsilon(\lambda_{P_u})c_1l}$ to I after the sample, with ϵ being the decadic molar extinction coefficient of reactant 1 at wavelength λ_{P_u} , c_1 being the concentration of reactant 1 and l being the optical path length. It is assumed that the intensity I_0 of the pump follows a square function with a width of Δt in time. Analogously it is assumed for the space domain that the intensity follows a square function, with a circular beam shape with radius r , so that the energy of the pump is $E_0 = I_0\pi r^2\Delta t$. The absorbed energy $\Delta E = \Delta I\pi r^2\Delta t$ in a 1-photon process is therefore given by

$$\Delta E = \Delta I\pi r^2\Delta t = (I_0 - I)\pi r^2\Delta t = E_0 (1 - 10^{-\epsilon(\lambda_{P_u})c_1l}). \quad (\text{A.1})$$

With the excitation wavelength λ_{P_u} known, one obtains for the total number of absorbed photons the expression

$$n_{abs} = \frac{\Delta E\lambda_{P_u}}{hc}, \quad (\text{A.2})$$

with h being the Planck constant and c being the speed of light. The number of absorbed photons is the same as the number of excited reactant 1 molecules n_{1e} .

It is assumed now that the pump beam is collimated over the path length l and that it is completely unpolarized. Note that this approximation does not lead to any additional anisotropy but only to an absolute error of the pump–probe signal ΔA_{max} , however as long as saturation effects can be neglected, such as an influence on n_{abs} due to the fact that the pump is polarized, the approximation yields satisfying results. With the mentioned approximations for the pump the illuminated volume V is given by

$$V = \pi r^2l. \quad (\text{A.3})$$

This volume contains n_1 reactant 1 molecules,

$$n_1 = c_1 V N_a, \quad (\text{A.4})$$

with N_a being the Avogadro constant.

The probability for excitation P_{Pu} is then given by

$$P_{Pu}(E_0, c_1, r, l, \lambda_{Pu}, \epsilon(\lambda_{Pu})) = \frac{n_{1e}}{n_1} = \frac{(1 - 10^{-c_1 l \epsilon(\lambda_{Pu})}) E_0 \lambda_{Pu}}{c c_1 \pi r^2 h l N_a}, \quad (\text{A.5})$$

and the maximum absorbance change ΔA_{GSBmax} due to the pure ground-state bleach (probing at the same wavelength as pumping) by

$$\Delta A_{GSBmax} = A_{Pu} - A_0 \quad (\text{A.6})$$

$$= \epsilon(\lambda_{Pu}) [1 - P_{Pu}(E_0, c_1, r, l, \lambda_{Pu}, \epsilon(\lambda_{Pu}))] c_1 l - (\epsilon(\lambda_{Pu}) c_1 l) \quad (\text{A.7})$$

$$= - \frac{(1 - 10^{-c_1 l \epsilon(\lambda_{Pu})}) E_0 \epsilon(\lambda_{Pu}) \lambda_{Pu}}{c \pi r^2 h N_a}, \quad (\text{A.8})$$

with A_{Pu} being the absorbance after excitation and A_0 being the absorbance prior to excitation. As can be seen the absorbance change is proportional to the intensity. Note that this is only true for low intensities, e.g. when only a small fraction of the present molecules is excited. When increasing the intensity multiphoton processes take place such as stimulated emission and the Beer–Lambert law breaks down. Study of these cases is beyond the scope of this chapter.

Substituting realistic values for the variables, e.g. from Chapter 4

- $E_0 = 30 \text{ nJ}$
- $c_1 = 0.0005 \text{ mol/l}$
- $r = 50 \text{ }\mu\text{m}$
- $l = 200 \text{ }\mu\text{m}$
- $\epsilon(\lambda_{Pu}) = 3 \cdot 10^4 \text{ l/(mol cm)}$
- $\lambda_{Pu} = 550 \text{ nm}$,

one obtains for example for $\Delta A_{GSBmax} \approx -26.2 \text{ mOD}$ for the pure ground-state bleach and an excitation probability of $P_{Pu} \approx 8.8\%$.

If probing of the ground-state bleach occurs at another wavelength than pumping ($\lambda_{Pr} \neq \lambda_{pu}$) the expression for ΔA_{GSBmax} becomes

$$\Delta A_{GSBmax} = \frac{c c_1 \pi r^2 h l N_a (\epsilon(\lambda_{Pr}) - \epsilon(\lambda_{pu})) - (1 - 10^{-c_1 l \epsilon(\lambda_{Pu})}) E_0 \epsilon(\lambda_{Pu}) \lambda_{Pu}}{c \pi r^2 h N_a}, \quad (\text{A.9})$$

with $\epsilon(\lambda_{Pr})$ being the extinction coefficient of the ground state at wavelength λ_{Pr} .

If the excited molecules furthermore feature an extinction coefficient $\epsilon_p(\lambda_{Pr}) \neq 0$ at the probing wavelength λ_{Pr} the absorption change ΔA_{max} changes to

$$\Delta A_{max} = A_{EPmax} + \Delta A_{GSBmax} \quad (\text{A.10})$$

$$= P_{Pu}(E_0, c_1, r, l, \lambda_{Pu}, \epsilon(\lambda_{Pr})) c_1 \epsilon_p(\lambda_{Pr}) l + \Delta A_{GSBmax}, \quad (\text{A.11})$$

because of the additional excited-state processes absorbed in A_{EPmax} , namely

- $\epsilon_p(\lambda_{Pr}) > 0$: excited-state absorption
- $\epsilon_p(\lambda_{Pr}) < 0$: stimulated emission.

It may be that the extinction coefficient ϵ depends on the polarization, e.g. for circular-dichroitic media. In this case the polarization has to be interpreted as an interference of a left-circularly polarized part a_{lcpl} and a right-circularly polarized part a_{rcpl} . The extinction coefficient ϵ is then given by

$$\epsilon = a_{lcpl}^2 \epsilon_{lcpl} + a_{rcpl}^2 \epsilon_{rcpl}, \quad (\text{A.12})$$

with ϵ_{lcpl} and ϵ_{rcpl} being the extinction coefficient for $lcpl$ and $rcpl$, respectively. For an arbitrary polarization with the normalized ($ss^* + pp^* = 1$) Jones vector $\begin{pmatrix} s \\ p \end{pmatrix}$ the right-circularly polarized part is given by

$$a_{rcpl} = \begin{pmatrix} s \\ p \end{pmatrix} \cdot \begin{pmatrix} 1 \\ -i \end{pmatrix} \frac{1}{\sqrt{2}} = \left| \frac{ip}{\sqrt{2}} + \frac{s}{\sqrt{2}} \right|, \quad (\text{A.13})$$

and the left-circularly polarized part by

$$a_{lcpl} = \begin{pmatrix} s \\ p \end{pmatrix} \cdot \begin{pmatrix} 1 \\ i \end{pmatrix} \frac{1}{\sqrt{2}} = \left| -\frac{ip}{\sqrt{2}} + \frac{s}{\sqrt{2}} \right|. \quad (\text{A.14})$$

B Anisotropy in pump–probe experiments

In a pump–probe transient-absorption experiment only a subensemble of the excited population can be probed. The probability that an excited molecule is probed depends amongst other things on the polarizations of the pump and the probe pulse. This dependence is exploited in anisotropy measurements that allow to determine angles between the participating transition dipole moments. In the next section a general approach to calculate the probing probability P_{Pr} is shown, which allows to directly calculate the subensemble that is probed and subsequently many experimentally relevant quantities (fourth section), such as the anisotropy or the magic angles (Section 3.1.4) in dependence on molecular and experimental parameters. Specially shaped transition dipole moments due to degeneration are treated in the fifth section. The sixth section shows how to handle the anisotropy of pump–repump–probe experiments. The chapter closes with an experimental suggestion for a shot-to-shot measurement of the anisotropy.

B.1 Derivation of anisotropy formula for 1-photon processes

In this section the probability P_{Pr} for one single molecule being successfully probed with a polarized probe beam after excitation with a polarized pump beam is calculated. This molecule is assumed to be excited. The probability P_{Pu} for this excitation is given in Appendix A. The probability P_{Pr} for successful probing depends on the polarization of pump and probe, the propagation direction of pump and probe and the angle α between the transition dipole moment for excitation (pump transition $|1\rangle \rightarrow |2\rangle$) and probing (probe transition $|2\rangle \rightarrow |3\rangle$). Note that only the directional properties will be treated in this chapter, for the intensity dependence see Appendix A. All electric fields are normalized to $I = 1$ in this chapter. This chapter calculates the probabilities for one molecule whose transition dipole moments (pump and probe) may for example be oriented as in Figure B.1. The following derivation occurs mostly in spherical coordinates. It is always assumed that $r = 1$ (unit sphere) and therefore r is left out in the equations of this section like for spherical harmonics.

It is first assumed that we want to calculate the probability to find the probe transition dipole moment of the individual excited molecule in the direction (θ, ϕ) . The probe transition dipole moment is for example oriented in direction $\vec{\mu}_{23start}(\theta, \phi)$,

$$\vec{\mu}_{23start}(\theta, \phi) = \begin{pmatrix} \sin(\theta) \cos \phi \\ \sin(\theta) \sin \phi \\ \cos(\theta) \end{pmatrix}, \quad (\text{B.1})$$

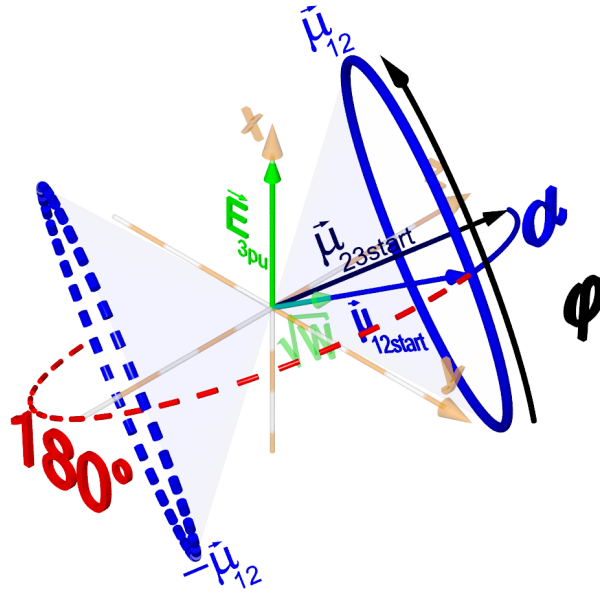


Figure B.1: The probe transition dipole moment $\vec{\mu}_{23start}$ of the excited molecule is assumed to be in direction of the black arrow. It follows that one of the pump transition dipole moments starting in the origin and ending on the right blue circle, $\vec{\mu}_{12}$, was excited previously, since $\vec{\mu}_{12}$ is the set of pump transition dipole moments enclosing the angle α with the probe transition dipole moment. One of these elements is given by the blue arrow, called $\vec{\mu}_{12start}$. The probability that excitation of this transition dipole moment is responsible for the excited probe transition dipole moment $\vec{\mu}_{23start}$ can be obtained via the projection of the three-dimensional pump polarization \vec{E}_{3pu} (green arrow in x direction) onto the $\vec{\mu}_{12start}$. This projection is illustrated as the opaque green arrow and labeled as \sqrt{W} , since the square of the length of this projection is proportional to the weight of the individual pump transition dipole moment $\vec{\mu}_{12start}$. This calculation has to be done for all other elements of $\vec{\mu}_{12}$, which can be mathematically described by a rotation around the probe transition dipole moment (black arrow) by the angle φ . Since the directions of the transition dipole moments are considered, the elements on the left dashed blue circle, which enclose the angle $\alpha + 180^\circ$ with the probe transition dipole moment, do not contribute to the probe transition dipole moment in direction $\vec{\mu}_{23start}$ but to the probe transition dipole moment in direction $-\vec{\mu}_{23start}$.

which is assumed to be the black arrow in Figure B.1.

It is known about the molecule that the pump and probe transition dipole moments enclose the angle α . Hence, only the excitation of the transition dipole moments enclosing the angle α with the probe transition dipole moment $\vec{\mu}_{23start}(\theta, \phi)$ can contribute for a successful probing. All these pump transition dipole moments start in the origin and end on the solid blue circle shown in Figure B.1. The set of these pump transition dipole moments is called $\vec{\mu}_{12}$. For the calculation further on it is necessary to identify one element of this set of pump transition dipole moments, $\vec{\mu}_{12start}(\theta, \phi, \alpha)$. The simplest is

given by

$$\vec{\mu}_{12start}(\theta, \phi, \alpha) = \begin{pmatrix} \sin(\theta - \alpha) \cos \phi \\ \sin(\theta - \alpha) \sin \phi \\ \cos(\theta - \alpha) \end{pmatrix}, \quad (\text{B.2})$$

because

$$\vec{\mu}_{23start}(\theta, \phi) \cdot \vec{\mu}_{12start}(\theta, \phi, \alpha) = \cos \alpha. \quad (\text{B.3})$$

All pump transition dipole moments ($\vec{\mu}_{12}$) that contribute to the direction $\vec{\mu}_{23start}$ can then be described by a rotation of $\vec{\mu}_{12start}(\theta, \phi, \alpha)$ around $\vec{\mu}_{23start}(\theta, \phi)$,

$$\vec{\mu}_{12}(\theta, \phi, \alpha, \varphi) = \text{Rot}(\varphi, \vec{\mu}_{23start}(\theta, \phi)) \cdot \vec{\mu}_{12start}(\theta, \phi, \alpha), \quad (\text{B.4})$$

as shown by the blue circle and the black bent arrow in Figure B.1. Note that an isotropic distribution for the pump transition dipole moments is assumed, meaning that the probability to find a pump transition dipole moment is independent on the direction (θ, ϕ) , i.e. $|\vec{\mu}_{12}(\theta, \phi, \alpha, \varphi)| = 1$. Note that this probability is not normalized. Normalization of the obtained probability is done later on only once. The condition that the probability to find a pump transition dipole moment is independent of the direction $\vec{\mu}_{12}(\theta, \phi, \alpha, \varphi)$ is not valid if any anisotropy is present before excitation, for example due to an orientation or alignment process, see Appendix B.2.2. In that case the probability to find a pump transition dipole moment depends on the direction $\vec{\mu}_{12}(\theta, \phi, \alpha, \varphi)$.

$\text{Rot}(\varphi, \vec{v})$ is the three-dimensional rotation matrix that rotates counter-clockwise around the axis $\vec{v} = \begin{pmatrix} n_x \\ n_y \\ n_z \end{pmatrix}$ by the angle φ with $\sqrt{n_x^2 + n_y^2 + n_z^2} = 1$,

$$\text{Rot}(\varphi, \vec{v}) = \begin{pmatrix} \cos \varphi + n_x^2(1 - \cos \varphi) & n_x n_y(1 - \cos \varphi) - n_z \sin \varphi & n_x n_z(1 - \cos \varphi) + n_y \sin \varphi \\ n_x n_y(1 - \cos \varphi) + n_z \sin \varphi & \cos \varphi + n_y^2(1 - \cos \varphi) & n_y n_z(1 - \cos \varphi) - n_x \sin \varphi \\ n_x n_z(1 - \cos \varphi) - n_y \sin \varphi & n_y n_z(1 - \cos \varphi) + n_x \sin \varphi & \cos \varphi + n_z^2(1 - \cos \varphi) \end{pmatrix}. \quad (\text{B.5})$$

All pump transition dipole orientations contributing to the probing direction $\vec{\mu}_{23start}$ (black arrow in Figure B.1) are then given by $\vec{\mu}_{12}$ (right blue circle in Figure B.1). Integration over them with their appropriate weight W yields the probability that in direction $\vec{\mu}_{23start}$ a probe transition dipole moment is located, whose corresponding pump transition dipole moment has been excited. Generally $W(\theta, \phi, \alpha, \varphi, \chi_{Pu}, \delta_{Pu})$ is given by the square of the scalar product of the three-dimensional polarization \vec{E}_{3Pu} onto the pump transition dipole ($\vec{\mu}_{12}$). It is assumed that propagation of the pump occurs into z direction, hence the three-dimensional polarization \vec{E}_{3Pu} is given by the component in x direction, $\cos \chi_{Pu}$, and y direction, $\sin \chi_{Pu} e^{i\delta_{Pu}}$ (corresponding to the Jones vector $\vec{E}_{Pu} = \begin{pmatrix} \cos \chi_{Pu} \\ \sin \chi_{Pu} e^{i\delta_{Pu}} \end{pmatrix}$ if $x \rightarrow s$ and $y \rightarrow p$, see Eq. 2.64 to Eq. 2.66 and Figure 7.8),

hence W is

$$W(\theta, \phi, \alpha, \varphi, \chi_{Pu}, \delta_{Pu}) = |\vec{E}_{3Pu}(\chi_{Pu}, \delta_{Pu}) \vec{\mu}_{12}(\varphi, \theta, \phi, \alpha)|^2 \quad (\text{B.6})$$

$$= |\cos \chi_{Pu} (-\cos \theta \cos \varphi \sin \alpha \sin \phi + \cos \alpha \sin \theta \sin \phi - \cos \theta \sin \alpha \sin \varphi) \quad (\text{B.7})$$

$$+ \sin \chi_{Pu} e^{i\delta_{Pu}} (\cos \theta \cos \phi \cos \varphi \sin \alpha + \cos \alpha \cos \theta \sin \theta + \sin \alpha \sin \theta \sin \varphi)|^2. \quad (\text{B.8})$$

Figure B.1 shows exemplarily how the appropriate weight W is obtained, in this case for s polarized pump (x direction, green arrow in Figure B.1) and the transition dipole moment $\vec{\mu}_{12start}$ (blue arrow). The opaque green arrow is the projection of the pump polarization direction (green arrow) onto the pump transition dipole moment $\vec{\mu}_{12start}$ (blue arrow). The square of the length of this projection gives the appropriate weight of the pump transition dipole moment $\vec{\mu}_{12start}$.

The interactions of the electric fields of the pump and probe with the transition dipole moments do not depend on the direction, i.e. $\vec{\mu}_{12}$ and $-\vec{\mu}_{12}$ give the same result for the interaction, see Eq. B.8. However, here the direction of the transition dipole moments are taken into consideration. Therefore the dashed blue circle, which are the pump transition dipole moments $-\vec{\mu}_{12}$, enclosing an angle of $\alpha + 180^\circ$ with the probe transition dipole moment, does not contribute to the probing in direction $\vec{\mu}_{23start}$. This is essential later on to distinguish between orientation and alignment in the obtained probabilities, see Section B.2.2. The transition dipole moments of the dashed blue circle are considered when determining the probability to find the probe transition dipole moment in $-\vec{\mu}_{23start}$ direction, thus they are not forgotten.

Now an integration is carried out over φ from 0 to 2π (Figure B.1), to obtain the probability $P3_{an}$, which is not properly normalized yet, that in the direction (θ, ϕ) a probe transition dipole moment is oriented whose pump transition dipole moment has been excited with the pump pulse of Jones vector $\begin{pmatrix} \cos \chi_{Pu} \\ \sin \chi_{Pu} e^{i\delta_{Pu}} \end{pmatrix}$. As stated above this is also a function of α , therefore

$$\begin{aligned} P3_{an}(\theta, \phi, \alpha, \chi_{Pu}, \delta_{Pu}) &= \int_0^{2\pi} W(\theta, \phi, \alpha, \varphi, \chi_{Pu}, \delta_{Pu}) d\varphi \\ &= \pi \left(\frac{1}{2} \cos^2 \theta (1 + \cos(2\phi) \cos(2\chi_{Pu})) \sin^2 \alpha \right. \\ &\quad \left. + \sin^2 \alpha (\cos^2 \chi_{Pu} \sin^2 \phi - 2 \cos \delta_{Pu} \cos \phi \cos \chi_{Pu} \sin^2 \theta \sin \phi \sin \chi_{Pu} + \cos^2 \phi \sin^2 \chi_{Pu}) \right. \\ &\quad \left. + \cos^2 \alpha \sin^2 \theta (1 + \cos(2\phi) \cos(2\chi_{Pu}) + \cos \delta_{Pu} \sin(2\phi) \sin(2\chi_{Pu})) \right). \quad (\text{B.9}) \end{aligned}$$

As a consistency check one can integrate over the spherical coordinates θ and ϕ to see that the volume of the distribution is indeed independent of α as expected,

$$\int_{\phi=0}^{2\pi} \int_{\theta=0}^{\pi} P3(\theta, \phi, \alpha, \chi_{Pu}, \delta_{Pu}) \sin \theta d\theta d\phi = \frac{8\pi^2}{3}. \quad (\text{B.10})$$

As a reminder, $P3(\theta, \phi, \alpha, \chi_{Pu}, \delta_{Pu})$ is proportional to the probability to find the probe transition dipole moment of the molecule in direction (θ, ϕ) . As it is assumed that the

molecule is already excited, the probability to find the probe transition dipole moment in any direction (θ, ϕ) needs to be 1. Therefore $P3$ can be normalized by dividing it by $\frac{8\pi^2}{3}$,

$$P3(\theta, \phi, \alpha, \chi_{Pu}, \delta_{Pu}) = P3_{an}(\theta, \phi, \alpha, \chi_{Pu}, \delta_{Pu}) \frac{3}{8\pi^2}, \quad (\text{B.11})$$

so that its integral is 1.

The distribution $P3$ needs to be multiplied with the distribution $P4$ which a polarized probe pulse can query in an isotropic medium. This distribution is given by the scalar product of the three-dimensional polarization vector of the probe and the probe transition dipole moment direction $\vec{\mu}_{23start}$.

The three-dimensional polarization vector is not as easily obtained as for the pump pulse, because now the angle β determines the angle between the wave vector of the pump and the probe. With the pump propagating always in z direction, one has to rotate the three-dimensional probe-polarization vector \vec{E}_{3Pr1} , constructed analogously to the three-dimensional pump-polarization vector \vec{E}_{3Pu} , by the angle β around an axis to obtain the correct three-dimensional pump polarization vector \vec{E}_{3Pr} . For simplicity it is declared that the s direction of the probe is always in x direction (like for the pump vector \vec{E}_{3Pu} , see also Figure 7.8), hence

$$E_{Pr} = \begin{pmatrix} \cos \chi_{Pr} \\ \sin \chi_{Pr} e^{i\delta_{Pr}} \\ 0 \end{pmatrix} \rightarrow \vec{E}_{3Pr1} = \begin{pmatrix} \cos \chi_{Pr} \\ \sin \chi_{Pr} e^{i\delta_{Pr}} \\ 0 \end{pmatrix}. \quad (\text{B.12})$$

The rotation has to be carried out around the x axis, so that the s direction is invariant to rotation, leading to the three-dimensional polarization vector \vec{E}_{3Pr} ,

$$\vec{E}_{3Pr}(\chi_{Pr}, \delta_{Pr}, \beta) = \begin{pmatrix} \cos \chi_{Pr} \\ e^{i\delta_{Pr}} \sin \chi_{Pr} \cos \beta \\ e^{i\delta_{Pr}} \sin \chi_{Pr} \sin \beta \end{pmatrix}. \quad (\text{B.13})$$

The distribution $P4$ is then given by

$$P4(\theta, \phi, \chi_{Pr}, \delta_{Pr}, \beta) = |\vec{\mu}_{23start}(\theta, \phi) \vec{E}_{3Pr}(\chi_{Pr}, \delta_{Pr}, \beta)|^2, \quad (\text{B.14})$$

leading to

$$P4(\theta, \phi, \chi_{Pr}, \delta_{Pr}, \beta) = |\cos \phi \cos \chi_{Pr} \sin \theta + e^{i\delta_{Pr}} \cos \theta \sin \beta \sin \chi_{Pr} + e^{i\delta_{Pr}} \cos \beta \sin \theta \sin \phi \sin \chi_{Pr}|^2. \quad (\text{B.15})$$

The distribution that is queried in a pump-probe experiment is given by $P5$,

$$P5(\theta, \phi, \alpha, \chi_{Pu}, \delta_{Pu}, \chi_{Pr}, \delta_{Pr}, \beta) = P3(\theta, \phi, \alpha, \chi_{Pu}, \delta_{Pu}) P4(\theta, \phi, \chi_{Pr}, \delta_{Pr}, \beta), \quad (\text{B.16})$$

and the probability P_{Pr} of this distribution is the volume of this distribution,

$$\begin{aligned}
P_{Pr}(\alpha, \chi_{Pu}, \delta_{Pu}, \chi_{Pr}, \delta_{Pr}, \beta) = & \\
& \int_{\phi=0}^{2\pi} \int_{\theta=0}^{\pi} P5(\theta, \phi, \alpha, \chi_{Pu}, \delta_{Pu}, \chi_{Pr}, \delta_{Pr}, \beta) \sin \theta d\theta d\phi = \\
& \frac{1}{80} \left(\sin^2 \alpha (26 - 2 \cos(2\beta) + \cos(2(\beta - \chi_{Pr}))) - 2 \cos(2\chi_{Pr}) + \cos(2(\beta + \chi_{Pr})) \right. \\
& - \cos(2\chi_{Pu}) (2(3 + \cos(2\beta)) \cos(2\chi_{Pr}) + 4 \sin^2 \beta) + 4 \cos^2 \alpha (7 + \cos(2\chi_{Pr})) \\
& + 4 \cos^2 \chi_{Pr} \cos(2\chi_{Pu}) + 2 (\cos(2\beta) - 2 \cos^2 \beta \cos(2\chi_{Pu})) \sin^2 \chi_{Pr} \\
& \left. + 4(1 + 3 \cos(2\alpha)) \cos \beta \cos \delta_{Pr} \cos \delta_{Pu} \sin(2\chi_{Pr}) \sin(2\chi_{Pu}) \right) \quad (\text{B.17})
\end{aligned}$$

and the probability that a probing is successful.

However, if P_{Pr} is a probability, it needs to be properly normalized. This is checked by assuming that the probing pulse is unpolarized, i.e. $P4$ should be replaced by the spherically symmetric distribution $P4_{sph}$. In this case the probing transition dipole moment can be oriented in any direction and is always detected. This can be achieved when realizing that if one detects simultaneously with a sum of linearly polarized pulses in x, y and z direction each contributing with their respective $P4$ distribution, $P4_{sph}$ becomes spherically symmetric (see Eq. B.1 for the last transformation),

$$P4_{sph} = P4(\theta, \phi, 0, 0, 0) + P4(\theta, \phi, 90^\circ, 0, 0) + P4(\theta, \phi, 90^\circ, 0, 90^\circ) \quad (\text{B.18})$$

$$= |\cos^2 \theta + \sin^2 \theta \cos^2 \phi + \sin^2 \theta \sin^2 \phi| = 1. \quad (\text{B.19})$$

As is not surprising $P_{Pr} = 1$ when probing with $P4_{sph} = 1$, since only a multiplication of $P3$ with 1 takes place,

$$\int_{\phi=0}^{2\pi} \int_{\theta=0}^{\pi} P3(\theta, \phi, \alpha, \chi_{Pu}, \delta_{Pu}) P4_{sph} \sin \theta d\theta d\phi = 1, \quad (\text{B.20})$$

because the volume of $P3$ has already been normalized to 1.

The equation for P_{Pr} gives the probability that successful probing takes place of a single molecule with arbitrary orientation and arbitrary polarization of the pump. The orientation of the coordinate system is defined by the propagation direction of the pump (in cartesian coordinates: z direction; in spherical coordinates: $(\theta = 0, \phi)$ direction) and the definition of the s component (x direction or $(\theta = 90^\circ)$).

With the knowledge of P_{Pr} one can directly derive the anisotropy r of Eq. 3.10 with

$$r(\alpha) = \frac{P_{Pr}(\alpha, 0, 0, 0, 0, 0) - P_{Pr}(\alpha, 0, 0, 90^\circ, 0, 0)}{P_{Pr}(\alpha, 0, 0, 0, 0, 0) + 2P_{Pr}(\alpha, 0, 0, 90^\circ, 0, 0)} \quad (\text{B.21})$$

$$= \frac{1}{10} (1 + 3 \cos(2\alpha)), \quad (\text{B.22})$$

which is in agreement with the literature.

In order to obtain the transient-absorption signal ΔA one also needs to know the actual maximum transient-absorption signal ΔA_{max} or the probability P_{Pu} (Eq. A.5) for excitation, which corresponds to the case of unpolarized excitation and probing. This depends on many additional parameters and is derived in Appendix A. The true transient-absorption signal ΔA is then given by

$$\Delta A = A_{EPmax} P_{Pr}(\alpha_{EP}, \chi_{Pu}, \delta_{Pu}, \chi_{Pr}, \delta_{Pr}, \beta) + \Delta A_{GSBmax} P_{Pr}(\alpha = 0, \chi_{Pu}, \delta_{Pu}, \chi_{Pr}, \delta_{Pr}, \beta), \quad (\text{B.23})$$

with the excited-state process having the maximum transient-absorption signal A_{EPmax} (see Eq. A.11) and enclosing the angle α_{EP} between pump and probe transition dipole moment. For the ground-state bleach signal ΔA_{GSBmax} , the angle between pump and probe transition dipole moment is $\alpha = 0$ as long as no rotation of the molecule between excitation and probing takes place, see Appendix B.2.1. ΔA_{GSB} can also be expressed only with A_0 , the absorbance prior to excitation (see Eq. A.5),

$$\Delta A_{GSB} = A_0(\lambda_{Pu}) P_{Pr}(\alpha = 0, \chi_{Pu}, \delta_{Pu}, \chi_{Pr}, \delta_{Pr}, \beta) P_{Pu}(E_0, c_1, r, l, \lambda_{Pu}, \epsilon_1(\lambda_{Pu})), \quad (\text{B.24})$$

Note that this equation holds only as long as the same wavelength is probed at which pumping occurs and no excited-state processes such as excited-state absorption or stimulated emission takes place, i.e. only ground-state bleach is probed.

B.2 Rotation of molecules

Non-linear molecules can rotate around three axes. This rotation is free in the gas phase, while it is strongly hindered in solution due to the Brownian motion. The rotational degrees of freedom influence the measured anisotropy in two possible ways. The first possibility is due to rotational diffusion after excitation, this is a random process and leads to a recovery of an isotropic distribution, as shown in the next subsection. The second possibility is to actively induce a partial alignment or orientation into the isotropic distribution of the molecules leading to an anisotropic distribution of the molecules already prior or during excitation as shown in the second subsection. Note that the latter is so far only possible in the gas phase.

B.2.1 Rotational diffusion

As shown in Section 7.3 and Appendix B.1 after photoexcitation an anisotropic distribution of the excited population is obtained that depends on the polarization of the pump as well as the angle α between excitation and probing, see especially Figure 7.6 and Figure 7.7. This distribution is only present very shortly after excitation. Thermodynamics dictate that at temperatures greater than a few Kelvin rotational states with quantum number $J \geq 1$ are populated (see for example Tab. 1 in [206]), hence the molecules rotate. Since the rotational distribution prior to excitation is random, the rotational distribution after excitation is random, too.

In case of a spherical molecule all three rotation axes are equal. In that case the loss of initial anisotropy r_0 to the anisotropy r at time Δt follows a monoexponential decay with time [71]

$$r(\Delta t) = r_0 e^{-\frac{\Delta t}{\theta}}, \quad (\text{B.25})$$

with θ being here the rotational correlation time

$$\theta = \frac{\eta V}{RT}, \quad (\text{B.26})$$

with V being the volume of the spherical molecule, η being the viscosity of the surrounding, R being the gas constant and T being the temperature. The anisotropy decay of more complex-shaped molecules is given in Chapter 12 of [71].

The measurement of the rotational correlation time is used for example to determine the structure of proteins, which have a rotational correlation time on the scale of a few nanoseconds, see for example [71, 207]. For small molecules rotation is faster and happens on the order of a few picoseconds, see for example [116].

Rotational diffusion has been implemented in a very simple way into the program used to simulate for example the ground-state circular-dichroism experiment of Section 7.4. Rotational diffusion is included in the calculation of P_{Pr} by substituting P_3 with P_{3-rot} ,

$$P_{3-rot} = (1 - rot)P_3 + rot\frac{3}{4\pi}, \quad (\text{B.27})$$

in Eq. B.17, with $rot = 0$ when no diffusional rotation has taken place and $r = 1$ after complete recovery of isotropy. The factor $\frac{3}{4\pi}$ is necessary so that the volume of P_{3-rot} is

always 1. However, rotational diffusion mostly destroys the anisotropy of the distribution and since anisotropy is among the topics of this thesis always disturbing the experiment, it was always assumed the “worst-case scenario” of $rot = 0$ in the simulation results given in this thesis.

B.2.2 Alignment and orientation of molecules

Interaction of a molecule with radiation is not limited to conventional absorption and emission of a photon. Radiation is an electromagnetic wave and hence a molecule that possesses a dipole or an induced dipole aligns itself according to the electrostatic force. This effect can be utilized to introduce an anisotropy in the sample. However this approach has so far only been proven in the gas phase at temperatures on the order of a few Kelvin, where the limit of isolated molecules in only one rotational quantum state is most valid, but not in the liquid phase due to the Brownian motion.

One has to distinguish between 1D alignment, 3D alignment, and orientation of molecules [208, 209]. 1D alignment means that one molecular axis is aligned parallel to an external axis, e.g. a laboratory axis. However, in such an aligned molecule rotation around the external axis is still allowed. In 3D alignment two molecular axes are aligned parallel to two external axes. In that case the molecule does not have any freedom to rotate around an axis anymore. On top of that, orientation also requires that the *direction* of the molecular axis points in a certain external direction. Alignment and orientation are expressed in the literature by $\langle \cos^2 \theta \rangle$ and $\langle \cos \theta \rangle$, respectively. These values are the mean of the projection (or its square) of the chosen molecular axis onto the external axis, with θ being the angle between the molecular and the external axis. A value of $\langle \cos^2 \theta \rangle = 1$ corresponds to perfect alignment, i.e. the molecular axis of all molecules are parallel to the external axis and a value of $\langle \cos \theta \rangle = 1$ to perfect orientation, i.e. the molecular direction of all molecules point in a certain external direction.

Alignment

Alignment can be achieved either with intense pulses that are much longer in time than the rotational time scale, called adiabatic alignment, or with short intense pulses, where the pulse length must be longer than the inverse of the Rabi frequency between the rovibronic transitions but shorter than the rotational time scale, called nonadiabatic alignment.

Nonadiabatic alignment In the case of nonadiabatic alignment, multiple Rabi cycling between the resonant rovibronic transitions allows to form a wavepacket spreading a large range of rotational quantum numbers [208]. This rotational wavepacket starts after the initial “kick” due to the ultrashort excitation pulse and propagates in time by dephasing and rephasing, see for example [210].

Note that the excitation wavelength does not need to be resonant with a transition [208]. In nonresonant excitation Raman processes take place with the selection rule $\Delta J = 0; \pm 2$. The nonresonant nature of such an experiment requires higher laser intensities, with the limit being the multiphoton ionization of the investigated molecule.

Adiabatic alignment In the case of adiabatic alignment a long intense laser pulse allows the rotational eigenstates to evolve adiabatically into eigenstates of the complete Hamiltonian, similar to “dressed states” [48]. In case of eigenstates of a free rotor these states are called pendular states. The induced anisotropy in adiabatic alignment persists only as long as the electromagnetic field is present, i.e. after switching the laser off it is lost in contrast to the wavepacket in nonadiabatic alignment.

Influence on anisotropy In order to obtain P_{Pr} in Appendix B.1 an isotropic mixture was assumed prior to excitation. This was expressed by the fact that in Eq. B.8 the pump transition dipole moment $\vec{\mu}_{12}$ has always the length $r = 1$, see also Eq. B.2 and Eq. B.4. It is assumed now that the alignment process leads to a partial alignment of the pump transition dipole moments $\vec{\mu}_{12}$. In order to include alignment one would have to determine the dependence of the pump transition dipole moment length r on the direction (θ, ϕ) and then substitute $\vec{\mu}_{12}$ by $r\vec{\mu}_{12}$ in Appendix B.1.

Qualitatively, an alignment parallel to the y axis, an angle of $\alpha = 0$ between pump and probe transition dipole moment and excitation with linearly polarized light in y direction would lead to a P_3 distribution being much more compressed in x and z direction compared to the top left graph of Figure 7.6 obtained without alignment. In case of $\alpha = 90^\circ$, top right in Figure 7.6, the distribution would be compressed into y direction.

Orientation

Orientation is much more ambitious, since the oscillating nature of the electromagnetic wave forbids that a polar molecule is fixed in its orientation in the laboratory frame [209]. Nevertheless, it is very attractive because it has been theoretically shown that a chiral control only due to the interaction with the electric field may be possible if the sample has been oriented [188]. Such a chiral control based on the electric field would exhibit enantioselectivities exceeding by far the conventional circular dichroism.

In order to realize orientation of molecules “brute-force” approaches have been exploited in which the molecules are placed inside a very strong static electric field. A similar approach is used in [206] in which a deflector with a static electric field is used on the one hand to orient a molecule with a large dipole moment in the gas phase and on the other hand to spatially distribute the rotational states according to their quantum number. Another way to achieve orientation with femtosecond laser pulses has been shown by Oda *et. al.* [211]. An interference of a fundamental femtosecond laser pulse (frequency ω) with its second harmonic (frequency 2ω) leads to peaking electric fields $E(t)$ in one direction when they have a relative phase $\phi \neq 0$,

$$E(t) = E_1(t) \cos(\omega t) + E_2(t) \cos(2\omega t + \phi), \quad (\text{B.28})$$

with E_1 and E_2 being the field amplitude of the fundamental and the second harmonic wave, respectively. This peaking is maximum if the phase is $\phi = \pm\frac{\pi}{2}$. Note that the mean value of $E(t)$ is zero independent of ϕ . However, since orientation is a highly nonlinear process, the peaking of the electric field in one direction leads to orientation in that direction.

Influence on anisotropy If a sample is oriented in one direction the transition dipole moments all point in one direction. Assume for example that the pump and probe transition dipole moment enclose an angle of $\alpha = 0^\circ$. Then the pump and probe transition dipole moments of the molecules, in case of perfect orientation for example in direction of the black arrow in Figure B.1, would all point exactly in that direction. There would be no transition dipole moment pointing in the inverse direction or any other direction, since they oriented and not aligned. This means that $\vec{\mu}_{12}$ is zero except for the direction in which the black arrow is pointing. Thus also W in Eq. B.8 and subsequently $P3$ in Eq. B.11 is zero except for the direction of the black arrow. Note that this is independent of the pump Jones vector \vec{E}_{3Pu} . The Jones vector of the pump only influences the volume of the distribution, therefore normalization in such an anisotropic distribution cannot be done as simply as for the isotropic distribution in Appendix B.1.

Summarizing, one can state that orientation would result in the loss of mirror-plane symmetry with respect to the x - z plane in the two top graphs of Figure 7.6, with the conditions given in the corresponding caption. In a perfect orientation the distribution would only be present on one side of this plane.

B.3 Multi-photon processes

In case of a multi-photon process the appropriate weight W_n is given by

$$W_n(\theta, \phi, \alpha, \varphi, \chi_{Pu}, \delta_{Pu}) = |\vec{E}_{3Pu}(\chi_{Pu}, \delta_{Pu}) \vec{\mu}_{12}(\varphi, \theta, \phi, \alpha)|^{2n}, \quad (\text{B.29})$$

with n being the order of the process. In case of a 2-photon process ($n = 2$) one obtains for the distribution $P3_2(\theta, \phi, \alpha, \chi_{Pu}, \delta_{Pu})$,

$$\begin{aligned} P3_2(\theta, \phi, \alpha, \chi_{Pu}, \delta_{Pu}) &= \int_{\varphi=0}^{2\pi} W_2(\theta, \phi, \alpha, \varphi, \chi_{Pu}, \delta_{Pu}) d\varphi = \\ &\frac{1}{256}\pi \left(12 \cos^4 \theta \sin^4 \alpha (2 + \cos(2(\phi - \chi_{Pu})) + \cos(2(\phi + \chi_{Pu}))) \right. \\ &+ 2 \cos \delta_{Pu} \sin(2\phi) \sin(2\chi_{Pu})^2 + 4 \left(24 \cos^4 \chi_{Pu} (2 \sin^4 \alpha \sin^4 \phi + \sin^2(2\alpha) \sin^2(\theta) \sin^2(2\phi)) \right. \\ &\quad \left. - 192 \cos \delta_{Pu} \cos \phi \cos^3 \chi_{Pu} \sin^4 \alpha \sin^3 \phi \sin \chi_{Pu} \right. \\ &\quad \left. + 288 \cos^2 \delta_{Pu} \cos^2 \phi \cos^2 \chi_{Pu} \sin^4 \alpha \sin^2 \phi \sin^2 \chi_{Pu} + 96 \cos \delta_{Pu} \cos \phi \cos \chi_{Pu} \sin \phi \right. \\ &\quad \left. (-2 \cos^2 \phi \sin^4 \alpha + \sin^2(2\alpha) \sin^2 \delta_{Pu} \sin^2(2\theta) \sin^2 \phi) \sin^3 \chi_{Pu} \right. \\ &\quad \left. + 48 \cos^4 \delta_{Pu} \cos^4 \phi \sin^4 \alpha \sin^4 \chi_{Pu} + 96 \cos^2 \delta_{Pu} \cos^4 \phi \sin^4 \alpha \sin^2 \delta_{Pu} \sin^4 \chi_{Pu} \right. \\ &\quad \left. + 48 \cos^4 \phi \sin^4 \alpha \sin^4 \delta_{Pu} \sin^4 \chi_{Pu} + 24 \cos^4 \delta_{Pu} \sin^2(2\alpha) \sin^2(2\theta) \sin^4 \phi \sin^4 \chi_{Pu} \right. \\ &\quad \left. + 24 \sin^2(2\alpha) \sin^4 \delta_{Pu} \sin^2(2\theta) \sin^4 \phi \sin^4 \chi_{Pu} + 12 \sin^2(2\alpha) \sin^2(2\delta_{Pu}) \sin^2(2\theta) \sin^4(\phi) \sin^4(\chi_{Pu}) \right. \\ &\quad \left. + 24 \cos^4 \delta_{Pu} \sin^2(2\alpha) \sin^2 \theta \sin^2(2\phi) \sin^4 \chi_{Pu} + 24 \sin^2(2\alpha) \sin^4 \delta_{Pu} \sin^2 \theta \sin^2(2\phi) \sin^4 \chi_{Pu} \right. \\ &\quad \left. + 12 \sin^2(2\alpha) \sin^2(2\delta_{Pu}) \sin^2 \theta \sin^2(2\phi) \sin^4 \chi_{Pu} + 8 \sin^2(2\alpha) \sin^2 \delta_{Pu} \sin^2 \theta \sin^4 \phi \sin^2(2\chi_{Pu}) \right. \\ &\quad \left. + 6 \sin^4 \alpha \sin^2 \delta_{Pu} \sin^2(2\phi) \sin^2(2\chi_{Pu}) - 24 \cos^2 \delta_{Pu} \sin^2(2\alpha) \sin^2 \theta \sin^2(2\phi) \sin^2(2\chi_{Pu}) \right. \\ &\quad \left. - 8 \sin^2(2\alpha) \sin^2 \delta_{Pu} \sin^2 \theta \sin^2(2\phi) \sin^2(2\chi_{Pu}) + 9 \cos^2 \delta_{Pu} \sin^2(2\alpha) \sin^2(2\theta) \sin^2(2\phi) \sin^2(2\chi_{Pu}) \right. \\ &\quad \left. + 3 \sin^2(2\alpha) \sin^2 \delta_{Pu} \sin^2(2\theta) \sin^2(2\phi) \sin^2(2\chi_{Pu}) + 8 \cos^4 \alpha \sin^4 \theta (2 + \cos(2(\phi - \chi_{Pu}))) \right. \\ &\quad \left. + \cos(2(\phi + \chi_{Pu})) + 2 \cos \delta_{Pu} \sin(2\phi) \sin(2\chi_{Pu}) \right)^2 \\ &\quad + 32 \cos^2 \alpha \sin^2 \alpha \sin^2 \theta \left(12 \cos^2 \delta_{Pu} \cos^2 \chi_{Pu} \sin^4 \phi \sin^2 \chi_{Pu} + \right. \\ &\quad \left. (2 + \cos(2\delta_{Pu})) \cos^4 \phi \sin^2(2\chi_{Pu}) \right) - 12 \cos \delta_{Pu} \sin^2(2\alpha) \sin^2(\theta) \sin(4\phi) \sin(4\chi_{Pu}) \\ &\quad + \cos^2 \theta \sin^2 \alpha \left(1536 \cos^2 \alpha \cos \phi \cos \chi_{Pu} \sin^2 \theta (\cos^3 \phi \cos^3 \chi_{Pu} \right. \\ &\quad \left. + 4 \cos \delta_{Pu} \cos^2 \phi \cos^2 \chi_{Pu} \sin \phi \sin \chi_{Pu} + 4 \cos^3 \delta_{Pu} \sin^3 \phi \sin^3 \chi_{Pu}) \right. \\ &\quad \left. + 2 \sin^2 \alpha (22 + 2 \cos(2\delta_{Pu}) + 3 \cos(2(\delta_{Pu} - 2\phi))) - 6 \cos(4\phi) + 3 \cos(2(\delta_{Pu} + 2\phi)) \right. \\ &\quad \left. - \cos(4\chi_{Pu}) (6(3 + \cos(2\delta_{Pu})) \cos(4\phi) - 4 \sin^2 \delta_{Pu}) - 24 \cos \delta_{Pu} \sin(4\phi) \sin(4\chi_{Pu}) \right) \end{aligned} \quad (\text{B.30})$$

which gives the probability to find a probe transition dipole moment whose corresponding pump transition dipole moment (both enclose the angle α) has been excited in a 2-photon process.

However, a straightforward analysis of the anisotropy as in the 1-photon process is not possible, as also explained in Section 7.4.3. For example a normalization is not as straightforward as for the 1-photon process, since the probability to find an excited molecule depends on the intensity and hence also on δ_{Pu} and χ_{Pu} , i.e. in circular

polarization the intensity is less compared to linear polarization. This relative phase dependence is contained in the probability distribution $P3_2$,

$$\int_{\theta=0}^{\pi} \int_{\phi=0}^{2\pi} P3_2(\theta, \phi, \alpha, \chi_{Pu}, \delta_{Pu}) \sin \theta d\theta d\phi = \frac{2}{15} \pi^2 (11 + \cos(2\delta_{Pu}) + 2 \cos(4\chi_{Pu}) \sin^2 \delta_{Pu}). \quad (\text{B.31})$$

Since a 2-photon process is not part of this thesis a further elaboration of the 2-photon process will not be done here.

B.4 Magic-angle conditions

Usually in pump–probe experiments the population of states is at the center of interest and not the orientational distribution. Therefore an experimental arrangement is necessary in which the angle α between the pump and probe transition dipole moment does not have any influence on the pump–probe signal via P_{Pr} ,

$$\frac{\partial P_{Pr}}{\partial \alpha} = 0. \quad (\text{B.32})$$

Indeed it is possible to find such a condition, as will be shown in this section.

B.4.1 Linearly polarized pump pulses

The conditions of linearly polarized pump in s direction and linearly polarized probe that enclose the angle χ_{Pr} with the s direction lead for the pump–probe signal intensity P_{Pr} to

$$P_{Pr}(\alpha, 0, 0, \chi_{Pr}, 0, \beta) = \frac{1}{60} \{7 + \cos[2\chi_{Pr}] + \cos[2\alpha][1 + 3 \cos(2\chi_{Pr})]\}. \quad (\text{B.33})$$

In this expression the angle β between pump and probe has no longer any influence because the pump is polarized in s direction and β rotates the probe polarization in such a way that the s direction is maintained (see Figure 7.8). Since the distribution $P3$ created by the pump is symmetric with respect to rotation around the polarization axis (s direction), see Section 7.3.1, the direction of the p polarization of the probe is irrelevant, since it always is orthogonal to the s direction of the pump and probe and hence the formula does not depend on β any more.

Finding the root of the differentiation of this equation with respect to α one arrives at

$$\chi_{Pr} = \pm \arccos\left(\pm \frac{1}{\sqrt{3}}\right) \approx n\pi \pm 54.735^\circ \quad (\text{B.34})$$

for the angle χ_{Pr} , corresponding directly to the magic angle χ_{MA} in Section 3.1.4. Note that the value of P_{Pr} is in that case $P_{Pr}(\alpha, 0, 0, \chi_{Pr} = \chi_{MA}, 0, \beta) = \frac{1}{3}$, hence only one third of the pumped population is probed in magic-angle configuration (see also Figure 3.5).

When assuming that the linear polarization of the probe is in s direction instead of the pump, $P_{Pr}(\alpha, \chi_{Pu}, \delta_{Pu}, 0, 0, \beta)$, one arrives at the same condition for χ_{Pu} . In this scenario the pump pulse and the probe enclose again the magic angle, but the pump pulse is not s polarized.

However, when assuming that the linear polarization of the pump is in p direction, $P_{Pr}(\alpha, 90^\circ, 0, \chi_{Pr}, 0, \beta)$, one arrives at the condition

$$\chi_{Pr} = \pm \arccos\left[\pm \frac{1}{\sqrt{3}\sqrt{\cos(\beta)^2}}\right], \quad (\text{B.35})$$

which is different from the condition of Eq. B.34 for $\beta \neq 0$. Whereas for small angles β the deviation from the conventional magic angle of $\approx n\pi \pm 54.735^\circ$ is very small, one nevertheless should pay attention in the experiment that either the linear polarization of the pump or the probe is parallel to the rotation axis (green arrow in Figure 7.8) that connects pump and probe wave vector.

B.4.2 Circularly polarized pump pulses

For circularly polarized light the condition for β to achieve an anisotropy-free signal derived by solving $\frac{\partial P_{Pr}(\alpha, 45^\circ, \frac{\pi}{2}, 90^\circ, 0, \beta)}{\partial \alpha} = 0$ is given by

$$\beta = \pm \frac{1}{2} \arccos \frac{1}{3} \approx \pm 35.264^\circ, \quad (\text{B.36})$$

in agreement with the literature [198]. Note that here, the angle between the wave vectors of pump and probe has to be set to the correct angle to get rid of anisotropy effects.

B.4.3 Arbitrarily polarized pump pulses

The arbitrary polarization is assumed to follow Eq. 7.5, hence a solution is to be found in which probing probability P_{Pr} is independent of α and the relative phase δ_{Pu} between the components of the Jones vector. Only the angle β (see Figure 7.8) between the wave vectors of pump and probe is available as degree of freedom, hence the pump–probe signal intensity is $P_{Pr}(\alpha, \chi_{Pu}, \delta_{Pu}, 90^\circ, 0, \beta)$. The condition for β follows to be

$$\beta = \pm \arccos \frac{1}{\sqrt{3}|\sin \chi_{Pu}|}, \quad (\text{B.37})$$

hence it still depends on the amplitude of the components of the pump described by χ_{Pu} . Note that $\chi_{Pu} \neq \theta$ for $\delta_{Pu} \neq 0$ (elliptical and circular polarizations) with θ being here the orientational angle of the Poincaré sphere (see Eq. 2.36). The relation of β with the amplitude of the components is shown in Figure 7.9.

B.5 Anisotropy of degenerate transition dipole moments

In degenerate systems also the transition dipole moment for the pump or probe transition might be degenerate, meaning that two or more equal transition dipole moments exist. This is especially often the case in highly symmetric molecules such as porphyrin or benzene. In these cases the transition dipole moment might not be represented by a vector in one direction but by a sum of vectors that form a disk for example. The anisotropy for such specially shaped transition dipole moments can also be modelled with the approach in Section B.1.

B.5.1 Degenerate pump transition dipole moments

This modeling is exemplarily done here with the assumption that there are two perpendicularly oriented degenerate pump transition dipole moments that form a disk (two-fold degenerate). In the following three ways will be presented, which all lead to the same result for the anisotropy.

Integration over an additional angle

The plane in which the transition dipole moments lie is identified by its normal \vec{n} . This normal is assumed to enclose the angle $\tilde{\alpha}$ with the probe transition dipole moment. This plane is obtained by defining the normal of the plane containing the transition dipole moments as \vec{n} as

$$\vec{n}(\theta, \phi, \tilde{\alpha}) = \begin{pmatrix} \sin(\theta - \tilde{\alpha}) \cos \phi \\ \sin(\theta - \tilde{\alpha}) \sin \phi \\ \cos(\theta - \tilde{\alpha}) \end{pmatrix}. \quad (\text{B.38})$$

One transition dipole moment that is an element of this plane is given by

$$\vec{\mu}_{12start}(\theta, \phi, \tilde{\alpha}) = \begin{pmatrix} \sin(\theta - \tilde{\alpha} - 90^\circ) \cos \phi \\ \sin(\theta - \tilde{\alpha} - 90^\circ) \sin \phi \\ \cos(\theta - \tilde{\alpha} - 90^\circ) \end{pmatrix}. \quad (\text{B.39})$$

Similar to before this single transition dipole moment is present in any direction given by the rotation of $\vec{\mu}_{12start}(\theta, \phi, \tilde{\alpha})$ around the probe transition dipole moment direction $\vec{\mu}_{23start}$,

$$\vec{\mu}_{23start}(\theta, \phi) = \begin{pmatrix} \sin(\theta) \cos \phi \\ \sin(\theta) \sin \phi \\ \cos(\theta) \end{pmatrix}, \quad (\text{B.40})$$

by the angle φ . All these transition dipole moments are therefore given by

$$\vec{\mu}_{12startall}(\varphi, \theta, \phi, \alpha) = \text{Rot}(\varphi, \vec{\mu}_{23start}) \vec{\mu}_{12start}(\theta, \phi, \alpha). \quad (\text{B.41})$$

However, any direction given by $\vec{\mu}_{12startall}(\varphi, \theta, \phi, \alpha)$ represents only one transition dipole moment of the plane of transition dipole moments given by the normal $\vec{n}_{12startall}$ to

$$\vec{n}_{12startall}(\varphi, \theta, \phi, \alpha) = \text{Rot}(\varphi, \vec{\mu}_{23start}(\theta, \phi)) \vec{n}(\theta, \phi, \alpha). \quad (\text{B.42})$$

All other transition dipole moments in that plane ($\vec{\mu}_{12all}$) are described by

$$\vec{\mu}_{12all}(\varphi, \omega, \theta, \phi, \alpha) = Rot(\omega, \vec{n}_{12startall}(\varphi, \theta, \phi, \alpha)) \vec{\mu}_{12startall}(\varphi, \theta, \phi, \alpha). \quad (\text{B.43})$$

The weight $W(\theta, \phi, \tilde{\alpha}, \varphi, \omega, \chi_{Pu}, \delta_{Pu})$ is therefore dependent also on φ and ω and given by

$$W(\theta, \phi, \tilde{\alpha}, \varphi, \omega, \chi_{Pu}, \delta_{Pu}) = |\vec{\mu}_{12all}(\varphi, \omega) \vec{E}_{3Pu}(\chi_{Pu}, \delta_{Pu})|. \quad (\text{B.44})$$

Integration over φ and ω gives for $P3_{an}(\theta, \phi, \tilde{\alpha}, \chi_{Pu}, \delta_{Pu})$

$$\begin{aligned} P3_{an}(\theta, \phi, \tilde{\alpha}, \chi_{Pu}, \delta_{Pu}) &= \int_{\varphi=0}^{2\pi} \int_{\omega=0}^{2\pi} W(\theta, \phi, \tilde{\alpha}, \varphi, \omega, \chi_{Pu}, \delta_{Pu}) d\varphi d\omega = \\ &= \frac{1}{4} \pi \left(4 \cos^2 \chi_{Pu} \sin^2 \alpha \sin^2 \theta + 4 \cos^2 \alpha (2 \cos^2 \theta + (1 - \cos(2\phi) \cos(2\chi_{Pu})) \sin^2 \theta) \right. \\ &\quad + 4 \cos^2 \theta \cos^2 \chi_{Pu} \sin^2 \alpha \sin^2 \phi - 4 \cos \delta_{Pu} \cos \phi \cos \chi_{Pu} \sin^2 \theta \sin \phi \sin \chi_{Pu} \\ &\quad + 4 \sin^2 \alpha \sin^2 \theta \sin^2 \chi_{Pu} + 4 \sin^2 \alpha \sin^2 \phi \sin^2 \chi_{Pu} \\ &\quad + 4 \cos^2 \phi \sin^2 \alpha (\cos^2 \chi_{Pu} + \cos^2 \theta \sin^2 \chi_{Pu}) \\ &\quad \left. - 3 \cos(2\alpha) \cos \delta_{Pu} \sin^2 \theta \sin(2\phi) \sin(2\chi_{Pu}) \right), \quad (\text{B.45}) \end{aligned}$$

whose volume is twice the one given by Eq. B.9, since there are two pump transition dipole moments present. Nevertheless, the probability to find an excited molecule needs to be 1, hence

$$P3_{an}(\theta, \phi, \tilde{\alpha}, \chi_{Pu}, \delta_{Pu}) = \frac{P3(\theta, \phi, \tilde{\alpha}, \chi_{Pu}, \delta_{Pu})}{\frac{16\pi^2}{9}}. \quad (\text{B.46})$$

Cross product

A much simpler calculation is possible by realizing that the probability for exciting any dipole moment lying in the plane given by Eq. B.38 is given by the probability to not-excite a pump transition dipole moment oriented in direction \vec{n} . In this case the weight W is given by the sine of the angle between the pump polarization direction and the transition dipole moment oriented in direction \vec{n} , obtainable via the length of the cross product of the two vectors,

$$W(\theta, \phi, \tilde{\alpha}, \varphi, \chi_{Pu}, \delta_{Pu}) = Abs\left(\vec{\mu}_{12start} \times \vec{E}_{3Pu}(\chi_{Pu}, \delta_{Pu})\right)^2, \quad (\text{B.47})$$

with $Abs(\vec{v})$ giving the length of the vector \vec{v} . In that case the same probability distribution $P3$ is obtained as given by Eq. B.46.

Sum of transition dipole moments

The third possibility is to treat every transition dipole moment of the sum of degenerate transition dipole moments individually. A successful pump event has taken place if either one of the transition dipole moments has been excited. Since the probabilities to excite the individual dipole moments are disjunct, the probability (W) that any pump event

has taken place to contribute to probing in a certain direction is given by the sum of the probabilities,

$$W(\theta, \phi, \tilde{\alpha}, \varphi, \chi_{Pu}, \delta_{Pu}) = \sum_{i=1}^N |\vec{E}_{3Pu}(\chi_{Pu}, \delta_{Pu}) \vec{\mu}_{i,12}(\varphi, \theta, \phi, \tilde{\alpha})|^2, \quad (\text{B.48})$$

with $\vec{\mu}_{i,12}$ being the orientation of the i -th pump transition dipole moment. In case of two perpendicular transitions forming a plane, whose normal encloses the angle $\tilde{\alpha}$ with the probe transition dipole moment (same definition as in the previous two cases),

$$\vec{\mu}_{1,12}(\theta, \phi, \tilde{\alpha}, \varphi) = \text{Rot}(\varphi, \vec{\mu}_{23\text{start}}(\theta, \phi)) \cdot \vec{\mu}_{1,12\text{start}}(\tilde{\alpha}) \quad (\text{B.49})$$

$$\vec{\mu}_{2,12}(\theta, \phi, \tilde{\alpha}, \varphi) = \text{Rot}(\varphi, \vec{\mu}_{23\text{start}}(\theta, \phi)) \cdot \vec{\mu}_{2,12\text{start}}(\tilde{\alpha}), \quad (\text{B.50})$$

with $\vec{\mu}_{1,12\text{start}}$ being one element of the plane, similar to Eq. B.2,

$$\vec{\mu}_{1,12\text{start}}(\theta, \phi, \tilde{\alpha}) = \vec{\mu}_{12\text{start}}(\theta, \phi, \tilde{\alpha}), \quad (\text{B.51})$$

and $\vec{\mu}_{2,12\text{start}}$ being $\vec{\mu}_{1,12\text{start}}(\theta, \phi, \tilde{\alpha})$ rotated by 90° around the normal \vec{n} of the plane,

$$\vec{\mu}_{2,12\text{start}}(\theta, \phi, \tilde{\alpha}) = \text{Rot}(90^\circ, \vec{n}(\theta, \phi, \tilde{\alpha})) \cdot \vec{\mu}_{1,12\text{start}}(\theta, \phi, \tilde{\alpha}). \quad (\text{B.52})$$

In case of two-fold degenerate probe transition dipole moments W becomes

$$W(\theta, \phi, \tilde{\alpha}, \varphi, \chi_{Pu}, \delta_{Pu}) = |\vec{E}_{3Pu}(\chi_{Pu}, \delta_{Pu}) \vec{\mu}_{1,12}(\varphi, \theta, \phi, \tilde{\alpha})|^2 + |\vec{E}_{3Pu}(\chi_{Pu}, \delta_{Pu}) \vec{\mu}_{2,12}(\varphi, \theta, \phi, \tilde{\alpha})|^2 \quad (\text{B.53})$$

With this approach again the same result is obtained for $P3$ as given by Eq. B.46.

Anisotropy for two-fold degenerate pump transition

The anisotropy $r(\tilde{\alpha})$ can be obtained in the same way as shown in Section B.1 for Eq. B.22. For the distribution given by Eq. B.46 $r(\tilde{\alpha})$ becomes

$$r(\tilde{\alpha}) = \frac{1}{20}[-1 - 3 \cos(2\tilde{\alpha})], \quad (\text{B.54})$$

in agreement with the literature [212–214]. Note that $\tilde{\alpha}$ is defined as the angle between the normal of the plane containing the two-fold degenerate pump transition dipole moments and the probe transition dipole moment.

B.5.2 Degenerate probe transition dipole moments

Assume now that the pump transition is not degenerate but the probe transition is. Similar to Section B.5.1 a two-fold degenerate probe transition is assumed, with the two probe dipole moments being perpendicular. The pump–probe experiment can be developed as a sum of individual experiments, each probing only one of the degenerate

transition dipole moments. For the determination of $P3$, the angle α describes here the smallest possible angle between the pump transition dipole moment and the plane in which the degenerate probe transition dipole moments lie. The plane can be described in the form of two orthogonal vectors, which are assumed to be the directions of the two orientations of the two-fold degenerate probe transition dipole moment. One of these vectors is then given by $\vec{\mu}_{23start}(\theta, \phi)$ if the corresponding pump transition dipole moment orientation is given by $\vec{\mu}_{12start}(\theta, \phi, \alpha)$. The respective other probe transition dipole moment is always orthogonal to $\vec{\mu}_{23start}(\theta, \phi)$ as well as $\vec{\mu}_{12start}(\theta, \phi, \alpha)$. Thus, it always encloses the angle 90° with the pump transition dipole moment, so that the corresponding pump transition dipole moment is always oriented in $\vec{\mu}_{12start}(\theta, \phi, 90^\circ)$ direction.

Therefore the two-fold degenerate probe transition dipole moment leads to a $P3_{deg.probe}$ being the sum of the $P3(\theta, \phi, \alpha, \chi_{Pu}, \delta_{Pu})$ and $P3(\theta, \phi, 90^\circ, \chi_{Pu}, \delta_{Pu})$. With this distribution, $P3_{deg.probe}$, known, the rest of the anisotropy derivation can be performed in the same way as shown in Section B.1. Since the magic angle from Section B.4.1 does not depend on α , the condition is the same for a two-fold degenerate probe transition dipole moment.

However, the anisotropy $r_{deg.pr}$ of this example differs from the non-degenerate case of Section B.1 and is given by

$$r_{deg.probe}(\alpha) = \frac{1}{20}[-1 + 3 \cos(2\alpha)], \quad (\text{B.55})$$

which can also be obtained via

$$r_{deg.probe}(\alpha) = \frac{1}{2}r(\alpha) + \frac{1}{2}r(90^\circ), \quad (\text{B.56})$$

with $r(\alpha)$ given by Eq. 3.10. Expressing the anisotropy r with $\tilde{\alpha} = \alpha \pm 90^\circ$, with $\tilde{\alpha}$ being the angle between the normal of the disk of probe transition dipole moments and the pump transition dipole moment, one obtains

$$r_{deg.probe}(\tilde{\alpha}) = \frac{1}{20}[-1 + 3 \cos(2\tilde{\alpha} \mp 180^\circ)] = \frac{1}{20}[-1 - 3 \cos(2\tilde{\alpha})], \quad (\text{B.57})$$

the same result as for the case of degenerate pump transition dipole moments of Section B.5.1.

Generally, $P3_{mult.probe}$ for multiple degenerate probe transitions is given by the sum of the individual probe transitions,

$$P3_{mult.probe}(\theta, \phi, \alpha_i, \dots, \alpha_N, \chi_{Pu}, \delta_{Pu}) = \frac{1}{N} \sum_{i=1}^N P3(\theta, \phi, \alpha_i, \chi_{Pu}, \delta_{Pu}), \quad (\text{B.58})$$

so that the integral of $P3$ is again 1.

Note that for overlapping transitions Eq. B.23 needs to be employed with the term $A_{EPmax} P_{Pr}(\alpha_{EP}, \chi_{Pu}, \delta_{Pu}, \chi_{Pr}, \delta_{Pr}, \beta)$ being replaced by a sum of terms. With this approach very large values for the anisotropy r (Eq. 3.10) can be obtained [116].

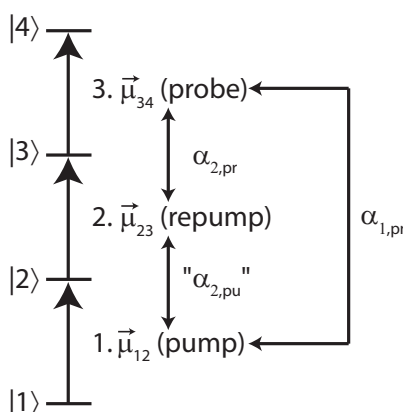


Figure B.2: In pump–repump–probe experiments the first transition (pump) is the excitation $|1\rangle \rightarrow |2\rangle$, the second transition (repump) is the excitation $|2\rangle \rightarrow |3\rangle$ and the probe transition (third transition) is for example the excitation $|3\rangle \rightarrow |4\rangle$. The transition dipole moments of all these transitions enclose certain angles in the molecular coordinate system. In the case of pump and repump experiments three angles are necessary to unambiguously describe the relative orientations of all transitions taking part in the excitation processes. The angle that is enclosed by pump and probe transition dipole moment is called here $\alpha_{1,pr}$ and the angle that is enclosed by the repump and probe transition dipole moment is called here $\alpha_{2,pr}$. The angle between the pump and repump transition dipole moment is given in this section via the angle between the projections of the pump and repump transition dipole moment on the plane normal to the probing direction. The angle between these two projections is $\alpha_{2,pu}$, but does not correspond to the true angle between the transition dipole moments (hence “ $\alpha_{2,pu}$ ”).

B.6 Anisotropy in pump–repump–probe experiments

In pump–repump–probe experiments a photochemical reaction is steered into one direction by re-exciting (repump) a transient species which was generated by a previous pulse (pump) (see Figure B.2). An example for such a reaction has been described in Section 4.5.

The approach in Section B.1 needs to be extended by the additional repump process, as shown in Figure B.3. Consider that the first transition (pump, $\vec{\mu}_{12}$) encloses an angle $\alpha_{1,pr}$ with the probe transition $\vec{\mu}_{34}$ (black arrow, see also Figure B.1), hence it can lie anywhere on the blue circle when probing in x direction (Figure B.3). The blue arrow describes one individual transition $\vec{\mu}_{12start}$, which lies in case of Figure B.3 in the z – x plane.

The second transition (repump, $\vec{\mu}_{23}$) encloses the angle $\alpha_{2,pr}$ with the probe transition μ_{34} . With the knowledge of $\alpha_{2,pr}$ one can only state that it needs to lie anywhere on the red circle in Figure B.3. However, a successful repump excitation could have only taken place if the respective pump transition dipole moment has also been excited. Assume that the transition dipole moment described by the blue arrow ($\vec{\mu}_{12start}$) has been excited. This fixes the orientation of the repump transition dipole moment, i.e. selects only two elements of the red circle ($\vec{\mu}_{23start1}$ and $\vec{\mu}_{23start2}$, shown as green arrows ending on the red circle). A mathematical description which element of the red circle is selected can

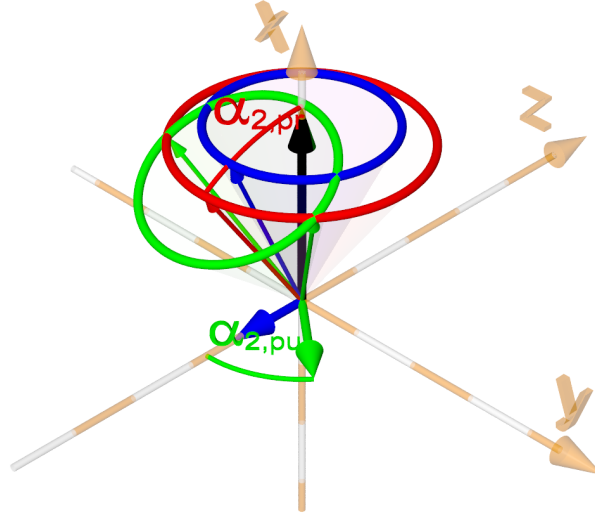


Figure B.3: In pump–repump–probe experiments the repump transition needs to have the correct orientation with respect to the pump [projection of pump and repump onto the plane normal to the probe transition dipole moment (black arrow) encloses the angle $\alpha_{2,pu}$] and the probe transition dipole moment (black, enclosing the angle $\alpha_{2,pr}$). The pump can be oriented in an isotropic mixture in any direction lying on the blue circle, when the probe transition dipole moment is oriented in the direction of the black arrow (see Figure B.1). Taking one individual transition of these, e.g. the blue arrow, the possible orientations of the repump are given by the green arrows that end on the red circle. The red circle describes all possible orientations of the repump transitions if the pump would not destroy the isotropy.

be done with the projection of the $\vec{\mu}_{12start}$ and $\vec{\mu}_{23start1}$ onto the plane (in Figure B.3 the y – z plane) normal to the probe transition μ_{34} (black arrow) yielding the short blue and green arrow in the y – z plane. These two projections enclose the angle $\alpha_{2,pu}$. The indirect description of the angle between the pump and repump transition dipole moment via the projection allows for an unambiguous and always valid description of the transition dipole moment directions in the molecular coordinate system.

For a successful probing of a pump–repump process not excitation of any of the repump transitions described by the red circle but only excitation of the ones given by the green arrows on the red circle after exciting the blue arrow needs to have taken place. With the probability for the excitation of the blue and green arrow known, the total probability for successful probing in a certain direction is obtained by rotation around the probe direction (black arrow in Figure B.3). This approach is the same as in Section B.1 and Figure B.1.

First one needs to find an expression for the orientations of the repump transition dipole moments $\vec{\mu}_{231}$ and $\vec{\mu}_{232}$, i.e. the green arrows ending on the red circle in Figure B.3. With φ describing the rotation of the system around the probe direction one obtains for $\vec{\mu}_{231}$

$$\vec{\mu}_{231}(\theta, \phi, \alpha_{2,pr}, \alpha_{2,pu}, \varphi) = \begin{pmatrix} \mu_x \\ \mu_y \\ \mu_z \end{pmatrix}, \quad (\text{B.59})$$

with

$$\begin{aligned} \mu_x = & \cos \alpha_{2,pr} \cos \phi \sin \theta + \sin \alpha_{2,pr} \sin \alpha_{2,pu} (\cos \varphi \sin \phi + \cos \theta \cos \phi \sin \varphi) \\ & + \cos \alpha_{2,pu} \sin \alpha_{2,pr} (-\cos \theta \cos \phi \cos \varphi + \sin \phi \sin \varphi), \end{aligned} \quad (\text{B.60})$$

and

$$\begin{aligned} \mu_y = & \sin \phi (-\cos \alpha_{2,pu} \cos \theta \cos \varphi \sin \alpha_{2,pr} + \cos \alpha_{2,pr} \sin \theta + \cos \theta \sin \alpha_{2,pr} \sin \alpha_{2,pu} \sin \varphi) \\ & - \cos \phi \sin \alpha_{2,pr} \sin (\alpha_{2,pu} + \varphi), \end{aligned} \quad (\text{B.61})$$

and

$$\mu_z = \cos \alpha_{2,pr} \cos \theta + \cos (\alpha_{2,pu} + \varphi) \sin \alpha_{2,pr} \sin \theta, \quad (\text{B.62})$$

with (θ, ϕ) describing the direction of $\vec{\mu}_{34}$, i.e. the probing direction (black arrow in Figure B.3). Note that $\vec{\mu}_{232}$ is obtained by substituting $\alpha_{2,pu} \rightarrow -\alpha_{2,pu}$ and that the distinction between $\vec{\mu}_{231}$ and $\vec{\mu}_{232}$ is the distinction between enantiomers.

In the second step one has to determine the probability that the pump transition dipole moment ($\vec{\mu}_{12}$) as well as the corresponding repump transition dipole moment ($\vec{\mu}_{231}$) has been excited to determine the correct W (Eq. B.8). These two probabilities are independent, hence the probability that both events (successful pump and repump) have taken place is given by the product of the individual probabilities,

$$\begin{aligned} W(\theta, \phi, \alpha_{1,pr}, \alpha_{2,pr}, \alpha_{2,pu}, \varphi, \chi_{pPu}, \delta_{pPu}, \chi_{rPu}, \delta_{rPu}) = \\ |\vec{E}_{3pPu}(\chi_{pPu}, \delta_{pPu}) \vec{\mu}_{12}(\theta, \phi, \varphi, \alpha_{1,pr})|^2 |\vec{E}_{3rPu}(\chi_{rPu}, \delta_{rPu}) \vec{\mu}_{231}(\theta, \phi, \alpha_{2,pr}, \alpha_{2,pu}, \varphi)|^2, \end{aligned} \quad (\text{B.63})$$

with $\vec{E}_{3rPu}(\chi_{rPu}, \delta_{rPu})$ being the three-dimensional polarization vector of the repump with the Jones vector $\begin{pmatrix} \cos \chi_{rPu} \\ \sin \chi_{rPu} e^{i\delta_{rPu}} \end{pmatrix}$ and $\vec{E}_{3pPu}(\chi_{pPu}, \delta_{pPu})$ being the three-dimensional polarization vector of the pump with the Jones vector being $\begin{pmatrix} \cos \chi_{pPu} \\ \sin \chi_{pPu} e^{i\delta_{pPu}} \end{pmatrix}$. Generally, this approach is valid for any number of pump pulses. First one has to determine the probability of excitation with Eq. B.59 and then multiply the probabilities of their respective excitation,

$$\begin{aligned} W(\theta, \phi, \alpha_{i,pr}, \alpha_{i,pu}, \dots, \alpha_{N,pr}, \alpha_{N,pu}, \varphi, \vec{E}_1, \dots, \vec{E}_N) = \\ \prod_{i=1}^N |\vec{E}_i \vec{\mu}_i(\theta, \phi, \alpha_{i,pr}, \alpha_{i,pu}, \varphi)|^2, \end{aligned} \quad (\text{B.64})$$

with \vec{E}_i being the three-dimensional polarization vector, similar to Eq. 2.64, and $\vec{\mu}_i$ being the transition dipole orientation of transition i given by Eq. B.59. Note that to achieve this generalization for the first transition ($i = 1$) $\alpha_{1,pu} = 0$ can be used.

With the appropriate weight W known, the subsequent steps of the anisotropy calculation can be done in the same way as shown in Section B.1. Unfortunately, the general

solution to this problem cannot be given here analytically because it is too complex. However, the numerical simulation is still possible, although it also takes some time. If one would want to use this approach to fit the parameters to experimental data, programming the numerical simulation onto GPUs is reasonable, since the calculations for all directions can be done in parallel. When defining a set of experimental parameters it is possible to find simpler expressions, e.g. for the anisotropy r_{\parallel} with parallel polarization of the pump pulses or the anisotropy r_{\perp} with perpendicular polarization of the pump pulses. However, these solutions are not discussed here, since any experimental evidence for their correctness has not been recorded yet.

Unfortunately, the probability distribution P_{Pr} for successful probing is the same for both orientations of the repump transition ($\alpha_{i,pu}$ and $-\alpha_{i,pu}$) and hence pump-repump-probe experiments do not allow to distinguish between enantiomers simply by choosing the right polarization directions.

B.7 Experimental realization

In order to record the anisotropy usually two measurements are necessary, one with pump and probe parallel (ΔA_{\parallel}) and one with pump and probe orthogonal (ΔA_{\perp}). The anisotropy r is then given by

$$r = \frac{\Delta A_{\parallel} - \Delta A_{\perp}}{\Delta A_{\parallel} + 2\Delta A_{\perp}}. \quad (\text{B.65})$$

This necessitates a rotation of the pump or probe polarization, hence, between the two measurements mostly lies a time during which the experimental parameters might change, e.g. the laser intensity, the pump spectrum, the spatial overlap, the sample concentration and many more. In order to obtain the best signal-to-noise ratio it is therefore very attractive to minimize the time between the measurement of ΔA_{\parallel} and ΔA_{\perp} . The minimum time possible is given by the laser repetition frequency corresponding to a shot-to-shot manner. However, this would necessitate the switching of the polarization between two consecutive laser pulses.

Both setups for polarization mirroring (Figure 7.2 and Figure 7.4) may be used to record the anisotropy in a shot-to-shot manner. Similar to the experimental arrangement used in Section 4.5 two optical choppers need to be used. But in contrast to the scheme used there, here only one optical chopper needs to be set to $\frac{1}{4}$ of the laser system repetition frequency f . This chopper is used to block the pump before the polarization-mirroring setup as shown in Figure B.4 (black pulses pass the chopper, grey pulses are blocked).

The second chopper is placed in the polarization-mirroring setup and switches between the original (o) and mirrored (m) polarization, i.e. blocks either the red or green path alternately so that always either of the two beams, original (red path) or mirrored (green path), may be transmitted (fourth line in Figure B.4). With the knowledge that a polarization with orientation θ_o is mirrored to a polarization with orientation $\theta_m = -\theta_o$, it is obvious that the incident polarization needs to be linearly polarized in $\theta_o = \pm 45^\circ$ direction. A subsequent $\frac{\lambda}{2}$ wave plate after the polarization-mirroring setup

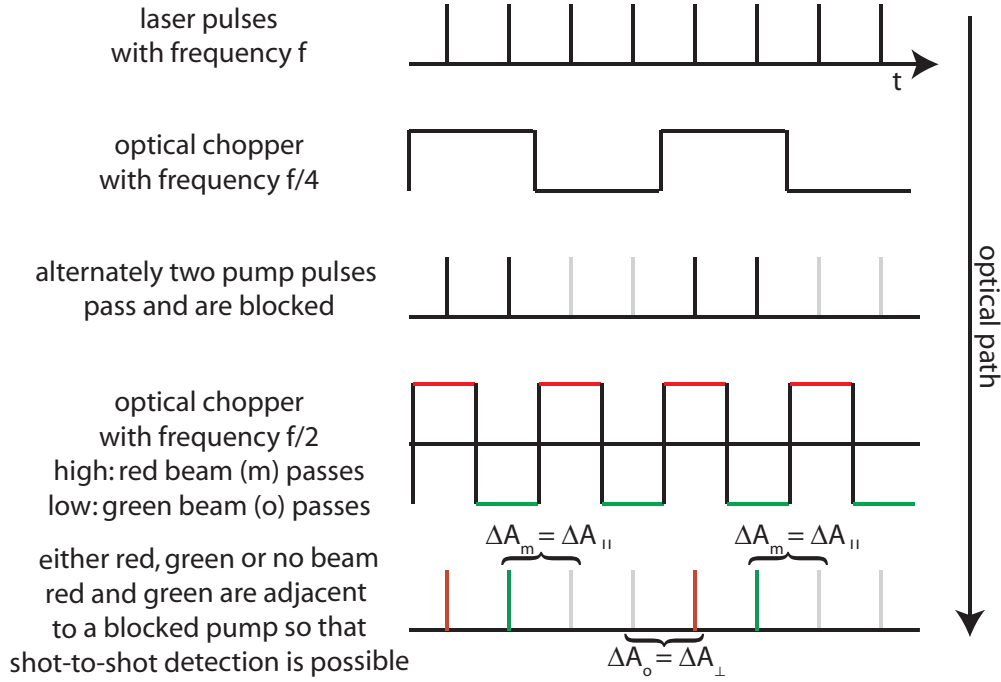


Figure B.4: The polarization-mirroring setups from Figure 7.2 and Figure 7.4 can be used to record the transient-absorption anisotropy in a shot-to-shot manner. The train of pulses with frequency f is the starting point (first line). The first optical chopper operating at a frequency of $\frac{f}{4}$ (second line) blocks two pump pulses (grey) and lets two pump pulses pass (black) alternately (third line) before the polarization-mirroring setup. The second chopper (fourth line) is placed inside the polarization-mirroring setup and blocks either the green (m : mirrored polarization) or red (o : original polarization) path (Figure 7.2 and Figure 7.4). After this chopper there exists always a position with blocked pump adjacent to every pump pulse. This allows therefore to measure $\Delta A_{||}$ and ΔA_{\perp} and therefore also the anisotropy in a shot-to-shot manner.

then yields linearly polarized light in 0° and 90° direction if its fast axis is oriented in 22.5° direction.

The transient-absorption signals $\Delta A_{||}$ and ΔA_{\perp} can now be recorded in a shot-to-shot manner, since adjacent to both pump pulses (o (red) and m (green)) one pump pulse is blocked (grey). The probe needs to be polarized vertically, i.e. s direction as used throughout this chapter.

Similar to Section 7.4.1 a very precise measurement of the intensity difference between o and m beam is necessary to correct the additional 0° mirror in the green (m) path when calculating the anisotropy r .

It is also conceivable to switch pump and probe, so that the probe polarization is mirrored with the polarization-mirroring setup. In this case a chopper needs to switch with the frequency $\frac{f}{4}$ between the original and mirror image of the probe. This has the advantage that the intensity difference between the o and m path is directly cancelled since the two probe intensities I (with pump) and I_0 (without pump), Eq. 3.2, are both

from the same optical path (o or m).

The second chopper needs to block and unblock alternately the pump pulse with frequency $\frac{f}{2}$. Unfortunately, this approach needs an achromatic $\frac{\lambda}{2}$ wave plate in order to generate the linearly polarized probe pulses in 0° and 90° direction. Probing in the visible spectral range is therefore only possible over small spectral regions.

The polarization-mirroring setup therefore promises as one further application a better signal-to-noise ratio for anisotropy measurements.

C Jones matrix of symmetric beamsplitters

The use of beamsplitters in the polarization-mirroring setup of Figure 7.2 and Figure 7.4 necessitates a calculation of the Jones matrix of the beamsplitters. The beamsplitters are assumed to be symmetric, meaning that the Jones matrix does not depend on whether the beam propagates from the front to the rear or vice versa. This is fulfilled for metallic beamsplitters. In those beamsplitters a metal (complex index of refraction n_2) film (thickness h) separates two glasses (indices of refraction n_1 and n_3 , which are assumed to be equal), as shown in Figure C.1. Whereas metal strongly absorbs the light, the extreme thinness of the metal film ($h < 100$ nm) gives rise to an evanescent field that is transmitted to the other side of the metal film. A beam that is transmitted or reflected in such a beamsplitter under an incident angle θ_{1i} realistic for further experiments (θ_{1i} close to 0, incident angles are labeled as θ_{xi} , angles of transmitted light θ_{xt} , see Figure C.1) encounters 4 interfaces where the index of refraction changes,

1. air \rightarrow glass ($\theta_{1i} \approx \theta_{1t} \approx 0^\circ$, Jones matrix $M_{air-glass}$)
2. glass \rightarrow metal ($\theta_{2i} \approx 45^\circ$, $\theta_{2t} \neq 0$ and complex, both angles enter the Jones matrix $M_{glass-metal-glass}$)
3. metal \rightarrow glass ($\theta_{3i} \neq 0$ and complex, $\theta_{3t} = \theta_{2i} \approx 45^\circ$, both angles enter the Jones matrix $M_{glass-metal-glass}$)
4. glass \rightarrow air ($\theta_{4i} \approx \theta_{4t} \approx 0^\circ$, Jones matrix $M_{glass-air}$),

with interface 2 and 3 being absorbed into one Jones matrix $M_{glass-metal-glass}$. Note that it is assumed here that the glass on both sides is of the same material ($n_1 = n_3$), otherwise the assumption $\theta_{3t} = \theta_{2i}$ is not valid and one would observe an angle between the incident beam and the outgoing beam of the beamsplitter ($\theta_{1i} \neq \theta_{4t}$).

For all these interfaces, the Fresnel coefficients $t_{\parallel,x}, t_{\perp,x}, r_{\parallel,x}, r_{\perp,x}$, with x being the interface number, need to be calculated and the corresponding Jones matrices need to be constructed (Eq. 2.55). Whereas the case for $M_{air-glass}$ and $M_{glass-air}$ is straightforward with the Fresnel coefficients from Eq. 2.53, the transmission of the evanescent field needs an extended description for the glass-metal-glass system. Since the metal is an absorbing medium, its index of refraction n_2 is complex, hence the Fresnel coefficients in which this index enters are also complex. Furthermore the angle $\theta_{3i} = \theta_{2t} = \arcsin \frac{n_1 \sin \theta_{2i}}{n_2}$ is also complex. The complex Fresnel coefficients will be written from now on in polar form

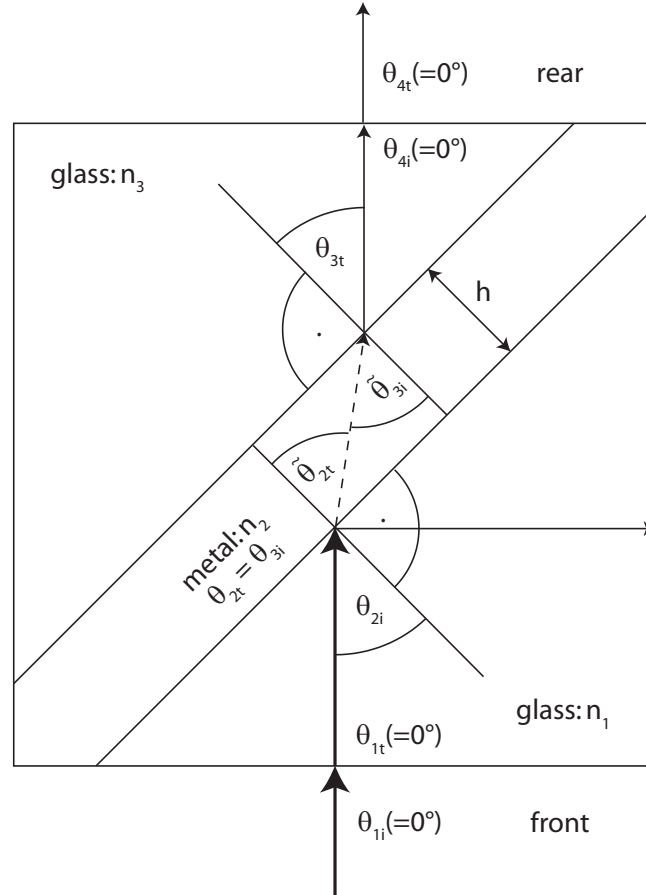


Figure C.1: A cubic non-polarizing beamsplitter consists of two glass surfaces (index of refraction n_1 and n_3) and a thin metal surface (index of refraction n_2) in-between (thickness h) them at an angle of 45° to the normal of the front and rear glass surface. It is assumed here that the front and rear glass are of the same material ($n_1 = n_3$). The small thickness of the metal layer leads to a small fraction of the light to be transmitted through the metal due to the presence of an evanescent field. A light beam that is transmitted or reflected by the beamsplitter (black arrow in the bottom) hits 4 interfaces where the index of refraction changes. The optical path is characterized at every interface with an incident angle (θ_{xi}) and an outgoing angle (θ_{xt}) between the surface normal and the wave vector of the light, with x denoting the interface number. The angle in the metal is complex, hence θ_{2t} and θ_{3i} cannot be expressed in the graph. Instead the angles $\tilde{\theta}_{2t}$ and $\tilde{\theta}_{3t}$ give the angle between the planes of constant real phase and the metal surface normal [38]. Since the real part on n_2 is for some metals smaller than 1 (for example silver), the beam may be refracted away from the surface normal when entering the metal.

following the notation

$$t_{\parallel,x} = \tau_{xp} e^{i\chi_{xp}} \quad (\text{C.1})$$

$$t_{\perp,x} = \tau_{xs} e^{i\chi_{xs}} \quad (\text{C.2})$$

$$r_{\parallel,x} = \rho_{xp} e^{i\phi_{xp}} \quad (\text{C.3})$$

$$r_{\perp,x} = \rho_{xs} e^{i\phi_{xs}}, \quad (\text{C.4})$$

$$(\text{C.5})$$

with x denoting the interface number.

Since the angle $\theta_{2t} = \theta_{3i}$ describing the propagation in the metal is complex, Snell's law does not directly give the angle of the propagation direction of the transmitted beam to the surface normal. While the amplitude of the electric field depends only on the penetration depth into the metal, i.e. the planes of constant amplitude are parallel to the metal surface, the planes of constant real phase enclose an angle $\tilde{\theta}_{3i} = \tilde{\theta}_{2t}$ with the normal of the metal surface [38],

$$\tilde{\theta}_{3i} = \tilde{\theta}_{2t} = \arcsin \left(\frac{\sin \theta_{2i}}{\sqrt{\sin^2 \theta_{2i} + \Re(n_2)^2 q^2 (\cos \gamma - \kappa \sin \gamma)^2}} \right), \quad (\text{C.6})$$

with $\cos \theta_{2t} = q e^{i\gamma}$ and $\kappa = \frac{\Im(n_2)}{\Re(n_2)}$ as used in [38]. The optical path length l is then given by

$$l = \frac{h}{\cos \tilde{\theta}_{2t}}, \quad (\text{C.7})$$

this dependence of the optical path length on the angle θ_{2t} is already included in the equations given below, although they do not explicitly depend on l . Note that the index of refraction of some metals is smaller than 1, e.g. silver $\Re(n) \approx 0.2$ [38], so that $\tilde{\theta}_{2t} > \theta_{2i}$ (as shown in Figure C.1).

A detailed derivation of the description of the evanescent field is given in the literature [38]. The resulting coefficients for reflection (r) and transmission (t) of the glass-metal-glass interface are given by

$$r_{\parallel, \text{glass-metal-glass}} = \frac{\rho_{2p} e^{i\phi_{2p}} + \rho_{3p} e^{-2v_2\eta} e^{i(\phi_{3p} + 2u_2\eta)}}{1 + \rho_{2p}\rho_{3p} e^{-2v_2\eta} e^{i(\phi_{2p} + \phi_{3p} + 2u_2\eta)}} \quad (\text{C.8})$$

$$r_{\perp, \text{glass-metal-glass}} = \frac{\rho_{2s} e^{i\phi_{2s}} + \rho_{3s} e^{-2v_2\eta} e^{i(\phi_{3s} + 2u_2\eta)}}{1 + \rho_{2s}\rho_{3s} e^{-2v_2\eta} e^{i(\phi_{2s} + \phi_{3s} + 2u_2\eta)}} \quad (\text{C.9})$$

$$t_{\parallel, \text{glass-metal-glass}} = \frac{\tau_{2p}\tau_{3p} e^{-v_2\eta} e^{i(\chi_{2p} + \chi_{3p} + u_2\eta)}}{1 + \rho_{2p}\rho_{3p} e^{-2v_2\eta} e^{i(\phi_{2p} + \phi_{3p} + 2u_2\eta)}} \sqrt{\frac{\cos \theta_{3t}}{n_3} \frac{\cos \theta_{2i}}{n_1}} \quad (\text{C.10})$$

$$t_{\perp, \text{glass-metal-glass}} = \frac{\tau_{2s}\tau_{3s} e^{-v_2\eta} e^{i(\chi_{2s} + \chi_{3s} + u_2\eta)}}{1 + \rho_{2s}\rho_{3s} e^{-2v_2\eta} e^{i(\phi_{2s} + \phi_{3s} + 2u_2\eta)}} \sqrt{\frac{n_3 \cos \theta_{3t}}{n_1 \cos \theta_{2i}}}, \quad (\text{C.11})$$

with $u_2 = \Re(n_2)$, $v_2 = \Im(n_2)$ and $\eta = \frac{2\pi}{\lambda_0} h$.

In order to obtain the complete Jones matrix M_{BS} of the beamsplitter, the Jones matrix of the glass-metal-glass system ($M_{glass-metal-glass}$) needs to be multiplied with the Jones matrices of the air-glass interfaces in its corresponding order,

$$M_{BS} = M_{glass-air} \cdot M_{glass-metal-glass} \cdot M_{air-glass}. \quad (\text{C.12})$$

Note that usually only the Fresnel coefficients depend on the wavelength λ_0 , but due to the evanescent field, $M_{glass-metal-glass}$ also depends on λ_0 via η . Figure C.2 shows the exemplary curves of the transmission and reflection coefficient for p and s polarized light (solid colored lines: absolute value, dashed colored lines: phase jump) as well as the total intensity loss due to the beamsplitter (black line).

In an ideal beamsplitter, s and p polarized component would have the same absolute value for the reflection and transmission coefficient ($\approx \frac{1}{\sqrt{2}}$). Furthermore this coefficient would not be wavelength-dependent. As can be seen in Figure C.1, the coefficients for s and p polarized light differ strongly and the wavelength dependence can also not be neglected when using such a beamsplitter. However, due to the use of rotating periscopes in Figure 7.4 all these effects are cancelled.

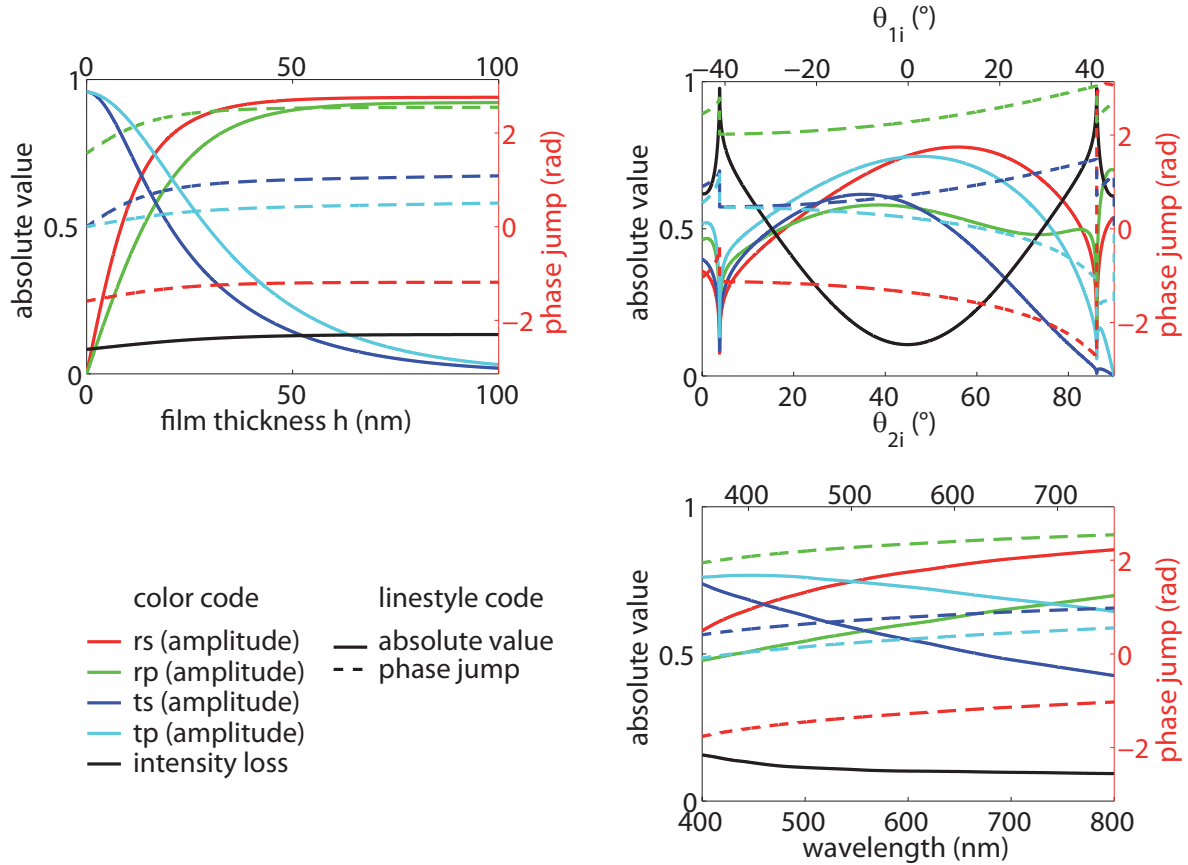


Figure C.2: Transmission (tx) and reflection coefficient (rx) for s ($x = s$) and p ($x = p$) polarized light (colored solid lines: absolute value; colored dashed lines: phase jump), as well as the intensity loss (black) at the beamsplitter dependent on the film thickness h (top left), the incident angle $\theta_{2i} = \theta_{1i} - 45^\circ$ (top right) and the wavelength (bottom right). The beamsplitter consists of BK7 glass on both sides and a thin metal silver film in-between, see Figure C.1. If not stated otherwise, the beamsplitter is characterized by the parameters: $h = 16.6$ nm, $\lambda_0 = 550$ nm and $\theta_{2i} = 45^\circ$. Note that the values plotted correspond to the complete beamsplitter, i.e. they include the intensity loss due to the interfaces air \rightarrow glass and glass \rightarrow air. For angles $|\theta_{1i}| \approx 42^\circ$ total internal reflection takes place at the rear glass \rightarrow air interface.

Bibliography

- [1] J. Briand, O. Bräm, J. Réhault, J. Léonard, A. Cannizzo, M. Chergui, V. Zanirato, M. Olivucci, J. Helbing, and S. Haacke.
Coherent ultrafast torsional motion and isomerization of a biomimetic dipolar photoswitch.
Physical Chemistry Chemical Physics **12**, 3178 (2010).
- [2] D. Polli, P. Altoe, O. Weingart, K. M. Spillane, C. Manzoni, D. Brida, G. Tomasello, G. Orlandi, P. Kukura, R. A. Mathies, M. Garavelli, and G. Cerullo.
Conical intersection dynamics of the primary photoisomerization event in vision.
Nature **467**, 440–443 (2010).
- [3] A. H. Zewail.
Femtochemistry: Atomic-Scale Dynamics of the Chemical Bond.
The Journal of Physical Chemistry A **104**, 5660–5694 (2000).
- [4] P. Nuernberger, G. Vogt, T. Brixner, and G. Gerber.
Femtosecond quantum control of molecular dynamics in the condensed phase.
Physical Chemistry Chemical Physics **9**, 2470–2497 (2007).
- [5] T. Brabec and F. Krausz.
Intense few-cycle laser fields: Frontiers of nonlinear optics.
Reviews of Modern Physics **72**, 545 (2000).
- [6] R. A. Kaindl, M. Wurm, K. Reimann, P. Hamm, A. M. Weiner, and M. Woerner.
Generation, shaping, and characterization of intense femtosecond pulses tunable from 3 to 20 μm .
Journal of the Optical Society of America B **17**, 2086 (2000).
- [7] J. Extermann, S. M. Weber, D. Kiselev, L. Bonacina, S. Lani, F. Jutzi, W. Noell, N. F. de Rooij, and J. Wolf.
Spectral phase, amplitude, and spatial modulation from ultraviolet to infrared with a reflective MEMS pulse shaper.
Optics Express **19**, 7580–7586 (2011).
- [8] G. Cerullo, A. Baltuška, O. D. Mücke, and C. Vozzi.
Few-optical-cycle light pulses with passive carrier-envelope phase stabilization.
Laser & Photonics Reviews **5**, 323–351 (2011).
- [9] A. M. Weiner.
Femtosecond pulse shaping using spatial light modulators.
Review of Scientific Instruments **71**, 1929 (2000).
- [10] A. Assion, T. Baumert, M. Bergt, T. Brixner, B. Kiefer, V. Seyfried, M. Strehle, and G. Gerber.
Control of Chemical Reactions by Feedback-Optimized Phase-Shaped Femtosecond Laser Pulses.
Science **282**, 919–922 (1998).
- [11] H. Rabitz, R. de Vivie-Riedle, M. Motzkus, and K. Kompa.
Whither the Future of Controlling Quantum Phenomena?
Science **288**, 824–828 (2000).

- [12] M. Shapiro and P. Brumer.
Coherent control of molecular dynamics.
Reports on Progress in Physics **66**, 859–942 (2003).
- [13] I. Fleming.
Frontier Orbitals and Organic Chemical Reactions.
First edition. Wiley (1976).
- [14] B. L. Feringa.
Molecular Switches.
Wiley-VCH Verlag GmbH, Berlin (2001).
- [15] A. V. Kulinich and A. A. Ishchenko.
Merocyanine dyes: synthesis, structure, properties and applications.
Russian Chemical Reviews **78**, 141–164 (2009).
- [16] R. C. Jones.
A New Calculus for the Treatment of Optical Systems. I. Description and Discussion of the Calculus.
Journal of the Optical Society of America **31**, 488–493 (1941).
- [17] V. Ramamurthy, J. C. Scaiano, and N. J. Turro.
Modern Molecular Photochemistry of Organic Molecules.
Palgrave Macmillan (2010).
- [18] A. Shirakawa, I. Sakane, M. Takasaka, and T. Kobayashi.
Sub-5-fs visible pulse generation by pulse-front-matched noncollinear optical parametric amplification.
<http://dx.doi.org/10.1063/1.123820> (1999).
- [19] J. Diels and W. Rudolph.
Ultrashort Laser Pulse Phenomena: Fundamentals, Techniques, and Applications on a Femtosecond Time Scale (Optics and Photonics Series).
0002nd edition. Academic Pr Inc (2006).
- [20] P. Nürnberger.
Adaptive Control of Quantum Systems with Femtosecond Laser Pulses.
Dissertation, Universität Würzburg (2007).
- [21] M. Wollenhaupt, A. Assion, and T. Baumert.
Femtosecond Laser Pulses: Linear Properties, Manipulation, Generation and Measurement.
In *Springer Handbook of Lasers and Optics*, pp. 937–983. Springer Science+Buisness Media, LLC
New York (2007).
- [22] T. Brixner, G. Krampert, P. Niklaus, and G. Gerber.
Generation and characterization of polarization-shaped femtosecond laser pulses.
Applied Physics B: Lasers and Optics **74**, 133–144 (2002).
- [23] J. Eichler, L. Dünkel, and B. Eppich.
Die Strahlqualität von Lasern.
Laser Journal **1**, 63–66 (2004).
- [24] E. Hecht.
Optik.
Fourth edition. Oldenbourg Wissenschaftsverlag, München (2005).

- [25] T. Brixner.
Adaptive Femtosecond Quantum Control.
Dissertation, Universität Würzburg (2001).
- [26] F. J. Buback.
Hochsensitive Spektroskope chiraler Systeme.
Diplomarbeit, Universität Würzburg (2007).
- [27] K. K. Sharma.
Optics: Principles and Applications.
First edition. Academic Press (2006).
- [28] T. Scharf.
Polarized Light in Liquid Crystals and Polymers.
First edition. Wiley-Interscience (2006).
- [29] M. Bonmarin and J. Helbing.
Polarization control of ultrashort mid-IR laser pulses for transient vibrational circular dichroism measurements.
Chirality **21**, E298–E306 (2009).
- [30] R. C. JONES.
A New Calculus for the Treatment of Optical Systems.
Journal of the Optical Society of America **31**, 500–503 (1941).
- [31] R. C. JONES.
A New Calculus for the Treatment of Optical Systems. IV.
Journal of the Optical Society of America **32**, 486–493 (1942).
- [32] R. C. Jones.
A new calculus for the treatment of optical systems VI. Experimental determination of the matrix.
Journal of the Optical Society of America **37**, 110 (1947).
- [33] R. C. Jones.
A new calculus for the treatment of optical systems V. A more general formulation, and description of another calculus.
Journal of the Optical Society of America **37**, 107 (1947).
- [34] R. C. JONES.
A New Calculus for the Treatment of Optical Systems. VII. Properties of the N-Matrices.
Journal of the Optical Society of America **38**, 671–683 (1948).
- [35] R. C. JONES.
New Calculus for the Treatment of Optical Systems. VIII. Electromagnetic Theory.
Journal of the Optical Society of America **46**, 126–131 (1956).
- [36] A. L. Fymat.
Jones's Matrix Representation of Optical Instruments. I: Beam Splitters.
Applied Optics **10**, 2499–2505 (1971).
- [37] A. L. Fymat.
Jones's Matrix Representation of Optical Instruments. 2: Fourier Interferometers (Spectrometers and Spectropolarimeters).
Applied Optics **10**, 2711–2716 (1971).

- [38] M. Born and E. Wolf.
Principles of Optics: Electromagnetic Theory of Propagation, Interference and Diffraction of Light.
7th edition. Cambridge University Press (1999).
- [39] W. Zinth and U. Zinth.
Optik. Lichtstrahlen - Wellen - Photonen.
Oldenbourg Wissenschaftsverlag, München (2005).
- [40] V. Sharma, M. Crne, J. O. Park, and M. Srinivasarao.
Structural Origin of Circularly Polarized Iridescence in Jeweled Beetles.
Science **325**, 449–451 (2009).
- [41] G. Yun, K. Crabtree, and R. A. Chipman.
Properties of the polarization ray tracing matrix.
In *Proceedings of SPIE*, pp. 66820Z–66820Z–12. San Diego, CA, USA (2007).
- [42] G. P. Moss.
Basic terminology of stereochemistry (IUPAC Recommendations 1996).
Pure and Applied Chemistry **68**, 2193–2222 (1996).
- [43] K. P. C. Vollhardt, N. E. Schore, and K. Peter.
Organische Chemie.
Fourth edition. Wiley-VCH Verlag GmbH & Co. KGaA (2005).
- [44] C. Cohen-Tannoudji, B. Diu, and F. Laloe.
Quantenmechanik Teil 1: Band 1.
Fourth edition. Gruyter (2009).
- [45] F. Schwabl.
Quantenmechanik.
6th edition. Springer, Berlin (2007).
- [46] J. A. Schellman.
Circular dichroism and optical rotation.
Chemical Reviews **75**, 323–331 (1975).
- [47] L. D. Barron.
Molecular light scattering and optical activity.
Cambridge Univ. Press, Cambridge [u.a.] (2009).
- [48] D. Tannor.
Introduction to Quantum Mechanics: A Time-Dependent Perspective.
University Science Books, Sausalito (2007).
- [49] G. Wedler.
Lehrbuch der Physikalischen Chemie: Fünfte, Vollständig Überarbeitete Und Aktualisierte Auflage.
Fifth edition. Wiley-VCH Verlag GmbH & Co. KGaA (2004).
- [50] J. Simons.
An experimental chemist's guide to ab initio quantum chemistry.
The Journal of Physical Chemistry **95**, 1017–1029 (1991).
- [51] A. Streitwieser, J. I. Brauman, and C. A. Coulson.
Supplemental tables of molecular orbital calculations, volume 1st. edition.
Pergamon Press, Oxford (1965).

- [52] R. Englman and J. Jortner.
The energy gap law for radiationless transitions in large molecules.
Molecular Physics: An International Journal at the Interface Between Chemistry and Physics
18, 145 (1970).
- [53] S. H. Lin.
Energy Gap Law and Franck–Condon Factor in Radiationless Transitions.
The Journal of Chemical Physics **53**, 3766 (1970).
- [54] W. Domcke, D. R. Yarkony, and H. Koppel.
Conical Intersections: Electronic Structure, Dynamics and Spectroscopy.
World Scientific Publishing (2004).
- [55] D. R. Yarkony.
Diabolical conical intersections.
Reviews of Modern Physics **68**, 985 (1996).
- [56] B. G. Levine and T. J. Martínez.
Isomerization Through Conical Intersections.
Annual Review of Physical Chemistry **58**, 613–634 (2007).
- [57] G. Klopman.
Chemical reactivity and the concept of charge- and frontier-controlled reactions.
Journal of the American Chemical Society **90**, 223–234 (1968).
- [58] L. Salem.
Intermolecular orbital theory of the interaction between conjugated systems. II. Thermal and photochemical cycloadditions.
Journal of the American Chemical Society **90**, 553–566 (1968).
- [59] L. Salem.
Intermolecular orbital theory of the interaction between conjugated systems. I. General theory.
Journal of the American Chemical Society **90**, 543–552 (1968).
- [60] K. Fukui.
Recognition of stereochemical paths by orbital interaction.
Accounts of Chemical Research **4**, 57–64 (1971).
- [61] R. Hoffmann and R. B. Woodward.
Conservation of orbital symmetry.
Accounts of Chemical Research **1**, 17–22 (1968).
- [62] W. T. Pollard and R. A. Mathies.
Analysis of Femtosecond Dynamic Absorption Spectra of Nonstationary States.
Annual Review of Physical Chemistry **43**, 497–523 (1992).
- [63] U. Megerle, I. Pugliesi, C. Schrieffer, C. Sailer, and E. Riedle.
Sub-50 fs broadband absorption spectroscopy with tunable excitation: putting the analysis of ultrafast molecular dynamics on solid ground.
Applied Physics B: Lasers and Optics **96**, 215–231 (2009).
- [64] E. Riedle, M. Beutter, S. Lochbrunner, J. Piel, S. Schenkl, S. Sporlein, and W. Zinth.
Generation of 10 to 50 fs pulses tunable through all of the visible and the NIR.
Applied Physics B: Lasers and Optics **71**, 457–465 (2000).

- [65] R. Siewertsen, F. Renth, F. Temps, and F. Sannichsen.
Parallel ultrafast E-C ring closure and E-Z isomerisation in a photochromic furylfulgide studied by femtosecond time-resolved spectroscopy.
Physical Chemistry Chemical Physics **11**, 5952–5961 (2009).
- [66] S. L. Logunov, V. V. Volkov, M. Braun, and M. A. El-Sayed.
The relaxation dynamics of the excited electronic states of retinal in bacteriorhodopsin by two-pump-probe femtosecond studies.
Proceedings of the National Academy of Sciences of the United States of America **98**, 8475–8479 (2001).
- [67] B. Dietzek, A. Yartsev, and A. N. Tarnovsky.
Watching Ultrafast Barrierless Excited-State Isomerization of Pseudocyanine in Real Time.
The Journal of Physical Chemistry B **111**, 4520–4526 (2007).
- [68] C. Schriever, S. Lochbrunner, E. Riedle, and D. J. Nesbitt.
Ultrasensitive ultraviolet-visible 20 fs absorption spectroscopy of low vapor pressure molecules in the gas phase.
Review of Scientific Instruments **79**, 013107 (2008).
- [69] L. Poisson, K. D. Raffael, B. Soep, J. Mestdagh, and G. Buntinx.
Gas-Phase Dynamics of Spiropyran and Spirooxazine Molecules.
Journal of the American Chemical Society **128**, 3169–3178 (2006).
- [70] I. H. M. van Stokkum, D. S. Larsen, and R. van Grondelle.
Global and target analysis of time-resolved spectra.
Biochimica et Biophysica Acta (BBA) - Bioenergetics **1657**, 82–104 (2004).
- [71] J. R. Lakowicz.
Principles of Fluorescence Spectroscopy.
Third edition. Springer, Berlin (2006).
- [72] F. Langhojer.
New techniques in liquid-phase ultrafast spectroscopy.
Dissertation, Universität Würzburg (2009).
- [73] M. Kullmann.
Transiente Absorptionsspektroskopie an einem molekularen Schalter auf Spiropyranbasis.
Diplomarbeit, Universität Würzburg (2009).
- [74] M. Förster.
Design and implementation of four-wave-mixing setups in the ultraviolet regime.
Master thesis, Universität Würzburg (2011).
- [75] S. Keiber.
Investigation of the Electron-Transfer Properties of a Neutral Mixed-Valence Polymer and Introduction of a Shot-to-Shot Readout Mechanism for High Repetition Rates.
Master thesis, Universität Würzburg (2011).
- [76] D. Reitzenstein, T. Quast, F. Kanal, M. Kullmann, S. Ruetzel, M. S. Hammer, C. Deibel, V. Dyakonov, T. Brixner, and C. Lambert.
Synthesis and Electron Transfer Characteristics of a Neutral, Low-Band-Gap, Mixed-Valence Polyradical.
Chemistry of Materials **22**, 6641–6655 (2010).

- [77] A. Hipke.
Ultrafast Dynamics of the Novel, Intrinsically Chiral Model Bisporphyrin β,β' -Linked Bis[Tetraphenylporphyrinato-Zinc(II)].
Diplomarbeit, Universität Würzburg (2011).
- [78] P. Maine, D. Strickland, P. Bado, M. Pessot, and G. Mourou.
Generation of ultrahigh peak power pulses by chirped pulse amplification.
IEEE Journal of Quantum Electronics **24**, 398–403 (1988).
- [79] R. W. Boyd.
Nonlinear Optics, Third Edition.
Third edition. Academic Press (2008).
- [80] R. Trebino.
Frequency-Resolved Optical Gating: The Measurement of Ultrashort Laser Pulses.
Har/Cdr edition. Springer Netherlands (2002).
- [81] P. N. Butcher and D. Cotter.
The Elements of Nonlinear Optics.
Cambridge University Press (1991).
- [82] P. Hamm, R. A. Kaindl, and J. Stenger.
Noise suppression in femtosecond mid-infrared light sources.
Optics Letters **25**, 1798–1800 (2000).
- [83] R. L. Fork, C. V. Shank, C. Hirlimann, R. Yen, and W. J. Tomlinson.
Femtosecond white-light continuum pulses.
Optics Letters **8**, 1–3 (1983).
- [84] M. Ziolk, R. Naskrecki, and J. Karolczak.
Some temporal and spectral properties of femtosecond supercontinuum important in pump-probe spectroscopy.
Optics Communications **241**, 221–229 (2004).
- [85] F. Langhojer, F. Dimler, G. Jung, and T. Brixner.
Ultrafast Photoconversion of the Green Fluorescent Protein Studied by Accumulative Femtosecond Spectroscopy.
Biophysical Journal **96**, 2763–2770 (2009).
- [86] F. Langhojer, F. Dimler, G. Jung, and T. Brixner.
Product accumulation for ultrasensitive femtochemistry.
Optics Letters **32**, 3346–3348 (2007).
- [87] D. Axelrod, D. E. Koppel, J. Schlessinger, E. Elson, and W. W. Webb.
Mobility measurement by analysis of fluorescence photobleaching recovery kinetics.
Biophysical Journal **16**, 1055–1069 (1976).
- [88] A. Steinbacher.
High-Precision Chirality-Sensitive Spectroscopy in the Liquid Phase.
Master thesis, Universität Würzburg (2010).
- [89] H. Dürr and H. Bouas-Laurent.
Photochromism: Molecules and Systems.
Elsevier, Amsterdam (2003).

- [90] H. Bouas-Laurent and H. Dürr.
Organic photochromism (IUPAC Technical Report).
Pure and Applied Chemistry **73**, 639–665 (2001).
- [91] G. Jiang, Y. Song, X. Guo, D. Zhang, and D. Zhu.
Organic Functional Molecules towards Information Processing and High-Density Information Storage.
Advanced Materials **20**, 2888–2898 (2008).
- [92] F. Würthner and J. Rebek.
Photoschaltbare Katalyse mit synthetischen Rezeptoren.
Angewandte Chemie **107**, 503–505 (1995).
- [93] M. V. Peters, R. S. Stoll, A. Kühn, and S. Hecht.
Photoswitching of Basicity.
Angewandte Chemie International Edition **47**, 5968–5972 (2008).
- [94] U. Al-Atar, R. Fernandes, B. Johnsen, D. Baillie, and N. R. Branda.
A Photocontrolled Molecular Switch Regulates Paralysis in a Living Organism.
Journal of the American Chemical Society **131**, 15966–15967 (2009).
- [95] J. Ern, A. T. Bens, H. Martin, K. Kuldova, H. P. Trommsdorff, and C. Kryschi.
Ring-Opening and -Closure Reaction Dynamics of a Photochromic Dithienylethene Derivative.
The Journal of Physical Chemistry A **106**, 1654–1660 (2002).
- [96] M. Murakami, H. Miyasaka, T. Okada, S. Kobatake, and M. Irie.
Dynamics and Mechanisms of the Multiphoton Gated Photochromic Reaction of Diarylethene Derivatives.
Journal of the American Chemical Society **126**, 14764–14772 (2004).
- [97] B. Heinz, S. Malkmus, S. Laimgruber, S. Dietrich, C. Schulz, K. Rück-Braun, M. Braun, W. Zinth, and P. Gilch.
Comparing a Photoinduced Pericyclic Ring Opening and Closure: Differences in the Excited State Pathways.
Journal of the American Chemical Society **129**, 8577–8584 (2007).
- [98] S. Draxler, T. Brust, S. Malkmus, J. A. DiGirolamo, W. J. Lees, W. Zinth, and M. Braun.
Ring-opening reaction of a trifluorinated indolylfulgide: mode-specific photochemistry after pre-excitation.
Physical Chemistry Chemical Physics **11**, 5019–5027 (2009).
- [99] M. Rini, A. Holm, E. T. J. Nibbering, and H. Fidder.
Ultrafast UV-mid-IR Investigation of the Ring Opening Reaction of a Photochromic Spiropyran.
Journal of the American Chemical Society **125**, 3028–3034 (2003).
- [100] N. P. Ernsting.
Transient optical absorption spectroscopy of the photochemical spiropyran-merocyanine conversion.
Chemical Physics Letters **159**, 526–531 (1989).
- [101] C. J. Wohl and D. Kuciauskas.
Excited-State Dynamics of Spiropyran-Derived Merocyanine Isomers.
The Journal of Physical Chemistry B **109**, 22186–22191 (2005).
- [102] H. Fidder, M. Rini, and E. T. J. Nibbering.
The Role of Large Conformational Changes in Efficient Ultrafast Internal Conversion: Deviations from the Energy Gap Law.
Journal of the American Chemical Society **126**, 3789–3794 (2004).

- [103] J. Hopley, U. Pfeifer-Fukumura, M. Bletz, T. Asahi, H. Masuhara, and H. Fukumura. *Ultrafast Photo-Dynamics of a Reversible Photochromic Spiropyran*. The Journal of Physical Chemistry A **106**, 2265–2270 (2002).
- [104] A. Holm, M. Rini, E. T. J. Nibbering, and H. Fidder. *Femtosecond UV/mid-IR study of photochromism of the spiropyran 1',3'-dihydro-1',3',3'-trimethyl-6-nitrospiro[2H-1-benzopyran-2,2'-(2H)-indole] in solution*. Chemical Physics Letters **376**, 214–219 (2003).
- [105] A. Holm, O. F. Mohammed, M. Rini, E. Mukhtar, E. T. J. Nibbering, and H. Fidder. *Sequential Merocyanine Product Isomerization Following Femtosecond UV Excitation of a Spiropyran*. The Journal of Physical Chemistry A **109**, 8962–8968 (2005).
- [106] M. Irie. *Diarylethenes for Memories and Switches*. Chemical Reviews **100**, 1685–1716 (2000).
- [107] M. A. Wolak, C. J. Thomas, N. B. Gillespie, R. R. Birge, and W. J. Lees. *Tuning the Optical Properties of Fluorinated Indolylfulgimides*. The Journal of Organic Chemistry **68**, 319–326 (2003).
- [108] H. Satzger, C. Root, and M. Braun. *Excited-State Dynamics of trans- and cis-Azobenzene after UV Excitation in the $\pi\pi^*$ Band*. The Journal of Physical Chemistry A **108**, 6265–6271 (2004).
- [109] S. Aramaki and G. H. Atkinson. *Spiroanthropyran photochromism: picosecond time-resolved spectroscopy*. Journal of the American Chemical Society **114**, 438–444 (1992).
- [110] T. Yuzawa, A. Shimojima, and H. Takahashi. *Photochromic reaction of 6-nitro-1',3',3'-trimethylspiro[2H-1-benzopyran-2,2'-indoline]: time-resolved resonance Raman and absorption study*. Journal of Molecular Structure **352-353**, 497–507 (1995).
- [111] H. Görner. *Photochromism of nitrospiropyrans: effects of structure, solvent and temperature*. Physical Chemistry Chemical Physics **3**, 416–423 (2001).
- [112] A. K. Chibisov and H. Görner. *Photochromism of spirobenzopyranindolines and spironaphthopyranindolines*. Physical Chemistry Chemical Physics **3**, 424–431 (2001).
- [113] N. W. Tyer and R. S. Becker. *Photochromic spiropyran. I. Absorption spectra and evaluation of the .pi.-electron orthogonality of the constituent halves*. Journal of the American Chemical Society **92**, 1289–1294 (1970).
- [114] R. Heiligman-Rim, Y. Hirshberg, and E. Fischer. *PHOTOCHROMISM IN SPIROPYRANS. PART IV.1 EVIDENCE FOR THE EXISTENCE OF SEVERAL FORMS OF THE COLORED MODIFICATION*. The Journal of Physical Chemistry **66**, 2465–2470 (1962).
- [115] M. Bletz, U. Pfeifer-Fukumura, U. Kolb, and W. Baumann. *Ground- and First-Excited-Singlet-State Electric Dipole Moments of Some Photochromic Spirobenzopyrans in Their Spiropyran and Merocyanine Form \ddagger* . The Journal of Physical Chemistry A **106**, 2232–2236 (2002).

- [116] G. R. Fleming.
Chemical Applications of Ultrafast Spectroscopy, volume 13 of *International Series of Monographs on Chemistry*.
Oxford University Press, USA (1986).
- [117] J. Hopley, V. Malatesta, R. Millini, L. Montanari, W. O. N. Parker, and Jr.
Proton exchange and isomerisation reactions of photochromic and reverse photochromic spiropyrans and their merocyanine forms.
Physical Chemistry Chemical Physics **1**, 3259–3267 (1999).
- [118] C. Schiele and G. Arnold.
Zur Struktur der photochromen Form des spiro-6-nitro-[2H-1-benzopyran-2,2'-1',3',3'-trimethylindolins].
Tetrahedron Letters **8**, 1191–1195 (1967).
- [119] R. D. B. Fraser and E. Suzuki.
Resolution of overlapping bands. Functions for simulating band shapes.
Analytical Chemistry **41**, 37–39 (1969).
- [120] J. Sevilla, M. Dominguez, F. Garcia-Blanco, and M. Blazquez.
Resolution of absorption spectra.
Computers & Chemistry **13**, 197–200 (1989).
- [121] I. Gómez, M. Reguero, and M. A. Robb.
Efficient Photochemical Merocyanine-to-Spiropyran Ring Closure Mechanism through an Extended Conical Intersection Seam. A Model CASSCF/CASPT2 Study.
The Journal of Physical Chemistry A **110**, 3986–3991 (2006).
- [122] Y. Sheng, J. Leszczynski, A. A. Garcia, R. Rosario, D. Gust, and J. Springer.
Comprehensive Theoretical Study of the Conversion Reactions of Spiropyrans: Substituent and Solvent Effects.
The Journal of Physical Chemistry B **108**, 16233–16243 (2004).
- [123] U. Åberg, E. Åkesson, and V. Sundström.
Excited state dynamics of barrierless isomerization in solution.
Chemical Physics Letters **215**, 388–394 (1993).
- [124] Q. Xu and G. R. Fleming.
Isomerization Dynamics of 1,1'-Diethyl-4,4'-Cyanine (1144C) Studied by Different Third-Order Nonlinear Spectroscopic Measurements.
The Journal of Physical Chemistry A **105**, 10187–10195 (2001).
- [125] G. Vogt, P. Nuernberger, G. Gerber, R. Improtta, and F. Santoro.
Femtosecond study on the isomerization dynamics of NK88. II. Excited-state dynamics.
The Journal of Chemical Physics **125**, 044513 (2006).
- [126] P. Nuernberger, G. Vogt, G. Gerber, R. Improtta, and F. Santoro.
Femtosecond study on the isomerization dynamics of NK88. I. Ground-state dynamics after photoexcitation.
The Journal of Chemical Physics **125**, 044512 (2006).
- [127] C. Rullière.
Laser action and photoisomerisation of 3,3'-diethyl oxadicyanone iodide (DODCI): Influence of temperature and concentration.
Chemical Physics Letters **43**, 303–308 (1976).

- [128] M. M. Awad, P. K. McCarthy, and G. J. Blanchard.
Photoisomerization of Cyanines. A Comparative Study of Oxygen- and Sulfur-Containing Species.
The Journal of Physical Chemistry **98**, 1454–1458 (1994).
- [129] I. Baraldi, F. Momicchioli, G. Ponterini, A. S. Tatikolov, and D. Vanossi.
Photoisomerization of simple merocyanines: a theoretical and experimental comparison with polyenes and symmetric cyanines.
Physical Chemistry Chemical Physics **5**, 979–987 (2003).
- [130] F. Momicchioli, I. Baraldi, and G. Berthier.
Theoretical study of trans-cis photoisomerism in polymethine cyanines.
Chemical Physics **123**, 103–112 (1988).
- [131] M. Caselli, F. Momicchioli, and G. Ponterini.
Modelling of the cis-trans partitioning in the photoisomerizations of cyanines and stilbene derivatives.
Chemical Physics Letters **216**, 41–46 (1993).
- [132] S. Rentsch.
Modeling of the fast photoisomerisation process in polymethine dyes.
Chemical Physics **69**, 81–87 (1982).
- [133] A. C. Benniston, A. Harriman, and C. McAvoy.
Photoisomerization of sterically hindered merocyanine dyes.
Journal of the Chemical Society, Faraday Transactions **93**, 3653–3662 (1997).
- [134] F. Würthner, S. Yao, T. Debaerdemaeker, and R. Wortmann.
Dimerization of Merocyanine Dyes. Structural and Energetic Characterization of Dipolar Dye Aggregates and Implications for Nonlinear Optical Materials.
Journal of the American Chemical Society **124**, 9431–9447 (2002).
- [135] Y. Futami, M. L. S. Chin, S. Kudoh, M. Takayanagi, and M. Nakata.
Conformations of nitro-substituted spiropyran and merocyanine studied by low-temperature matrix-isolation infrared spectroscopy and density-functional-theory calculation.
Chemical Physics Letters **370**, 460–468 (2003).
- [136] A. V. Kulinich, N. A. Derevyanko, A. A. Ishchenko, S. L. Bondarev, and V. N. Knyukshto.
Structure and fluorescence properties of indole cyanine and merocyanine dyes with partially locked polymethine chain.
Journal of Photochemistry and Photobiology A: Chemistry **200**, 106–113 (2008).
- [137] C. Lenoble and R. S. Becker.
Photophysics, photochemistry, kinetics, and mechanism of the photochromism of 6'-nitroindolinospiropyran.
The Journal of Physical Chemistry **90**, 62–65 (1986).
- [138] A. Gahlmann, I. Lee, and A. H. Zewail.
Direct Structural Determination of Conformations of Photoswitchable Molecules by Laser Desorption-Electron Diffraction.
Angewandte Chemie International Edition **49**, 6524–6527 (2010).
- [139] J. A. Kloepfer, V. H. Vilchiz, V. A. Lenchenkov, A. C. Germaine, and S. E. Bradforth.
The ejection distribution of solvated electrons generated by the one-photon photodetachment of aqueous $I^{sup -}$ and two-photon ionization of the solvent.
The Journal of Chemical Physics **113**, 6288 (2000).

- [140] T. Lippert, A. Koskelo, and P. O. Stoutland.
Direct Observation of a Photoinduced Wolff Rearrangement in PMMA Using Ultrafast Infrared Spectroscopy.
Journal of the American Chemical Society **118**, 1551–1552 (1996).
- [141] T. Lippert and P. O. Stoutland.
Laser-material interactions probed with picosecond infrared spectroscopy.
Applied Surface Science **109-110**, 43–47 (1997).
- [142] G. T. Burdzinski, J. Wang, T. L. Gustafson, and M. S. Platz.
Study of Concerted and Sequential Photochemical Wolff Rearrangement by Femtosecond UV-vis and IR Spectroscopy.
Journal of the American Chemical Society **130**, 3746–3747 (2008).
- [143] G. Burdzinski, J. Réhault, J. Wang, and M. S. Platz.
A Study of the Photochemistry of Diazo Meldrum's Acid by Ultrafast Time-Resolved Spectroscopies.
The Journal of Physical Chemistry A **112**, 10108–10112 (2008).
- [144] B. D. Grant, N. J. Clecak, R. J. Twieg, and C. G. Willson.
Deep UV photoresists I. Meldrum's diazo sensitizer.
IEEE Transactions on Electron Devices **28**, 1300–1305 (1981).
- [145] M. Endo, Y. Tani, M. Sasago, N. Nomura, and S. Das.
Application of Photobleachable Positive Resist and Contrast Enhancement Material to KrF Excimer Laser Lithography.
Japanese Journal of Applied Physics **28**, 2357–2361 (1989).
- [146] M. A. Winnik, F. Wang, T. Nivaggioli, Z. Hruska, H. Fukumura, and H. Masuhara.
Photoreaction of Meldrum's diazo in poly(methyl methacrylate) matrixes.
Journal of the American Chemical Society **113**, 9702–9704 (1991).
- [147] H. Fujiwara, Y. Nakajima, H. Fukumura, and H. Masuhara.
Laser Ablation Dynamics of a Poly(methyl methacrylate) Film Doped with 5-Diazo Meldrum's Acid.
The Journal of Physical Chemistry **99**, 11481–11488 (1995).
- [148] C. Hahn, T. Lippert, and A. Wokaun.
Comparison of the Ablation Behavior of Polymer Films in the IR and UV with Nanosecond and Picosecond Pulses.
The Journal of Physical Chemistry B **103**, 1287–1294 (1999).
- [149] P. Hamm.
Coherent effects in femtosecond infrared spectroscopy.
Chemical Physics **200**, 415–429 (1995).
- [150] M. Frisch, G. Trucks, H. Schlegel, G. Scuseria, M. Robb, J. Cheeseman, J. Montgomery, T. Vreven, K. Kudin, J. Burant, J. Millam, S. Iyengar, J. Tomasi, V. Barone, B. Men-
nucci, M. Cossi, G. Scalmani, N. Rega, G. Petersson, H. Nakatsuji, M. Hada, M. Ehara,
K. Toyota, R. Fukuda, J. Hasegawa, M. Ishida, T. Nakajima, Y. Honda, O. Kitao, H. Nakai,
M. Klene, X. Li, J. Knox, H. Hratchian, J. Cross, V. Bakken, C. Adamo, J. Jaramillo,
R. Gomperts, R. Stratmann, O. Yazyev, A. Austin, R. Cammi, C. Pomelli, J. Ochterski,
P. Ayala, K. Morokuma, G. Voth, P. Salvador, J. Dannenberg, V. Zakrzewski, S. Dapprich,
A. Daniels, M. Strain, O. Farkas, D. Malick, A. Rabuck, K. Raghavachari, J. Foresman,
J. Ortiz, Q. Cui, A. Baboul, S. Clifford, J. Cioslowski, B. Stefanov, G. Liu, A. Liashenko,

- P. Piskorz, I. Komaromi, R. Martin, D. Fox, T. Keith, A. Laham, C. Peng, A. Nanayakkara, M. Challacombe, P. Gill, B. Johnson, W. Chen, M. Wong, C. Gonzalez, and J. Pople. *Gaussian 03, Revision C.02* (2003).
- [151] A. D. Becke.
Density-functional exchange-energy approximation with correct asymptotic behavior.
Physical Review A **38**, 3098 (1988).
- [152] A. D. Becke.
Density-functional thermochemistry. III. The role of exact exchange.
Journal of Chemical Physics **98**, 5648–5652 (1993).
- [153] C. Lee, W. Yang, and R. G. Parr.
Development of the Colle-Salvetti correlation-energy formula into a functional of the electron density.
Physical Review B **37**, 785 (1988).
- [154] A. Bogdanova and V. Popik.
Wavelength-Dependent Photochemistry of Diazo Meldrum's Acid and Its Spirocyclic Isomer, Diazirino Meldrum's Acid: Wolff Rearrangement versus Isomerization.
Journal of the American Chemical Society **125**, 1456–1457 (2003).
- [155] P. Rudolf, J. Buback, J. Aulbach, P. Nuernberger, and T. Brixner.
Ultrafast Multisequential Photochemistry of 5-Diazo Meldrum's Acid.
Journal of the American Chemical Society **132**, 15213–15222 (2010).
- [156] V. Nikolaev, V. Shevchenko, M. Platz, and N. Khimich.
Chemistry of diazocarbonyl compounds: XXV. Comparative photochemistry of diazo compounds and sulfur ylides of the 1,3-dioxane-4,6-dione series.
Russian Journal of Organic Chemistry **42**, 815–827 (2006).
- [157] W. Kirmse.
100 Years of the Wolff Rearrangement.
European Journal of Organic Chemistry **2002**, 2193–2256 (2002).
- [158] T. Livinghouse and R. V. Stevens.
A direct synthesis of spiro-activated cyclopropanes from alkenes via the irradiation of isopropylidene diazomalonate.
Journal of the American Chemical Society **100**, 6479–6482 (1978).
- [159] A. P. Scott and L. Radom.
Harmonic Vibrational Frequencies: An Evaluation of Hartree-Fock, Moller-Plesset, Quadratic Configuration Interaction, Density Functional Theory, and Semiempirical Scale Factors.
The Journal of Physical Chemistry **100**, 16502–16513 (1996).
- [160] J. Buback, M. Kullmann, F. Langhojer, P. Nuernberger, R. Schmidt, F. Würthner, and T. Brixner.
Ultrafast bidirectional photoswitching of a spiropyran.
Journal of the American Chemical Society **132**, 16510–16519 (2010).
- [161] J. Pacansky and J. R. Lyerla.
Photochemical Decomposition Mechanisms for AZ-Type Photoresists.
IBM Journal of Research and Development **23**, 42–55 (1979).
- [162] D. Wolpert, M. Schade, and T. Brixner.
Femtosecond midinfrared study of the photoinduced Wolff rearrangement of diazonaphthoquinone.
The Journal of Chemical Physics **129**, 094504 (2008).

- [163] A. Bogdanova and V. Popik.
Experimental and Theoretical Investigation of Reversible Interconversion, Thermal Reactions, and Wavelength-Dependent Photochemistry of Diazo Meldrum's Acid and Its Diazirine Isomer, 6,6-Dimethyl-5,7-dioxo-1,2-diaza-spiro[2,5]oct-1-ene-4,8-dione.
Journal of the American Chemical Society **125**, 14153–14162 (2003).
- [164] J. Wang, J. Kubicki, T. L. Gustafson, and M. S. Platz.
The Dynamics of Carbene Solvation: An Ultrafast Study of p-Biphenyltrifluoromethylcarbene.
Journal of the American Chemical Society **130**, 2304–2313 (2008).
- [165] Y. Zhang, G. Burdzinski, J. Kubicki, S. Vyas, C. M. Hadad, M. Sliwa, O. Poizat, G. Buntinx, and M. S. Platz.
Study of the S1 Excited State of para-Methoxy-3-phenyl-3-methyl Diazirine by Ultrafast Time Resolved UV-Vis and IR Spectroscopies and Theory.
Journal of the American Chemical Society **131**, 13784–13790 (2009).
- [166] J. Wang, J. Kubicki, H. Peng, and M. S. Platz.
Influence of Solvent on Carbene Intersystem Crossing Rates.
Journal of the American Chemical Society **130**, 6604–6609 (2008).
- [167] G. Burdzinski and M. S. Platz.
Ultrafast time-resolved studies of the photochemistry of diazo carbonyl compounds.
Journal of Physical Organic Chemistry **23**, 308–314 (2010).
- [168] D. Williams, G. Timateo, and G. Walter.
The Infra-red Absorption of Mixtures of Water and Organic Liquids.
Journal of Physical Chemistry **41**, 645–649 (1937).
- [169] E. T. Nibbering, H. Fidder, and E. Pines.
Ultrafast Chemistry: Using Time-Resolved Vibrational Spectroscopy for Interrogation of Structural Dynamics.
Annual Review of Physical Chemistry **56**, 337–367 (2005).
- [170] V. V. Popik.
The role of molecular geometry in the Wolff rearrangement of β -alpha;-diazocarbonyl compounds — Conformational control or structural constraints?
Canadian Journal of Chemistry **83**, 1382–1390 (2005).
- [171] P. Fischer and F. Hache.
Nonlinear optical spectroscopy of chiral molecules.
Chirality **17**, 421–437 (2005).
- [172] C. Niezborala and F. Hache.
Measuring the dynamics of circular dichroism in a pump-probe experiment with a Babinet-Soleil Compensator.
Journal of the Optical Society of America B **23**, 2418–2424 (2006).
- [173] J. Helbing and M. Bonmarin.
Vibrational circular dichroism signal enhancement using self-heterodyning with elliptically polarized laser pulses.
The Journal of Chemical Physics **131**, 174507 (2009).
- [174] X. Xie and J. D. Simon.
Protein conformational relaxation following photodissociation of carbon monoxide from carbon-monoxymyoglobin: picosecond circular dichroism and absorption studies.
Biochemistry **30**, 3682–3692 (1991).

- [175] S. Milder, S. Bjorling, I. Kuntz, and D. Kliger.
Time-resolved circular dichroism and absorption studies of the photolysis reaction of (carbon-monooxy)myoglobin.
Biophysical Journal **53**, 659–664 (1988).
- [176] J. W. Lewis, R. A. Goldbeck, D. S. Kliger, X. Xie, R. C. Dunn, and J. D. Simon.
Time-resolved circular dichroism spectroscopy: experiment, theory, and applications to biological systems.
The Journal of Physical Chemistry **96**, 5243–5254 (1992).
- [177] A. Trifonov, I. Buchvarov, A. Lohr, F. Würthner, and T. Fiebig.
Broadband femtosecond circular dichroism spectrometer with white-light polarization control.
Review of Scientific Instruments **81**, 043104 (2010).
- [178] W. Moffitt, R. B. Woodward, A. Moscowitz, W. Klyne, and C. Djerassi.
Structure and the Optical Rotatory Dispersion of Saturated Ketones.
Journal of the American Chemical Society **83**, 4013–4018 (1961).
- [179] G. Hänisch and G. Beier.
Ein Polarimeter zur Messung schneller chemischer Reaktionen.
Fresenius' Zeitschrift für Analytische Chemie **261**, 280–286 (1972).
- [180] P. D. Rice, Y. Y. Shao, S. R. Erskine, T. G. Teague, and D. R. Bobbitt.
Specific rotation measurements from peak height data, with a Gaussian peak model.
Talanta **36**, 473–478 (1989).
- [181] D. R. Bobbitt and E. S. Yeung.
Improvements in Detectabilities in Polarimeters Using High-Frequency Modulation.
Applied Spectroscopy **40**, 407–410 (1986).
- [182] J. Lee and D. Su.
Improved common-path optical heterodyne interferometer for measuring small optical rotation angle of chiral medium.
Optics Communications **256**, 337–341 (2005).
- [183] S. R. Systems.
Digital Lock-In Amplifiers SR810 and SR830 (1997).
- [184] Y. Guo and W. S. Jenks.
Photolysis of Alkyl Aryl Sulfoxides: α -Cleavage, Hydrogen Abstraction, and Racemization.
The Journal of Organic Chemistry **62**, 857–864 (1997).
- [185] D. R. Lide.
CRC handbook of chemistry and physics.
CRC Press, Boca Raton, FLa. [u.a.] (2009).
- [186] A. G. Griesbeck and U. J. Meierhenrich.
Asymmetric Photochemistry and Photochirogenesis.
Angewandte Chemie International Edition **41**, 3147–3154 (2002).
- [187] S. S. Bychkov, B. A. Grishanin, and V. N. Zadkov.
Laser synthesis of chiral molecules in isotropic racemic media.
Journal of Experimental and Theoretical Physics **93**, 24–32 (2001).
- [188] M. Shapiro, E. Frishman, and P. Brumer.
Coherently Controlled Asymmetric Synthesis with Achiral Light.
Physical Review Letters **84**, 1669 (2000).

- [189] Y. Fujimura, L. González, K. Hoki, J. Manz, and Y. Ohtsuki.
Selective preparation of enantiomers by laser pulses: quantum model simulation for H₂POSH.
Chemical Physics Letters **306**, 1–8 (1999).
- [190] A. Bornschlegl, C. Logé, and U. Boesl.
Investigation of CD effects in the multi photon ionisation of R-(+)-3-methylcyclopentanone.
Chemical Physics Letters **447**, 187–191 (2007).
- [191] C. Toro, L. De Boni, N. Lin, F. Santoro, A. Rizzo, and F. E. Hernandez.
Two-Photon Absorption Circular Dichroism: A New Twist in Nonlinear Spectroscopy.
Chemistry - A European Journal **16**, 3504–3509 (2010).
- [192] K. Mori, Y. Ishibashi, H. Matsuda, S. Ito, Y. Nagasawa, H. Nakagawa, K. Uchida, S. Yokojima, S. Nakamura, M. Irie, and H. Miyasaka.
One-Color Reversible Control of Photochromic Reactions in a Diarylethene Derivative: Three-Photon Cyclization and Two-Photon Cycloreversion by a Near-Infrared Femtosecond Laser Pulse at 1.28 microns.
Journal of the American Chemical Society **133**, 2621–2625 (2011).
- [193] M. Berberich, A. Krause, M. Orlandi, F. Scandola, and F. Würthner.
Toward Fluorescent Memories with Nondestructive Readout: Photoswitching of Fluorescence by Intramolecular Electron Transfer in a Diaryl Ethene-Perylene Bisimide Photochromic System13.
Angewandte Chemie International Edition **47**, 6616–6619 (2008).
- [194] Y. Ishibashi, M. Fujiwara, T. Umesato, H. Saito, S. Kobatake, M. Irie, and H. Miyasaka.
Cyclization Reaction Dynamics of a Photochromic Diarylethene Derivative as Revealed by Femtosecond to Microsecond Time-Resolved Spectroscopy.
The Journal of Physical Chemistry C **115**, 4265–4272 (2011).
- [195] T. Okuyama, Y. Tani, K. Miyake, and Y. Yokoyama.
Chiral Helicenoid Diarylethene with Large Change in Specific Optical Rotation by Photochromism1,2.
The Journal of Organic Chemistry **72**, 1634–1638 (2007).
- [196] E. J. Galvez.
Achromatic polarization-preserving beam displacer.
Optics Letters **26**, 971–973 (2001).
- [197] M. Ninck, A. Galler, T. Feurer, and T. Brixner.
Programmable common-path vector field synthesizer for femtosecond pulses.
Optics Letters **32**, 3379–3381 (2007).
- [198] M. Cho.
Two-dimensional circularly polarized pump-probe spectroscopy.
The Journal of Chemical Physics **119**, 7003 (2003).
- [199] G. Ghosh.
Handbook of optical constants of solids.
Academic Press (1998).
- [200] A. Diaspro, P. Bianchini, G. Vicdomini, M. Faretta, P. Ramoino, and C. Usai.
Multi-photon excitation microscopy.
Biomedical engineering online **5**, 36 (2006).

- [201] I. V. Hertel, I. Shchatsinin, T. Laarmann, N. Zhavoronkov, H. Ritze, and C. P. Schulz.
Fragmentation and Ionization Dynamics of C60 in Elliptically Polarized Femtosecond Laser Fields.
Physical Review Letters **102**, 023003 (2009).
- [202] Y. Chen, J. T. Yang, and H. M. Martinez.
Determination of the secondary structures of proteins by circular dichroism and optical rotatory dispersion.
Biochemistry **11**, 4120–4131 (1972).
- [203] E. Chen, R. A. Goldbeck, and D. S. Kliger.
Nanosecond time-resolved polarization spectroscopies: Tools for probing protein reaction mechanisms.
Methods **52**, 3–11 (2010).
- [204] T. Dartigalongue and F. Hache.
Precise alignment of a longitudinal Pockels cell for time-resolved circular dichroism experiments.
Journal of the Optical Society of America B **20**, 1780–1787 (2003).
- [205] P. Nuernberger, K. F. Lee, A. Bonvalet, M. H. Vos, and M. Joffre.
Multiply excited vibration of carbon monoxide in the primary docking site of hemoglobin following photolysis from the heme.
J. Phys. Chem. Lett. **1**, 2077–2081 (2010).
- [206] F. Filsinger, J. Küpper, G. Meijer, L. Holmegaard, J. H. Nielsen, I. Nevo, J. L. Hansen, and H. Stapelfeldt.
Quantum-state selection, alignment, and orientation of large molecules using static electric and laser fields.
The Journal of Chemical Physics **131**, 064309 (2009).
- [207] R. McCalley, E. Shimshick, and H. McConnell.
The effect of slow rotational motion on paramagnetic resonance spectra.
Chemical Physics Letters **13**, 115–119 (1972).
- [208] H. Stapelfeldt and T. Seideman.
Colloquium: Aligning molecules with strong laser pulses.
Reviews of Modern Physics **75**, 543 (2003).
- [209] K. Yamanouchi, G. Gerber, and A. D. Bandrauk.
Progress in Ultrafast Intense Laser Science VI: 6.
First edition. Springer Berlin Heidelberg (2010).
- [210] F. Rosca-Pruna and M. J. J. Vrakking.
Experimental Observation of Revival Structures in Picosecond Laser-Induced Alignment of I₂.
Physical Review Letters **87**, 153902 (2001).
- [211] K. Oda, M. Hita, S. Minemoto, and H. Sakai.
All-Optical Molecular Orientation.
Physical Review Letters **104**, 213901 (2010).
- [212] J. N. Moore, P. A. Hansen, and R. M. Hochstrasser.
Iron-carbonyl bond geometries of carboxymyoglobin and carboxyhemoglobin in solution determined by picosecond time-resolved infrared spectroscopy.
Proceedings of the National Academy of Sciences **85**, 5062–5066 (1988).

-
- [213] V. B. Borisov, U. Liebl, F. Rappaport, J. Martin, J. Zhang, R. B. Gennis, A. A. Konstantinov, and M. H. Vos.
Interactions between Heme d and Heme b₅₉₅ in Quinol Oxidase bd from Escherichia coli: A Photoselection Study Using Femtosecond Spectroscopy†.
Biochemistry **41**, 1654–1662 (2002).
- [214] M. Lim, T. A. Jackson, and P. A. Anfinrud.
Orientalional distribution of CO before and after photolysis of MbCO and HbCO: A determination using time-resolved polarized mid-IR spectroscopy.
J. Am. Chem. Soc. **126**, 7946–7957 (2004).

Acknowledgements

At last, I want to thank all the people who have contributed in any way to this thesis. Among those I want to mention explicitly:

- Prof. Dr. Tobias Brixner for giving me a lot of liberties in the selection of my experiments, for his professional support and that he motivated me to accept new challenges.
- Dr. Patrick Nürnberger for being interested instantly in any given problem, as abstruse or simple it may be. With his almost infinite knowledge he was able to help in any situation I bothered him with. Especially I want to thank him for his never-ending patience assuring that any question is welcome.
- Andreas Steinbacher for showing a great deal of initiative in any situation, for his great LabVIEW skills, and for taking over and investing in the challenging polarimeter project.
- Martin Kullmann for bearing my impatience and for continuing very successfully the BIPS experiments.
- Sebastian Schott for having the decisive idea to calculate the anisotropy and for his efforts to realize the polarization-mirroring setup.
- Philipp Rudolf for including me in the DMA project, for his steady optimism and for his enjoyable nature.
- Ulrike Selig on the one hand for the professional support that I have called on many times. On the other hand for her friendship, her loyalty and her open and straightforward character, which, if necessary, does not shy from critical words.
- Florian Langhojer for everything he has taught me. Without his support this thesis would not have been possible at all.
- Frank Dimler for being such a helpful person.
- Ralf Schmidt for the synthesis of 6,8-dinitro BIPS.
- My lab students Anja Krischke and Daniel Schilling who contributed to several parts of this work.
- The people supporting us in the background: The workshops managed by Wolfgang Liebler and Jürgen Zimmermann, our technical staff Belinda Böhm and Sabine Fuchs, and our secretary Andrea Hoffelner.

- A. and F. Lohmüller for their POV-Ray tutorial on <http://www.f-lohmueller.de> that allowed for many graphics in this thesis.
- The “Fonds der Chemischen Industrie” for financial support.
- Andreas Steinbacher, Florian Kanal, Patrick Nürnberger, Philipp Rudolf, Sebastian Schott and Ulrike Selig for carefully and patiently proofreading this thesis.
- The PC1 team for the friendly and helpful atmosphere, especially for winning the ChemCup two times in a row.
- The developers of Wormux and Quake as well as the people in the PC1 that played these games.
- My parents, Elisabeth and Michael, and my sister, Franziska, for their endless support during my whole life.
- My wife Verena for her faith in me, her love, support and patience.